UNIVERSITY OF BARI ALDO MORO

Department of Earth and Geo-Environmental Sciences

PH.D. IN GEOSCIENCES

CYCLE XXXVIII

Academic Discipline: SOLID EARTH GEOPHYSICS – GEO/10

THESIS TITLE

REGIONAL SCALE IDENTIFICATION OF SLOPE SUSCEPTIBILITY TO CO-SEISMIC LANDSLIDES IN URBAN AND PERI-URBAN AREAS OF DAUNIA (APULIA REGION – SOUTHERN ITALY)

PhD student:
Dr. Flaviana Fredella

Fredella
Flaviana
25.05.2026
18:55:36
UTC

Supervisors:
Prof. Vincenzo Del Gaudio
Dr. Janusz Wasowski

VINCENZO
DEL
GAUDIO
26.05.2026
08:22:21
GMT+02:00

Co-Supervisors:
Dr. Paola Capone
Dr. Nicola Venisti

Coordinator:
Prof. Roberto Sulpizio

ROBERTO
SULPIZIO
27.05.2026
09:34:50
GMT+02:00

FINAL EXAM 2026

Funded by the European Union - Next Generation EU, Mission 4 Component 2 CUP H93C22000610002 Investment 1.3 Ministerial Decree no. 341 of 15 March 2022 - National Recovery and Resilience Plan. Project: "RETURN - multi-Risk sciEnce for resilienT commUnities undeR a changiNg climate" Cod: PE00000005

ABSTRACT

The aim of this thesis is to propose and test advances in developing an expeditious procedure for identifying the slopes most susceptible to earthquake-induced landslides on a regional scale, in order to determine the areas most prone to develop critical issues following a seismic event. This procedure could provide useful information for improving preparedness for future seismic scenarios and seismic emergency management.

To this end, we revisited a probabilistic approach proposed by Del Gaudio et al. in 2003 for estimating the resistance demand posed to slopes by seismicity. Based on Newmark's model of 1965, it estimates the critical acceleration that a slope should have to keep the probability of exceeding critical values of Newmark's displacement during seismic shaking with an energy level measured by Arias intensity within a precautionary limit. Compared to previous implementations of this approach, the main novelty introduced in the present work is the different way in which the site effect is incorporated into the assessment of the resistance demand. Previously it was introduced at the stage of evaluating seismic shaking exceedance probability by including, within the adopted ground motion prediction model, a site factor dependent on a qualitative classification of the soil type or the average of S-waves velocity in the first 30 meters of subsoil (V_{S30}). In this work the site effect is introduced by means of a site-specific amplification factor expressed in terms of Arias intensity. An average value of this amplification factor and the relative standard deviation were calculated for multiple seismic inputs representative of relevant seismic scenarios by using 1D lithostratigraphic modeling of the site response. For this modeling, data deriving from seismic microzonation studies were used with a major role played by advanced analysis of ambient noise recordings, while neglecting topographic effect, which was assumed to have a lesser influence. Average and standard deviation of the amplification factors were then used to modify the exceedance probability of different level of Arias intensity expected for unamplified site conditions.

As further refinement, to calculate the slope resistance demand to seismic shaking, a new simple empirical relationship was used to estimate the Newmark displacement, which was specifically calibrated on data from the study area. This relationship proved to have a better predictive capability than other more general relationships calibrated on data from different regions, even those characterized by a more complex functional form.

While, however, the use of more specific predictive equation of Newmark's displacement was found to have a limited influence on the assessment of the resistance demand, incorporating a site-specific amplification factor produced a significant increase. Compared to using V_{S30}-based amplification factors, those obtained by incorporating a site-specific value calculated using the procedure tested in this work led to values greater by a factor of up to 4 and the resulting resistance demand was found to increase by a factor of up to about 3.

The topography-related effect was also investigated at a site in the study area using 2D modeling of the site response. The test results confirmed – at least for the site analyzed in this work – that the pure topographic effect produces a lower effect, increasing shaking energy at most by 60%.

TABLE OF CONTENTS

1. INTRODUCTION

1.1 Motivation

This study is part of the European research program RETURN, which aims to increase the resilience of communities with respect to the effects of environmental multi-hazards. In particular, the study is part of the spoke VS2 – “Ground instabilities”, aimed at parameterizing the weight of predisposing, preparatory and triggering factors, as well as developing methodologies to quantitatively reconstruct ground instability scenarios through probabilistic and deterministic approaches at scales ranging from local to regional.

In this context, this PhD thesis is a contribution to studies aimed at mitigating the impact that earthquakes can have on a territory paying attention to possible co-seismic phenomena, which can both increase the damage already caused by an earthquake and inflict further damage to structures and infrastructures that had resisted the direct effect of the earthquake itself.

Among co-seismic phenomena, landslides produce the greatest damage effects: they can damage areas with an extension that depends on various factors, such as the magnitude and the depth of the event, the geological and topographical conditions of the area and the amplitude, frequency and duration of the seismic shaking. Seismic-induced landslides can occur at considerable distances from the epicenter of the earthquake; in this regard, Keefer (1984) reported such phenomena at distances ranging from tens to hundreds of kilometers from the source of events with a magnitude of 6 to 7. An example of an earthquake that triggered many landslides is the Wenchuan earthquake (May 12, 2008–M = 7.9), which triggered about 200.000 landslides responsible for about 20.000 victims, also inflicting a lot of damage to communication routes (Fan et al., 2018).

A role in the activation of slope failures can be played by the amplification effects of seismic shaking, which in general increase the problems associated with the occurrence of earthquakes. There are two types of amplification: i) lithostratigraphic and ii) topographic amplification. The lithostratigraphic amplification is caused by the presence of softer material resting on a stiffer substratum, creating an impedance contrast which causes constructive interference between the incident and reflected waves within the surface layer (Baise et al., 2016; Mayoral et al., 2019) and consequently amplification of the ground motion and extension of the seismic shaking duration; the topographic amplification is due to the waves diffraction by different surface irregularities which focuses the seismic waves energy on the top of the relief (Geli et al., 1988; Glinsky et al., 2019). Both mechanisms amplify seismic shaking at site-specific frequencies.

Earthquake damaging effects can be aggravated when amplification and landslide phenomena combine with each other, since the presence of pre-existing landslides could amplify the ground motion and, at the same time, facilitate the reactivation of the landslide itself (Bozzano et al., 2008).

The aim of this work is to make advances in the development of methodologies for identifying and classifying slopes potentially susceptible to seismically induced landslides, in urban and peri-urban areas, with expeditious methods that can be applied over large areas, rather than at the scale of an individual slope.

In this regard, data collected during ongoing Seismic Microzonation (SM) studies were exploited. These studies identify and classify local hazard factors subdividing the territory into "microzones" with different local hazard properties. One of the SM objectives is to identify the slopes potentially prone to instability under seismic shaking and to characterize their behavior. This information is necessary for urban planning and emergency management preparedness (SM Working Group, 2015).

1.2 State of the art

In the context of seismic-induced landslides at the regional scale, several works have been conducted with the aim of developing approaches for evaluating slopes potentially susceptible to this phenomenon (Del Gaudio et al., 2003; Saygili and Rathje, 2009; Sun and Huang, 2023; Ojomo et al., 2024).

Some works have made use of empirical relationships proposed in previous studies (e.g., Jibson et al., 2000; Saygili and Rathje, 2008; Romeo, 2000) to predict expected values of the Newmark displacement D_N, defined as a simplified measure of the permanent displacement produced along a potential sliding surface of the ground motion generated by an earthquake and described by an accelerogram (Newmark, 1965). Empirical relations link D_N to i) a parameter describing the expected seismic shaking for given seismic scenarios, such as the Arias intensity (Arias, 1970), and ii) a parameter representing the shear strength of the slope materials, such as the slope critical acceleration. In this regard, starting from an accelerometric recording, the induced displacement is evaluated along the sliding surface as the effect of seismic ground accelerations acting for the time intervals in which they exceed a resistance threshold expressed as "critical acceleration". This depends on the slope angle and on the geotechnical parameters of the slope materials (i.e., cohesion, friction angle, pore pressure). Some authors (e.g., Wilson and Keefer, 1985) proposed critical thresholds of Newmark displacement for different landslide types, whose exceedance makes likely the slope failure: 10 cm for soil slopes and 2 cm for rock slopes.

This approach has been initially used for fixed seismic scenarios (e.g., Jibson et al., 2000) where, considering an event with specific features, the values of a shaking parameter expected at the sites of the study area are estimated using empirical attenuation relationships which predict how this parameter changes as a function of the event magnitude and the site distance from the seismic source; these values are then applied to the slopes that could be hit by the scenario event and, based on the resulting Newmark displacement value, the susceptibility of the analyzed slopes to seismic-induced landslides is assessed.

Other approaches have dealt with the same problem for a probabilistic definition of expected seismic shaking. In this regard, Del Gaudio et al. (2003) proposed a methodology for calculating the critical acceleration value $(A_c)_x$ required to maintain the probability of exceeding a critical threshold of Newmark displacement less than a defined probability (e.g., 10% in 50 years), depending on the seismicity characteristics of the study area. In this approach, the authors used simplified empirical relationships, which estimate the Newmark displacement expected for a given seismic shaking on a slope characterized by a specific value of critical acceleration. The values of critical acceleration $(A_c)_x$ obtained in this way are considered as an estimator of the seismic resistance demand for the slopes, and they must have this resistance to keep a low probability of landsliding under the seismic conditions typical of that area.

This approach was used also by Rajabi et al. (2013) and Chousianitis et al. (2016), where the obtained values of $(A_c)_x$ were compared with the actual values of the critical acceleration a_c present on the slopes, in order to identify the slopes most prone to earthquake-induced landslides. However, in this first implementation of the approach, the possible presence of site response was only roughly taken into account, just using ground motion prediction equation (GMPE) including a term representing the site response in a simplified way (e.g., through conventional soil categories or mean velocity of S-wave velocity down to 30 m). This simplification could cause a considerable underestimation of the increase of ground shaking affecting landslide-prone slopes, where the susceptibility to seismically induced landslides can be strongly increased by the presence of lithostratigraphic (e.g., Bourdeau and Havenith, 2008) or topographic (e.g., Harp et al., 1981; Harp and Jibson, 2002; Sepulveda et al., 2005) amplification effects. Lithostratigraphic and topographic amplification effects can also combine in a complex manner because of the presence of irregular surfaces (Falcone et al., 2023) and slope material layering into the relief. This can modify the resonance frequencies (Ashford et al., 1997) and create variation of amplification from the top to the base of the relief (e.g., Bouckovalas et al., 2005; Rizzitano et al., 2014).

An example of landslide activation due to site amplification was shown by Bozzano et al. (2008). These authors studied the Salcito landslide, in Molise region (South-Center Italy), which was seismically reactivated on 31 October 2002, 30 km away from the epicenter of an earthquake of magnitude 5.4. According to the Keefer observations synthetized in a diagram (Keefer, 1984), such an earthquake could induce a landslide at most at about 10 km from the epicenter. However, a numerical modeling showed that the reactivation may have been produced by a “self-excitation”: considering that the pre-existing landslide body is composed by soft material on a rigid substratum, this promoted a stratigraphic amplification that favored the landslide reactivation.

Taking all this into account, in order to improve the methodologies to identify the slopes susceptible to earthquake-induced landslides, there is the need to incorporate these amplification effects, because they can considerably increase the resistance demand of slopes and their susceptibility to this kind of phenomenon.

1.3 Research objectives

The research project aims at defining a simplified and expeditious procedure for assessing the slopes susceptibility to seismically induced landslides, also considering the possible presence of site amplification effects, in order to make some progress in the development of this kind of methodologies, with a special focus on urban and peri-urban areas.

This approach addresses applications at a regional scale, rather than focusing on single slopes; for this reason, it is necessary to define a method that allows a preliminary and quick reconnaissance of the slopes most prone to earthquake-induced landsliding, on which further investigation should be carried out.

To experiment with these methodological advancements, we selected the Daunia Mountains in the Apulia region (south-eastern Italy) as a test area, where a large amount of data has been collected in ongoing SM studies.

Here we employed an approach based on the determination of the resistance demand $(A_c)_x$ that the slopes must have to resist the seismic triggering of earthquake-induced landslides. For a quick preliminary characterization of the influence of site response on the increase of resistance demand, the tested approach was integrated with simplified estimations of the amplification factors, based on widespread ambient seismic noise analysis results, made available for urban and peri-urban areas in this Daunia area by ongoing SM studies.

Aside from this introductory chapter, which has outlined the current state of the art and defined the main objectives of the research, the thesis is structured into five central chapters and a final concluding chapter. Each chapter focuses on a specific aspect of the study and contributes to addressing the overall research question.

Chapter 2 offers a detailed description of the study area. It begins with a general overview of the geological and geomorphological features of the region, followed by an in-depth analysis of the lithological units present. It also addresses the distribution of landslides across the municipalities of the Daunia Mountains and concludes with a discussion on the area's seismicity.

Chapter 3 represents the transition into the methodological phase of the study, focusing on the estimation of the seismic resistance demand. It begins by describing the methodology used to calculate the resistance demand without accounting for local site effects. A new empirical relationship is then proposed for the estimation of Newmark displacement, specifically developed for the Daunia Mountains area.

Chapter 4 presents the implementation of one-dimensional numerical modeling for site response analysis, aimed at evaluating lithostratigraphic effects on ground motion amplification. It includes a description of the developed methodology, a validation phase conducted in an external area where accelerometric data were available for comparison, and the subsequent application of the procedure across the various municipalities within the study area.

Chapter 5 addresses 2D numerical modeling carried out using more advanced software compared to 1D simulations. This modeling aims to test the relevance of topographic effects on site response. The chapter also explores the potential influence of site amplification on the estimation of seismic resistance demand and discusses possible directions for future developments based on the findings obtained.

Finally, the concluding chapter provides a concise summary of the work carried out and the main results achieved. It highlights the strengths demonstrated by the application of the proposed methodology, as well as its limitations, thereby offering a critical perspective on the research and its potential for future improvement.

The flowchart of the procedure followed in this study is shown in Fig. 1.1. The top right corner of the opening box in each column indicates the chapter in which the various steps were described, ultimately leading to the calculation of the resistance demand, both under standard site conditions and when incorporating the site effect.

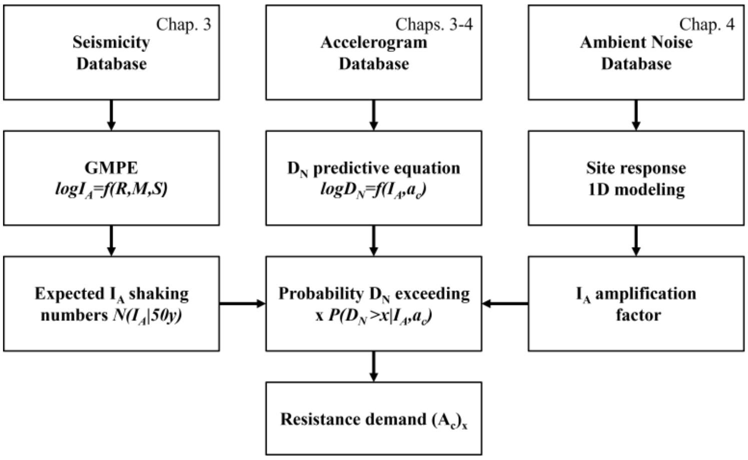

Fig. 1.1: Flowchart of the procedure followed in this study, leading up to the calculation of the resistance demand.

2. GEOLOGICAL SETTING OF THE STUDY AREA

2.1 Geological setting

The Daunia Mountains are located in the northern-western part of the Apulia region, in southern-Italy, and represent the eastern portion of the southern Apennine Chain. With an area of 1460 km^2, the Daunia Mountains include 25 municipalities: Accadia, Alberona, Anzano di Puglia, Biccari, Bovino, Candela, Carlantino, Casalnuovo Monterotaro, Casalvecchio di Puglia, Castelluccio Valmaggiore, Castelnuovo della Daunia, Celenza Valfortore, Celle di San Vito, Deliceto, Faeto, Monteleone di Puglia, Motta Montecorvino, Panni, Pietramontecorvino, Rocchetta Sant'Antonio, Roseto Valfortore, Sant'Agata di Puglia, San Marco la Catola, Volturara Appula and Volturino.

It is a hilly/low mountainous area (Fig. 2.1), where the municipality with the lowest elevation is Pietramontecorvino (456 m a.s.l.), while Monteleone di Puglia has the highest elevation, at 842 m a.s.l.. Overall, the elevation ranges from 55 to 1152 m a.s.l., the latter being reached at Monte Cornacchia.

The Daunia Mountains represent a portion of the foreland-thrust belt system, that consists of the Apennines Chain, the Bradanic Trough and the Apulian Foreland (Spalluto et al., 2021; Mostardini and Merlini, 1986; Casero et al., 1988; Patacca et al., 1990; Pescatore et al., 1999; Patacca and Scandone, 2007).

The Southern Apennines were generated by compressional tectonics, which occurred during the Alpine Orogeny (late Mesozoic-Cenozoic), preserved in the outer margin, whereas the inner sector is characterized by extensional faulting affecting the pre-existing fold-and-thrust structures (Ardizzone et al., 2023; Bronzetti et al., 2009; Schiatterella et al., 2003). They can be described as a duplex system composed of Mesozoic-Tertiary carbonates covered by a thick layer of platform and basin materials (Spalluto et al., 2021; Scandone et al., 2003).

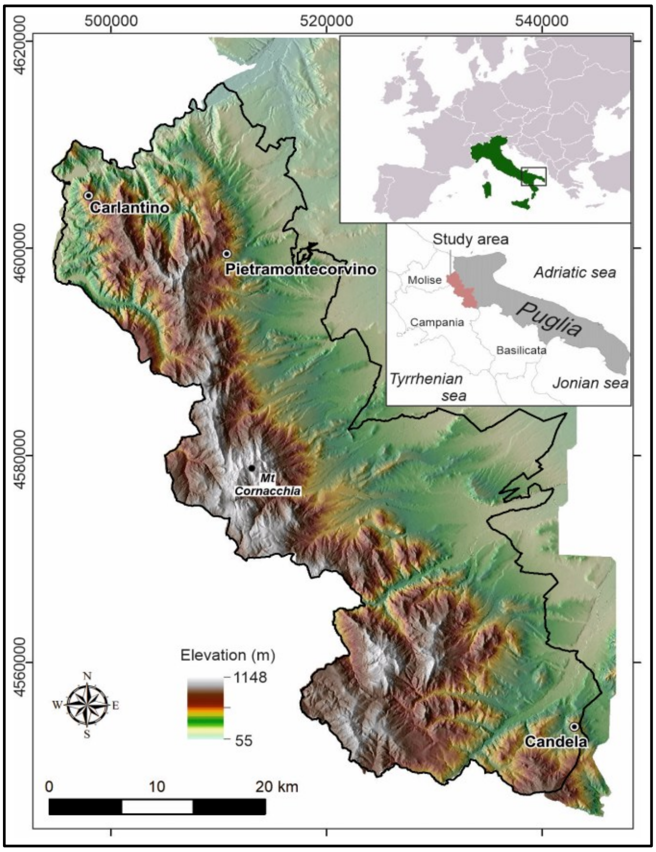

Fig. 2.1: Location map and Digital Terrain Model (DTM) at 8 m resolution of the Daunia Mountains (after Ardizzone et al., 2023). The insets illustrate the geographical location of the study area within the Apulia region.

The Daunia Mountains is the most deformed transitional area between the advanced fronts of the Apennine Chain and the westernmost part of the foreland, where the chain units were thrust on the deposits of the foreland itself (Crostella and Vezzani, 1964; Dazzaro et al., 1998; Del Gaudio et al., 2003), during the interaction between the African plate (Apulian foreland) and the European plate (Corsica-Sardinia foreland), which was fundamental in creating the current configuration of the Apennines (Vezzani et al., 2010).

The tectonic units of Daunia Mountains have been thrust over the Bradanic Trough units, which lie over the carbonate units of the Apulian foreland, dating from the Mesozoic-Cenozoic (Refice et al., 2019). In this sector of the chain there are also several NW-SE oriented fault-propagation folds and thrusts, interrupted laterally by sub-vertical strike-slip faults oriented in NE-SW direction (Pieri et al., 2011; Spalluto et al., 2021).

According to Ardizzone et al. (2023), the Daunia Mountains can be divided into two different portions:

- the western sector, characterized by flyschoid lithologies rich in clay component, with different mechanical properties and influenced by the presence of numerous folds and faults (Cotecchia et al., 2020; Losacco et al., 2021; Pellicani et al., 2014b);
- the eastern sector, characterized by the formation of Sub-Apennine clays (often overlaid by terraced fluvial deposits), with the presence of alluvial deposits that result in slopes slightly inclined toward the NE.

Fig. 2.2 shows the south-central part of the Daunia Mountains where, especially in the western sector, units are present that belong to the Daunia Tectonic Unit (Cretaceous to Upper Miocene time interval).

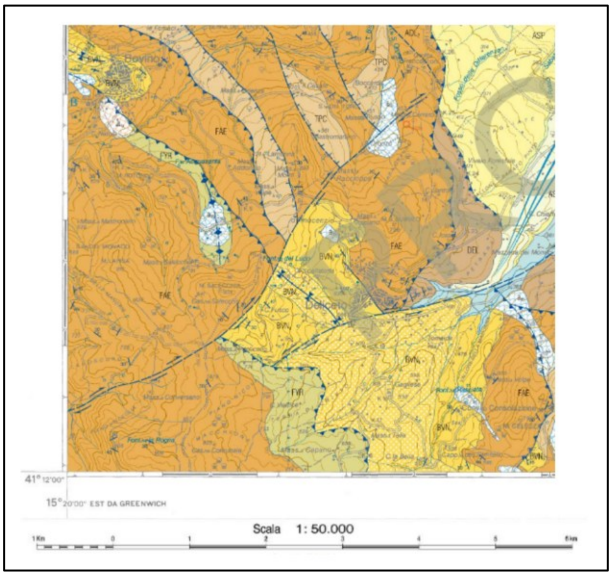

Fig. 2.2: South-Western portion of sheet 421 "Ascoli Satriano" of the CARG project at scale 1:50.000 where the municipalities of Bovino and Deliceto appear. Some representative units of the western sector of Daunia Mountains are present, including ASP, BVN_a, BVN_b, DEL, FAE, FYR and TPC (ISPRA, Progetto CARG) – See text for the description of the units.

From the bottom to the top, there are: Flysch Rosso (FYR), Flysch di Faeto (FAE) and the Toppo Capuana clayey marls (TPC). Among the intra-Apennine marine deposits, the oldest formation is the Messinian Deliceto Sands (DEL), while the most recent formation is the Pliocene Bovino Synthema (BVN) (Ciaranfi et al., 2011).

In detail:

- **FYR** (Cretaceous? – Aquitanian) represents the basal portion of the Daunia Tectonic Unit. It is an alternation of thin layers of polychrome argillites interbedded with yellowish calcilutites, calcarenites and calcirudites, with dark flint lists inside, which can vary in thickness from a few cm to several dm, attributable to distal turbidites. The maximum thickness found is around 100 m;

- **FAE** (Langhian – Serravallian) is an alternation of layers and banks of calcarenites, calcirudites, calcilutites, calcareous marls and marly clays. It rests on the FYR and gradually transitions to TPC. Downward, layers of medium- to coarse-grained calcarenites can be found interspersed with gray-greenish-white clay marls; upward, on the other hand, it is easy to encounter calcarenites, calcilutites, and calcareous marls. Numerous slumps levels have been found, which, together with chaotic levels, allow hypothesizing attribution to turbiditic processes within a basinal environment close to the base of the escarpment;

- **TPC** (Tortonian p.p.): this is the highest term of the Daunia Unit. It consists of beds of dark-gray marls and marly clays intercalated with a few thin layers of fine, silicoclasitic and calciclastic arenites, probably attributed to deep basinal areas. It is often covered by significant debris blankets. The maximum thickness does not exceed 100 m. Upward it transitions to the Bovino Synthema;

- **DEL** (Tortonian – Messinian): it is a succession of layered, poorly cemented sands, with lenticulate levels of polygenic conglomerate, and clay-silt layers, suggesting a variable continental to shallow marine environment. The thickness is on the order of 100 m;

- **BVN** (Piacenzian): it consists of two different portions. The lower portion (Castello Schiavo Sandstones and Conglomerates - **BVN$_a$**) has a total thickness around 120 m and consists of rounded sandstones and conglomerates of a silicoclastic nature and with a granule-supported texture, grouped in layers varying in thickness from a few dm to a few meters and lenticular in shape. The upper portion (Vallone Meridiano Clays and Sands - **BVN$_b$**) consists of an alternation of silty clays in strata varying in thickness from a few cm to one meter, with a total thickness of about 80 m, where thin intercalations of sands in the interior are also recognized.

The eastern portion of the Daunia Mountains includes Bradanic Trough Units, developed from the outer front of the Apennine thrusts. This is an important foredeep terrigenous succession that is overlain by the Daunia Tectonic Unit. It includes the Sub-Apennine Clays (**ASP**, Upper Pliocene – Lower Pleistocene), which are important predominantly clayey-silty foredeep successions. The thickness of this unit reaches up to 1700 m in some points, and there may be intercalations of allochthonous bodies of different thicknesses within it. This unit is characterized by a monoclinal (10°-15°) dipping to the ENE and covered by alluvial cone deposits.

The geomorphology of Daunia Mountains has been influenced by prolonged tectonic stresses. This, in combination with the presence of areas of different composition and erodibility allowed the formation of gentle slopes in clay materials and steeper slopes on stiffer material (Ciarcia et al., 2003; Wasowski et al., 2010; Zumpano et al., 2020; Losacco et al., 2021; Spalluto et al., 2021; Ardizzone et al., 2023).

2.2 Landsliding

Landslides are the most widespread and significant geological hazard that can occur along the Apennine Chain. These phenomena can cause several problems because they can damage and block the main communication routes, creating a significant impact on the social and economic life of the local population and, in the most serious cases, even causing casualties. Attention to these phenomena has grown considerably in recent years, mainly due to the constant expansion of urban areas into landslide-prone areas, thus causing an increase in related damage.

The units of this portion of the chain are characterized by the widespread presence of clay materials with poor geotechnical properties; this, in combination with the geomorphological characteristics of the area, which is characterized by moderate to high reliefs, and the high degree of tectonic deformation of sedimentary successions, makes this area particularly prone to landslides. Most of the Daunia municipalities have experienced landslide problems in the past, highlighting the critical nature of this area from this point of view.

In general, the prevalent types of landslides in the Daunia Mountains are earthflows and slump earthflows. These are mostly slow movements that involve soil and earth and only secondarily the rockier components of the formations (Wasowski et al., 2010, 2012; di Lernia et al., 2022; Zumpano et al., 2020). Composite movements often occur: they start as rotational slumps in the more competent materials and then turn into flows, which can move for hundreds of meters, or even kilometers, until flatter areas are encountered (Spalluto et al., 2021; Ciaranfi et al., 2011; Parise et al., 2012).

The main factors triggering landslides are related to precipitation events that increase groundwater pressure and consequently reduce the resistance of the materials that make up the slopes (Wasowski et al., 2010; Crozier, 1986; Wieczorek, 1996). Furthermore, the presence of significant erosion contributes to the development of landslides: this is often favored by improper land use where human activity, especially related to agricultural practices, can greatly alter the slope materials' mechanical properties, significantly destabilizing them. Since the 1950s, there has been a general decrease in rainfall throughout Italy, and this has also been recorded in Southern Italy, with a significant decrease in winter rainfall (Wasowski et al., 2010; Brunetti et al., 2004; Piccarreta et al., 2004; Polemio and Casarano, 2004). Lower precipitation should lead to increased slope stability, thus reducing instability phenomena. However, landslides have increased in Daunia region, highlighting the significant impact of anthropogenic alterations and the occurrence of extreme rainfall events (Parise and Wasowski, 2000; Limongelli et al., 2006). For example, as highlighted by Wasowski et al. (2010), from 1976 to 2006 there was a 160% increase in the frequency of landslides (Fig. 2.3). Regardless of the underestimation of landslide data in the 1976 inventory, which may be due to a lack of information from earlier times, in 2006 there was still an increase in landslide activity of approximately 120%; this could be due to i) changes in land use, as there has been a sharp increase in human/agricultural activities and cultivated land, which translates into a higher spatial and temporal frequency of landslides, especially superficial ones, and ii) climate changes.

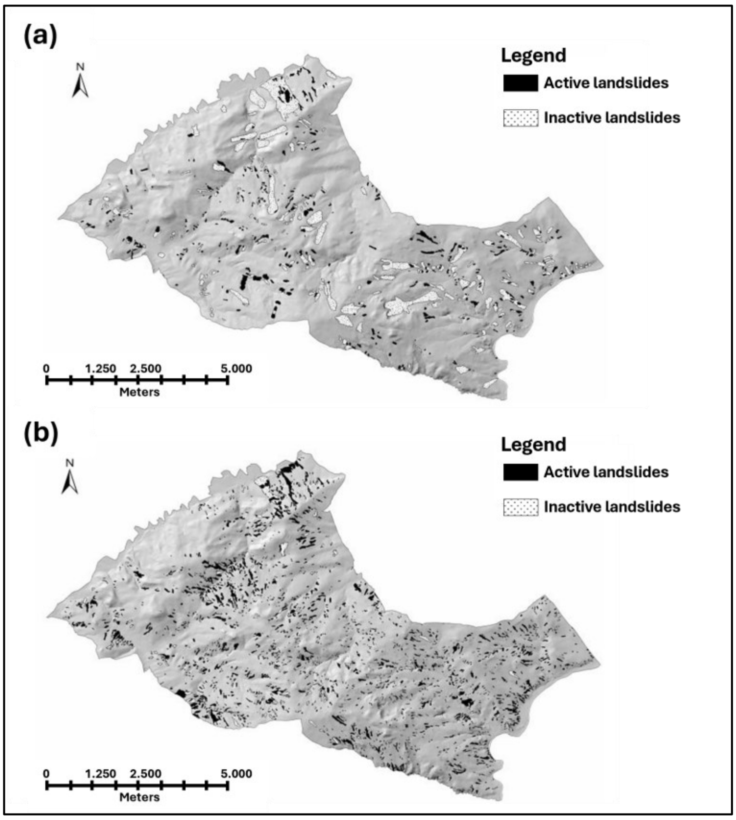

*Fig. 2.3: Example of the evolution of landslides activity in the municipality of Rocchetta Sant'Antonio. Comparison between the 1976 inventory (**a**) and the 2006 inventory (**b**), where a 160% increase in landslide frequency in the area can be observed (Wasowski et al., 2010).*

Earthquakes represent another important factor in triggering landslides. Seismic shaking can initiate a landslide during the seismic shaking or activate it with a delay of a few hours to days in response to alterations induced in hydrogeological conditions. Seismically induced landslides can occur because of moderate to strong earthquakes, even at considerable distances from the epicenter. By analyzing a large database of earthquake-induced landslides, Keefer (1984) defined – for different types of landslides – indicative curves of the maximum distance from the epicenter of an earthquake at which a landslide can be triggered, depending on the magnitude of the event (Fig. 2.4).

Some examples of landslides triggered by important earthquakes in the Daunia Mountains were reported by Boschi et al. (1997) and Romeo and Delfino (1997), and summarized by Del Gaudio et al. (2003):

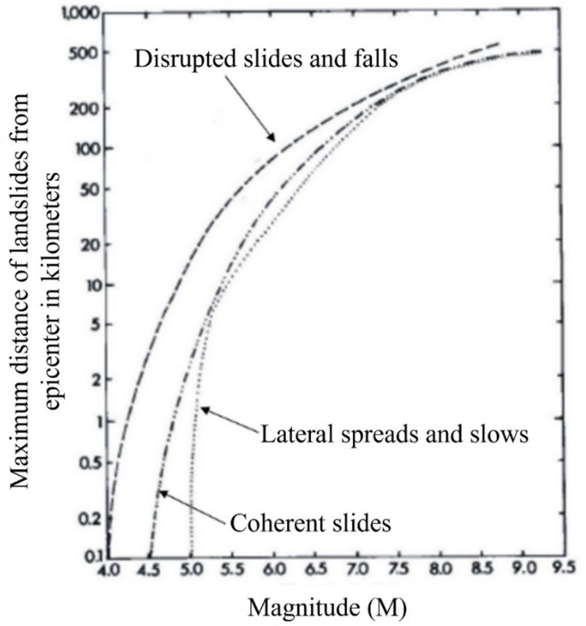

Fig. 2.4: Keefer curves showing, for various types of landslides (disrupted slides and falls, lateral spreads and slows, and coherent slides), the maximum distance at which landslides were observed to occur as a function of the magnitude of the event (Keefer, 1984).

- 30 July 1627, M_s=6.7, Roseto Valfortore;
- 23 July 1930, M_s=6.7, Rocchetta Sant'Antonio;
- 23 November 1980, M_s=6.8, Sant'Agata di Puglia;
- 23 November 1980, M_s=6.8, Bovino;
- 23 November 1980, M_s=6.8, Volturino.

The information about the landslides recorded in the Daunia Mountains is provided by the IFFI project (inventory of landslide phenomena in Italy), the national database that collects all the data relating to landslides occurred in Italy.

This inventory was created by ISPRA (Higher Institute for Environmental Protection and Research), in collaboration with the Italian regions, and contains over 620,000 landslides distributed throughout the country.

Overall, in the Daunia Mountains, the degree of landslide hazard varies from high to very high. The level of flood hazard, on the other hand, is low, except along the main watercourses in the study area (e.g., the Cervaro and Carapelle rivers, which are mainly torrential in nature) (Fig. 2.5).

The analysis of the information on landslides contained in the IFFI inventory indicates that the worst situations are found in the municipalities of Bovino, Carlantino, Panni, Volturara Appula and San Marco la Catola. More details are reported below.

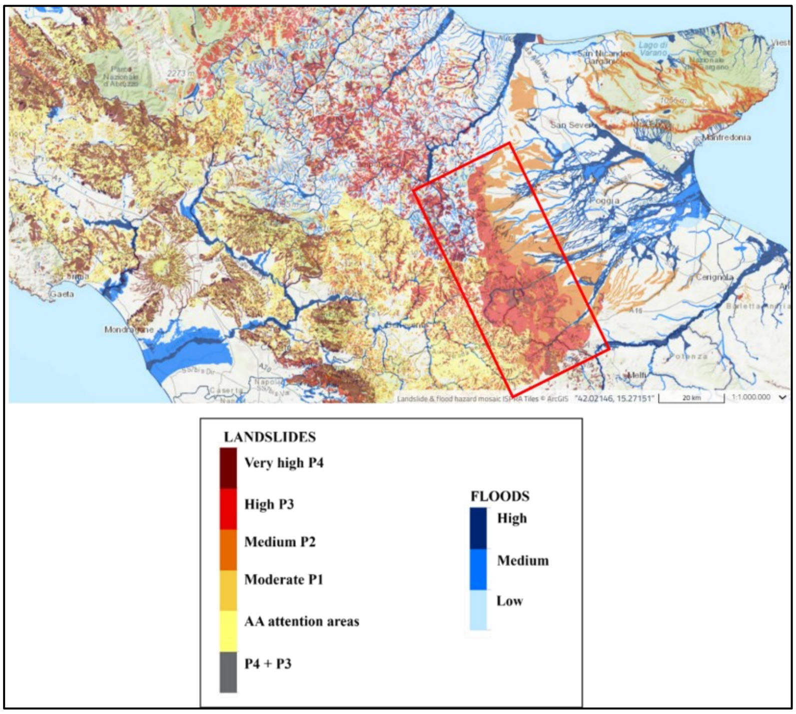

Fig. 2.5: Representation of the degree of hazard (for landslides and floods) in the province of Foggia in general and in the Daunia Mountains area (red rectangle). The legend shows a landslide hazard level ranging from moderate to very high (P1, P2, P3 and P4), with the addition of an AA level and one that combines P4 and P3; flood hazard has only three levels ranging from low to high (ISPRA, IFFI project, updated to 2024).

BOVINO

The municipality of Bovino is one of the worst affected by slope instability problems, mainly because few landslides affect parts of the town and are constantly evolving. The municipality has approximately 36 landslides (Fig. 2.6): 55.6% are rotational/translational landslides, 25% are complex landslides, 13.9% are collapse/toppling landslides, and the remaining 5.6% are slow-moving landslides. Some of the most extensive landslides are relics, but many are dormant and could be reactivated by intense rainfall or even by improper land use.

CARLANTINO

Carlantino has 52 landslides within its municipal territory (Fig. 2.7). Most of these (51.9%) are slow-moving landslides, 32.7% are complex movements, 13.5% are rotational/translational slides, and for the remaining 1.9%, the movement could not be reconstructed. The landslides are large, almost all of them dormant and developed on flyschoid lithologies with a high clay content. The mapping shows the channels along which the materials slide due to gravity.

PANNI

The territory of the municipality of Panni is mostly covered by landslides. There are approximately 20 landslides (Fig. 2.8), half of which are rotational/translational landslides, and the other half are complex movement landslides. These are very extensive landslides, covering an area of up to 2,046,425.34 m^2, and in some cases extending into the neighboring municipality of Accadia. Most of these landslides are relict or stabilized, while a few remain dormant.

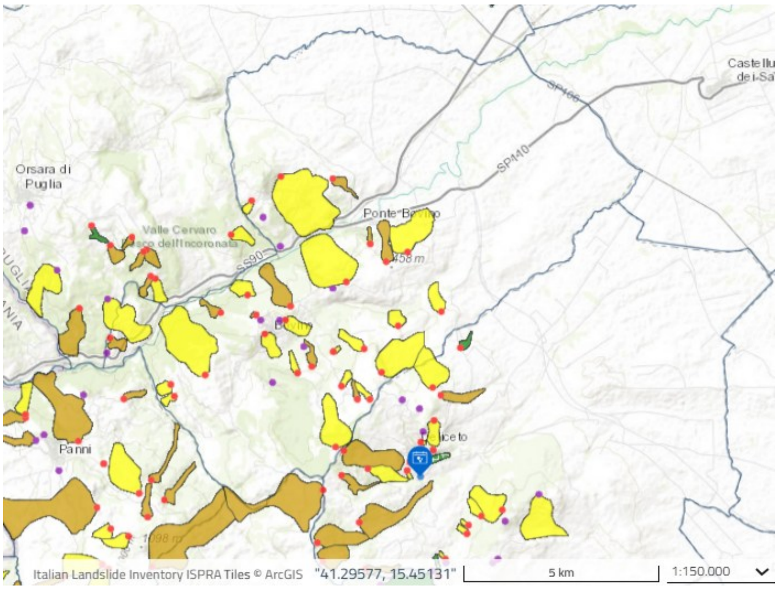

Fig. 2.6: Distribution of landslide phenomena in the municipality of Bovino (ISPRA, IFFI project).

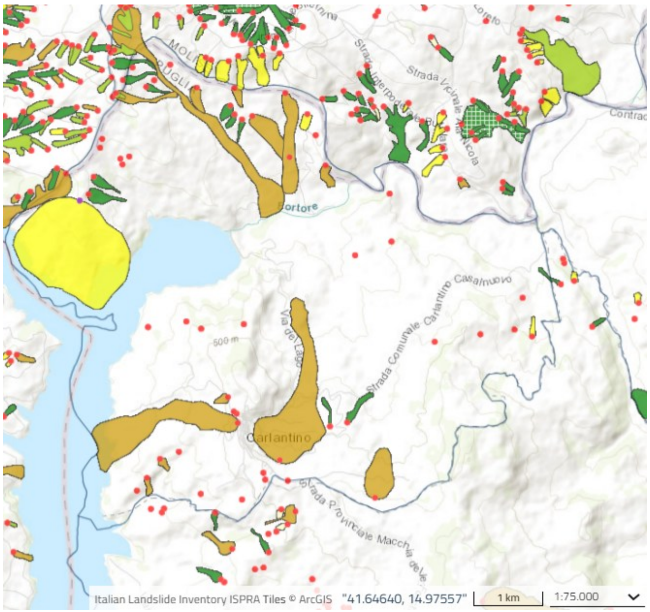

Fig. 2.7: Distribution of landslide phenomena in the municipality of Carlantino (ISPRA, IFFI project).

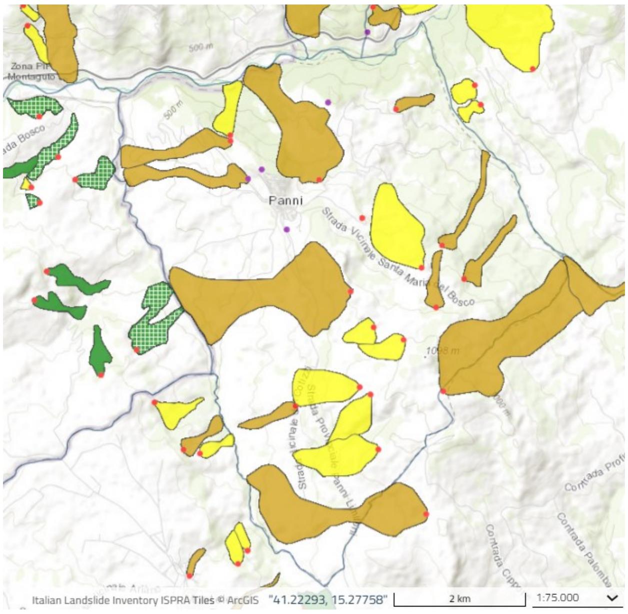

Fig. 2.8: Distribution of landslide phenomena in the municipality of Panni (ISPRA, IFFI project).

CELENZA VALFORTORE

The municipality of Celenza Valfortore has 62 landslides (Fig. 2.9), some of which are very extensive (up to 899,604.82 m^2). In 67.7% of cases, these are slow-moving landslides, in 12.9% rotational/translational landslides, in 8.1% complex movement landslides, in 4.8% fast-moving landslides, and the remaining 6.5% are undefined. Many are active/reactivated/suspended, and some are dormant.

SAN MARCO LA CATOLA

The municipality of San Marco la Catola has 54 landslides (Fig. 2.10), of which 66.7% are flow landslides, 13% are rotational/translational landslides, 9.3% are rapid flow landslides, 9.3% have complex movement, and the remaining 1.9% have undefined movement. The landslides are large and involve some parts of the town, reaching an area of up to 1,430,462.87 m^2. The largest landslides are all active/reactivated/suspended, while the smaller ones are dormant. All landslides involve predominantly clayey soils.

Fig. 2.9: Distribution of landslide phenomena in the municipality of Celenza Valfortore (ISPRA, IFFI project).

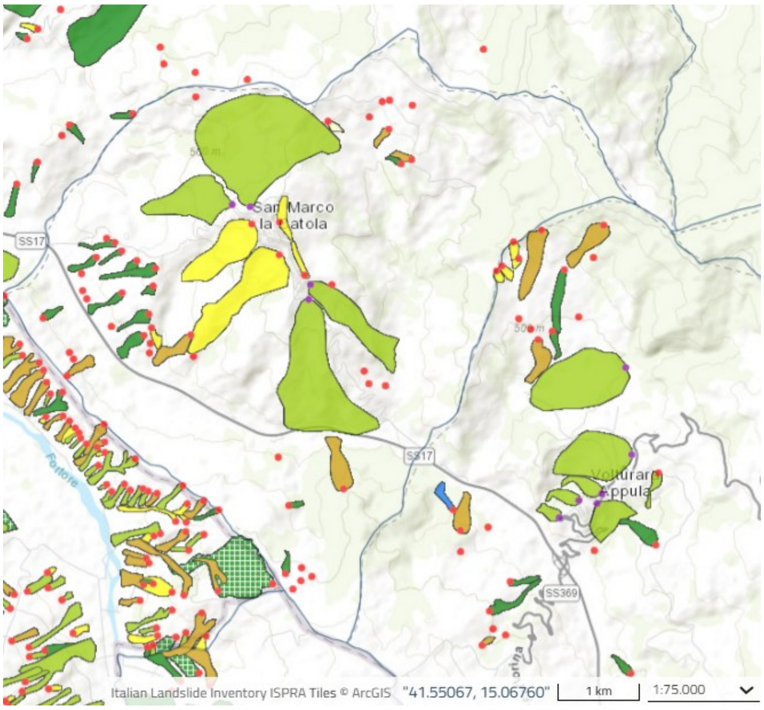

Fig. 2.10: Distribution of landslide phenomena in the municipality of San Marco la Catola (ISPRA, IFFI project).

VOLTURARA APPULA

The municipality of Volturara Appula has 46 recorded landslides (Fig. 2.11). The smallest covers an area of approximately 10,000 m^2, while the largest covers an area of 648,994.29 m^2. Fifty percent of the landslides are slow-moving, 17.4% have complex movement, 15.2% are fast-moving, 13% are rotational/translational, 2.2% are sinkings, and the remaining 2.2% are undefined. Most of the landslides are active/reactivated/suspended, especially those involving the town areas, but some are dormant.

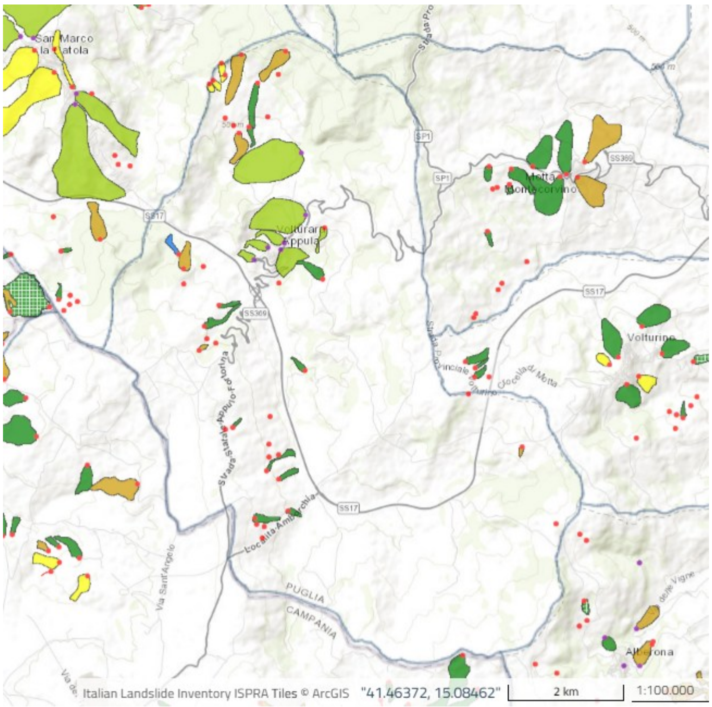

Fig. 2.11: Distribution of landslide phenomena in the municipality of Volturara Appula (ISPRA, IFFI project).

2.3 Seismicity

Although the Daunia Mountains are not crossed by recognized seismogenic structures (see Fig. 2.12), it is nevertheless very important to pay attention to the seismogenic sources in the neighboring regions, as the earthquakes generated by them could affect the study area.

Fig. 2.12: Location of seismogenic sources in the surroundings of the Daunia area, outlined by the red oval (DISS Working Group, 2025).

Table 2.1 lists the main seismogenic sources close to the study area as reported by the DISS catalog (Database of Individual Seismogenic Sources - DISS Working Group, 2025).

Table 2.1: Main seismogenic sources surrounding the study area. For each source, the following information is provided: DISS identification code (ID), name, min-max ranges of depth (km), strike, dip, rake (°) and slip rate (mm/y) and maximum recorded moment magnitude M_w.

DISS-ID	**NAME**	**MIN-MAX DEPTH (km)**	**MIN-MAX STRIKE (°)**	**MIN-MAX DIP (°)**	**MIN-MAX RAKE (°)**	**MIN-MAX SLIP RATE (mm/y)**	**MAX M_w**
ITCS003	Ripabottoni-San Severo	6-25	254-281	75-90	180-220	0.1000-0.5000	7.1
ITCSS04	Castelluccio dei Sauri-Trani	11-22.5	259-280	70-90	170-190	0.1000-0.5000	7.3
ITCS057	Pago Veiano-Montaguto	11-25	267-287	60-80	220-240	0.1000-1.0000	6.8
ITCS084	Mirabella Eclano-Monteverde	1-16	265-289	55-75	230-250	0.1000-1.0000	6.9
ITCS089	Rapolla-Spinazzola	12-23	259-280	70-90	170-190	0.1000-0.5000	7.0
ITIS006	Ufita Valley	1.5-14.5	~275	~64	~237	0.1000-1.0000	6.6
ITIS052	San Giuliano di Puglia	12-19.9	~267	~82	~203	0.1000-0.5000	5.8
ITIS053	Ripabottoni	12-20	~261	~86	~195	0.1000-0.5000	5.7
ITIS081	Melfi	12-22.8	~269	~80	~180	0.1000-0.5000	6.3
ITIS082	Ascoli Satriano	13-21.3	~269	~80	~180	0.1000-0.5000	6.0
ITIS088	Bisaccia	1.5-15	~280	~64	~237	0.1000-1.0000	6.7
ITIS092	Ariano Irpino	11-25	~277	~70	~230	0.1000-1.0000	6.9

The suffix "IS" in the DISS-ID identifies individual sources, while "CS" indicates composite sources:

- ITIS053 and ITIS052 are part of ITCS003;
- ITIS006 and ITIS088 are part of ITCS084;
- ITIS082 is part of ITCS004;
- ITIS092 is part of ITCS057;
- ITIS081 is part of ITCS089.

These are all normal-fault structures, evidence of the extensional tectonic that characterizes much of the Apennines and this portion of the southern Apennines.

The seismogenic zoning of the national territory plays an important role in defining the seismic hazard for the Italian area. Successive versions of this zoning have been adopted for the definition of earthquake-resistant design in the national building code, moving on from the seismogenic zoning ZS4 (Scandone, 1997) to ZS9 (Meletti et al., 2004). A recent update (ZS16 – Visini et al., 2022) has not yet been formally adopted as the official basis for seismic hazard assessment in Italian provisions, therefore here we still follow the ZS9 version. This zoning divides Italy into 36 seismogenic zones (Fig. 2.13), which is fewer than in the previous zoning, as some smaller zones have been merged into larger ones. This change reflects the need to increase the number of events in the seismic record of these zones in order to make the statistical basis for determining seismicity rates more robust.

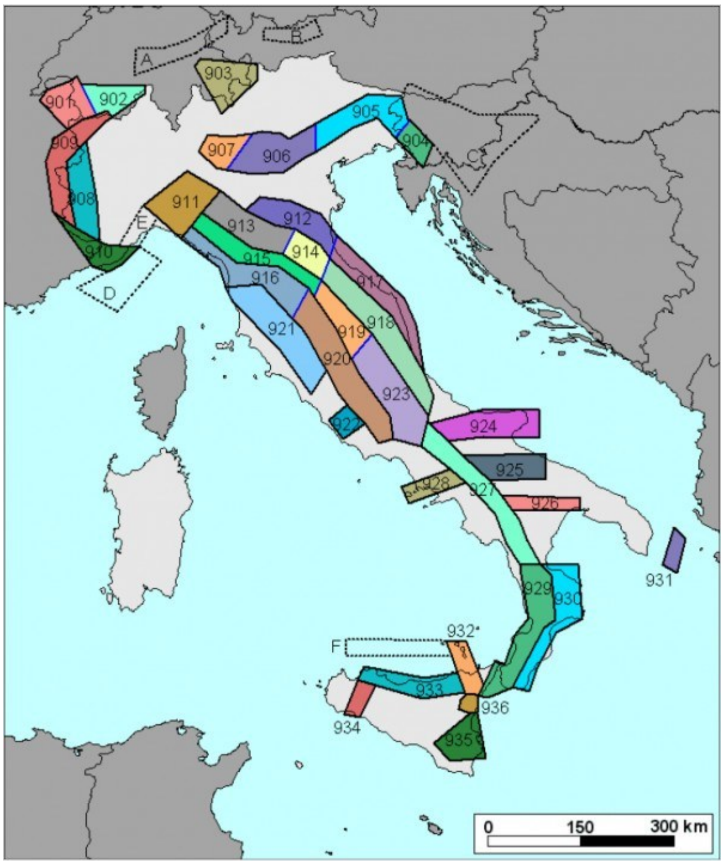

Fig. 2.13: ZS9 seismogenic zoning. The seismogenic zones that divide Italy are represented by polygons identified by a number (from 901 to 936). Additional zones identified by letters from A to F were not used to assess seismic hazard (Meletti et al., 2004).

The closest seismogenic zones relevant for the seismic hazard in Daunia are identified by the numbers 924, 925 and 927.

- Zone 924: oriented E-W with right strike-slip kinematics; it includes the Mattinata Fault, which is considered one of the most active faults in the northern part of Apulia;
- Zone 925: also oriented E-W with right strike-slip kinematics;
- Zone 927: includes the area with the greatest release of energy caused by the extension affecting the southern Apennines and runs along the axial sector of the southern part of the Apennines. It represents the intra-Apennine extensional domain.

From a seismic point of view, the study area is not particularly active. The Daunia is characterized by isolated episodes of moderate seismicity, with long intervals of quiescence.

Thanks to the Italian Macroseismic Database DBMI15 (Locati et al., 2022), updated to version 4.0 – it is possible to consult a set of macroseismic intensity data relating to Italian earthquakes from 1000 to 2020. By selecting all the municipalities that are part of the Daunia Mountains, it is possible to obtain information on the main earthquakes felt in the study area with a magnitude ≥ 5 (Table 2.2).

The database includes earthquakes since the year 1000; the earthquakes preceding this date are very difficult to date and identify (Piccardi, 1998; Valensise et al., 2004) because the further back in time they occurred, the greater the uncertainty. On the other hand, however, paleo-seismic studies show that some structures – which in the past have caused strong earthquakes in Italy – can reactivate even at intervals of 1000, 3000 or 5000 years (Fracassi and Valensise, 2007; Valensise and Pantosti, 2001).

The oldest major earthquake felt in the municipalities of the Daunia Mountains occurred on **December 5, 1456**, in the central-southern Apennines. The shaking map for this earthquake is shown in Fig. 2.14. This was a very significant earthquake that affected a large part of central and southern Italy. A peculiarity of this event is the nearly simultaneous activation of several segments of a seismogenic structure (Teramo et al., 1999). Various interpretations have been proposed in the literature: since the area of damage is very extensive, some workers have hypothesized that the epicentral area was between L'Aquila and Melfi (Baratta, 1901), while others have placed it between L'Aquila and Salerno (Meletti et al., 1988), observing the areas with the highest degree of shaking.

Table 2.2: List of major events felt in the Daunia Mountains from 1456 to 2002. For each event felt, the following information is provided: date, time, epicentral area, minimum and maximum intensity MCS felt in all the municipality of the Daunia Mountains, epicentral intensity and moment magnitude. The events are listed in chronological order (data from Locati et al., 2022).

DATA	TIME	EPICENTRAL AREA	INTENSITY	EPICENTRAL INTENSITY	M_w
1456/12/05	-	Central-southern Apennines	7-9	11	7.19
1627/07/30	10:50	Capitanata	7-8	10	6.66
1646/05/31	-	Gargano	7-8	10	6.72
1694/09/08	11:40	Irpinia-Basilicata	6-8	10	6.73
1731/03/20	20:03	Tavoliere delle Puglie	7	9	6.33
1732/11/29	07:40	Irpinia	5-7	10-11	6.75
1851/08/14	13:20	Vulture	5-8	10	6.52
1857/12/16	21:15	Basilicata	4-7	11	7.12
1875/12/06	-	Gargano	4-7	8	5.86
1889/12/08	-	Gargano	4	7	5.47
1895/08/09	17:38:20	Adriatico Centrale	3-4	6	5.11
1897/05/28	22:40:02	Ionio	3-4	6	5.46
1905/11/26	-	Irpinia	2-4	7-8	5.18
1910/06/07	02:04	Irpinia-Basilicata	3-7	8	5.76
1913/10/04	18:26	Molise	3-5	7-8	5.35
1915/01/13	06:52:43	Marsica	4-5	11	7.08
1930/07/23	00:08	Irpinia	5-9	10	6.67
1948/08/18	21:12:20	Gargano	6-7	7-8	5.55
1962/08/21	18:19	Irpinia	5-7	9	6.15
1975/06/19	10:11	Gargano	4-6	6	5.02
1980/11/23	18:34:52	Irpinia-Basilicata	6-7	10	6.81
1984/05/07	17:50	Monti della Meta	3-5	8	5.86
1984/05/11	10:41:49.27	Monti della Meta	3-4	7	5.47
1991/05/26	12:25:59.42	Potentino	2-6	7	5.08
1995/09/30	10:14:33.86	Gargano	3-6	6	5.15
2002/10/31	10:32:59.05	Molise	5-6	7-8	5.74
2002/11/01	15:09:01.92	Molise	4-7	7	5.72

This event was felt in the towns of the Daunia Mountains area with an intensity ranging from VII to IX on the MCS (Mercalli – Cancani - Sieberg) scale. The municipalities with the highest intensity (IX) were Motta Montecorvino, Accadia and Sant'Agata di Puglia.

Another significant earthquake occurred on **July 23, 1930**, identified as one of the twenty strongest events of the last four centuries (Gizzi, 2010). The epicenter of this event was located by Boschi et al. (2000) approximately 25 km northwest of Melfi, in the province of Potenza (Basilicata region); it affected an area of approximately 6,500 km^2, impacting Campania, Basilicata and Apulia regions, striking mainly the area between Melfi and Ariano Irpino (province of Avellino, Campania region), but it was also strongly felt in the Daunia Mountains. The shaking map for this important earthquake is shown in Fig. 2.15.

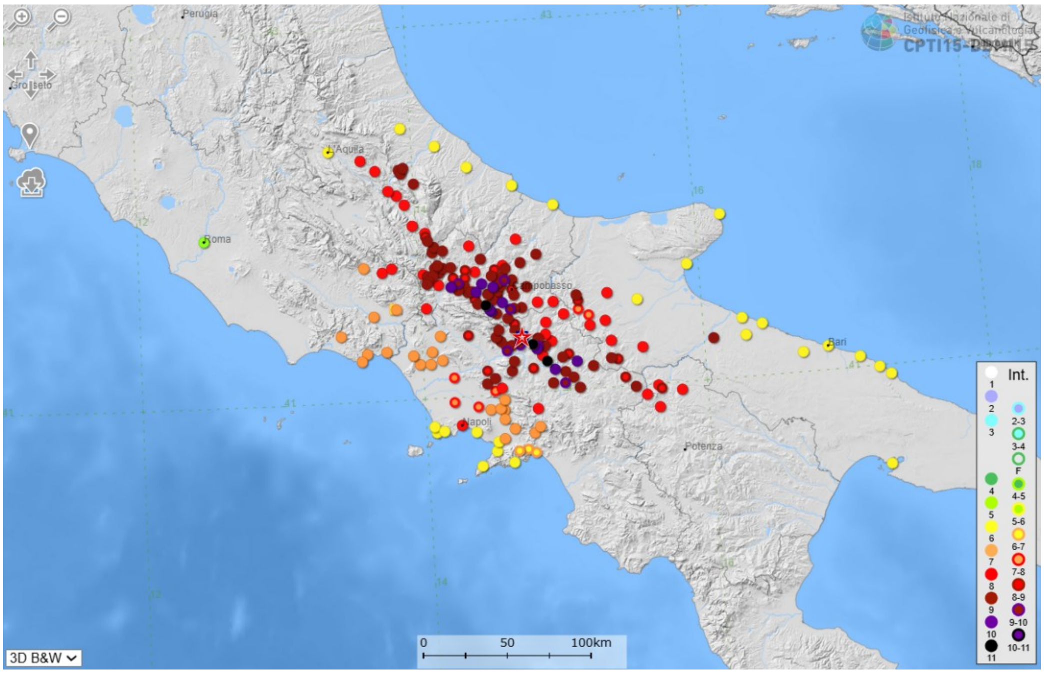

Fig. 2.14: Shaking map for the May 12, 1456 event, obtained from macroseismic data (CPTI15, Rovida et al., 2022).

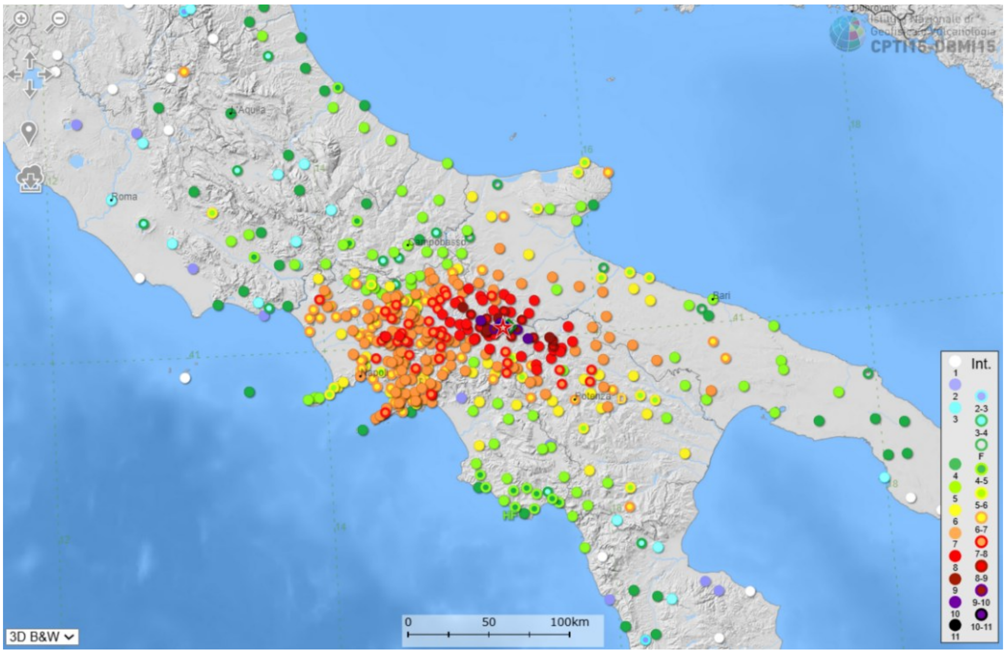

Fig. 2.15: Shaking map for the July 23, 1930 event, obtained from macroseismic data (CPTI15, Rovida et al., 2022).

In the municipalities of Daunia, the impact of this event was variable: in the northernmost municipalities, closer to the Molise region, the event was felt with an intensity of V-VI, while in the municipalities closer to the border with the Campania region (e.g., Accadia, Sant'Agata di Puglia and Rocchetta Sant'Antonio), the event was felt with an intensity of up to IX. One of the municipalities most affected by this event was Accadia, which was completely destroyed. This forced the population to leave the old village (called “Rione Fossi”) and build a new town a little further away.

One of the most powerful earthquakes in recent Italian history was undoubtedly the one that occurred on **November 23, 1980**. The epicenter of the event was in Irpinia-Basilicata, and it caused over 2,900 casualties, mainly in the province of Avellino and Potenza. However, it was also felt in the municipalities of Daunia, with an intensity ranging from VI to VII (Fig. 2.16).

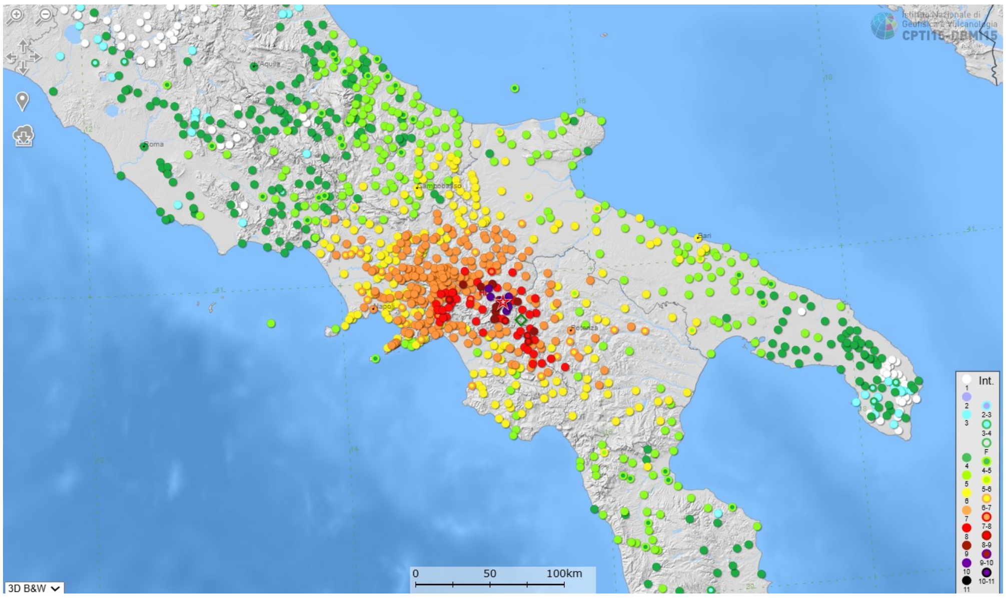

Fig. 2.16: Shaking map for the November 23, 1980 event, obtained from macroseismic data (CPTI15, Rovida et al., 2022).

An overall picture of the impact of historical seismicity on the slope stability of the study area can be obtained by the spatial distribution of the maximum Arias intensity associated with past earthquakes. In this regard, Del Gaudio et al. (2003) created a map of maximum Arias intensity values (Fig. 2.17) by applying an empirical attenuation relationship to events reported by the Italian catalog of destructive earthquakes of Camassi and Stucchi (1997). The Arias intensity (Arias, 1970) represents the total energy transmitted to the ground during a seismic shaking and it is expressed as:

$$I_A = \frac{\pi}{2g}\int_0^{t_0} a(t)^2\,dt \qquad [2.1]$$

where *a(t)* is the ground acceleration at the time *t* and t_0 is the total duration of the seismic ground motion recording. The attenuation relationship used for creating this map is the one proposed by Sabetta and Pugliese (1996):

$$log_{10}I_A = -4.066 + 0.911M - 1.818log_{10}(R^2 + 5.3^2)^{\frac{1}{2}} + 0.244S_1 + 0.139S_2 \pm 0.397 \qquad [2.2]$$

where the Arias intensity is expressed as a function of the earthquake magnitude M and the epicentral distance R, and the dummy variables S_1 and S_2 are used to represent the site effect, assigning to them a combination of binary values: (0, 0) for stiff rocks, (1, 0) for shallow soils and (0, 1) for deep soils.

From this map, it is possible to observe that the entire territory of the Daunia Mountains was affected by a significant Arias intensity, ranging from 0.4 m/s in the central area to a maximum of 7.5 m/s in the southern portion. These values exceed the critical threshold of 0.32 m/s, which Keefer and Wilson (1989) proposed for the seismic triggering of landslides on soil slopes. The I_A values in the southern part of the Daunia Sub-Apennine appear to be higher, as this area was affected by the major Irpinia events. This map also marks the localities with the documented cases of earthquake-induced landslides occurred in the study area.

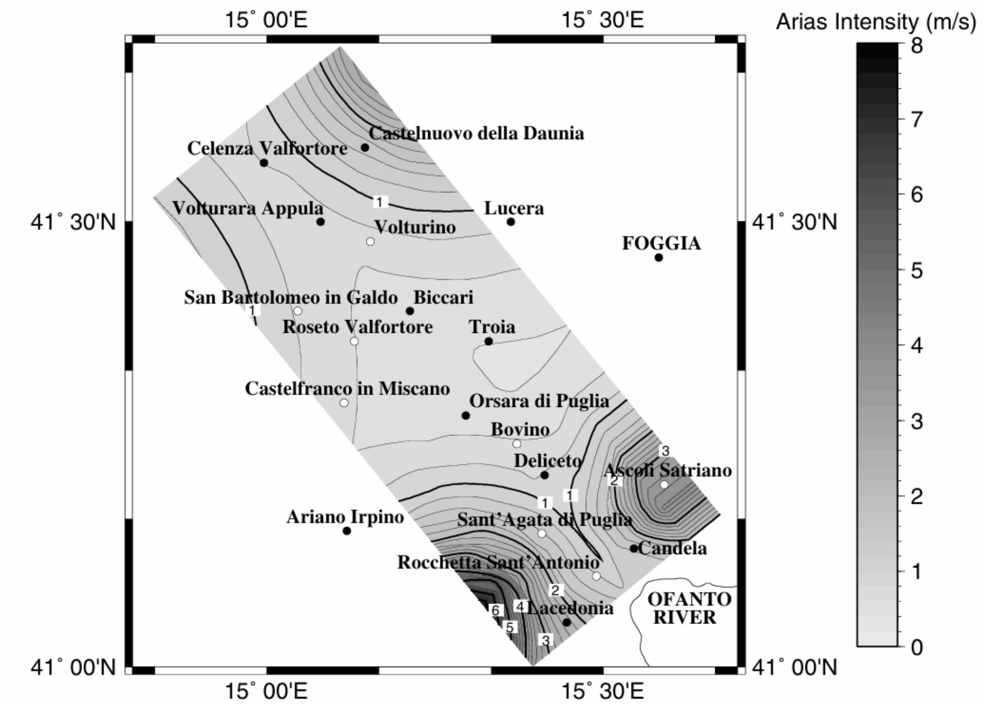

Fig. 2.17: Map of the maximum Arias intensity (m/s) estimated for the historical earthquakes that affected the Daunia Mountains. The white dots represent the localities where historically earthquake-induced landslides occurred in the study area (from Del Gaudio et al., 2003).

3. REGIONAL SCALE ESTIMATION OF BASIC SLOPE RESISTANCE DEMAND TO SEISMIC FAILURES

3.1 Computation of slope resistance demand neglecting site response

3.1.1 Methodological fundamentals

A first step in identifying slopes susceptible to earthquake-induced landslides is to define the basic slope resistance demand imposed by local seismicity at a regional scale, without taking site effects into account, which will be addressed later.

Del Gaudio et al. (2003) proposed a method for probabilistic assessment of resistance demand at a regional scale, considering the seismogenic zones surrounding the study area (the Daunia Mountains, both in their work and in this one) and their respective seismicity rates, as well as ground motion prediction equations (GMPE) to estimate the level of seismic shaking expected. This work was inspired by a research conducted by Wilson and Keefer in 1985, who proposed a method to identify slopes susceptible to earthquake-induced landslides, based on the exceedance of critical thresholds of two parameters: 1) Arias intensity and 2) Newmark displacement:

1) Arias intensity (I_A) represents the measure of total energy transmitted to the ground during a seismic shake, represented by equation [2.1]: it is often used as a benchmark to relate seismic shaking to soil deformation effects (Wilson and Keefer, 1985; Harp and Wilson, 1995; Jibson et al., 2000; Rathje and Saygili, 2008);
2) Newmark displacement (D_N) (Newmark, 1965) represents the measure of permanent displacement (in cm) generated by seismic shaking along a potential sliding surface.

To estimate Newmark's displacement the landslide is modelled as a rigid block placed on a potential sliding surface inclined at an angle α (Fig. 3.1a). For this inclination, the block has a critical acceleration a_c, which represents the maximum shear resistance opposed by cohesion and friction to sliding under static conditions, as well as the acceleration exerted by seismic shaking on the block that must be exceeded to initiate the slope failure.

In the event of seismic shaking described by a strong motion recording, when the ground acceleration in the downslope direction exceeds the predefined critical acceleration a_c, the block begins to slide along the inclined surface. During seismic shaking, the downslope motion of the block can be slowed down by shear resistance, with the contribution of the seismic shaking itself when directed upslope, until the motion stops or even reverses, depending on the resultant force. The downslope motion then resumes when the downslope acceleration exceeds the critical acceleration again.

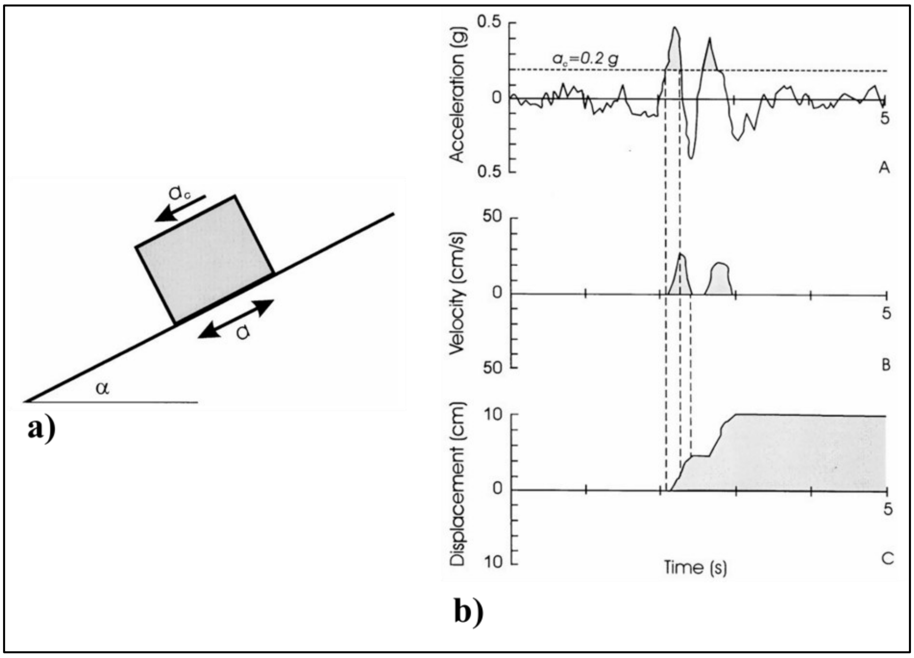

*Fig. 3.1: **a**) Rigid block placed on a plane inclined at an angle α, where a is the ground acceleration imposed by a seismic shaking, while a_c is the critical acceleration required to start the movement along the surface; **b**) Newmark's permanent displacement analysis example: by setting a critical acceleration a_c = 0.2 g and (A) identifying the portion of the acceleration recording where a > a_c, a first integration (B) yields the velocity as a function of time, while a second integration (C) yields the displacement (after Jibson et al., 2000).*

Therefore, the total displacement caused by seismic shaking is calculated by first integrating accelerations to obtain the sliding velocity (in cm/s) of the block and then integrating velocities to obtain the displacement (in cm) undergone by the block (Fig. 3.1b), according to the equation:

$$D_N = \int_0^{t0} \int_0^{t0} \ddot{u}(t) dt\, dt \quad [3.1].$$

Here $\ddot{u}(t)$ is the block's relative acceleration with respect to the sliding surface at time t and t_0 is the total duration of the seismic shaking. $\ddot{u}(t)$ is measured as the resultant of the seismic ground acceleration and the shear resistance mobilized up to a maximum given by the critical acceleration a_c. It depends on geotechnical and geomorphological parameters of the slope and is expressed by Newmark (1965) as:

$$a_c = (FS - 1) g sin\alpha \quad [3.2]$$

where FS is the static safety factor, g is the acceleration due to gravity and α is the slope inclination. In calculating D_N from equation [3.1], while the block is stationary $\ddot{u}(t)$ is assumed to be zero until the seismic ground acceleration exceeds a_c.

Regarding the Arias intensity, Wilson and Keefer (1985) and Keefer and Wilson (1989) identified critical thresholds of I_A for triggering different types of landslides, whose exceedance was estimated using relationships where I_A is derived as a function of event source magnitude and distance. The thresholds proposed by these authors are:

- 0.11 m/s for falls, disrupted slides and avalanches;
- 0.32 m/s for slumps, block slides and earth flows;
- 0.54 m/s for lateral spread and flows.

Wilson and Keefer (1985) also identified Newmark displacement critical thresholds for triggering different types of landslides:

- 10 cm for slumps, block slides and slow earth flows (coherent landslides);
- 2 cm for rock falls, rockslides and rock avalanches (disrupted landslides).

On this basis, a probabilistic definition of the resistance demand $(A_c)_x$ was introduced. This parameter represents the critical acceleration a_c that a slope must have to keep the probability of exceeding a critical threshold x of Newmark displacement D_N within a pre-defined probability (e.g., 10% in 50 years).

$(A_c)_x$ can be calculated using empirical relationships that link Newmark displacement D_N with i) Arias intensity I_A, as a measure of seismic forcing, and ii) critical acceleration a_c, as a measure of slope resistance. Several relationships of this type have been calibrated using earthquake records from different parts of the world, such as the one proposed by Jibson et al. in 2000, according to which:

$$logD_N = 1.521logI_A - 1.993loga_c - 1.546 \pm 0.375 \qquad [3.3]$$

calibrated using 275 accelerometer recordings obtained from 13 events that occurred mainly in California.

Following the same functional form as [3.3], Romeo (2000) proposed an empirical relationship calibrated using 190 accelerometric recordings from 17 Italian earthquakes obtained from the Italian accelerometric database, according to which:

$$logD_N = 1.891logI_A - 2.621loga_c - 2.089 \pm 0.562 \qquad [3.4].$$

Del Gaudio et al. (2003) proposed a procedure for creating maps of the resistance demand $(A_c)_x$, representing the spatial distribution of critical acceleration values for which there is a certain probability that a critical threshold x of Newmark displacement will be exceeded in a fixed time interval T. The creation of these maps is important for identifying the most susceptible areas to earthquake-induced landslides.

The steps followed by the aforementioned work are as follows (Fig. 3.2):

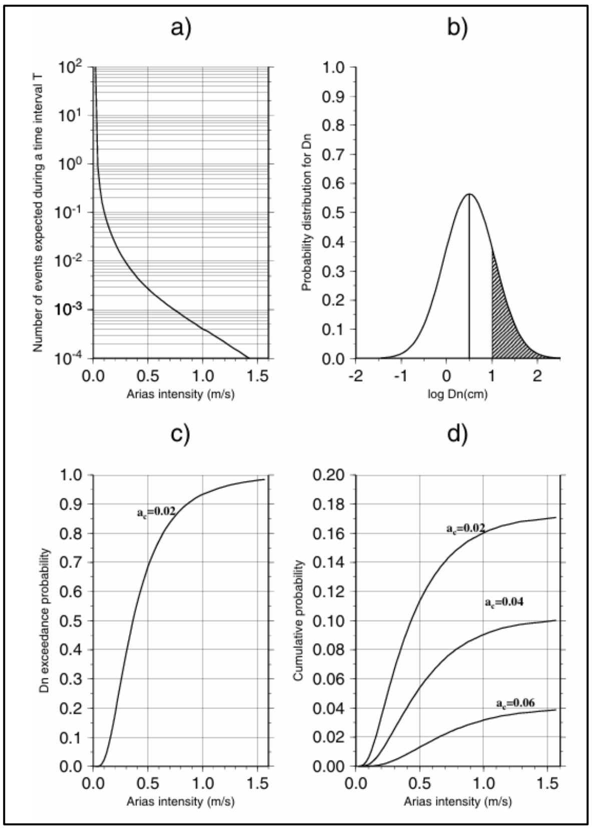

*Fig. 3.2: Steps to calculate the resistance demand $(A_c)_X$: **a)** estimate the number of expected events capable of generating different values of I_A over time T; **b)** calculate the exceeding probability of the critical threshold x of D_N (set at 10 cm in this example) for each combination of I_A and a_c, using empirical formula to estimate the median value of D_N ($10^{0.5}$ in this example). The shaded area represents the integration from x to infinity of the probability distribution curve of D_N obtained by assuming a lognormal distribution; **c)** calculate the cumulative exceeding probability of D_N for a fixed value of a_c and for all expected values of I_A multiplying the values obtained in **a)** by the values obtained in **b)**; **d)** repeat the calculation **c)** for different values of a_c until the target exceedance probability value is reached (e.g., 10% in 50 years) (from Del Gaudio et al., 2003).*

1) Set a critical Newmark displacement threshold *x* based on the type of landslides typically present in the study area;
2) Define a time interval *T* and a target exceedance probability relevant for planning landslide effect prevention measures;
3) Divide the study area into a regular grid;
4) Estimate the number of expected events capable of generating shakings with I_A within different value intervals over time *T* at each node of the grid (Fig. 3.2a);

5) Calculate the probability that D_N exceeds the critical threshold x for a fixed critical acceleration value a_c and for each locally expected I_A intervals, using empirical relationships like [3.3] or [3.4] and integrating from x to infinity the probability curve obtained assuming a lognormal distribution of D_N values around the values predicted by the used empirical relationship (Fig. 3.2b);
6) Multiply the probability of D_N exceeding the threshold calculated for each I_A interval by the number of events expected for the same interval in each node of the grid and sum the results to obtain the probability of D_N exceeding the critical threshold x in the time interval T and for a fixed value of a_c;
7) Repeat steps 5 and 6 for different values of a_c until a value is found for which the fixed D_N exceeding probability is reached at each node of the grid.

In step 7), the search for the a_c value providing the fixed D_N exceeding is carried out using the bisection method: it starts from a minimum $a_{c,min}$ and a maximum $a_{c,max}$ (extreme values) and takes the average value $a_{c,av}$; with this value, it checks whether the probability that D_N exceeds x is greater or less than the target one. To do this, it multiplies the probability that $D_N \geq x$, estimated for $a_{c,av}$ and the central value of different I_A intervals, by the number of events expected to cause I_A within these intervals and adds up the results. It continues the search iteratively, narrowing the $a_{c,min}$ - $a_{c,max}$ interval to the lower or upper half (depending on whether the previously obtained probability of D_N exceeding x is lower or higher than the target value). The search stops when the a_c search range is less than the level of approximation specified in input and, at this point, the average of the range extremes is adopted as the final a_c value required to keep the probability of D_N exceeding the pre-defined critical threshold (10 cm in this study) within the target probability.

Considering that the study area is mainly affected by coherent landslides, such as slumps and earthflows, a critical displacement threshold of Newmark x=10 cm was fixed for the creation of these maps, as well as a target exceeding probability of 10% in 50 years (Fig. 3.3), a value commonly adopted for standard seismic hazard assessment.

The following tools available at the time were used:

- the ZS4 seismogenic zoning (Scandone, 1997);
- the Italian damaging earthquakes declustered catalog (Camassi and Stucchi, 1997), to obtain the seismicity rates of each seismogenic zone located near the study area;
- the attenuation relationship of Sabetta and Pugliese (1996) [2.2] for estimating I_A from magnitude M and epicentral distance R of the seismic events;
- the code SEISRISK III (Bender and Perkins, 1987) to calculate the occurrence probability of seismic shaking within discretized I_A intervals in 50 years at each node of the grid;
- the Romeo (2000) relationship [3.4] that links D_N with I_A and a_c.

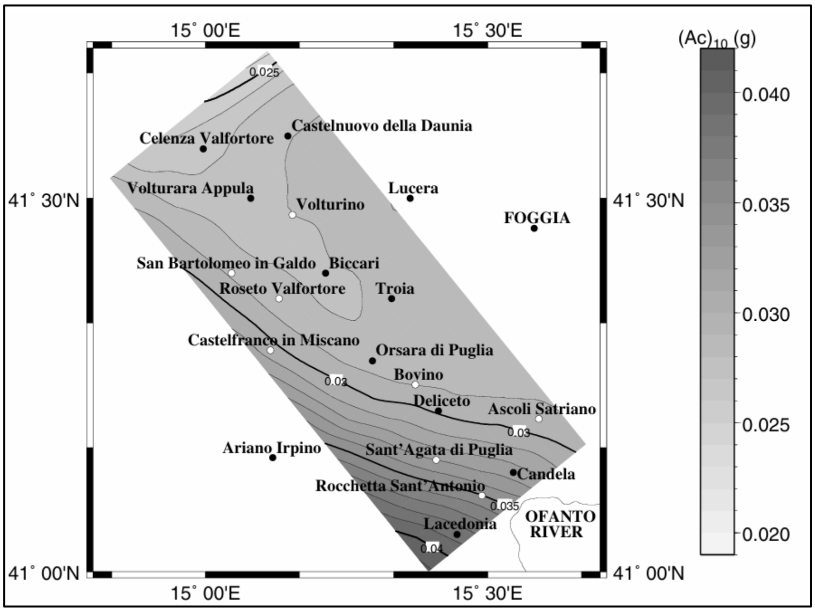

Fig. 3.3: Map showing the distribution of $(A_c)_x$ values (in g) calculated considering a critical Newmark displacement threshold x=10 cm and a 10% probability of exceeding that threshold in 50 years. The white dots represent the localities where historically earthquake-induced landslides occurred in the study area (from Del Gaudio et al., 2003).

3.1.2 Implementation of the seismic hazard estimate update

In this thesis work, all the computations carried out for the Daunia Mountains were repeated using available updated tools:

- the ZS9 seismogenic zoning (Meletti et al., 2004);
- the CPTI 2015 seismic catalog (Rovida et al., 2022);
- the new attenuation relationship proposed by Sabetta et al. (2021);
- the R-CRISIS software (Ordaz et al., 2017).

The attenuation relationship used to update the map is the most recent one proposed by Sabetta et al. (2021), which follows the same functional form as that proposed by Lanzano et al. (2019), i.e.:

$$log_{10}Y = a + F_M(M_w, SOF) + F_D(M_w, R) + F_S(V_{S,30}) + \varepsilon \qquad [3.5]$$

where Y represents the seismic shaking parameter (in this case corresponding to the Arias intensity), F_M represents the source term, F_D the distance term and F_S the site-effect term.

When Y=I_A, the term F_M has the following expression:

$$F_M(M_W) = f_j SOF_j + b_{11}M_W + b_{21}{M_W}^2 \qquad [3.6]$$

while the other two terms have a common expression for any Y parameter in the form:

$$F_D(M_W, R) = [c_1(M_W - M_{ref}) + c_2]log_{10}\sqrt{{R_{JB}}^2 + h^2} + c^3\sqrt{{R_{JB}}^2 + h^2} \qquad [3.7]$$

$$F_S(V_{S,30}) = klog_{10}(\frac{V_S}{800}) \qquad \text{where} \begin{cases} V_{S,30}\ for\ V_{S,30} \leq 1500\ m/s \\ 1500\ m/s\ otherwise \end{cases} \qquad [3.8].$$

In these expressions:

- a, b_1, b_2, c_1, c_2, c_3, f_j, and k are the coefficients obtained by a mixed-effects regression following Bates et al. (2015);
- M_{ref} represents a reference magnitude;

- h indicates the pseudo-depth accounting for Y saturation at distance 0;
- R_{JB} is the Joyner and Boore distance (Joyner and Boore, 1981), which represents the minimum horizontal distance between a site and the surface projection of the fault rupture;
- SOF_j indicates a dummy variable that can assume value 0 or 1 according to the event Style Of Faulting, for which the associated coefficients f_j provide the effect on Y. In particular, j=1 for strike-slip, j=2 for reverse and j=3 for normal faults, though f_3 was constrained to zero, assuming normal faults as the reference mechanism;
- ε represents the total residual associated with the median prediction.

These parameters, calibrated for the I_A regression (expressed in cm/s), are shown in Table 3.1.

Table 3.1: Calibrated parameters and statistical index of the I_A regression. For each parameter the value resulting from the regression is shown together with the statistical p-Value and the regression standard error (SE) (from Sabetta et al., 2021).

Parameter	**Value**	**p-Value**	**SE**
a	-2.2907	0.0006	0.6713
b_{11}	1.4033	1.339E-08	0.2467
b_{21}	-0.0881	0.0001	0.0227
c_1	0.4870	2.443E-186	0.0161
c_2	-1.0667	2.699E-90	0.0520
c_3	-0.0054	6.706E-75	0.0003
k	-1.0309	9.135E-66	0.0594
f_1	0.1185	0.0442	0.0589
f_2	-0.0176	0.7564	0.0569
M_{ref}	7.5	-	-
h (km)	5.0	-	-
σ	0.574		

The decision to use this new attenuation relationship instead of that previously employed (Sabetta and Pugliese, 1996: see equation [2.2]) is supported by the findings shown in Fig. 3.4. This graph illustrates how the new relationship improves predictions of the expected Arias intensity, particularly for higher magnitudes. The plotted curves represent the expected Arias intensity values as a function of distance up to 50 km for earthquakes of magnitude 7. (red), 6. (yellow) and 5. (green), according to the old relationship (solid line), and the new ones for i) strike-slip faults (dashed line) and ii) normal faults (dash-dotted line). Comparatively, I_A values calculated for real accelerograms are plotted as a function of the epicentral distance of the recording site, with a color scale representing the relative magnitude. These accelerograms are representative of seismic scenarios relevant for the study area and were used in the following stages of this study to calibrate new D_N predicting equations.

Although the number of real accelerogram data is limited and presents a certain scattering, it is evident that they are closer to the curves representing the most recent attenuation relationship calibrated on a larger dataset, which includes recordings of magnitude up to 8. This is in contrast to the maximum of 6.9 used in the calibration of the Sabetta and Pugliese (1996) equation.

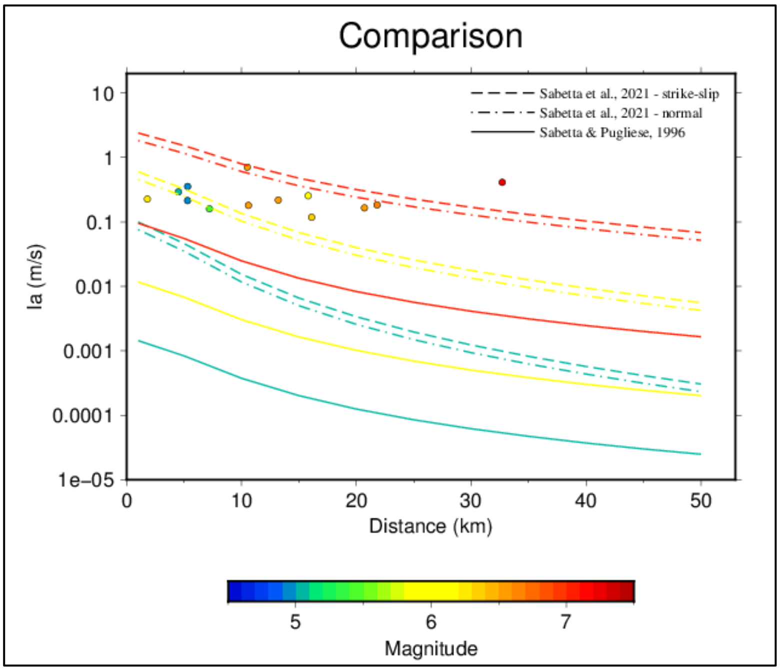

Fig. 3.4: Graphical representation of the attenuation relationships for the Arias intensity (in m/s) as a function of distance (in km), as proposed by Sabetta and Pugliese (1996) (solid line), Sabetta et al. (2021) for strike-slip (dashed line) and normal faults (dash-dotted line). Dots represent real accelerogram data. Curve and dot colors indicate magnitude, according to the chromatic scale at the bottom.

Another update to the work carried out by Del Gaudio et al. (2003) was the use of the more recent **R-CRISIS** code (Ordaz et al., 2017). The software can calculate the probability of exceeding a given intensity value within a defined time interval for selected sites.

On the main screen of the software (Fig. 3.5), it is possible to enter the elements required to compute the seismic hazard of the study area. In general, using a probabilistic approach for this calculation, there are three main elements that the software needs:

- the source geometry;
- the earthquake occurrence;
- the attenuation model.

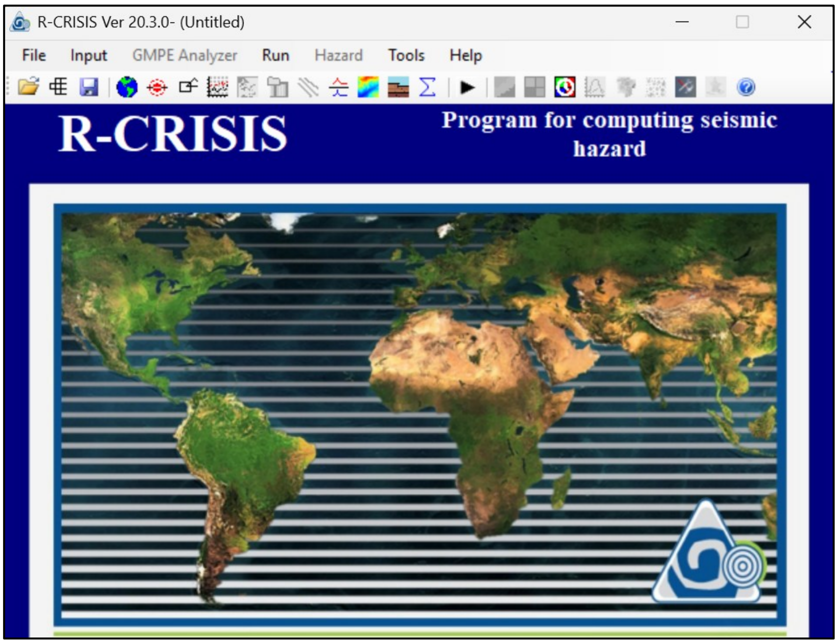

Fig. 3.5: R-CRISIS (version 20.3.0) software main screen showing menu items (first line) and buttons (second line) for setting the different stages of the seismic hazard calculation (Ordaz et al., 2017).

In detail:

- the source geometry, described as the portion of the Earth capable of generating an earthquake, can be modeled in different ways: areal sources (modelled as polygons identified by a set of vertices arranged in

2D or 3D), linear sources (i.e., polylines with constant depth) and point sources (i.e., grids of points). These different types of sources can be combined in the same project;

- the earthquakes occurrence can be modeled as either a Poissonian or non-Poissonian process. The software requires the seismicity of the study area to be expressed as the probability of having *N* earthquakes of a given magnitude *M* during the next *T* years. There are several statistical models that can be used to represent the occurrence of earthquakes (modified Gutenberg-Richter model, characteristic-earthquake model, generalized non-Poissonian model and Generalized Poissonian model), but it is preferable to use simple models, to provide a smaller number of parameters;
- the ground motion prediction models (GMPM), or attenuation relationships, are empirical equations or tables that provide the prediction of seismic shaking expected at a specific site based on i) the energy of the earthquake (magnitude) and ii) the distance from the source. Due to geometric and anelastic attenuation, seismic shaking decreases as distance increases.

  The attenuation models can be provided to the software in the form of: attenuation tables (prepared outside the software and then imported in a specific format), built-in models (i.e., the most commonly used attenuation laws that are already implemented in the software and can be selected from a list), generalized models (i.e., non-parametric descriptions of the ground shaking produced by an earthquake) and hybrid models (where different types of attenuation models are linearly combined).

The data can be entered in any order in different steps, by clicking on the various icons. Some of these steps are essential, while others are optional.

First, a map of the area where hazard is to be calculated and/or localities of interest can be entered, but this is not mandatory. To provide geographical references, in this specific case, the 25 municipalities of the Daunia Mountains were entered in the “MAP DATA” section (Fig. 3.6) by creating a specific ASCII format file.

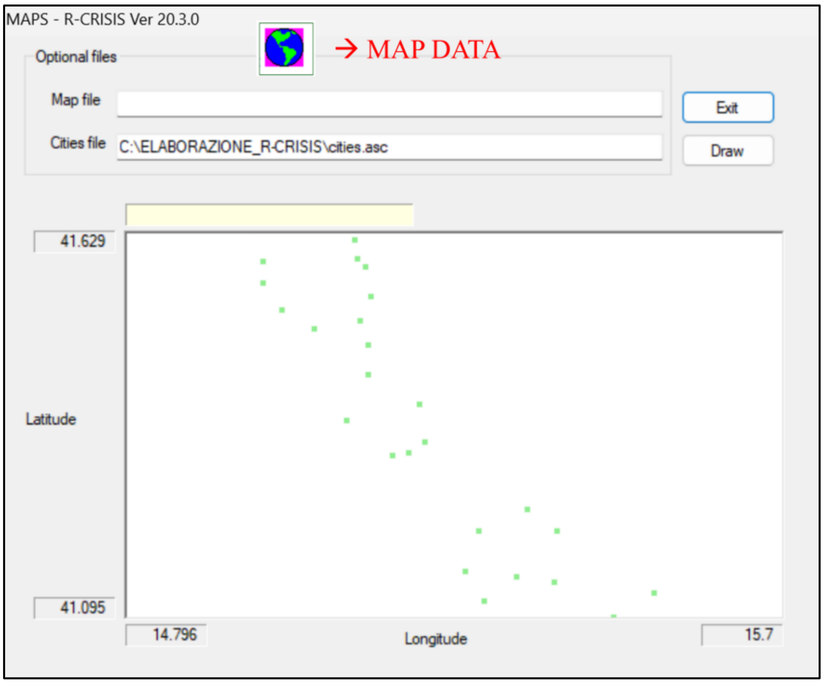

Fig. 3.6: “Map data” section with the 25 Daunia municipalities location (green points) for quickly identifying the study area.

The ASCII file used to represent these municipalities is shown in Fig. 3.7, where the format required to create it is as follows: the first line shows the number of sites to be represented, while the second line onwards shows the name of the region, the name, the longitude and the latitude (WGS-84) of the municipality.

The sites where the seismic hazard calculation will actually be performed are provided in the “DATA OF COMPUTATION SITES” section. The sites can be provided in the form of a regular grid of nodes or a list of sites.

```
25
APULIA,            Alberona,                  15.124,     41.434
APULIA,            Anzano di Puglia,          15.285,     41.124
APULIA,            Biccari,                   15.195,     41.397
APULIA,            Carlantino,                14.981,     41.591
APULIA,            Casalnuovo Monterotaro,    15.105,     41.621
APULIA,            Casalvecchio di Puglia,    15.111,     41.595
APULIA,            Castelnuovo della Daunia,  15.120,     41.583
APULIA,            Celenza Valfortore,        14.983,     41.561
APULIA,            Celle di San Vito,         15.182,     41.327
APULIA,            Deliceto,                  15.385,     41.222
APULIA,            Faeto,                     15.160,     41.326
APULIA,            Monteleone di Puglia,      15.259,     41.166
APULIA,            Pietramontecorvino,        15.128,     41.543
APULIA,            Roseto Valfortore,         15.097,     41.373
APULIA,            San Marco la Catola,       15.007,     41.526
APULIA,            Sant'Agata di Puglia,      15.380,     41.151
APULIA,            Volturara Appula,          15.053,     41.497
APULIA,            Volturino,                 15.125,     41.478
APULIA,            Bovino,                    15.342,     41.251
APULIA,            Candela,                   15.515,     41.136
APULIA,            Castelluccio Valmaggiore,  15.201,     41.343
APULIA,            Accadia,                   15.330,     41.160
APULIA,            Motta Montecorvino,        15.115,     41.508
APULIA,            Panni,                     15.276,     41.223
APULIA,            Rocchetta Sant'Antonio,    15.460,     41.103
```

Fig. 3.7: ASCII file used to represent the municipalities of the study area, one for each row, which includes the name of the region, the name, the longitude and the latitude of the municipality.

To create the grid (Fig. 3.8), the relative option must be selected, then providing longitude and latitude of the grid's origin point, the increment of latitude and longitude and the number of lines in both directions. This creates a very large grid, which can be cropped to delimit the area of interest (e.g., in this case, the area around the 25 Daunia municipalities), so that the calculation is performed only on the nodes inside this area.

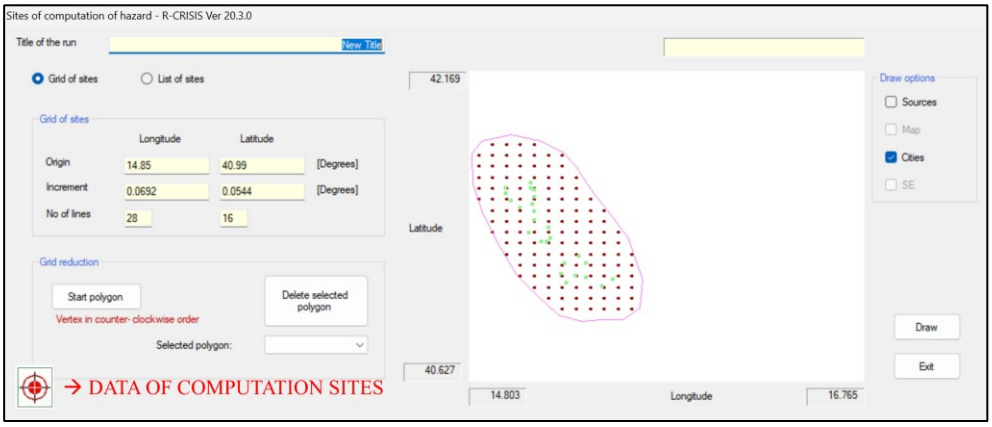

Fig. 3.8: "Data of computation sites" section used to define the cropped grid where the software must perform the computation.

The computation can also be performed at individual points by selecting the "list of sites" option in the same section (Fig. 3.9) and importing a file in the same ASCII format as that shown in Fig. 3.7.

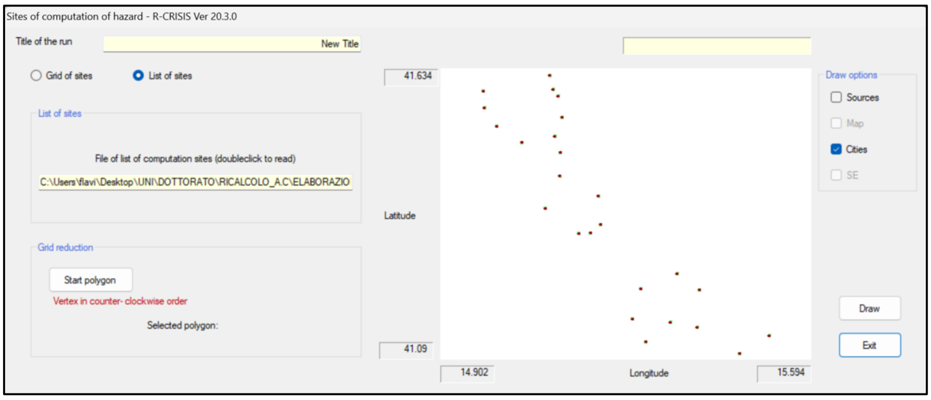

Fig. 3.9: List of sites where the software must perform the computation.

The next mandatory step is to enter the geometry of the seismic sources of interest in the “SOURCE GEOMETRY DATA” section (Fig. 3.10). Considering that within the ZS9 seismogenic zoning (Meletti et al., 2004) only zones that influence the seismicity of Daunia are relevant, the seismic sources selected for this study were the east to west stretching zones Z924 and Z925, characterized by strike-slip faults, and the zone Z927, parallel to the Apennine chain and characterized by normal faults.

*Fig. 3.10: “Sorce geometry data” section in which the seismogenic sources Z924 (**a**), Z925 (**b**) and Z927 (**c**) are represented in light red. The 25 Daunia municipalities locations are represented in green.*

Another piece of mandatory information to be provided is that in the "DATA ON SPECTRAL ORDINATES" section, where the option relating to the shaking parameter (e.g., PGA, spectral accelerations of different periods, intensity) for which the hazard will be calculated must be entered (Fig. 3.11). In this work, the Arias intensity I_A was used (setting the structural period to zero). The lower and the upper limits of I_A for which the exceedance probability has to be calculated were set to 0.01 m/s and 5 m/s, respectively. This was based on the Arias intensity values expected for the study area according to the relationship [3.5], to ensure coverage of a relevant range for the purposes of the study, excluding events too weak or too rare to significantly contribute to the slope resistance demand according to the D_N predictive equations.

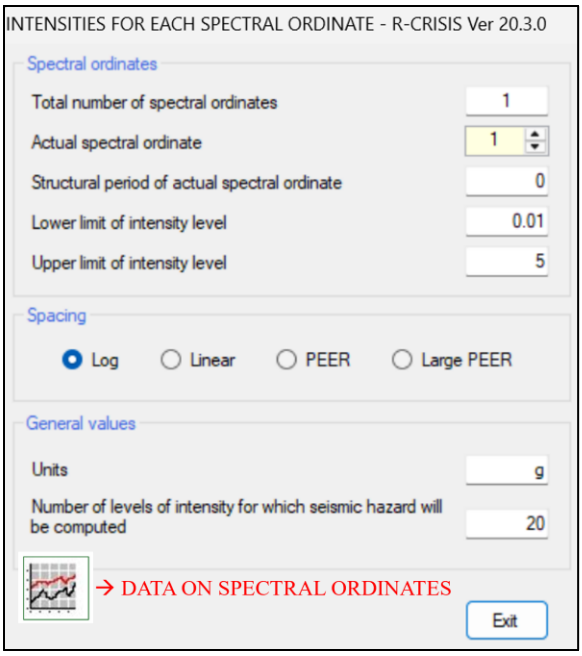

Fig. 3.11: "Data on spectral ordinates" section, where the specifications for the output tables are defined.

The next mandatory step is to define the seismicity characteristics of each previously selected zone by filling in the "SEISMICITY DATA" section. To define the seismicity of the sources, some fundamental parameters must be specified (Fig. 3.12):

- M_0: represents the minimum magnitude to be considered in hazard assessment, which should be not lower than the magnitude threshold from which the available seismic catalog can be considered complete;

- λ_0: represents the exceedance rate of M_0, expressed in earthquakes/year;

- Expected value of β: indicates, for each source, the rate at which the number N of events exceeding a magnitude M decreases logarithmically according to the Gutenberg-Richter relationship (Gutenberg and Richter, 1944) expressed in terms of natural logarithms as $ln(M)=\alpha - \beta \cdot M$;

- Coefficient of variation of β: indicates the coefficient of variation of the aforementioned β value (i.e., the expected β value divided by the associated standard error resulting from regression);

- Number of magnitudes: represents the number of magnitude classes to be used to obtain the results. The default setting is 9;

- M_u: indicates the expected maximum magnitude value for each source;

- Uncertainty range (+/-): indicates the uncertainty range of the maximum magnitude.

The M_u values were obtained directly from the report on the ZS9 seismogenic zoning (Meletti et al., 2004). To obtain M_0, λ_0 and β, however, a specific procedure was followed, based on the most recent seismic catalog (CPTI 2015 - Rovida et al., 2022).

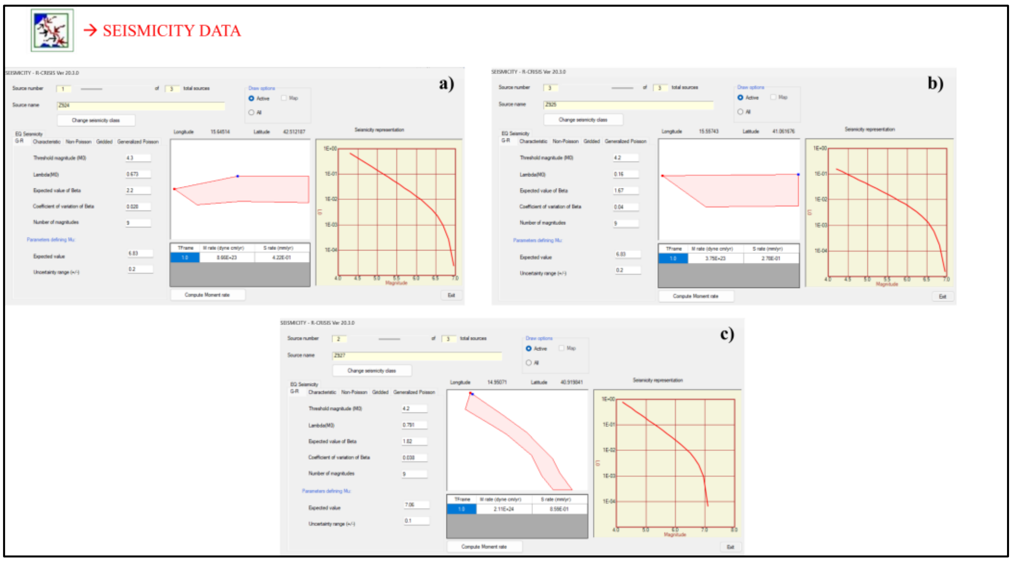

Fig. 3.12: "Seismicity data" section, where the values for the seismic features of each source must be defined.

First, the events reported in the seismic catalog falling within each of the three seismogenic zones of interest were extracted. This selection was made using SELEZCPTI, a FORTRAN program written for this purpose, which took the seismic catalog and the vertices of the zones as input. The lists of the obtained events were then de-clustered, by assuming each sequence of events recorded within 3 months and 30 km of each other as a cluster and retaining, for each cluster, only the main shock (the event with the maximum magnitude). The de-clustered list of events was fed into another FORTRAN program (called TASSISM), which allows the calculation of seismicity rates from the list of the events in the zone, based on the exam of the resulting cumulative Gutenberg-Richter curve normalized on a fixed time span, starting, for each magnitude interval, from a specified year after which the catalog was evaluated to be complete. The following parameters are given as input to this program for each zone: a) the number of years over which to normalize the number of events (usually assumed to be 100), b) the maximum magnitude, c) the last year covered by the catalog, d) the number of magnitude classes for which the year since the catalog is complete is provided, e) the magnitude thresholds for these magnitude intervals and f) the associated year from which completeness is achieved.

The program returns the coefficients of a and b of a cumulative Gutenberg-Richter equation expressed in decimal logarithms obtained by regression on the number of events normalized over 100 years. The TASSISM output is used for calculating M_0, λ_0 and β. M_0 is estimated from a graph where the logarithm of the cumulative number of events of increasing magnitude M is plotted against the magnitude itself: the lower bound below which the curve deviates from linearity is assumed to represent the minimum magnitude value M_0 for which the catalog can be considered complete.

To obtain the value of β, the Gutenberg-Richter coefficient b obtained from TASSISM is multiplied by *ln(10)*. Finally, since for Gutenberg-Richter:

$$log_{10}\lambda_0 = a - bM_0 \qquad [3.9]$$

then:

$$\lambda_0 = 10^{a-bM_0} \qquad [3.10]$$

where a and b are the Gutenberg-Richter coefficients obtained from TASSISM and M_0 is the completeness threshold (for each zone). However, the value of λ_0 thus obtained must be divided by 100 because the TASSISM program returns results normalized over 100 years, while R-CRISIS requires the number of exceedances in a single year.

Overall, the values of the parameters entered in the "SEISMICITY DATA" section in this work are summarized in Table 3.2.

Table 3.2: Values of completeness magnitude threshold (M_0), excess rate of M_0 (λ_0), expected value of β, coefficient of variation of β, number of magnitudes, expected maximum magnitude (M_u) and uncertainty range of M_u for each seismogenic sources considered.

Source	M_0	λ_0	Expected β	Coeff. variat. of β	n° of M	Expected M_u	+/- of M_u
Z924	4.3	0.673	2.20	0.028	9	6.83	0.2
Z925	4.2	0.16	1.67	0.040	9	6.83	0.2
Z927	4.2	0.791	1.82	0.038	9	7.06	0.1

After defining the seismic characteristics of each selected zone, the program requires data to be entered into the "ATTENUATION DATA" section, where the attenuation models to be used in each zone must be defined (Fig. 3.13). This section already includes a series of GMPMs, which are automatically implemented within the software, but it is also possible to import relationships that are not present, as was done in this specific case.

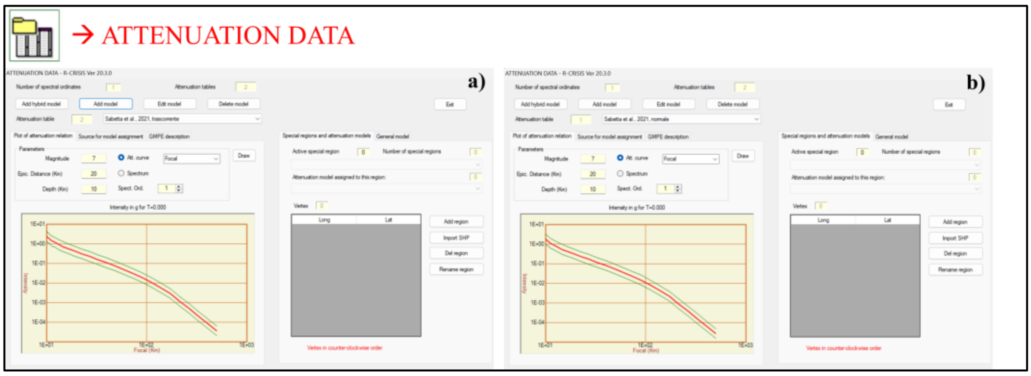

*Fig. 3.13: "Attenuation data" section, where the information about the GMPM (Sabetta et al., 2021) used is defined, both for (**a**) strike-slip and (**b**) normal fault.*

As mentioned above, the attenuation relationship used is that of Sabetta et al. (2021). To introduce it into the R-CRISIS software, files with extension .ATM (Fig. 3.14) containing the following parameters were created:

- 1^{st} row: minimum magnitude (4.0), maximum magnitude (7.5) and number of magnitude intervals (8);
- 2^{nd} row: minimum distance (1 km), maximum distance (300 km), number of distance intervals (10) and distance type (3 = Joyner and Boore distance);
- 3^{rd} row: structural period (set to 0), standard deviation (0.574, as reported in Table 3.1), maximum acceleration and depth coefficient (not used);
- following rows: I_A values calculated for all combinations of magnitude and distance, setting the dummy variable SOF_1 of equation [3.6] to 0 for normal faults (therefore for zone Z927) and 1 for strike-slip faults (therefore for zones Z924 and Z925), while SOF_2 was set to 0 for both cases.

a)

```
      4.0      7.5       8
      1.0      300.0     10   3
      0.000      0.574     0.000
0.00840966  0.00736404  0.00497662  0.00205501  0.00050223  0.0000875   0.00001218  0.0000013   0.0000000892  0.00000000268
0.02656295  0.0235269   0.01644227  0.00732046  0.00201334  0.0004042   0.0000654   0.00000815  0.000000651   0.0000000228
0.07580961  0.06791463  0.04908393  0.02356206  0.00729264  0.00168718  0.00031733  0.00004611  0.0000043     0.000000176
0.195489    0.1771381   0.1323936   0.06852331  0.02386727  0.00636318  0.00139125  0.00023566  0.00002562    0.00000122
0.455481    0.4174561   0.3226594   0.1800584   0.07057821  0.02168387  0.00551129  0.00108812  0.00013801    0.00000768
0.9588888   0.8889135   0.7105126   0.4275023   0.1885769   0.06676501  0.01972656  0.0045397   0.00067163    0.0000436
1.823964    1.710245    1.413674    0.9170932   0.4552569   0.1857424   0.06379696  0.01711302  0.00295338    0.0002237
3.134832    2.973083    2.541422    1.777618    0.9930578   0.4668994   0.1864226   0.05828758  0.01173424    0.00103703
```

b)

```
      4.0      7.5       8
      1.0      300.0     10   3
      0.000      0.574       0.000  0.000
0.01104786  0.00967422  0.00653784  0.00269969  0.00065978  0.00011494  0.000016    0.00000171  0.000000117 0.0000000352
0.03489605  0.03090755  0.0216004   0.00961697  0.00264495  0.00053101  0.00008591  0.00001071  0.000000856 0.00000003
0.09959195  0.08922023  0.06448213  0.03095375  0.00958042  0.00221647  0.00041688  0.00006058  0.00000565  0.000000231
0.2568161   0.2327084   0.1739269   0.09001986  0.0313547   0.00835939  0.0018277   0.00030958  0.00003366  0.00000161
0.5983706   0.5484169   0.4238814   0.2365448   0.0927194   0.02848635  0.00724024  0.00142948  0.0001813   0.00001009
1.259703    1.167776    0.9334086   0.5616147   0.2477357   0.08770997  0.02591501  0.00596386  0.00088233  0.00005728
2.396162    2.246768    1.85716     1.204796    0.5980762   0.244012    0.0838108   0.02248158  0.00387988  0.00029388
4.118265    3.905773    3.338695    2.335278    1.304591    0.6133711   0.2449055   0.07657306  0.01541541  0.00136236
```

*Fig. 3.14: .ATM files used as GMPM for (**a**) normal and (**b**) strike-slip faults, obtained by calculating I_A values in m/s for different combinations of magnitude and distance, using the relationship described by Sabetta et al. (2021).*

The "GLOBAL PARAMETERS" section is the last one to be filled in (Fig. 3.15). In this section, general parameters for the computation procedure must be provided, and in particular:

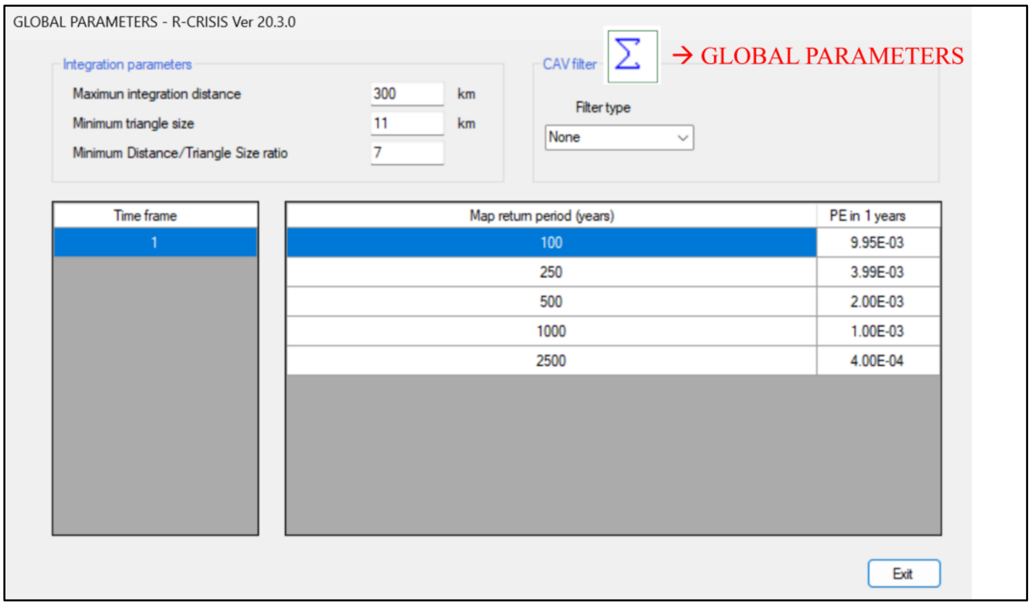

Fig. 3.15: "Global parameters" section, where general parameters for the computation procedure are set.

- the maximum distance within which sources must be considered (set at 300 km, as in the case of the data used for creating the .ATM files);
- minimum size of source triangular subdivision into sub-sources (left at the default value of 11 km);
- the minimum allowed for the ratio between the site-source distance and the triangular sub-source size (left at the default value of 7);
- CAV filter type depending on absolute cumulative velocity (not used);
- time interval over which to calculate the seismic hazard (set at 1 year);
- mean return times for which results will be mapped.

After entering all the mandatory parameters, the run can be performed. From the "Input" Menu, it is optionally possible to select the "Set output files" item to restrict the output files required. For calculating the slope resistance demand the file needed is that with extension .gra (Fig. 3.16), which reports two columns for each node of the grid or for each point provided by the list of sites (whose coordinates are indicated under the heading "SITE"):

- the first column indicates the Arias intensity levels for which the computation was performed, according to the specifications provided in the "DATA ON SPECTRAL ORDINATES" section;
- the second indicates the exceedance rates calculated for each corresponding intensity level.

```
Site:           15.3420      41.2510                  Bovino  APULIA
Intensity 1    T=0.000
    Level      Time Frame 1
1.00000E-002  3.41083E-002
1.38692E-002  2.68464E-002
1.92354E-002  2.08079E-002
2.66780E-002  1.58722E-002
3.70002E-002  1.19302E-002
5.13163E-002  8.85412E-003
7.11715E-002  6.50028E-003
9.87091E-002  4.72642E-003
1.36902E-001  3.40495E-003
1.89871E-001  2.42883E-003
2.63336E-001  1.71216E-003
3.65226E-001  1.18776E-003
5.06539E-001  8.04759E-004
7.02528E-001  5.26021E-004
9.74349E-001  3.25447E-004
1.35134E+000  1.85670E-004
1.87420E+000  9.47380E-005
2.59937E+000  4.18809E-005
3.60511E+000  1.55434E-005
5.00000E+000  4.69972E-006
```

Fig. 3.16: Example of .gra output file generated after running the R-CRISIS software. The detail shows the results obtained for the municipality of Bovino, obtained from the second run concerning the calculation exclusively on the list of the 25 municipalities of the Daunia Mountains.

In the specific case of this work, two runs were performed: one using a grid of points covering the entire Daunia area, and one using a list of points (i.e., the 25 municipalities of Daunia Mountains), in order to obtain accurate results for the sites of greatest interest.

3.1.3 Implementation of the basic slope resistance demand estimates

The .gra file obtained from R-CRISIS was then used to calculate the slope resistance demand. For this purpose, the EXCRIT program written in FORTRAN was used, which calculates the critical acceleration $(A_c)_x$ for which a target probability that the Newmark displacement D_N exceeds a critical threshold x in a given time interval T is reached. This probability is estimated according to relationships linking D_N to Arias intensity and critical acceleration.

The EXCRIT program requires information on the annual rates of occurrence of events locally causing shaking with I_A values within selected intervals, which can be drawn from the .gra file. Before using it, however, this file must be modified by adding a third column (Fig. 3.17) containing the annual rate occurrence of events with an I_A within a certain range, obtained by subtracting each value in the second column from the previous one. This operation must be performed for all grid nodes and for all 25 Daunia Mountains municipalities for which the R-CRISIS software has obtained a result, creating a single file.

```
 INTENSITY 1
  15.3420      41.2510
1.00000E-02  3.41083E-002
1.38692E-02  2.68464E-002   7.26190E-003
1.92354E-02  2.08079E-002   6.03850E-003
2.66780E-02  1.58722E-002   4.93570E-003
3.70002E-02  1.19302E-002   3.94200E-003
5.13163E-02  8.85412E-003   3.07608E-003
7.11715E-02  6.50028E-003   2.35384E-003
9.87091E-02  4.72642E-003   1.77386E-003
1.36902E-01  3.40495E-003   1.32147E-003
1.89871E-01  2.42883E-003   9.76120E-004
2.63336E-01  1.71216E-003   7.16670E-004
3.65226E-01  1.18776E-003   5.24400E-004
5.06539E-01  8.04759E-004   3.83001E-004
7.02528E-01  5.26021E-004   2.78738E-004
9.74349E-01  3.25447E-004   2.00574E-004
1.35134E+00  1.85670E-004   1.39777E-004
1.87420E+00  9.47380E-005   9.09320E-005
2.59937E+00  4.18809E-005   5.28571E-005
3.60511E+00  1.55434E-005   2.63375E-005
5.00000E+00  4.69972E-006   1.08437E-005
```

Fig. 3.17: Example of the .gra file, modified from the R-CRISIS output, for the municipality of Bovino: a third column is added by subtracting each value in the second column from the previous one.

The EXCRIT program allows the use of D_N-I_A-a_c relationships according to one of the following functional forms:

1) Jibson et al. (2000):

$$logD_N = a_1 \log I_A - b_1 \log a_c - c_1 \quad [3.11]$$

2) Jibson (1993):

$$logD_N = a_2 \log I_A - b_2 a_c + c_2 \quad [3.12]$$

3) Chousianitis et al. (2014):

$$logD_N = a_3 \log I_A - b_3 \log a_c + c_3 \log I_A \log a_c - d_3 \quad [3.13].$$

In the input file, some parameters must be defined in the following order (see Fig. 3.18):

- 1st line → header, which must match that of the .gra file obtained from R-CRISIS (INTENSITY 1);
- 2nd line → 6 parameters:
    - **iopf**: mixed XY option where X=**ifm** is the input data format, which is 0 for data in the format of the output of SEISRISK III (Bender and Perkins, 1987) and 1 for generic input data formats, and Y=**iop** is the option to specify the functional form of the D_N-I_A-a_c relationship, which can take the values 01, 02 or 03 for equations [3.11], [3.12] and [3.13], respectively;
    - **sodn**: Newmark's critical displacement threshold (set at 10 cm in this study);
    - **probexc**: probability of exceeding the sodn threshold;
    - **time**: time (in years) to which probexc refers (set at 50 years, in this study);
    - **preac**: precision in estimating $(A_c)_x$ (set at 0.0001);
    - **aimax**: maximum Arias intensity for calculating Newmark displacement (set at 5 m/s);
- 3rd line → number of coefficients of the empirical relationship;
- 4th line → coefficients and standard deviation of the empirical relationship;
- 5ft line → name of the input file reporting the rate of occurrence of events with different I_A;
- 6th line → input data reading format.

```
  INTENSITY 1
101  10.  0.10  50  0.0001  5.0      iopf,sodn,probexc,time,preac,aimax
3
1.891  -2.621   -2.089   0.562
Daunia_Fredella_con_siti.gra
(e11.5,14x,e15.5)
```

Fig. 3.18: Input file for the EXCRIT program, with specifications of the parameters used in the first phase of the work.

An initial computation of the basic slope resistance demand was made considering a 10% probability of exceeding the D_N=10 cm threshold in 50 years, using equation [3.4], which has the functional form as [3.11], assuming that the errors in D_N estimation follow a lognormal distribution. The resulting output file (Fig. 3.19) reports the resistance demand value for each site.

```
 INTENSITY 1
   14.850     41.534 0.34637E-01
   14.850     41.588 0.38788E-01
   14.850     41.643 0.41351E-01
   14.850     41.697 0.42145E-01
   14.850     41.752 0.38971E-01
   14.919     41.371 0.27313E-01
   14.919     41.425 0.24384E-01
   14.919     41.480 0.26031E-01
   14.919     41.534 0.33295E-01
   14.919     41.588 0.38910E-01
   14.919     41.643 0.39825E-01
   14.919     41.697 0.40314E-01
   14.919     41.752 0.37994E-01
   14.919     41.806 0.35736E-01
   14.988     41.262 0.36224E-01
   14.988     41.316 0.28839E-01
   14.988     41.371 0.23285E-01
   14.988     41.425 0.21576E-01
   14.988     41.480 0.23651E-01
   14.988     41.534 0.30426E-01
   14.988     41.588 0.36713E-01
```

Fig. 3.19: Example of the output of the EXCRIT program, where the resistance demand has been calculated for each site indicated in the .gra file.

The resistance demand obtained with these input parameters across the entire Daunia Mountains area ranges from a minimum of 0.016g to a maximum of 0.045g (Fig. 3.20).

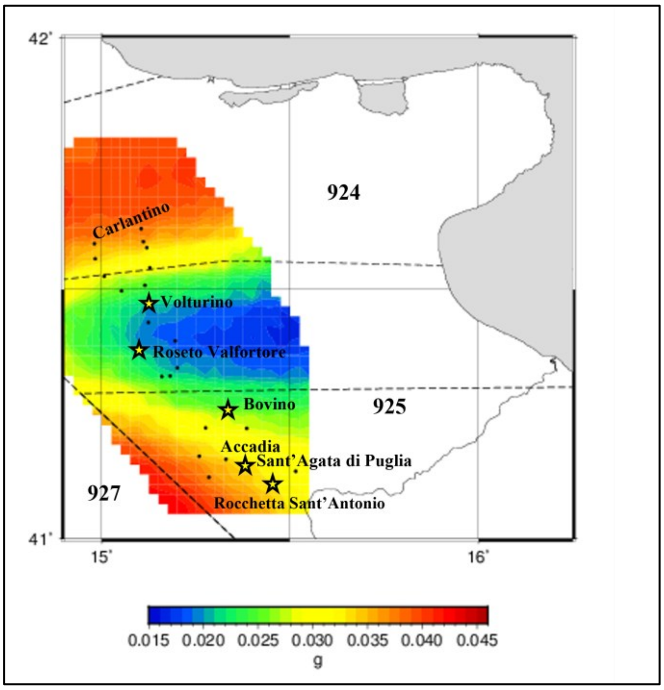

Fig. 3.20: Map of $(A_c)_{10}$ values calculated for a 10% probability in 50 years of exceeding D_N=10 cm using Romeo (2000) relationship, the R-CRISIS software, the ZS9 seismogenic zoning, the new I_A attenuation relationship by Sabetta et al. (2021) and the new CPTI15 seismic catalog (Rovida et al., 2022). Site dynamic response not considered. Black dashed lines outline the seismogenic zones closest to the Daunia Mountains (924, 925 and 927 according to ZS9). Black dots indicate the locations of Daunia municipalities, while stars mark municipalities that have been affected by earthquake-induced landslides in the past (Bovino, Rocchetta Sant'Antonio, Roseto Valfortore, Sant'Agata di Puglia and Volturino).

3.2 A new empirical relation for Newmark displacement estimation for Daunia region

The first applications of the previously described approach to estimate the slope resistance demand to seismic failures in Daunia (Del Gaudio et al., 2003) and Irpinia (Del Gaudio and Wasowski, 2004) produced rather low values, always below 0.1g. To verify the reliability of these results two aspects have been critically re-examined thereafter:

1) The D_N-I_A-a_c relationship [3.4] that was used had been calibrated on recordings of seismic events representative of heterogeneous seismic scenarios distributed throughout Italy (190 accelerograms related to 17 earthquakes); these recordings covered a limited time interval (1976-1984) and magnitude range (between 4.6 and 6.9), failing to reach the

maximum of 7.32 reported by Italian historical seismic catalog (CPTI15 catalog - Rovida et al., 2022);

2) The employed attenuation relationships quantified the effect of site dynamic response in an overly simplistic manner.

The first of these two issues is addressed here through the definition of a new empirical relationship linking D_N to I_A and a_c, which is specifically calibrated for the Daunia Mountains region. The second issue will be discussed in the next chapter.

3.2.1 Calibration

To calibrate the new relationship, the SLAMMER program (**S**eismic **LA**ndslide **M**ovement **M**odeled using **E**arthquake **R**ecords - Jibson et al., 2013) was used. The program can conduct a sliding-block analysis to estimate the Newmark's displacements according to the procedure described in Section 3.1. To conduct this analysis, the program can use a database of built-in strong-motion records, but it is also possible to add other recordings relevant to the case study.

For the present study, 224 accelerograms representative of the most relevant seismic scenarios for the seismic hazard of the study area were selected. Of these 224 accelerograms:

- 91 were obtained using the procedure developed by Pierri et al. (2025) to select the seismic inputs required by Seismic Microzonation (SM) studies to model the site response in the 25 municipalities of Daunia. According to the SM Working Group (2015), seven accelerograms are required at each modeling site for this purpose. They must satisfy the requirements of i) seismo-compatibility (to represent the most significant seismic scenarios affecting the study area) and ii) spectrum-compatibility (good matching of the average response spectrum with the design spectra locally prescribed for reference site conditions). For each municipality, the procedure proposed by Pierri et al. (2025) identifies a set of 7 accelerograms that best satisfy the aforementioned requirements. This set consists of 4 real accelerograms found in strong-motion databases and 3 additional time series selected within a large number of simulated accelerograms generated according to the procedure described by Sabetta et al. (2021). However, since many municipalities (being close to each other and having similar design spectra) include the same real accelerograms, duplicates were eliminated when forming the set of recordings used to calibrate the new D_N-I_A-a_c relationship;

- 133 additional accelerograms were obtained from 1D modeling of the site response carried out on 19 sites for which the amplification factor was calculated using data derived from the SM studies. These accelerograms represent the acceleration time series obtained as a result of the propagation of seismic waves from the bedrock towards the surface, having applied the seismic input (the 7 accelerograms mentioned above) to the base. They represent examples of accelerograms amplified by lithostratigraphic effects compared to those constituting the seismic input of the SM studies, which represent the shaking expected under standard reference site conditions.

The 224 accelerograms were first adapted to the program's reading format: since they were originally in cm/s^2, they were converted to g using the “UTILITIES” section (Fig. 3.21), which also removes the header.

Fig. 3.21: "Utilities" section of the SLAMMER code for converting the original accelerometer from cm/s^2 to g, removing the header.

After importing all the accelerograms into the user-built database and grouping them by municipality, the actual analysis was carried out in the "RIGOROUS ANALYSES" section, in three steps:

- STEP 1: SELECT RECORDS (Fig. 3.22). All the previously imported accelerograms were entered in the "SELECT INDIVIDUAL RECORDS" box. When the accelerograms are selected, the program automatically returns Peak Ground Acceleration and Arias intensity values;

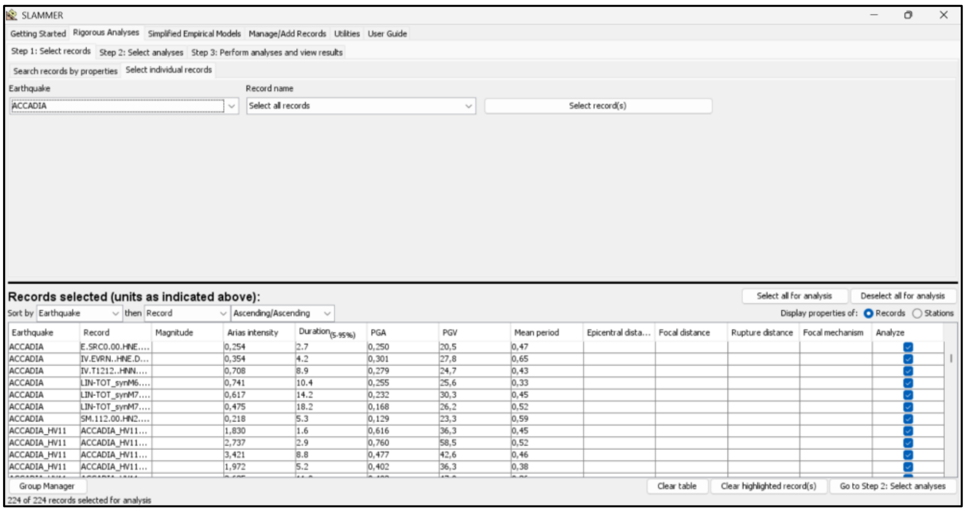

Fig. 3.22: "Select records" box of the rigorous analyses for adding individual records. The program provides the value of PGA and I_A for each of them.

- STEP 2: SELECT ANALYSES (Fig. 3.23). The following options must be set: i) the properties of the analysis, including: units (metric, to obtain a displacement in cm), scaling (not applied in this case) and critical acceleration (set to a constant value in g) and ii) the type of analysis (RIGID BLOCK and DOWNSLOPE ONLY in this case);

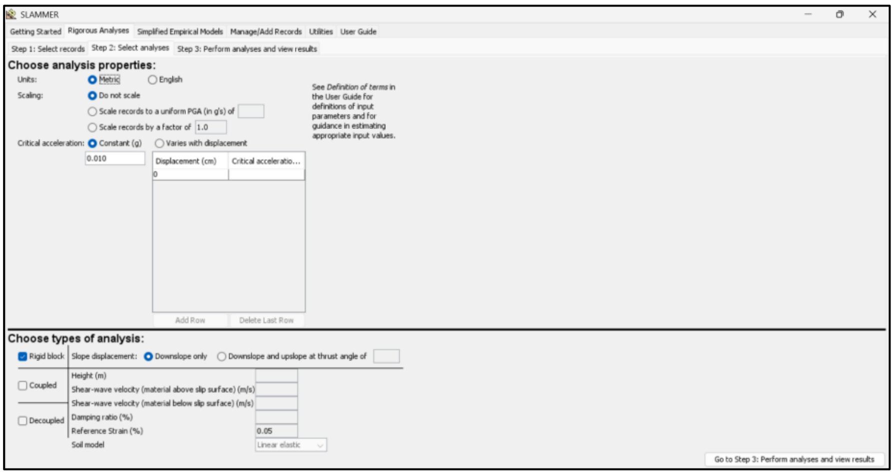

Fig. 3.23: "Select analyses" box of the rigorous analyses. The analysis properties and the type of analyses to perform need to be specified.

- STEP 3: PERFORM ANALYSES AND VIEW RESULTS (Fig. 3.24). Specifying the number of decimal places in the output (3 in this case), the run can be performed and the output file containing the analysis results are generated.

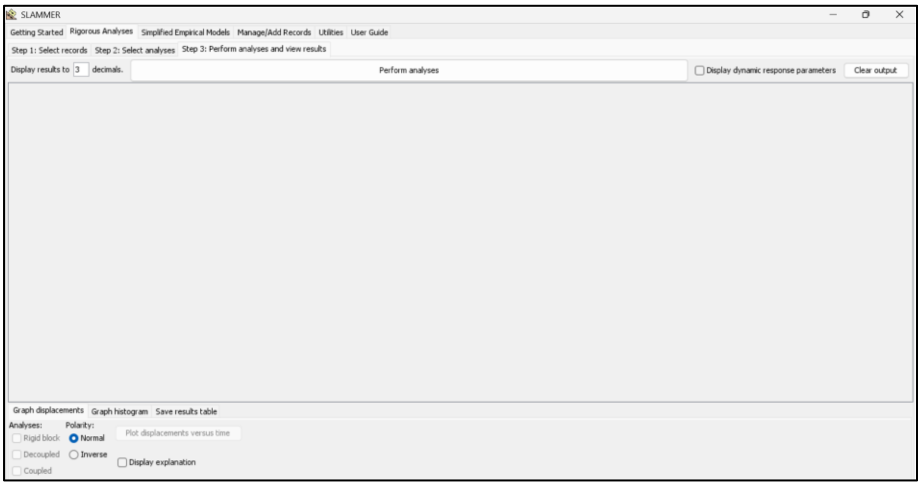

Fig. 3.24: "Perform analyses and view results" box of the rigorous analyses, in which the number of decimal places of the results must be defined and the run is started.

The D_N was estimated for different a_c values within a range selected, at this stage of the work, by dividing the minimum and maximum PGA by 10. For the 224 accelerograms used, the PGA range is 0.120g - 0.859g, so the a_c range was set to 0.010g - 0.080g. This range was divided into 10 equally spaced intervals on a logarithmic scale, and 11 different a_c values were identified (Table 3.3). By entering one of these a_c values in the "CHOOSE ANALYSIS PROPERTIES" box of the RIGOROUS ANALYSIS at each run, 11 different output files were obtained (Fig. 3.25).

Table 3.3: PGA/10 range and the 11 critical acceleration values used to calculate Newmark displacement, in order to simulate different slope conditions.

Range of PGA/10 (g)	**a_c values for computing D_N (g)**
0.010-0.080	0.010
	0.012
	0.015
	0.019
	0.023
	0.028
	0.035
	0.043
	0.053
	0.065
	0.080

```
Earthquake  Record      Rigid block (cm)Normal  Rigid block (cm)Inverse Rigid block (cm)Average     Decoupled (cm)Normal
Decoupled (cm)Inverse   Decoupled (cm)Average       Coupled (cm)Normal  Coupled (cm)Inverse Coupled (cm)Average
ACCADIA             E.SRC0.00.HNE.D.IT-1976-0030.ACC.MP.ASC             20,524  23,513  22,019
ACCADIA             IV.EVRN..HNE.D.EMSC-20181226_0000014.ACC.MP.ASC     38,240  53,495  45,868
ACCADIA             IV.T1212..HNN.D.EMSC-20161030_0000029.ACC.MP.ASC    61,303  58,668  59,986
ACCADIA             LIN-TOT_synM6.5R00ss17                              46,428  45,957  46,193
ACCADIA             LIN-TOT_synM7.0R10ss04                              63,144  55,888  59,516
ACCADIA             LIN-TOT_synM7.0R20ss13                              64,475  52,896  58,686
ACCADIA             SM.112.00.HN2.D.IS-2000-0053.ACC.MP.ASC             34,479  26,027  30,253
ALBERONA            A.D0531.00.HNE.D.TK-1999-0415.ACC.MP.ASC            38,420  38,185  38,303
ALBERONA            LIN_TOT_synM7.0R20ss10                              60,659  55,069  57,864
ALBERONA            LIN_TOT_synM7.5R30ss11                              72,155  60,943  66,549
ALBERONA            LIN_TOT_synM7.5R40ss05                              60,833  51,666  56,250
ALBERONA            SM.101.00.HN3.D.IS-2000-0053.ACC.MP.ASC             26,391  34,169  30,280
ANZANO_DI_PUGLIA    LIN_TOT_synM6.5R00ss00_ANZANO                       57,955  57,453  57,704
ANZANO_DI_PUGLIA    LIN_TOT_synM7.0R00ss18                              108,351 62,545  85,448
ANZANO_DI_PUGLIA    LIN_TOT_synM7.0R10ss15_ANZANO                       95,714  114,661 105,188
BICCARI             IV.T1256..HNE.D.EMSC-20161030_0000029.ACC.MP.ASC    18,144  20,467  19,306
BICCARI             LOG_TOT_synM7.0R10ss08                              38,648  41,166  39,907
BICCARI         LOG_TOT_synM7.0R20ss09                                  48,889  52,791  50,840
BICCARI         LOG_TOT_synM7.5R30ss18                                  94,071  91,525  92,798
BICCARI         SM.108.00.HN2.D.IS-2000-0048.ACC.MP.ASC                 29,172  11,111  20,142
BOVINO          LIN_TOT_synM6.5R00ss08_BOVINO                           44,408  44,104  44,256
BOVINO          LIN_TOT_synM7.0R10ss07_BOVINO                           48,334  65,440  56,887
BOVINO          LIN_TOT_synM7.0R20ss08                                  56,502  45,509  51,005
BOVINO          SM.101.00.HN3.D.IS-2008-0054.ACC.MP.ASC                 23,109  19,432  21,270
CANDELA         LIN_TOT_synM6.5R00ss03                                  56,765  54,703  55,734
CANDELA         LIN_TOT_synM7.0R00ss14_CANDELA                          91,908  84,089  87,999
CANDELA         LIN_TOT_synM7.0R10ss17_CANDELA                          51,668  54,890  53,279
CARLANTINO          IT.SVN.00.HGN.D.EMSC-20181226_0000014.ACC.MP.ASC    16,815  17,361  17,088
CARLANTINO          IV.EVRN..HNN.D.EMSC-20181226_0000014.ACC.MP.ASC     14,110  14,222  14,166
```

Fig. 3.25: Example of SLAMMER program output file referring to the calculation performed for a_c=0.010g. In addition to an initial header, each output file shows the name of the accelerogram and the corresponding estimated D_N value. Specifically, three different D_N values are reported: one calculated for the accelerogram original polarity, one calculated by reversing polarity and an average of the two polarities.

The resulting D_N values obtained for the different combinations of 224 accelerograms and 11 a_c values were divided in:

- 1 regression dataset, to obtain the coefficients and calibrate the new relationship;
- 2 validation datasets, to verify the predictive capability of the relationship obtained.

In order to obtain a regression dataset that represents all the possible seismic scenarios expected in the study area in a balanced manner, a selection of accelerograms was made based on the Arias intensity values. Since I_A covers a range from 0.12 to 6.37 m/s, this range was divided into 32 intervals with a step of 0.2 m/s (Table 3.4).

Table 3.4: Arias intensity intervals used to balance the datasets in order to uniformly select accelerograms representative of all possible seismic scenarios in the Daunia area.

I_A (m/s) intervals selected to identify the regression dataset	
0.12-0.32	3.32-3.52
0.32-0.52	3.52-3.72
0.52-0.72	3.72-3.92
0.72-0.92	3.92-4.12
0.92-1.12	4.12-4.32
1.12-1.32	4.32-4.52
1.32-1.52	4.52-4.72
1.52-1.72	4.72-4.92
1.72-1.92	4.92-5.12
1.92-2.12	5.12-5.32
2.12-2.32	5.32-5.52
2.32-2.52	5.52-5.72
2.52-2.72	5.72-5.92
2.72-2.92	5.92-6.12
2.92-3.12	6.12-6.32
3.12-3.32	6.32-6.52

For each of these 32 intervals, one to three accelerograms were selected, resulting in 65 accelerograms (12 non-amplified and 53 amplified) to build the regression dataset. The remaining 159 accelerograms were similarly divided into two validation datasets to test the predictive capability of the obtained relationship on data different from that used for its calibration.

Fig. 3.26 shows the combinations of magnitude and distance of the three datasets recordings, while Fig. 3.27 shows the I_A distribution histograms, grouping them into wider intervals.

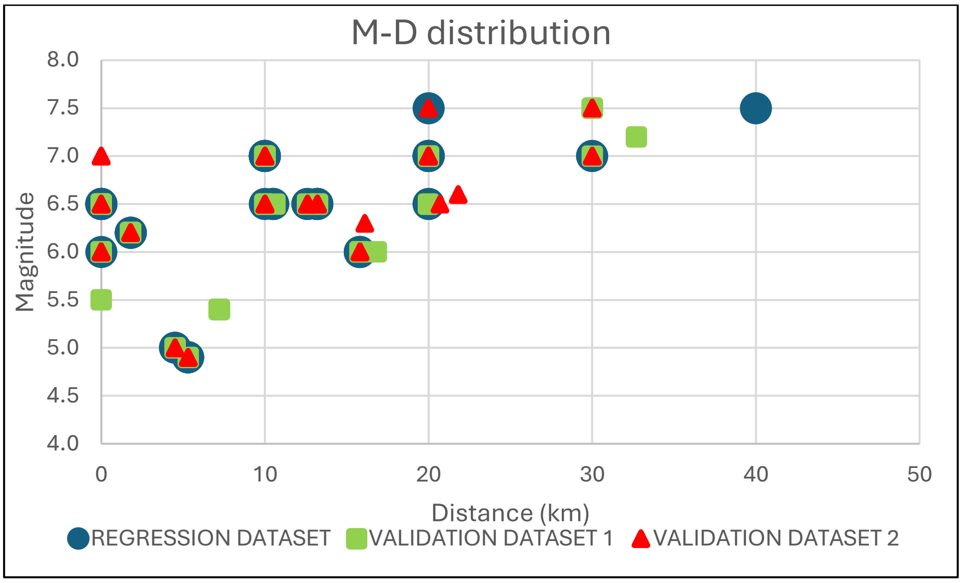

Fig. 3.26: Distribution of magnitude-distance combinations within the regression dataset (blue), validation dataset 1 (green) and validation dataset 2 (red).

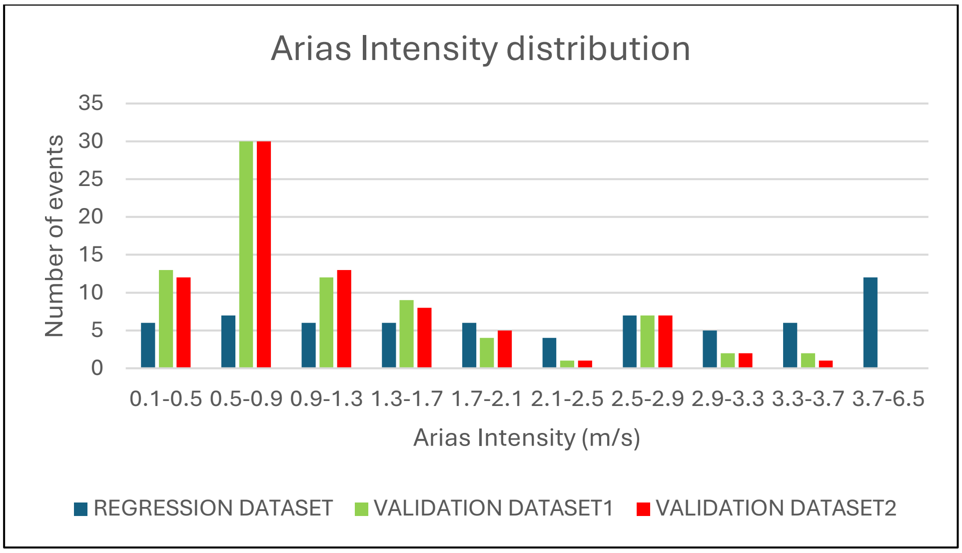

Fig. 3.27: Histograms of the Arias intensity distribution in the regression dataset (blue), validation dataset 1 (green) and validation dataset 2 (red).

The entire regression dataset consists of 715 D_N values (65 accelerograms x 11 a_c values); this dataset was used to perform multivariate regression between D_N (dependent variable) and I_A and a_c (independent variables), to obtain the coefficients of a relationship with the functional form [3.11]. In addition to this first regression, two more were performed to verify the robustness of the results obtained, constructing two more datasets as follows:

- regression 2 → different accelerograms respect to the first regression were selected for each one of the 32 I_A intervals;
- regression 3 → the accelerograms were selected in order to have a balanced distribution of magnitude-distance-Arias intensity between the regression and validation datasets.

As shown in Table 3.5, the regressions return quite consistent coefficients, given that their uncertainty intervals, expressed as the best fitting parameter values ± the relative standard errors, overlap.

Table 3.5: Coefficients and statistics for regressions 1, 2 and 3.

Regression Coefficients	Regression 1		Regression 2		Regression 3	
	Value	St. Err.	Value	St. Err.	Value	St. Err.
a_1	0.987	0.020	0.987	0.021	0.965	0.040
b_1	-0.946	0.024	-0.928	0.024	-0.965	0.022
c_1	-0.070	0.038	-0.062	0.039	-0.099	0.025
Regression Statistics						
R^2	0.851		0.843		0.842	
St. Err.	0.180		0.181		0.184	
Data number	715		682		649	

To further refine the regression datasets, the outliers were eliminated. They were identified using a boxplot representing the distribution of regression residuals (Fig. 3.28), calculated as differences ε between the logarithms of the rigorously calculated $D_{N,c}$ and the empirically estimated $D_{N,e}$ Newmark displacements.

After removing the outliers (i.e., the residuals below the first quartile or above the third quartile by 1.5 times the interval between these quartiles), the regression was repeated. This process of removing outliers and re-performing the regression was repeated until no outliers remained.

Table 3.6 shows the results of the three regressions after removing the outliers (27 for regression 1, 10 for regression 2 and 23 for regression 3), which once again show good consistency between the coefficients, with the exception of coefficient a_1 of regression 2, which differs from those of the other regressions by more than twice its standard error.

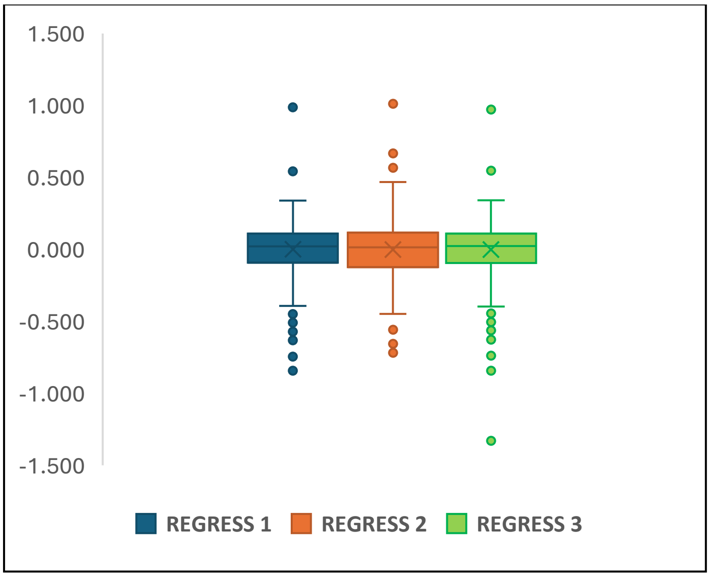

Fig. 3.28: Boxplot of regression residuals distribution. The whiskers (horizontal segments) represent the limits beyond which the outliers are identified. Data outside these whiskers are considered outliers and are removed from the datasets.

Table 3.6: Coefficients and statistics for regressions 1, 2 and 3, after removing the outliers.

Regression Coefficients	Regression 1		Regression 2		Regression 3	
	Value	St. Err.	Value	St. Err.	Value	St. Err.
a_1	0.962	0.016	1.007	0.019	0.946	0.033
b_1	-0.901	0.019	-0.920	0.022	-0.924	0.018
c_1	0.022	0.031	-0.053	0.035	-0.016	0.020
Regression Statistics						
R^2	0.888		0.870		0.882	
St. Err.	0.141		0.163		0.144	
Obs	688		672		626	

Finally, given the good consistency between the results of regression 1 and regression 3, they were used as a reference to define the new D_N-I_A-a_c relationship for the Daunia area, using the coefficients obtained from regression 1– as it has the smallest standard error – according to the equation:

$$logD_N = 0.962logI_A - 0.901loga_c + 0.022 \pm 0.141 \quad [3.14].$$

3.2.2 Validation tests

The regression standard error (0.141) is much lower than that of the Romeo's relationship (0.562), based on the same functional form but calibrated on a national dataset, which suggests the greater effectiveness of a relation obtained specifically for the study area. However, to verify the predictive capability of the equation obtained, two validation datasets – containing different accelerograms from those used for regression – were entered into SLAMMER for a rigorous calculation of the Newmark displacements values $D_{N,c}$. These values were compared with those estimated empirically with the new calibrated regression ($D_{N,e}$), having previously removed the outliers from the two validation datasets.

In this way, it was also possible to evaluate the frequency distribution of errors in the D_N estimates provided by equation [3.14]. The root mean square of the logarithmic estimation errors (RMSE) relative to N estimations, is given by:

$$RMSE = \sqrt{\frac{\sum_N (\log D_{N,c} - \log D_{N,e})^2}{N}} \quad [3.15]$$

and results in values of 0.160 and 0.173 for validation datasets 1 and 2, respectively, which are only slightly higher than that obtained for the regression dataset 1. This confirms the good predictive capabilities of the relationship obtained.

The new calibrated relationship for Daunia was then used to recalculate the resistance demand. However, a preliminary verification was conducted about the assumption of a lognormal distribution of prediction errors, both on the regression dataset and the two validation datasets.

An initial check was carried out graphically by comparing the exceedance probability curves of the three datasets with the curves expected for a lognormal distribution of estimation errors (Fig. 3.29). These curves were obtained by normalizing the estimation errors ε by the standard error σ resulting from regression residuals.

For each dataset, the normalized values were sorted in ascending order and assigned a sequential number. The ratio between each number and the total number of samples in the dataset represents the fraction of values less than or equal to the corresponding normalized error; the complement to 1 of each fraction therefore represents the corresponding probability of exceeding it.

Looking at the graphs, the estimation error curves of regression dataset and validation dataset 2 (Fig. 3.29a/c) fit well with those of the normal distribution, but this doesn't happen in validation dataset 1 (Fig. 3.29b), where the curves are very different.

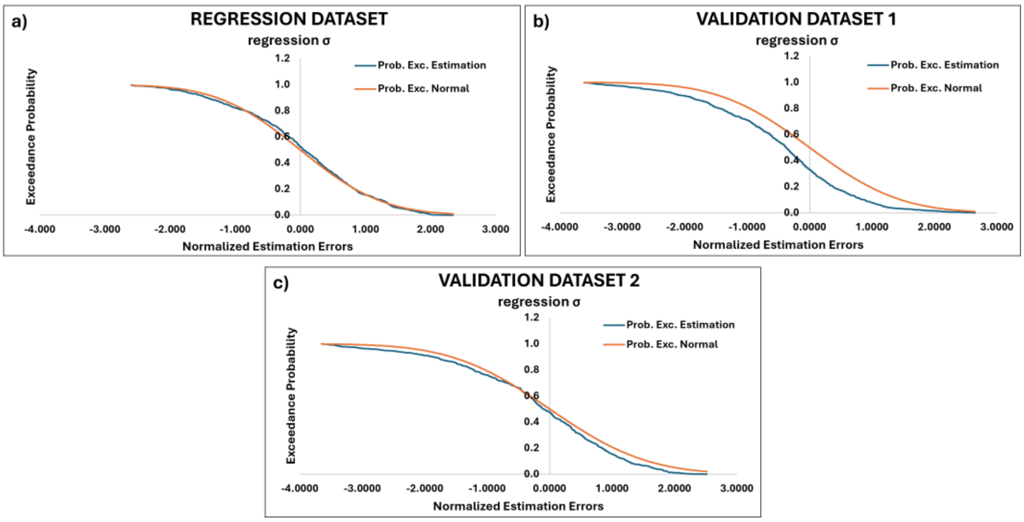

*Fig. 3.29: Comparison between the exceedance probabilities of the normalized estimation errors ε (blue curve) and those expected for a normal distribution (orange curve) for the regression dataset (**a**), validation dataset 1 (**b**) and validation dataset 2 (**c**).*

To quantitatively verify the reliability of the assumption of a lognormal distribution of the estimation errors, a chi-squared test was performed. The normalized errors observed were divided into classes with a step of 0.5σ, starting from the class centered on error 0, extending up to classes centered on -3.0σ and +3.0σ, and including extreme cases of $\varepsilon < -3$ and $> +3$ in two additional classes. For each normalized class, the percentage of the estimation errors observed in that class ($\%_{obs}$) and that expected in a normal distribution ($\%_{norm}$) were calculated to obtain the chi-squared value:

$$\chi^2 = \sum \frac{(\%_{obs} - \%_{norm})^2}{\%_{norm}} \qquad [3.16].$$

This operation was performed on both the regression dataset and the two validation datasets, assuming the lognormality of the error distribution as the hypothesis to be tested against the opposite null hypothesis. The results obtained for the three datasets are shown in Tables 3.7, 3.8 and 3.9, whereas Table 3.10 summarizes the results of the three datasets compared to the critical threshold that should not be exceeded for rejecting the null hypothesis with a significance

Table 3.7: Chi-squared test results for the regression dataset. Columns report for each class: central values of normalized error classes, number of errors observed for each class, its percentage, the percentage expected for a lognormal distribution and the relative contribution to the chi-squared value. At the bottom of the last column, the total chi-squared value is reported.

REGRESSION DATASET				
Normalized Class	n. obs	freq. % obs	freq. % norm	$\chi 2$
< -3	0	0.00	0.06	0.058
-2.50	6	0.87	0.56	0.169
-2.00	18	2.62	1.65	0.560
-1.50	33	4.80	4.41	0.035
-1.00	64	9.30	9.18	0.002
-0.50	72	10.47	14.99	1.365
0.00	132	19.19	19.15	0.000
0.50	142	20.64	19.15	0.116
1.00	113	16.42	14.99	0.138
1.50	70	10.17	9.18	0.107
2.00	34	4.94	4.41	0.065
2.50	4	0.58	1.65	0.696
> 3	0	0.00	0.56	0.563
				Σ=3.873

Table 3.8: Chi-squared test results for the validation dataset 1. Columns report for each class: central values of normalized error classes, number of errors observed for each class, its percentage, the percentage expected for a lognormal distribution and the relative contribution to the chi-squared value. At the bottom of the last column, the total chi-squared value is reported. Anomalously high discrepancies are highlighted in red.

VALIDATION DATASET 1				
Normalized Class	n. obs	freq. % obs	freq. % norm	$\chi 2$
<-3	16	1.89	0.06	**58.121**
-2.5	33	3.90	0.56	**19.720**
-2.0	37	4.37	1.65	4.454
-1.5	76	8.97	4.41	4.734
-1.0	82	9.68	9.18	0.027
-0.5	138	16.29	14.99	0.114
0.0	183	21.61	19.15	0.316
0.5	136	16.06	19.15	0.499
1.0	79	9.33	14.99	2.138
1.5	41	4.84	9.18	2.055
2.0	13	1.53	4.41	1.871
2.5	10	1.18	1.65	0.135
>3	3	0.35	0.56	0.078
				Σ=94.262

level of 0.05 for the number of degrees of freedom equal to 10 for the regression dataset and 12 for the validation datasets.

Table 3.9: Chi-squared test results for the validation dataset 2. Columns report for each class: central values of normalized error classes, number of errors observed for each class, its percentage, the percentage expected for a lognormal distribution and the relative contribution to the chi-squared value. At the bottom of the last column, the total chi-squared value is reported. Anomalously high discrepancies are highlighted in red.

VALIDATION DATASET 2				
Normalized Class	n. obs	freq. % obs	freq. % norm	$\chi 2$
<-3	18	2.15	0.06	**75.720**
-2.5	28	3.34	0.56	**13.701**
-2.0	28	3.34	1.65	1.721
-1.5	48	5.73	4.41	0.397
-1.0	79	9.43	9.18	0.006
-0.5	80	9.55	14.99	1.976
0.0	157	18.74	19.15	0.009
0.5	146	17.42	19.15	0.155
1.0	124	14.80	14.99	0.002
1.5	74	8.83	9.18	0.014
2.0	46	5.49	4.41	0.266
2.5	9	1.07	1.65	0.203
>3	1	0.12	0.56	0.350
				Σ=94.521

Table 3.10: Summary of the results of the chi-squared test. For each dataset the table reports the degree of freedom, the critical threshold that should not be exceeded for rejecting the null hypothesis with a significance level of 0.05 and the observed χ^2.

	Degree of freedom	**Critical χ^2**	**Experimental χ^2**
Regression dataset	10	18.307	3.873
Validation dataset 1	12	21.026	**94.262**
Validation dataset 2	12	21.026	**94.521**

For the regression dataset, the χ^2 test is passed, showing a good agreement with a lognormal distribution. For both validation datasets, however, the test is not passed, and the null hypothesis cannot be rejected. However, few classes contribute significantly to this result and correspond to the estimation errors that deviate negatively by more than 2.25σ from the predictions of [3.14]; this indicates that, in such cases, the empirical equation strongly overestimates D_N compared to its actual value. These data (highlighted in red in Tables 3.8 and 3.9) represent only 5.79% for the validation dataset 1 and 5.49% for the validation dataset 2. These values are much greater than the 0.62% expected for a normal distribution but, in any case, these are small percentages and their effect on the calculation of the probability of exceeding critical D_N thresholds could be negligible.

Some tests were carried out to try to better understand the origin of these anomalous data. First, the accelerograms of the two validation datasets associated with the highest normalized errors were identified, and accelerograms similar in terms of magnitude M, distance D, PGA, I_A and a_c were chosen in the regression dataset to understand whether specific combinations of these parameters played a significant role (Table 3.11).

Table 3.11: Comparison between parameters of the validation dataset accelerograms with the highest normalized estimation errors, and regression dataset accelerograms with similar properties in terms of M, D (km), PGA (g), I_A (m/s) and a_c (g).

	Accelerogram	**M**	**D (km)**	**PGA (g)**	**I_A (m/s)**	**a_c (g)**	**Estim. Normalized error**
Regr. dataset	BOVINO - HV15n_REALE3	6.20	1.80	0.389	0.63	0.065	-0.726
Valid. Dataset	BOVINO - HV14n_REALE3	6.20	1.80	0.304	0.62	0.065	-3.423
Regr. dataset	ANZANO - LIN_TOT_synM7.0R10ss15	7.00	10.00	0.286	1.14	0.08	-2.588
Valid. Dataset	ROCCHETTA - LIN_TOT_synM7.0R10ss09	7.00	10.00	0.286	1.14	0.08	-3.287

A first examined case involves two accelerograms of the same event, amplified according to two site models (HV14n and HV15n), both relating to the same town of Bovino, one included in the regression dataset and the other in the validation dataset. For these accelerograms, the event magnitude and distance are the same, but PGA differs significantly (0.389 and 0.304g), while I_A is almost the same (0.63 and 0.62 m/s). These accelerograms produce very different estimation errors (-0.7σ and -3.4σ, respectively). The second case comprises two synthetic accelerograms obtained for two different localities (Anzano and Rocchetta), for the same seismic scenario (M = 7.0, D = 10 km), characterized by equal PGA (0.286g) and similar I_A (1.11 and 1.14 m/s). In this case too, the result for the accelerogram in the validation dataset (Rocchetta) is strongly negative (-3.3σ), but the difference from that in the regression dataset (Anzano) is less pronounced (-2.6σ). Searching for the cause of such differences in the normalized errors, the Fourier spectra of the pairs of accelerograms were compared (Fig. 3.30). Furthermore, considering that differences in D_N estimates may be related to different durations of the time windows in which critical acceleration is exceeded, the time series were compared with the partial results of the numerical double integration leading to the calculation of D_N (Figs. 3.31-3.32).

Regarding the pair of accelerograms from BOVINO (HV15n_REALE3 and HV14n_REALE3), despite having identical or very similar parameters (M, D, I_A), they produce a very different D_N value (7.0 cm for the first and 2.5 cm for the second, considering the mean values; 8.1 cm for the first and 2.9 cm for the second, considering the results obtained by reversing the accelerogram polarity, shown in Fig. 3.31). Therefore, they were compared to understand whether these differences could be attributed to the influence of parameters that are not taken into account in the empirical relationships used to estimate D_N.

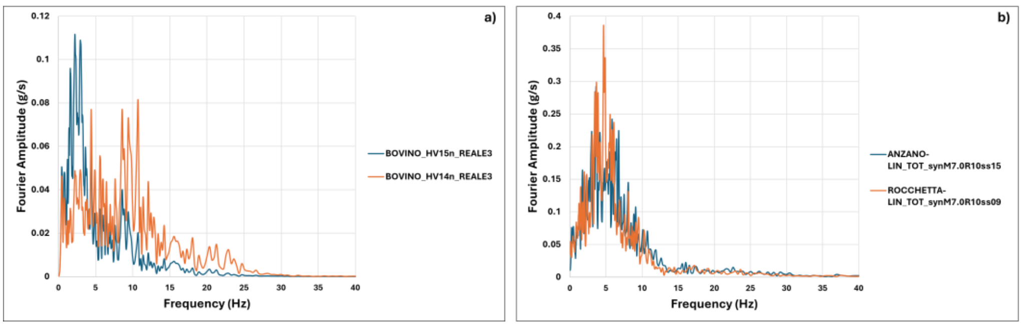

*Fig. 3.30: Fourier amplitude spectrum for the first (**a**) and the second (**b**) pair of accelerograms examined in comparison.*

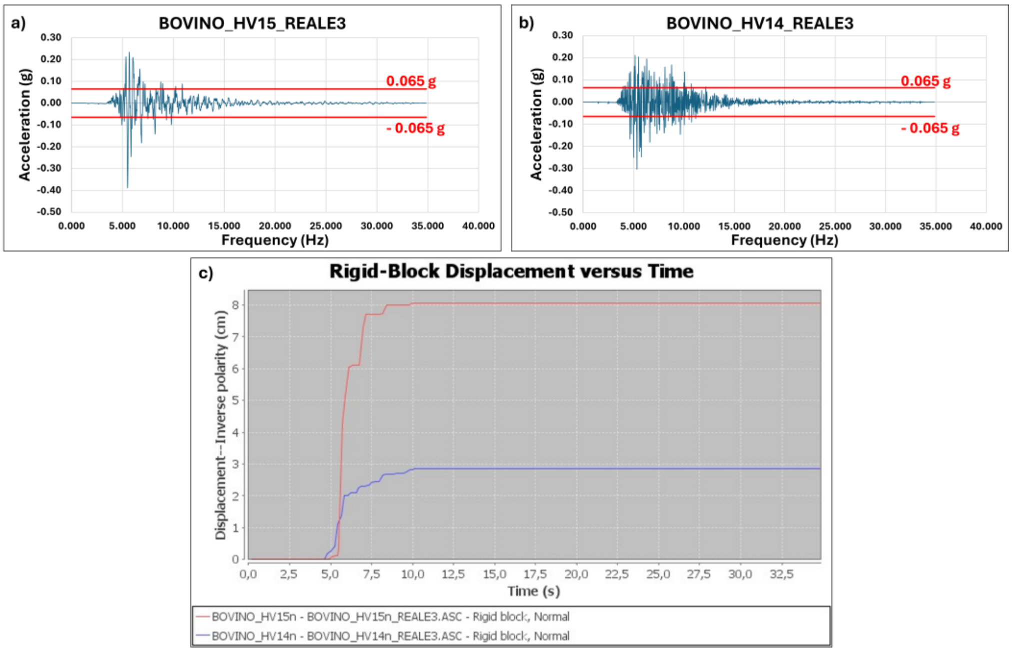

*Fig. 3.31: Accelerograms (**a**) BOVINO_HV15n_REALE3 and (**b**) BOVINO_HV14n_REALE3 with indication of the level of critical acceleration (in red) in both positive and negative directions, for the cases of calculations carried out using the accelerogram original and reversed polarity, respectively. Panel (**c**) shows the D_N cumulative curve for reversed accelerogram polarity, obtained from SLAMMER.*

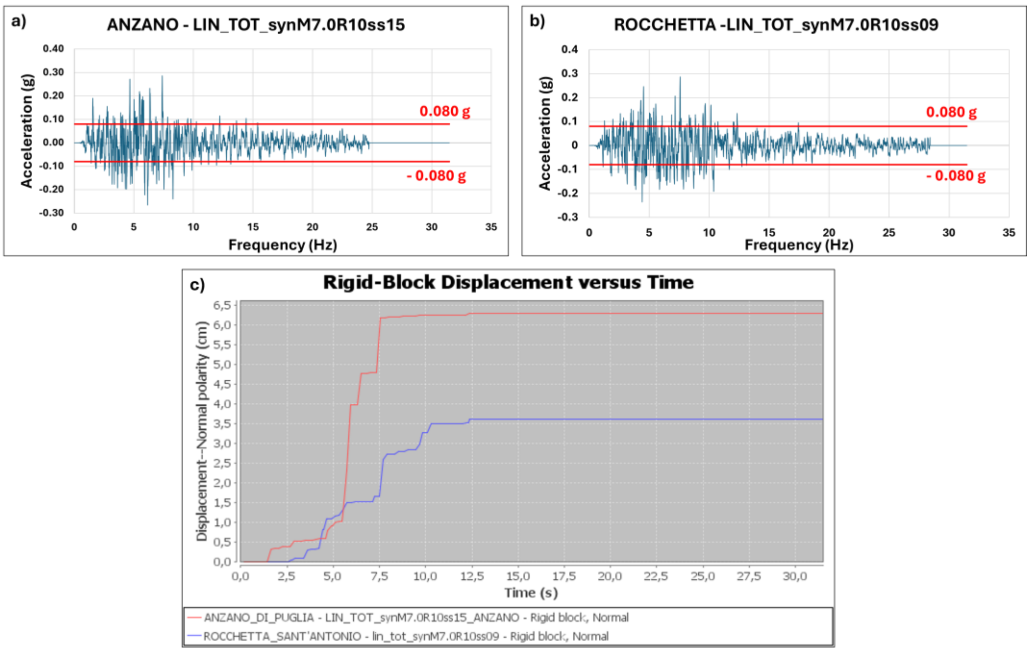

*Fig. 3.32: Accelerograms (**a**) ANZANO-LIN_TOT_symM7.0R10ss15 and (**b**) ROCCHETTA-LIN_TOT_symM7.0R10ss09 with indication of the critical acceleration (in red) in both positive and negative directions, for the cases of calculations carried out using the accelerogram original and reverse polarity, respectively. Panel (**c**) shows the D_N cumulative curve for normal polarity obtained from SLAMMER.*

These two accelerograms were obtained by modeling the site dynamic response at two different sites (HV15n and HV14n), starting from the same accelerogram recorded under reference site conditions. The HV15n accelerogram has much more energy at lower frequencies (< 10 Hz) than HV14n (Fig. 3.30a). The different frequency contents are therefore attributable to the different site response. Comparing the two accelerograms reveals that HV15n has relatively fewer, but larger, low-frequency peaks exceeding the critical acceleration a_c (both in positive and negative direction), whereas HV14n has more high-frequency, but smaller, peaks (Fig. 3.31a-b). The fact that the I_A is practically the same in both accelerograms can be explained as a compensatory effect between the number/frequency of peaks and their amplitudes. Since smaller high-frequency peak gives a lesser contribution to the integral of accelerations exceeding a_c, differences in peaks amplitude and frequency content, with the same total signal energy, appear to lead to very different D_N estimates in the two cases.

This explanation is confirmed by the comparison of the graphs of the cumulative displacement D_N (Fig. 3.31c): the maximum differentiation between the two accelerograms is observed around 5-6 s, coinciding with the passage of the major low-frequency peaks in the HV15n accelerogram.

The same procedure was applied to the other pair of accelerograms with similar properties (ANZANO - LIN_TOT_synM7.0R10ss15 and ROCCHETTA - LIN_TOT_synM7.0R10ss09). These are two simulated accelerograms chosen as seismic input for modeling site response in SM studies to be conducted in two towns (Anzano and Rocchetta, respectively). In this case M, D and PGA are identical and I_A differs only slightly (1.11 and 1.14 m/s, respectively), but D_N differs significantly (4.8 cm and 3.9 cm respectively, considering the mean values; 6.3 cm and 3.6 cm respectively, considering the normal polarity values), although by a smaller amount than in the previous case.

Comparing the two accelerograms (Fig. 3.32a-b), the first appears to have more peaks of larger amplitude (> 0.2g) within a smaller overall number of peaks exceeding a_c but, in this case, the frequency content does not appear to be so different (Fig. 3.30b). Thus, only one of the two factors causing the difference in the previous case (peak larger amplitudes and frequencies) seems to be operating here and a difference in the D_N estimate (Fig. 3.32c) is present, but not as pronounced as in the previous case.

Therefore, what can be deduced from these observations is that by using a relationship depending only on I_A and a_c, factors that could make an important contribution to differentiating the resulting D_N values (e.g., amplitudes and frequency of major peaks) are overlooked, thus leading to a larger scattering of errors in the estimation of D_N, which may be very high in some cases.

3.3 Update of Daunia regional map of slope resistance demand

The first application of the procedure for calculating resistance demand, as mentioned in section 3.1, was carried out by Del Gaudio et al. in 2003, who produced a map of resistance demand values calculated for a 10% probability in 50 years of exceeding D_N=10 cm. This exceedance probability is adopted by the Italian building code as the maximum level permitted for exceeding the Life-Safety Limit State in case of ordinary buildings.

To verify how much the adoption of a new software for calculating exceedance rates, a new seismogenic zoning, a new seismic catalog and a new attenuation relationship affect the calculation of resistance demand, the map created in 2003 was compared with the one updated using the most recent tools now available but maintaining the D_N predicting equation [3.4] (Fig. 3.33).

In both maps, the site response was taken into account by using the site factor included in the attenuation relationship used. In the first map (Fig. 3.33a), the resistance demand values are rather low (about 0.04g at most), below the threshold of 0.05g that Wilson and Keefer (1985) proposed to consider as the minimum threshold for paying attention to seismically induced landslide hazard. Indeed, for ac < 0.05g, the slopes are so close to the limit equilibrium that they are more likely to be subjected to landslides due to more frequent non-seismic causes (e.g., meteorological events), before the next seismic event. In the second map (Fig. 3.33b), on the other hand, the resistance demand values were generally higher and almost doubled (up to a maximum of 0.083g).

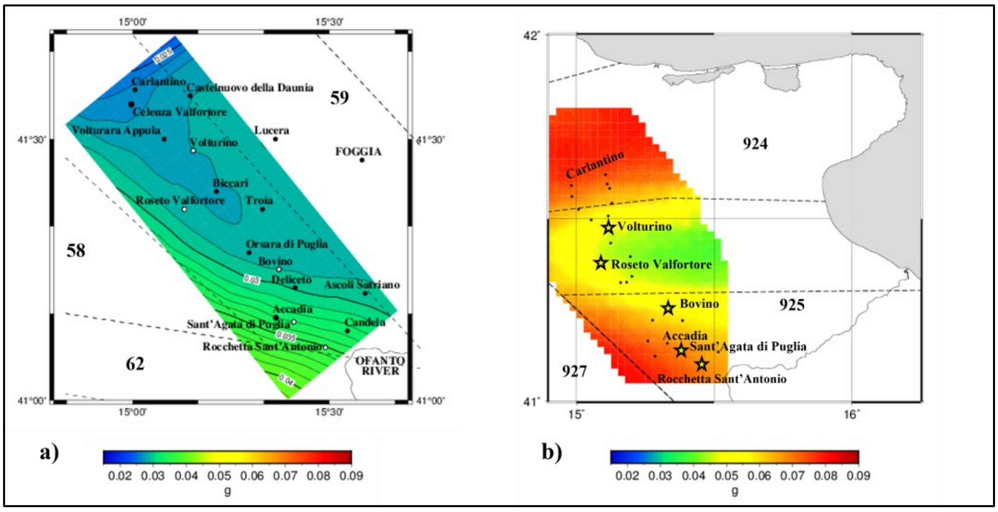

*Fig. 3.33: Map of $(A_c)_{10}$ values calculated for a 10% probability in 50 years of exceeding D_N=10 cm using Romeo (2000) relationship **a)** obtained by Del Gaudio et al. (2003) and modified by adding a color scale and **b)** updated using the R-CRISIS software, the ZS9 seismogenic zoning, the new I_A attenuation relationship by Sabetta et al. (2021) and the new CPTI15 seismic catalog (Rovida et al., 2022), incorporating the site factor. In both maps the dashed black lines represent the boundaries of the seismogenic zones closest to the Daunia Mountains: **a)** 58-59-62 according to ZS4 and **b)** 924-925-927 according to ZS9. White circles in **a)** and stars in **b)** mark the municipality location where historically earthquake-induced landslides occurred.*

This difference in the values of $(A_c)_{10}$ can be attributed to the use of a different attenuation relationship in the calculation of the expected I_A values: the relationship proposed by Sabetta and Pugliese (1996) considers a site factor that depends on a qualitative site classification of the soil type, while that proposed by Sabetta et al. (2021) introduces a site factor that depends on the average shear-wave velocity of the top 30 meters of the subsoil (V_{S30}). Using the former in the study of 2003, slope site conditions were assimilated to the class of “deep soil” (characterized by a velocity between 400 m/s and 800 m/s over a thickness > 20 m) to which the GMPM attributed an increase of I_A by a factor 1.4. In the new calculation, adopting a site factor according to equation [3.8] for the I_A

calculation and assuming V_{S30} = 250 m/s, based on the available SM data, implies an increase of I_A by a factor 3.3, which is approximately twice that of the previous calculation.

The spatial distribution of $(A_c)_{10}$ values appears to be strongly influenced by the proximity of seismogenic zones: in the old map, the highest values are recorded in the southernmost portion, within the seismogenic zone 62 of ZS4, while in the updated map maxima are recorded within the seismogenic zones 924, 925 and 927 of ZS9.The greater differences between the two maps are found in the northernmost part of the Daunia Mountains where, near the municipality of Celenza Valfortore, $(A_c)_{10}$ is equal to 0.026g on the old map and approximately 0.070g on the updated one.

Therefore, while the use of a different seismogenic zoning affects the pattern of spatial distribution of $(A_c)_{10}$ values, the use of a different attenuation relationship – which models the site effect differently – has a major influence on the resulting $(A_c)_{10}$ values, which can increase considerably.

In the first phase, the map of $(A_c)_{10}$ values were calculated for a 10% probability in 50 years that D_N exceeds 10 cm. According to the Italian building code (Ministero delle Infrastrutture e dei Trasporti, 2018), this is the safety limit to be respected in designing common buildings to ensure that seismic events do not endanger the people who live there. Indeed, designing a building to resist shakings with a 10% probability of being exceeded within 50 years implies a 90% probability that the building will not be subjected to seismic shaking that compromises the required level of safety during its useful life. On the other hand, slope failures could affect and damage not only common buildings, but also strategic structures (such as hospitals, roads, electrical networks and aqueducts), and therefore a higher safety level should be required. For this reason, slope resistance demand assessments were also carried out considering a 5% probability of exceedance in 50 years (corresponding to a 95% safety level) to comply with the requirements for verifying the Collapse Prevention Limit State, thus assimilating a slope failure to a building collapse that endangers the surrounding area.

Fig. 3.34 shows the map of $(A_c)_{10}$ values calculated for a 5% probability in 50 years of exceeding D_N=10 cm using Romeo (2000) relationship and the new available tools. With this new level of safety, the values of $(A_c)_{10}$ ranging from a minimum of 0.023g to a maximum of 0.068g were obtained. Compared with that obtained for a 10% probability of exceedance (Fig. 3.20), there is an increase in the resistance demand values, especially in the northernmost and southernmost parts of the Daunia Mountains, where the values rose from approximately 0.035/0.040g to approximately 0.050/0.060g, with an increase implying a more cautious approach.

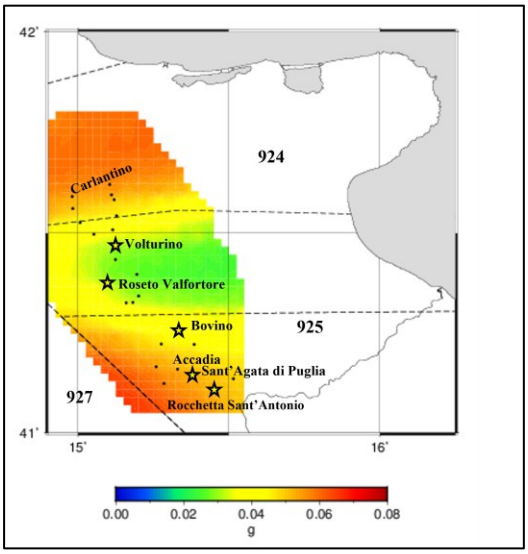

Fig. 3.34: Map of $(A_c)_{10}$ values calculated for a 5% probability in 50 years of exceeding D_N=10 cm using i) Romeo (2000) relationship, ii) the R-CRISIS software, iii) the ZS9 seismogenic zoning, iv) the new I_A attenuation relationship by Sabetta et al. (2021) and v) the new CPTI15 seismic catalog (Rovida et al., 2022). The seismogenic zones closest to the Daunia Mountains (924, 925 and 927 according to ZS9) are shown. Black dots and stars as in Fig. 3.20.

A further issue addressed in this study was to evaluate the relevance of using a relationship calibrated ad hoc for the study area to estimate D_N from I_A and a_c, rather than using more general relationships reported in the literature. In this regard, the predictive capability of the new empirical relationship [3.14] was verified and compared with that of the relationships proposed by Jibson et al. [3.3] and Romeo [3.4]. Another relationship proposed by Romeo (2000) calibrated for Italy was considered, which includes an additional ground motion parameter (i.e., the PGA value) used to normalize the a_c values, according to the following expression:

$$logD_N = 0.607logI_A - 3.719\frac{a_c}{PGA} + 0.852 \qquad [3.17].$$

The D_N values estimated using these empirical relationships for the two validation datasets accelerograms were compared with the D_N values calculated rigorously using the SLAMMER software to determine estimation errors. The results of this test of predictive capability are shown in Table 3.12.

Table 3.12: Results of the test of predictive capability performed on the two validation datasets using the new regional-specific relationship and other more general equations available in literature. For each relationship and for both validation datasets, minimum, maximum and average logarithmic errors are reported with the relative RMSE. The lowest RMSE values are highlighted in red.

		New empirical eq. [3.14]	**Jibson et al. eq. [3.3]**	**Romeo eq. [3.4]**	**Romeo eq. [3.17]**
	Log errors				
	MIN	-0.443	-0.944	-1.940	-0.772
Validation Dataset 1	MAX	0.313	0.494	0.394	0.223
	MEAN	-0.065	-0.176	-0.605	-0.305
	RMSE	**0.160**	0.342	0.787	0.364
	Log errors				
	MIN	-0.446	-0.830	-1.863	-0.756
Validation Dataset 2	MAX	0.355	0.576	0.549	0.191
	MEAN	-0.017	-0.120	-0.555	-0.245
	RMSE	**0.161**	0.303	0.742	0.307

The results obtained show that the predictive capability of the new empirical relationship [3.14] is better than that of the other relationships: its estimation errors are much lower for both validation datasets. Furthermore, the mean logarithmic error is close to 0, indicating a good balance between overestimations and underestimations of the D_N value.

Equations [3.3] and [3.4] show results that deviate both positively and negatively from the experimental data, although with a prevalence of cases in which D_N is overestimated, thus creating an excess of negative residuals, especially in relation [3.4].

From the scatter plots obtained for the two validation datasets (Fig. 3.35) using Romeo's relationship [3.4] (Fig. 3.35a/b), it can be seen that overestimations are mainly recorded for low a_c values (from 0.010 to 0.019g), for which more than 1/3 of the logarithmic residuals are less than the mean value by more than 1 standard error (±0.562, obtained from relation [3.4]), within the entire I_A range.

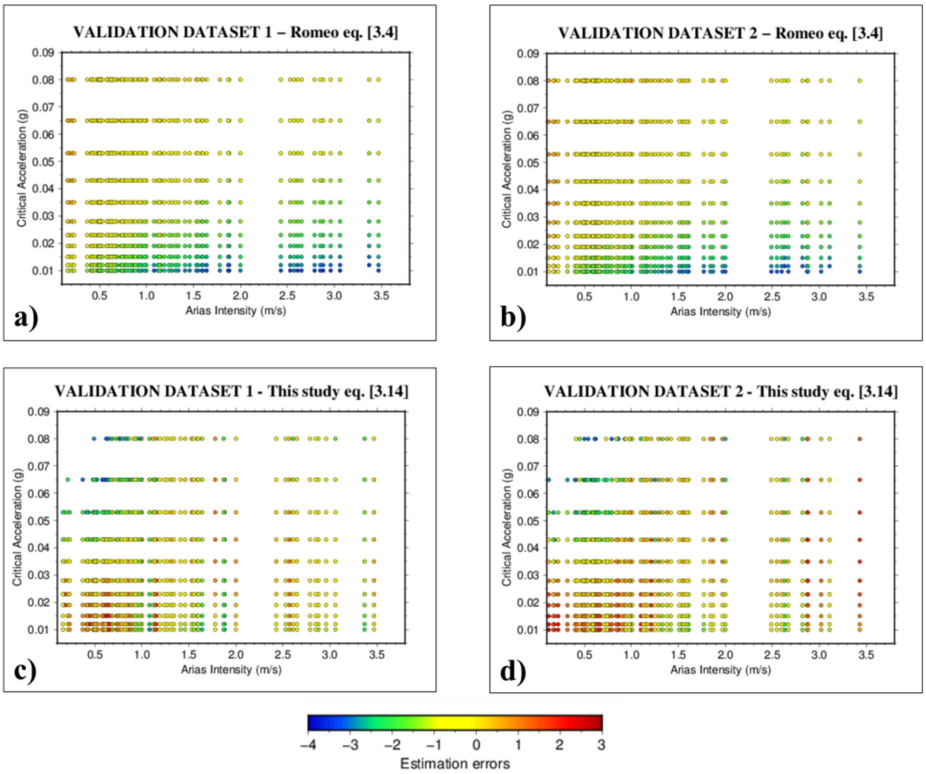

*Fig. 3.35: Scatter plots of normalized estimation errors (represented using a color scale) obtained by applying **(a/b)** Romeo's relationship [3.4] and **(b/c)** the new relationship calibrated for the Daunia Mountains [3.14] to the two validation datasets, as a function of critical acceleration a_c and Arias intensity I_A.*

Using the new relationship calibrated for the Daunia Mountains [3.14] (Fig. 3.35c/d), on the other hand, the distribution of errors appears better balanced across the different I_A-a_c combinations.

The results obtained using the relationship [3.17] proposed by Romeo in 2000 show a RMSE close to that obtained with the relationship [3.3] proposed by Jibson et al. (2000) but higher compared to that obtained with the new predictive equation [3.14].

At this point, a further test was carried out by calibrating a relationship with the same functional form as [3.17] but using specific data for the study area:

$$\log D_N = 0.666 log I_A - 3.996 \frac{a_C}{PGA} + 0.511 \qquad [3.18].$$

The obtained regression statistics were compared with those previously obtained using the simpler relationship [3.14] (Table 3.13). In this comparison as well, the equation [3.14] proved to have better predictive capability, providing a lower regression standard error (0.141 vs. 0.172) and a lower RMSE (0.160 vs. 0.199 for validation dataset 1 and 0.161 vs. 0.188 for validation dataset 2).

Table 3.13: Comparison of regression statistics and predictive capability test results obtained using equation [3.14] and [3.18].

	Regression Statistics	
	Eq. [3.14]	Eq. [3.18]
R^2	0.888	0.864
St. Err.	0.141	0.172
Obs	688	703
	Predictive Capability	
	RMSE	RMSE
Validation Dataset 1	0.160	0.199
Validation Dataset 2	0.161	0.188

These results show that regional-specific equations have better predictive capability, even in their most simplified form (as in the case of equation [3.14]), and therefore no benefit seems to derive from using multiple ground shaking parameters, especially in applications to probabilistic estimations, where conditional probabilities should be assigned to combinations of multiple parameters.

The map of $(A_c)_{10}$ values was then obtained, both for 10% and 5% exceedance probability, using the new empirical relationship calibrated specifically for the Daunia area (Fig. 3.36).

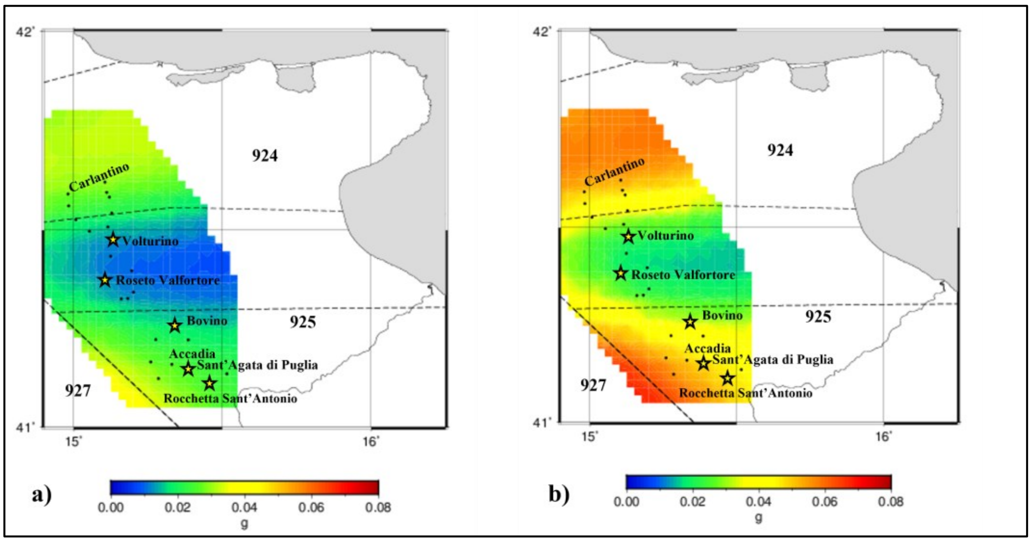

*Fig. 3.36: Map of $(A_c)_{10}$ values calculated for (**a**) 10% and (**b**) 5% probability in 50 years of exceeding D_N=10 cm using i) the new empirical relationship calibrated for the Daunia Mountains, ii) the R-CRISIS software, iii) the ZS9 seismogenic zoning, iv) the new I_A attenuation relationship by Sabetta et al. (2021) and v) the new CPTI15 seismic catalog (Rovida et al., 2022). The seismogenic zones closest to the Daunia Mountains (924, 925 and 927 according to ZS9) are shown. Black dots and stars as in Fig. 3.20.*

For a 10% probability in 50 years, the values of $(A_c)_{10}$ range from a minimum of 0.008g to a maximum of 0.039g, while those obtained for a 5% probability in 50 years range from 0.013g to 0.071g.

As final test, the impact of using the new D_N-I_A-a_c relationship on the estimation of resistance demand was also assessed by observing the differences in the $(A_c)_{10}$ values obtained using non-regional-specific relationships such as [3.3] by Jibson et al. and [3.4] by Romeo compared to those obtained using the new relationship [3.14] (Fig. 3.37) for a 5% probability in 50 years that D_N exceeds 10cm.

What emerges is a slight change in the values of $(A_c)_{10}$ when using different D_N-I_A-a_c relationships; indeed, the greatest difference is equal to 0.020g, found in the S-W portion of the study area and obtained using the Jibson et al. relationship (Fig. 3.37a). Thus, the results obtained using a D_N predictive relationship specific to an Italian region appear more similar to those obtained using a relationship calibrated on other Italian accelerograms than on data from a completely different area.

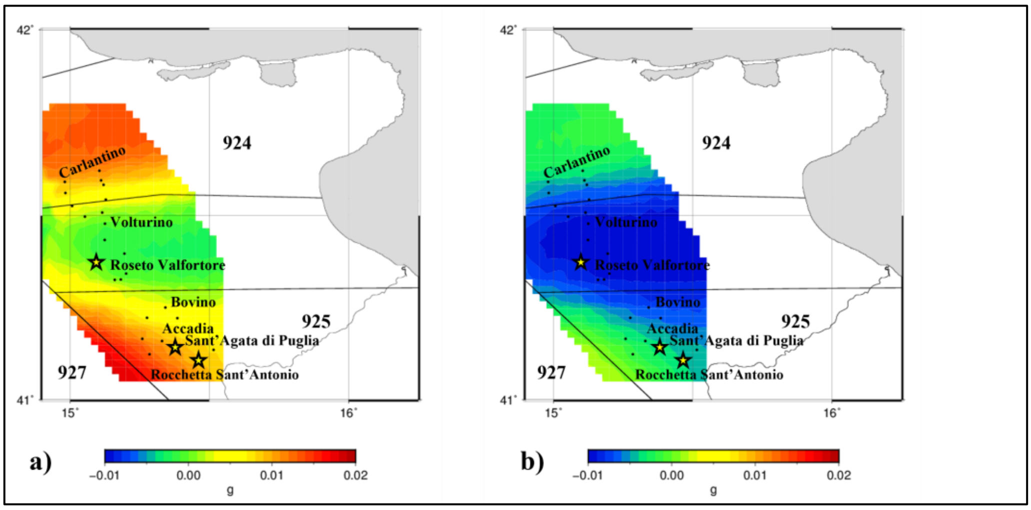

*Fig. 3.37: Maps of differences in $(A_c)_{10}$ values found using **(a)** the relationship [3.3] by Jibson et al. and **(b)** the relationship [3.4] by Romeo compared to those obtained using the new relationship [3.14] calibrated for the Daunia Mountains. The seismogenic zones closest to the Daunia Mountains (924, 925 and 927 according to ZS9) are shown. Black dots and stars as in Fig. 3.20.*

4. 1D MODELING FOR ESTIMATING LITHOSTRATIGRAPHIC AMPLIFICATION

4.1 Methodology

The relationship proposed by Sabetta et al. (2021) [3.5] can be used to calculate the expected I_A values when estimating the seismicity-posed slope resistance demand. This relationship includes a term representing the site effect as a function of V_{S30} value only. However, considering the site effect in a less simplistic manner is fundamental, as the presence of possible site amplifications – stratigraphic and/or topographic (see Chapter 1) – could significantly increase the site response.

Indeed, using a generic D_N-I_A-a_c relationship for calculating $(A_c)_x$, like this:

$$\log D_N = a \log I_A - b \log a_c + c \qquad [4.1]$$

the presence of an I_A amplified by a factor AF would result in a median increase of the resistance demand by a factor equal to:

$$K = AF^{\frac{a}{b}} = AF^{1.07} \qquad [4.2]$$

having set a = 0.962 and b = 0.901, according to the equation [3.14] calibrated for the Daunia Mountains area.

In this regard, therefore, it is necessary to incorporate the dynamic site response into the procedure for estimating the slope resistance demand.

In the initial phase of the work, only lithostratigraphic amplification was taken into account, because i) it is simpler to evaluate than topographic one (which would require complex 2D/3D site response modeling) and ii) comparative tests have shown that the purely topographic effect produces smaller amplification factors than lithostratigraphic one. Numerical modeling of site response conducted by Lee et al. (2009) in Taiwan and by Legesse and Mammo (2024) in Ethiopia provided, at most, topographic amplification factors of 1.6–2 in terms of PGA, while Zhan et al. (2020) obtained amplification factors in the range of

1.3–1.5 in terms of PGD (Peak Ground Displacement). In contrast, where modeling was carried out to compare purely topographic effects with combined lithostratigraphic and topographic effects, both in terms of spectral amplifications (e.g., Glinksy et al., 2019; Luo et al., 2020), the former provided amplification factors of up to 2.5, while the latter provided factors of up to 8.

To incorporate the lithostratigraphic effect into the procedure for calculating the slope resistance demand, a methodology has been developed that calculates the amplification factor expressed in terms of Arias intensity from a 1D modeling of the site response. This modeling is based on vertical profiles of shear waves velocity (V_S) derived from the inversion of Rayleigh wave ellipticity curves obtained from ambient noise analysis, conducted using the **HVIP technique** (**H**orizontal to **V**ertical ratio from **I**nstantaneous **P**olarization - Del Gaudio, 2017).

4.1.1 Determination of Rayleigh wave ellipticity curves from ambient noise analysis

This HVIP technique extracts Rayleigh wave packets from noise recordings and calculates their ellipticity (i.e., the H/V ratio of the horizontal-to-vertical component amplitude of ground motion), which varies with frequency depending on the vertical distribution of seismic wave velocity in the subsoil. Compared to the standard HVSR (**H**orizontal-to-**V**ertical **S**pectral **R**atio) method (Nakamura, 1989), commonly used to identify the site resonance frequencies, the HVIP technique provides more stable estimates of the H/V peak amplitudes, which are better correlated with the velocity contrast between surface layers and bedrock responsible for site amplification. Indeed, the amplitude of the H/V ratios resulting from the HVSR analysis also depends on the proportion of the different types of waves that contribute to the noise, which depends on environmental conditions and can vary over time (cf. Bonnefoy-Claudet et al., 2006; Del Gaudio et al., 2021). The HVIP technique, on the other hand, extracts only the Rayleigh waves from the noise recording, by obtaining a H/V curve which can be more reliably used to constrain the vertical velocity profile below the recording site. Inverting the H/V curve in terms of a velocity model, with the support of a few additional constraints, provides the basis for a numerical modeling of the site response and, consequently, estimation of the amplification factor.

To estimate the Rayleigh wave ellipticity as a function of frequency, this technique first applies narrow-band filtering to the noise recording, centered on a set of frequencies of interest. Then, it performs an instant-by-instant polarization analysis by transforming the real signal into a complex-valued analytic signal. For a single-component signal, the analytic signal is obtained by adding an imaginary part in this way:

$$u_c(t) = u(t) + i\hat{u}(t) = A(t)e^{i\Phi(t)} \qquad [4.3]$$

where $u(t)$ is the initial signal, representing the real part of a vector moving on a complex plane, $\hat{u}(t)=H[u(t)]$ is the Hilbert transform of the initial signal, $A(t)$ is the modulus of the vector, $\Phi(t)$ is the vector phase and i is the imaginary unit. The vector projection onto the real axis represents the real ground motion, while the Hilbert transform corresponds to its imaginary part.

For a multi-component signal, equation [4.3] takes the following form:

$$\vec{u}_c(t) = \vec{u}\,(t) + i\vec{\hat{u}}\,(t) = \vec{A}(t)^{i\Phi t} \qquad [4.4]$$

where $\vec{A}$(t) is a multidimensional complex vector, assuming a vector character also in real space, and $\Phi(t)$ is the real phase.

In the case of two- or three-component signals, the ground particle motion can be decomposed into a series of elements consisting of segments of ellipses whose axes' length and orientation in space vary gradually from one instant to the next. The elliptical trajectory lies on the plane of the two components for two-dimensional signals and on a plane with variable attitude for three-dimensional signals.

Orientation and amplitude of the major semi-axis $\vec{a}(t)$ and minor semi-axis $\vec{b}(t)$ of the elliptical trajectories can be obtained, instant by instant, from the phase shifts Φ_0 that maximize the modulus of the real part of the vector [4.4]. This phase shift can be calculated through the equation (Morozov and Smithson, 1996):

$$\Phi_0 = \frac{1}{2}\arg\left[\frac{1}{2}\sum_k (u_k + i\hat{u}_k)^2\right] \qquad [4.5]$$

where u_k are the components (two or three, depending on the signal) of the vector $\vec{u}_c(t)$ and the sum is calculated over the set of components of the analytical signal.

The two semi-axes of the ellipse can be obtained from the following formulas:

$$\vec{a}(t) = Re[e^{-i\Phi_0}\vec{u}_c(t)] \qquad [4.6]$$

$$\vec{b}(t) = Re\left[e^{-i\left(\Phi_0+\frac{\pi}{2}\right)}\vec{u}_c(t)\right] \qquad [4.7].$$

The elliptical trajectory attitude in the three-dimensional case can be defined by the planarity vector $\vec{p}(t)$, given by the vector product between $\vec{a}(t)$ and $\vec{b}(t)$ (Schimmel and Gallart, 2003): when $|\vec{a}(t)| \gg |\vec{b}(t)|$, the elliptical trajectory degenerates into a rectilinear trajectory.

Rayleigh waves are characterized by elliptical polarization in a vertical plane with one of the two semiaxis in the horizontal direction, Love waves have linear polarization in the horizontal direction, while P- and S-waves have variably oriented linear polarization. A useful criterion for identifying Love waves is based on the rectilinearity parameter (Schimmel and Gallart, 2004):

$$rl = 1 - \frac{|\vec{b}(t)|}{|\vec{a}(t)|} \qquad [4.8]$$

where:

- if $\vec{a}(t) = \vec{b}(t)$, $rl = 0$ and the polarization is circular;
- if $\vec{b}(t) = 0$, $rl = 1$ and the polarization is rectilinear;

- if $\vec{a}(t) \neq \vec{b}(t) \neq 0$, rl is $<$ 1 and the polarization is elliptical.

Rayleigh waves can be identified when the instantaneous elliptical trajectory meets the following two conditions:

i) the planarity vector (perpendicular to the ellipse) is horizontal;
ii) the semi-axes are one horizontal and one vertical, interchangeably.

Love waves are identified when:

iii) the major semi-axis is horizontal;
iv) $rl = 1$.

However, these identification criteria may not be met exactly due to contamination from simultaneous waves of different types. Therefore, signal samples are identified as belonging to Rayleigh or Love waves if conditions i) and ii), or iii) and iv) are met to a certain degree of approximation. Furthermore, at frequencies close to the resonance ones for the site, Rayleigh waves also tend to approach horizontal rectilinearity and, in such a situation, some signal samples may meet the conditions for classification as both Rayleigh and Love waves. Therefore, a rectilinearity threshold is also introduced to distinguish between the two types of waves, with only Love waves that exceed this threshold. While this could result in the loss of a few samples of the Rayleigh wave ellipticity curve near the resonance peak frequency, for the purposes of the curve inversion in terms of a velocity profile, the effect on the inversion results can be minimal if the rest of the estimated and theoretical ellipticity curves closely match.

The method implementation goes through a preliminary phase of selecting the filtering parameters that optimize the construction of the dataset of samples classified as Rayleigh type, such that it is sufficiently robust for a reliable definition of the average properties of these waves but limiting contaminations due to the overlap of other types of waves. Therefore, selection criteria are adopted to identify a small percentage of samples in which Rayleigh waves are highly predominant. For this purpose, the HVIP algorithm extracts all samples in which $\vec{a}(t)$, $\vec{b}(t)$ and $\vec{p}(t)$ deviate from the expected direction at most by a selectable small angle (typically 5-10°). Furthermore, a signal sample is identified as belonging to Rayleigh waves only if it is part of a series of samples that satisfy the set conditions, in order to avoid considering individual samples that satisfy the mentioned conditions i) and ii) by chance but are not part of a Rayleigh wave train. For this reason, therefore, a threshold is set for the number of consecutive samples with Rayleigh-type polarization. This threshold varies by case and is defined in a preliminary phase, which identifies, on a reduced set of trial frequencies, the combination of filtering parameters generating the minimum scattering of the H/V values for individual samples around the average values at each frequency, while producing a consistent number of H/V estimates. The filtering parameters are considered adequate if at least 1% of the total number of samples is classified as belonging to Rayleigh waves. Since an ambient noise recording contains a few hundred thousand samples, this means that a few thousand samples are extracted from the recording at each analyzed frequency, over which the average properties of Rayleigh waves are determined.

After this preliminary stage of selection of the optimal filtering parameters, the H/V ratio can be calculated at a higher frequency resolution (typically 0.05 Hz) in the final processing phase. By applying analytical transforms separately to the horizontal and vertical components, it is possible to estimate the amplitude H and amplitude V respectively, instant by instant. The horizontal component of the elliptical trajectory would degenerate into a rectilinear trajectory if the ground motion consisted only of Rayleigh waves, but the polarization is generally not perfectly linear due to the overlap of other types of waves. Thus, the analytic transformation of the combination of the two horizontal components defines the properties of an elliptical particle motion lying on a horizontal plane. The major axis of this ellipse can be considered the best estimate of the amplitude H of the horizontal Rayleigh waves component, attributing the transverse component to the contamination of other waves. To obtain the variation in amplitude of the vertical component, on the other hand, the analytical transform is applied to the vertical component. Finally, the instantaneous H/V ratios of Rayleigh wave samples obtained at each analyzed frequency are averaged to determine a curve of ellipticity as a function of frequency.

The HVIP analysis is performed using the FORTRAN program **hvanasig8.f**, which operates in two phases. In a preliminary phase, analysis is conducted with low spectral resolution and using different combinations of input parameters, in order to identify those that minimize the scattering of H/V values around the average value for each frequency. In the input file required for this stage (Fig. 4.1), the following parameters must be specified:

```
0  1  1  3  2  1  3 -1                                          iop,iod,ioh,ifm,ip1,ip2,ip3,ncomp
  125.  79                                                        azcomp,nfcomp
 0.50
 0.75
 1.00
 1.25
 1.50
 1.75
 2.00
 2.25
 2.50
 2.75
 3.00
 3.25
 3.50
 3.75
 4.00
 4.25
 4.50
 4.75
 5.00
 5.25
 5.50
 5.75
```

Fig. 4.1: Example of input file for the preliminary phase of the hvanasig8.f program.

- **iop** → option for printing data, which can take different values:
  - 0: only the average values of the output parameters are printed;
  - 1: the output parameters for each sample are printed;
  - 2: only the output parameters of Rayleigh-type samples are printed;
  - -2: in addition to Rayleigh-type parameters, a file prepared for graphing in GMT (Generic Mapping Tools - Wessel et al., 2019) is also printed;

    - 3: the output parameters of both Rayleigh-type and Love-type samples are printed;
    - 4: only the output parameters of Love-type samples are printed.
- **iod** → option to apply a linear detrend: 0 = no, 1 = yes;
- **ioh** → option to apply the Hamming window: 0 = no, 1 = yes;
- **ifm** → to identify the input file format:
    - 0: V2 format;
    - -1: SG2 format;
    - -2: Teledyne format;
    - -3: Tromino format.
- **ip1**, **ip2**, **ip3** → indication of the order of the three components: 1 = east, 2 = north, 3 = vertical;
- **ncomp** → number of azimuths for which the program performs a comparative analysis with synthetic control signals and/or the analysis of the scattering of the instantaneous H/V values obtained around the average value. If it is 0, no comparative analysis is performed, while if it is less than 0, the scattering analysis is performed;
- -**azcomp** → azimuth values for which the comparison/scattering analysis is performed. If it is 0, the analysis is performed with respect to the average calculated for all the azimuths;
- **nfcomp** → number of frequencies for which the scattering analysis is performed. These frequencies are indicated in the following lines.

After the lines indicating the control frequencies used, there are the parameters that control the different analyses (Fig. 4.2), namely:

```
ohAccadiaHV01-1_10g_90r_20.05
41  0.0078125   1. 1199.   0. 10. 10. 10.  -0.90 20 10.  1   79  0.
nhead,pas,ti,dt,eps,sodR,soda,sodL,sorl,nmin,daz,iof,nfc,dstft
0.05  -0.25 -0.20 0.20 0.25                                       beta,ftb,fcb,fca,fta
 0.50  0.75  1.00  1.25  1.50  1.75  2.00  2.25  2.50  2.75  3.00  3.25  3.50  3.75  4.00  4.25
 4.50  4.75  5.00  5.25  5.50  5.75  6.00  6.25  6.50  6.75  7.00  7.25  7.50  7.75  8.00  8.25
 8.50  8.75  9.00  9.25  9.50  9.75 10.00 10.25 10.50 10.75 11.00 11.25 11.50 11.75 12.00 12.25
12.50 12.75 13.00 13.25 13.50 13.75 14.00 14.25 14.50 14.75 15.00 15.25 15.50 15.75 16.00 16.25
16.50 16.75 17.00 17.25 17.50 17.75 18.00 18.25 18.50 18.75 19.00 19.25 19.50 19.75 20.00
HV01-1.dat
ohAccadiaHV01-1_10g_90r_20.1
41  0.0078125   1. 1199.   0. 10. 10. 10.  -0.90 20 10.  1   79  0.
nhead,pas,ti,dt,eps,sodR,soda,sodL,sorl,nmin,daz,iof,nfc,dstft
0.10  -0.25 -0.20 0.20 0.25                                       beta,ftb,fcb,fca,fta
ohAccadiaHV01-1_10g_90r_20.2
41  0.0078125   1. 1199.   0. 10. 10. 10.  -0.90 20 10.  1   79  0.
nhead,pas,ti,dt,eps,sodR,soda,sodL,sorl,nmin,daz,iof,nfc,dstft
0.20  -0.25 -0.20 0.20 0.25                                       beta,ftb,fcb,fca,fta
ohAccadiaHV01-1_10g_90r_20.3
41  0.0078125   1. 1199.   0. 10. 10. 10.  -0.90 20 10.  1   79  0.
nhead,pas,ti,dt,eps,sodR,soda,sodL,sorl,nmin,daz,iof,nfc,dstft
0.30  -0.25 -0.20 0.20 0.25                                       beta,ftb,fcb,fca,fta
ohAccadiaHV01-1_10g_90r_20.4
41  0.0078125   1. 1199.   0. 10. 10. 10.  -0.90 20 10.  1   79  0.
nhead,pas,ti,dt,eps,sodR,soda,sodL,sorl,nmin,daz,iof,nfc,dstft
0.40  -0.25 -0.20 0.20 0.25                                       beta,ftb,fcb,fca,fta
ohAccadiaHV01-1_10g_90r_20.5
41  0.0078125   1. 1199.   0. 10. 10. 10.  -0.90 20 10.  1   79  0.
```

Fig. 4.2: Analysis control parameters to be entered in the input file of the hvanasig8 program in its preliminary phase.

- **nhead** → number of header lines preceding the recording data file;
- **pas** → sampling step;
- **ti** → time in seconds of the first sample to be analyzed;
- **dt** → length in seconds of the recording interval to be analyzed;
- **eps** → damping coefficient to calculate the analytical signal phase;
- **sodR** → maximum angular deviation of the planarity vector from the horizontal, to classify Rayleigh-type waves;
- **soda** → maximum angular deviation of the major axis of the ellipse from the horizontal, to classify Rayleigh-type waves;
- **sodL** → maximum threshold of inclination of the major axis of the ellipse, to classify Love-type waves;
- **sorl** → minimum threshold of the rectilinearity parameter, to classify Love-type waves. If *sorl* < 0, -*sorl* is also used to indicate the maximum value of rectilinearity, to classify Rayleigh-type waves;
- **nmin** → minimum number of consecutive samples with the same type of polarization, to identify a packet of Rayleigh or Love waves;
- **daz** → azimuth interval of the directional analysis;
- **iof** → to indicate the type of filtering to be performed on the data:
  - 0: no filtering;
  - 1: Gaussian filter with fixed bandwidth;

    - -1: Gaussian filter with bandwidth proportional to center frequency;
    - 2: triangular filter with fixed bandwidth;
    - -2: triangular filter with bandwidth proportional to the center frequency;
    - 3: Ormsby filter with fixed bandwidth;
    - -3: Ormsby filter with bandwidth proportional to the center frequency.
- **nfc** → number of frequencies to analyze;
- **dstft** → window length for performing a time variation analysis of the spectral content using STFT (Short Time Fourier Transform): if it is 0, it is not applied;
- **beta** → parameter to control the bandwidth for Gaussian filtering (standard deviation of the Gaussian distribution) or triangular filtering (half width of the passband);
- **ftb**, **fcb**, **fca**, **fta** → frequencies delimiting the passband of the Ormsby filter around the center frequency;
- **fc** → list of *nfc* frequencies to be analyzed;
- **file3** → recording data input file name;
- **output6** → basic name of output files.

Based on previous experiences, Gaussian filtering was adopted and the search for parameters that optimize the analysis results was restricted to combinations of two possible values of **sorl** (0.90 and 0.95) and six values for **beta** (0.05, 0.10, 0.20, 0.30, 0.40 and 0.50), while setting the parameters **sodR**, **soda** and **sodL** to 10° and **nfc** to 20. This produces 12 possible combinations of parameters, resulting in as many groups of output files, one with the basic name of output files specified in input and five others whose names are derived from the first by adding the extensions .cur, .ist, .istL, .istR, .polR. Among the 12 possible solutions, the parameter combination that minimizes the scattering of the instantaneous H/V values around the average values calculated for each control azimuth is selected, as indicated by two summary output files with extension .comp and .sum. From the .sum file, which summarizes the results of the scattering analysis, the lowest scatter solution is identified as satisfying two additional requirements: i) the average number of Rayleigh-type samples must be at least 100 and ii) the average number of Rayleigh-type samples must be at least 1% of the total data of the analyzed signal.

Once the best combination of input parameters has been identified, it is applied to the main phase of the analysis, which is extended to a larger number of frequencies. The input file (Fig. 4.3) contains the same parameters as the preliminary phase, but i) no scattering analysis is performed, ii) only the combination of input parameters that proved to be optimal is used and iii) the frequencies to be analyzed have a tighter step. Once processing is complete, six output files are produced, among which the file with extension .istR reports, for each analyzed frequency, the mean estimated value of Rayleigh wave ellipticity over the samples polarized in specified azimuth intervals.

```
0  1  1  3  2  1  3  0                                   iop,iod,ioh,ifm,ip1,ip2,ip3,ncomp
ohAccadiaHV01-1_10g_90r_20.5
41  0.0078125   1. 1199.   0. 10. 10. 10.  -0.90 20 10.  1   475  0.
nhead,pas,ti,dt,eps,sodR,soda,sodL,sorl,nmin,daz,iof,nfc,dstft
0.50  -0.25 -0.20 0.20 0.25                                   beta,ftb,fcb,fca,fta
0.30
0.35
0.40
0.45
0.50
0.55
0.60
0.65
0.70
0.75
0.80
0.85
0.90
0.95
1.00
1.05
1.10
1.15
1.20
1.25
1.30
1.35
1.40
```

Fig. 4.3: Example of input file of the hvanasig8 program for the analysis main phase.

A smoothing is applied to these values with a specific program named **smoothHVIP** using the Konno and Ohmachi (1998) function. From the output file a curve of mean Rayleigh wave ellipticity as a function of frequency can be obtained as an average over all polarization directions, together with the relative standard deviation.

4.1.2 Rayleigh wave ellipticity curve inversion in terms of 1D velocity profile

Assuming that this ellipticity curve depends on the stratigraphy of the area beneath the noise recording site, it is used as a target curve inverted in terms of vertical velocity profile of S waves using the **DINVER** software (Wathelet, 2005).

This software is based on the "neighborhood algorithm" (Sambridge, 1999), a stochastic search method that randomly samples the multidimensional space of solutions (with one dimension for each model parameter) on the basis of previous results: where optimal solutions cannot be found, sampling is less dense than in areas with better solutions. The program creates sets of 1D velocity models for which – by modifying various parameters from time to time – there is a rapid convergence towards solutions that minimize the misfit function, expressed as:

$$misfit = \sqrt{\sum_{i=1}^{n_f} \frac{(x_{di}-x_{ci})^2}{\sigma_i n_f}} \qquad [4.9].$$

Here n_f represents the sampled frequencies, x_{di} and x_{ci} are the measured and the calculated ellipticity, respectively, and σ_i is a measure of the ellipticity uncertainty.

To set the inversion of the ellipticity curves in terms of seismic stratigraphy, the program requires the user to specify a number of layers and, for each layer, a search range for P-wave velocity, thickness, Poisson ratio, S-wave velocity and density (Fig. 4.4). The information relating to these parameters can be guided from the results of other surveys carried out near the noise measurements; due to the non-uniqueness of the problem solution, independent constraints are necessary to obtain a velocity profile that is as close to reality as possible, especially in the most superficial part, which contributes most significantly to

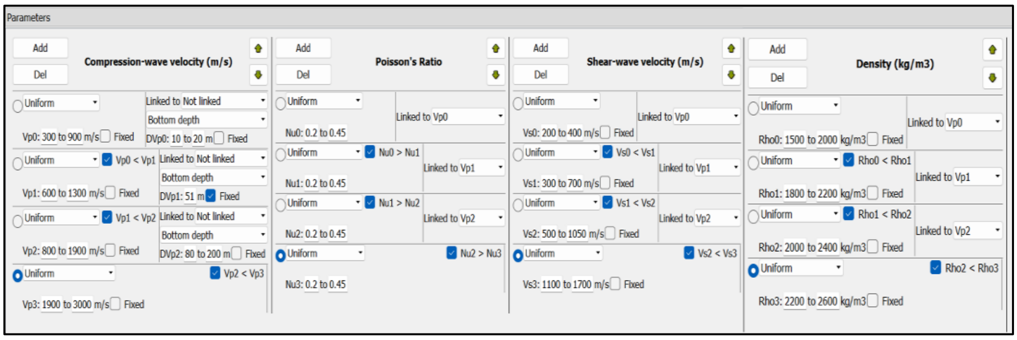

Fig. 4.4: Example of screenshot showing the user interface of the Dinver software to perform the inversion of the ellipticity curve, where the search ranges for P-wave velocity, thickness, Poisson's ratio, S-wave velocity and density of the identified layers must be defined.

site amplification. These constraints are mostly related to some values of thickness or velocity of the most superficial layers of the model, which can be obtained from borehole stratigraphies and geophysical surveys.

4.1.3 1D modeling of site response

The vertical S-wave velocity profile obtained can be used as one of the inputs required by the **STRATA** software (Kottke et al., 2013) to perform 1D modeling of the site response. This software requires that processing options and input data are entered through different panels of the program user interface.

GENERAL SETTINGS (Fig. 4.5), where it is required to specify:

- TYPES OF ANALYSES (linear elastic, linear equivalent EQL, frequency dependent EQL) and the approach to follow (time series or random vibration theory);

- SITE PROPERTY VARIATION optionally activated to perform analyses that account for the variability/uncertainties of subsoil models through a specified number of realizations adopting specified criteria for the description of subsoil model variability;

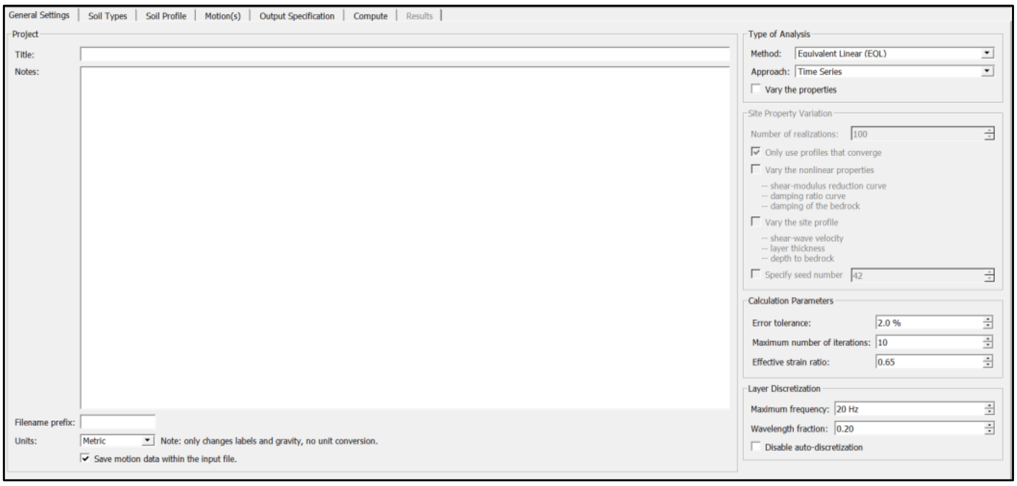

Fig. 4.5: "General settings" section, where processing options and calculation parameters are specified.

- CALCULATION PARAMETERS to be used to account for non-linear soil response, including the error tolerance, the maximum number of iterations and the effective strain ratio to be used during processing;
- LAYER DISCRETIZATION parameters controlling the subdivision of actual layers into sub-layers, whose maximum thickness is fixed as a function of the maximum frequency f_{max} of interest, layer velocity V_s and a specified wavelength fraction λ_{frac} according to the formula:

$$h_{max} = \lambda_{frac} \frac{V_s}{f_{max}} \quad [4.10].$$

SOIL TYPES (Fig. 4.6), identified by a name, for which the following properties of the material that constitutes the model layers must be defined: volume weight, shear modulus G/G_{max} model, damping model and damping limit. For the G/G_{max}

and damping models, it is possible to choose built-in curves provided by the software or create customized ones.

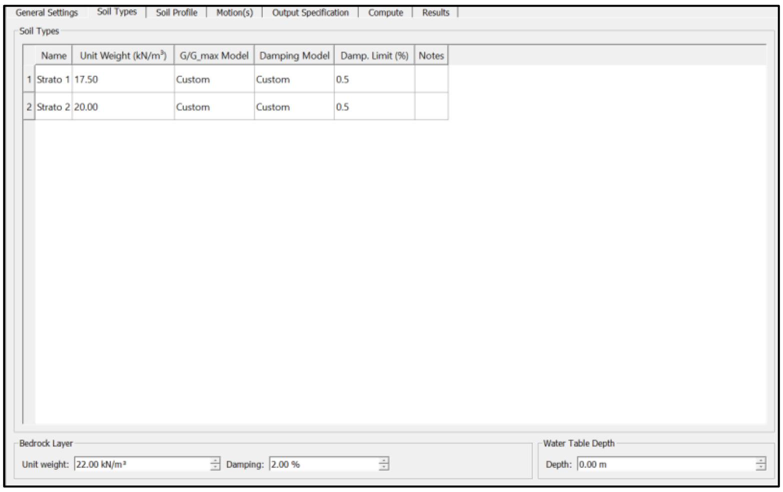

	Name	Unit Weight (kN/m³)	G/G_max Model	Damping Model	Damp. Limit (%)	Notes
1	Strato 1	17.50	Custom	Custom	0.5	
2	Strato 2	20.00	Custom	Custom	0.5	

Fig. 4.6: Example of "soil types" input section, where properties of layer materials are specified.

SOIL PROFILE (Fig. 4.7), describing the series of layers forming the subsoil model: for each layer, the soil type must be specified (among those previously described), together with the S-wave velocity and thickness.

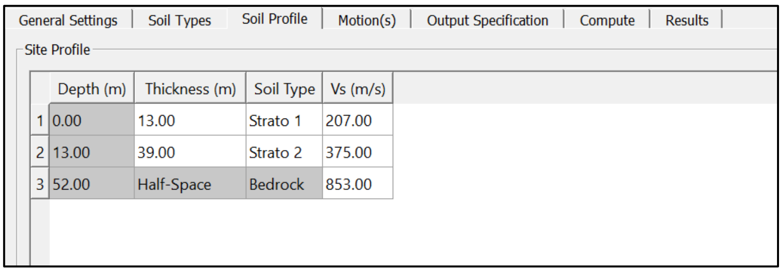

	Depth (m)	Thickness (m)	Soil Type	Vs (m/s)
1	0.00	13.00	Strato 1	207.00
2	13.00	39.00	Strato 2	375.00
3	52.00	Half-Space	Bedrock	853.00

Fig. 4.7: Example of "soil profile" input section, where information about depth, thickness and S-wave velocity must be specified for each layer of the subsoil model.

MOTION(S) (Fig. 4.8), where seismic inputs and depth at which to apply them for the site response modeling must be entered; if it is specified as a set of time series, file containing digital accelerograms have to be uploaded specifying number of samples (point count), time step, scale factor, data reading format, unit of measurement, PGA, start and stop line of the data to be used. It can also be specified whether the provided time series represent ground motion recordings acquired at the surface that need to be deconvolved to represent ground motion incoming from the bedrock.

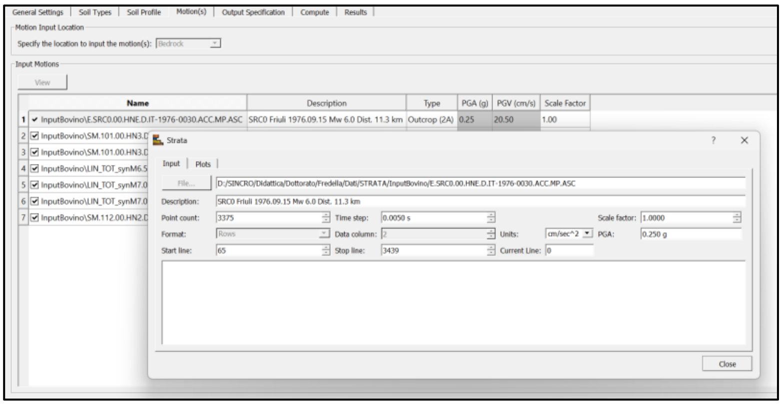

Fig. 4.8: Example of "motion(s)" input section for the case of seismic inputs expressed as an acceleration time series contained in a file to be uploaded.

The OUTPUT SPECIFICATIONS must also be defined, specifying the outputs to obtain at the end of the processing. The following can be obtained:

- vertical profiles of various parameters, including the Arias intensity;
- time series, including those for acceleration, displacement and velocity;
- response and Fourier spectra, where the acceleration response spectrum or the Fourier amplitude spectrum can be selected;
- ratios between parameters at two different depths, including spectral ratios.

Except for profiles, it is also necessary to specify the position at which to perform the calculation (whether at the surface or at the bedrock) and the type of waves to be considered: one-way waves only, round-trip waves, or waves within the layer between the surface and the bedrock.

For the objective of this study, as output option the calculation of the acceleration time series at the surface was selected to obtain the amplified accelerogram at the surface due to the propagation of seismic waves starting from the bedrock, both in graphical and tabular form (Fig. 4.9).

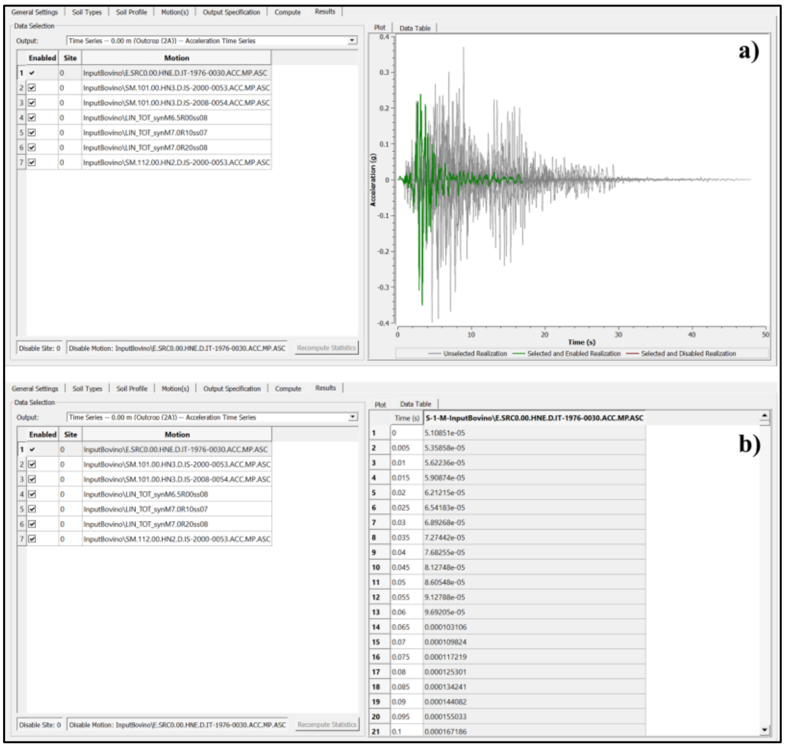

*Fig. 4.9: Example of acceleration time series, showing an amplified accelerogram obtained at the surface after processing with STRATA software, both in **a**) graphical **b**) and tabular form.*

Having obtained the amplified accelerograms at the surface, the Arias intensity can be calculated for each of them using the relationship [2.1] and compared with that of the corresponding input accelerograms. By calculating the ratio between these two values of I_A, the amplification factor

$$AF = \frac{I_A(output)}{I_A(input)} \qquad [4.11]$$

can be obtained for each accelerogram as well the average and standard deviation for different seismic inputs applied to the same site model.

4.1.4 Incorporation of site amplification in estimating the slope resistance demand

To incorporate amplification factors when estimating slope resistance demand, an option was included in the EXCRIT code (see Section 3.1.3) that allows users to modify the probabilistic I_A values provided by R-CRISIS for reference site conditions for local sites, using the average and standard deviation of *AF* values estimated with the procedure described in previous sections. Selecting this option causes the program to apply to the I_A expected with a probability p_I on reference site conditions, a set of *nf* amplification factors determined for the specific site as logarithmic mean values in *nf* intervals distributed around the overall *AF* average. Each of these amplification factors is assigned an occurrence probability p_F, assuming a lognormal distribution. Then, a probability $p_I \cdot p_F$ is assigned to each of the amplified I_A values resulting from multiplying the values expected on reference site conditions by each of the *nf* amplification factors. Finally, the amplified I_A values, along with their respective occurrence probabilities, are used to calculate D_N exceedance probabilities from the predictive equation [3.14] for site-specific amplified ground shaking conditions.

An example of EXCRIT code input file used to calculate the resistance demand incorporating *AF* is shown in Fig. 4.10.

a)

```
  INTENSITY 1
101  10.  0.05  50  0.0001  -5.0
iopf,sodn,probexc,time,preac,aimax
3
0.962  -0.901   0.022   0.141
Daunia_Fredella_con_siti_FA_log.gra
(e11.5,14x,e15.5)
```

b)

```
  INTENSITY 1
   15.4600        41.1030      0.          0.     0.       0
1.00000E-02  3.79678E-002
1.38692E-02  3.01170E-002   7.85080E-003
1.92354E-02  2.36196E-002   6.49740E-003
2.66780E-02  1.83199E-002   5.29970E-003
3.70002E-02  1.40623E-002   4.25760E-003
5.13163E-02  1.06931E-002   3.36920E-003
7.11715E-02  8.05942E-003   2.63368E-003
9.87091E-02  6.01887E-003   2.04055E-003
1.36902E-01  4.44990E-003   1.56897E-003
1.89871E-01  3.25219E-003   1.19771E-003
2.63336E-01  2.34440E-003   9.07790E-004
3.65226E-01  1.66066E-003   6.83740E-004
5.06539E-01  1.14769E-003   5.12970E-004
7.02528E-01  7.64546E-004   3.83144E-004
9.74349E-01  4.81869E-004   2.82677E-004
1.35134E+00  2.79811E-004   2.02058E-004
1.87420E+00  1.44778E-004   1.35033E-004
2.59937E+00  6.43963E-005   8.03817E-005
3.60511E+00  2.38072E-005   4.05891E-005
5.00000E+00  7.10669E-006   1.67005E-005
```

c)

```
  INTENSITY 1
   15.3292       41.1549     0.808        0.103    2.5      5
1.00000E-02  3.92554E-02
1.38692E-02  3.10516E-02   8.20380E-03
1.92354E-02  2.42718E-02   6.77980E-03
2.66780E-02  1.87604E-02   5.51140E-03
3.70002E-02  1.43605E-02   4.39990E-03
5.13163E-02  1.09023E-02   3.45820E-03
7.11715E-02  8.21558E-03   2.68672E-03
9.87091E-02  6.14469E-03   2.07089E-03
1.36902E-01  4.55718E-03   1.58751E-03
1.89871E-01  3.34514E-03   1.21204E-03
2.63336E-01  2.42289E-03   9.22250E-04
3.65226E-01  1.72406E-03   6.98830E-04
5.06539E-01  1.19732E-03   5.26740E-04
7.02528E-01  8.02046E-04   3.95274E-04
9.74349E-01  5.07990E-04   2.94056E-04
1.35134E+00  2.95844E-04   2.12146E-04
1.87420E+00  1.53278E-04   1.42566E-04
2.59937E+00  6.82214E-05   8.50566E-05
3.60511E+00  2.52185E-05   4.30029E-05
5.00000E+00  7.51499E-06   1.77035E-05
```

*Fig. 4.10: Example of EXCRIT code input file: (**a**) shows the variables iopf, sodn, probexc, time, preac and aimax, as well as the number of parameters and their values used to compute the resistance demand; (**b**) and (**c**) show the I_A occurrence probability data for sites where the amplification effect is not accounted for or is, respectively; for the latter case, next to the site coordinates, the logarithm of the average amplification factor and the logarithm of the standard deviation are reported, followed by the number of standard deviations delimitating the range of the AF estimation uncertainty to be considered in I_A occurrence probability estimations and the number of intervals into which this range is divided.*

Fig. 4.10a shows the input file in which the parameters necessary for calculating $(A_c)_{10}$ (see Section 3.1.3) must be specified, where *aimax* is set to a negative value if the amplification factor is required to be taken into account.

Figs. 4.10b-c show, respectively, examples of data for a site where the effect of the amplification factor is not required and for a site where *AF* has been estimated. Four parameters are specified next to the site coordinates:

1) *fa* → the logarithm of the average amplification factor;
2) *sdfa* → the logarithm of the associated standard deviation;
3) *sdmax* → the number of standard deviations delimitating the range of the *AF* estimation uncertainty to be considered in I_A occurrence probability estimations (set to 2.5);
4) *nsd* → the number of intervals into which to divide the previously defined uncertainty range between –*sdmax* and +*sdmax* (set to 5).

For sites where *AF* is not available (Fig. 4.10b), these four parameters are set to 0.

4.2 Procedure validation in the test area of Caramanico Terme (Central Italy)

To test the procedure described in section 4.1, and to evaluate uncertainties in estimating amplification factors, the procedure was applied to a set of test sites in the area of Caramanico Terme (Abruzzo region, Central Italy) (Fig. 4.11). Here the amplification factors estimated with the outlined procedure can be directly compared with those resulting from analyzing accelerometer recordings acquired during the same events on landslide-prone slopes and on a nearby bedrock outcrop used as a reference.

4.2.1 Test sites characteristics and ground motion data used for the validation test

Starting from 2002, a permanent accelerometer network has been installed in the area around the town of Caramanico Terme to investigate the site dynamic response of slopes under seismic loading (Del Gaudio and Wasowski, 2007; 2011). This area was chosen for two reasons:

1) it is located in one of the most seismically active areas of Italy, within the Central Apennines, struck in the past by many strong earthquakes (Wasowski and Del Gaudio, 2000) and characterized by a 10% probability that the PGA exceeds 0.25-0.35g in 50 years;
2) there are slopes composed of Quaternary colluvial material resting on impermeable Pliocene substrate, ranging from moderately inclined to steep, which are very prone to landslides (Wasowski and Del Gaudio, 2000).

Although landslides are often triggered here by rainfall that remobilizes smaller portions of pre-existing large landslide bodies (Wasowski, 1998), landslides triggered by earthquakes are also reported, which has stimulated further investigation.

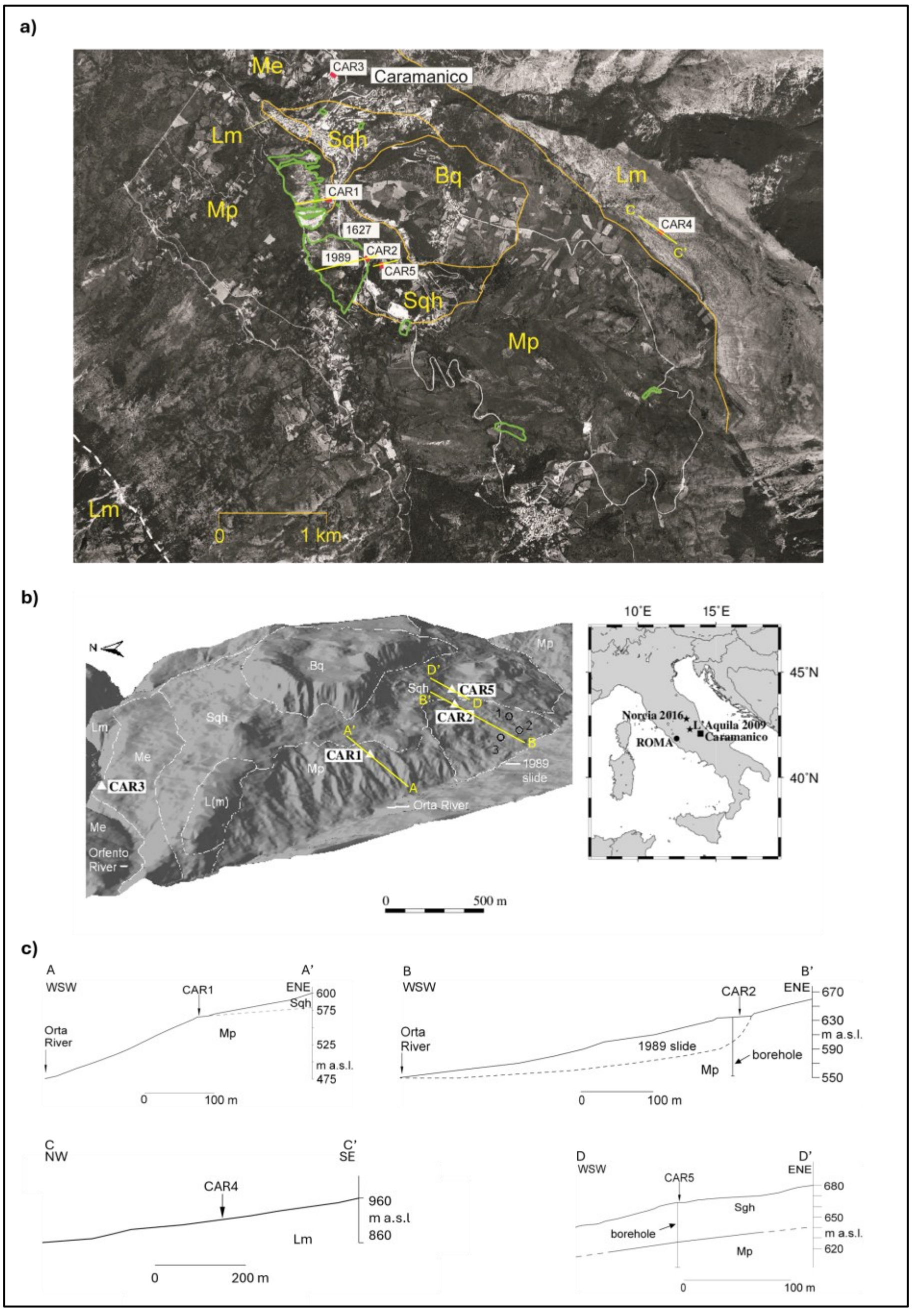

*Fig. 4.11: Caramanico test area. Panel (**a**) shows the orthophoto indicating the position of the CAR1-2-3-4-5 accelerometer stations. Panel (**b**) shows the digital elevation model of the area with the four stations located on landslide-prone slopes; the inset on the right shows the geographical location of Caramanico Terme, with stars representing the epicenters of the mainshocks of the 2009 L'Aquila and 2016 Central Italy seismic sequences. The lithological units are identified by the following acronyms: Lm=Miocene limestone; Me=Messinian sandy-silty deposits with carbonate breccia; Mp=Pliocene mudstone; Bq=Quaternary limestone megabreccia; Sqh=Quaternary and Holocene soils (colluvium and artificial ground) (modified from Del Gaudio and Wasowski, 2011). Both panels show the area of the 1989 landslide. Panel (**c**) shows schematic geological sections across the hillslope sites of stations CAR1-2-4-5 along traces highlighted in yellow in previous panels; m a.s.l. means meters above sea level (after Fredella et al., 2025).*

The final configuration of the Caramanico Terme local accelerometric network consisted of five stations (Fig. 4.11):

- **CAR1** (42.152°N, 14.002°E), situated on a slope with an inclination of 18° towards WSW, composed of Pliocene mudstones;
- **CAR2** (42.147°N, 14.008°E), located 600 m SSE of CAR1, on a slope inclined 11° towards WSW, at the head of a landslide that, in 1989, remobilized 30-40 m of colluvial deposits overlying Pliocene mudstones;
- **CAR3** (42.163°N, 14.003°E), positioned on the rim of a gorge approximately 50 m deep, on Messinian carbonate breccia deposits overlying Miocene limestones;
- **CAR4** (42.150°N, 14.039°E), situated 2 km from the town center, on a slope inclined 8°, consisting of outcropping Miocene limestones;
- **CAR5** (42.147°N, 14.009°E), located about 200 m from CAR2, on the same colluvial material, in an area with a slope of less than 7°, upslope of the 1989 landslide.

For about 20 years, these stations have recorded a total of over 400 earthquakes, including some of the most significant earthquakes occurred in Italy in recent times, namely the L'Aquila earthquake (April 6, 2009 - M_w=6.3) and the Central Italy seismic sequence (August 24, 2016 - Amatrice - M_w=6.0 and October 30, 2016 - Norcia - M_w=6.5). However, for the purposes of the present study, the recordings at the CAR3 station were not considered because the site response – being on the rim of a gorge – could be strongly influenced by topographical effects.

On the other hand, considering the relatively flat morphology and the outcropping of rock at the site of the CAR4 station, it was taken as a reference station. This choice received further support from the observation that the accelerograms recorded here do not appear to be affected by significant amplification effects. Consequently, the accelerometer recordings acquired at this station were used both as seismic inputs to estimate the amplification factors using the procedure described above and as a reference ground motion for the direct calculation of the amplification factors via comparison with the accelerometer recordings acquired at stations located on Caramanico soil slopes.

To validate the described procedure for estimating amplification factors in terms of Arias intensity, accelerometer recordings of all events with magnitude M ≥ 4 recorded simultaneously at stations CAR1, CAR2, CAR4 and CAR5 were selected (Table 4.1). For each component of each recording, the associated Arias intensity can be calculated according to the equation [2.1]. However, only the horizontal components (EW and NS) of the accelerometric recordings were considered for calculating the Arias intensity, since these components are more relevant to effects on slope stability.

Table 4.1: List of events recorded simultaneously at CAR1, CAR2, CAR4 and CAR5(M ≥ 4). Date and start time of the event, focus coordinates (latitude, longitude and depth), magnitude and the mean epicentral distance $\bar{d}$ from the stations on slopes are reported (Fredella et al., 2025).

ID	DATE	TIME	LAT (N)	LON (E)	DEPTH (Km)	M	$\bar{d}$
1	22/07/2007	17:25:51	41.905	13.671	15.7	4.0	38.77
2	06/04/2009	01:32:26	42.334	13.334	8.8	6.3	59.07
3	06/04/2009	02:37:04	42.366	13.340	10.1	4.6	59.93
4	06/04/2009	23:15:26	42.451	13.364	8.6	4.8	62.60
5	07/04/2009	09:26:28	42.342	13.388	10.2	4.7	55.27
6	07/04/2009	17:47:21	42.275	13.464	15.1	5.3	46.83
7	07/04/2009	21:35:26	42.380	13.376	7.4	4.2	57.90
8	09/04/2009	00:52:47	42.484	13.343	15.4	5.1	66.10
9	09/04/2009	03:14:44	42.338	13.437	18.0	4.2	51.40
10	09/04/2009	04:32:39	42.445	13.420	8.1	4.0	58.40
11	09/04/2009	19:38:16	42.501	13.356	17.2	4.9	66.30
12	13/04/2009	21:14:24	42.504	13.363	7.5	4.9	66.00
13	23/04/2009	21:49:00	42.233	13.479	9.3	4.0	44.43
14	22/06/2009	20:58:40	42.446	13.356	14.2	4.5	62.90
15	28/02/2015	03:16:18	41.950	13.534	10.6	4.1	44.83
16	26/10/2016	17:10:36	42.880	13.128	8.7	5.4	108.63
17	26/10/2016	19:18:05	42.909	13.129	7.5	5.9	110.93
18	30/10/2016	06:40:17	42.832	12.111	9.2	6.5	105.70

Previous studies (Del Gaudio and Wasowski, 2007; 2011) pointed out that the horizontal seismic dynamic response at the sites of the Caramanico stations located on slopes shows directional variations, mainly related to anisotropy of slope material properties. However, in view of calculating at each site an amplification factor from a 1D modeling of site response, the average of Arias intensity over all directions was calculated for each event recording, using the following expression:

$$\overline{I_A} = \frac{1}{2\pi}\int_{\alpha=0}^{2\pi}\int_{t=0}^{t_0}[a_E(t)^2 \cdot \sin^2\alpha + a_N(t)^2 \cdot \cos^2\alpha + a_E(t) \cdot a_N(t) \cdot \sin 2\alpha]dt\,d\alpha = \frac{1}{2}\left(I_{A_E} + I_{A_N}\right) \quad [4.12]$$

where a_E and a_N represent the ground acceleration components in the EW and NS directions, respectively, α is the azimuth angle between 0 and 2π (in radians), while I_{A_E} and I_{A_N} are the Arias intensities calculated for the EW and NS components, respectively.

4.2.2 Determination of 1D velocity profile from ambient noise recording analysis

At stations CAR1, CAR2 and CAR5, seismic ambient noise was also recorded and analyzed to study the site response (Del Gaudio et al., 2008). The acquisitions were made using a portable tromograph model Tromino, which consists of a 10x14x8cm instrument containing an orthogonal triad of velocimeter sensors. Following the guidelines of the European project SESAME (**S**ite **E**ffect**S** assessment using **AM**bient **E**xcitations), the acquisitions were carried out by adopting i) a sampling rate of 128 samples per second and ii) an acquisition duration of 15 min (sufficient to analyze low frequencies, down to 0.3 Hz).

These recordings were more recently re-analyzed using the HVIP technique described in section 4.1.1 to obtain the Rayleigh wave ellipticity curves. As azimuths along which to perform the scattering analysis in the preliminary stage of parameter optimization (see variable **azcomp)**, the directions of the maximum

H/V peaks resulting from a standard HVSR analysis were chosen, i.e., 5° for CAR1 and 95° for both CAR2 and CAR5.

Considering that the anisotropy of the site response determines variations in the average value of the H/V ratio for Rayleigh waves polarized in different directions, a directional weighted average of the H/V values was calculated. The output file with the .istR extension reports the mean H/V values of the recording samples with Rayleigh-type polarization as a function of frequency and azimuth (see example in Fig. 4.12). These data were used to calculate the directional average of the logarithmic values of the H/V ratio from 0 to 20 Hz, with a step of 0.05 Hz, weighing data from different polarization azimuth intervals proportionally to the corresponding percentages of samples falling within those intervals.

> Istogramma polarizzazioni tipo Rayleigh

> Az	% az	Fre	H/V	H/V-s.d.	H/V+s.d.	H/V/s.d.l	H/V*s.d.l
-5.	0.71610E+01	0.30000E+00	0.71439E+00	-0.28300E-01	0.14571E+01	0.30935E+00	0.16497E+01
-5.	0.10454E+02	0.35000E+00	0.21749E+01	0.11189E+01	0.32309E+01	0.11927E+01	0.39672E+01
-5.	0.10976E+02	0.40000E+00	0.26212E+01	0.16117E+01	0.36308E+01	0.12182E+01	0.56470E+01
-5.	0.12080E+02	0.45000E+00	0.24951E+01	0.10057E+01	0.39845E+01	0.10119E+01	0.62020E+01
-5.	0.11799E+02	0.50000E+00	0.24951E+01	0.14538E+01	0.35364E+01	0.13094E+01	0.48101E+01
-5.	0.12800E+02	0.55000E+00	0.24949E+01	0.13465E+01	0.36432E+01	0.11052E+01	0.56609E+01
-5.	0.49865E+01	0.60000E+00	0.17721E+01	0.89509E+00	0.26492E+01	0.88117E+00	0.36993E+01
-5.	0.50410E+01	0.65000E+00	0.23867E+01	0.17038E+01	0.30697E+01	0.14432E+01	0.41461E+01
-5.	0.42832E+01	0.70000E+00	0.15417E+01	0.64197E+00	0.24415E+01	0.69256E+00	0.38201E+01
-5.	0.31483E+01	0.75000E+00	0.11406E+01	0.17352E+00	0.21076E+01	0.39802E+00	0.33578E+01
-5.	0.34984E+01	0.80000E+00	0.98632E+00	0.26229E+00	0.17103E+01	0.42948E+00	0.23536E+01
-5.	0.58824E+01	0.85000E+00	0.10126E+01	0.41603E+00	0.16091E+01	0.49786E+00	0.20894E+01
-5.	0.48926E+01	0.90000E+00	0.12740E+01	0.52897E+00	0.20191E+01	0.55925E+00	0.30702E+01
-5.	0.31491E+01	0.95000E+00	0.17139E+01	0.72026E+00	0.27075E+01	0.65899E+00	0.47427E+01
-5.	0.31656E+01	0.10000E+01	0.17862E+01	0.94146E+00	0.26309E+01	0.81309E+00	0.45987E+01
-5.	0.15160E+01	0.10500E+01	0.15460E+01	0.96197E+00	0.21300E+01	0.89112E+00	0.32324E+01
-5.	0.10711E+02	0.11000E+01	0.14356E+01	0.75715E+00	0.21140E+01	0.80287E+00	0.28728E+01
-5.	0.62716E+01	0.11500E+01	0.15992E+01	0.62714E+00	0.25713E+01	0.72278E+00	0.37484E+01
-5.	0.76962E+01	0.12000E+01	0.20929E+01	0.84701E+00	0.33388E+01	0.84524E+00	0.52992E+01
-5.	0.10488E+02	0.12500E+01	0.27144E+01	0.12604E+01	0.41684E+01	0.11374E+01	0.66187E+01
-5.	0.17042E+01	0.13000E+01	0.30374E+01	0.14922E+01	0.45826E+01	0.14205E+01	0.67262E+01
-5.	0.10209E+02	0.13500E+01	0.29656E+01	0.15074E+01	0.44238E+01	0.16012E+01	0.57405E+01
-5.	0.20317E+02	0.14000E+01	0.27671E+01	0.15343E+01	0.39998E+01	0.17058E+01	0.46383E+01
-5.	0.61033E+01	0.14500E+01	0.26380E+01	0.16444E+01	0.36316E+01	0.17522E+01	0.40294E+01
-5.	0.35956E+01	0.15000E+01	0.25642E+01	0.17383E+01	0.33900E+01	0.17355E+01	0.38143E+01
-5.	0.77428E+01	0.15500E+01	0.25095E+01	0.17576E+01	0.32615E+01	0.16946E+01	0.37350E+01
-5.	0.42910E+01	0.16000E+01	0.25372E+01	0.17298E+01	0.33447E+01	0.17111E+01	0.38005E+01
-5.	0.00000E+00	0.16500E+01	0.27081E+01	0.16953E+01	0.37210E+01	0.18078E+01	0.42044E+01

*Fig. 4.12: Initial part of the HVIP analysis output file with the .istR extension obtained for CAR1. For each frequency, the following quantities are reported: central values of 10° azimuth intervals (az); % of samples with polarization azimuth falling in this intervals (% az) for the analyzed frequency (Fre); H/V mean ratio; mean minus (H/V-s.d.) and plus (H/V+s.d.) one standard deviation; H/V divided (H/V/s.d.) and multiplied (H/V*s.d.) by 10 to the logarithmic standard deviation.*

The logarithmic standard deviation was also calculated in order to obtain a measure of the uncertainties affecting the average ellipticity values, as required by the DINVER software. Fig. 4.13 shows the Rayleigh wave ellipticity curves obtained at stations CAR1, CAR2 and CAR5 with the corresponding uncertainty intervals.

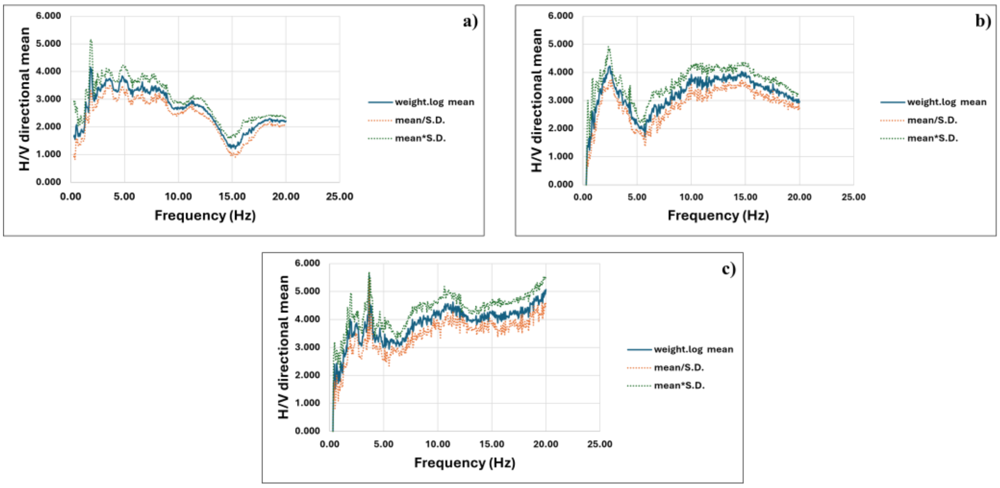

Fig. 4.13: Weighted average ellipticity curves calculated from the results of HVIP processing. For each average curve, the range of uncertainty expressed in terms of variability within one logarithmic standard deviation is shown.

Near the accelerometer stations, along with noise measurements, ReMi type surveys (Louie, 2001) were also conducted in order to obtain additional information on the physical properties of the materials (Coccia et al., 2010). These, together with information obtained from borehole stratigraphy, provide constraints on thickness and velocity of S-waves. Specifically, borehole stratigraphy available at station CAR5 (Fig. 4.14) was used to constrain the thickness of the most superficial colluvial deposits, while constraints relating to the main velocity changes at stations CAR1 and CAR2 were extracted from ReMi surveys, as no additional information was available.

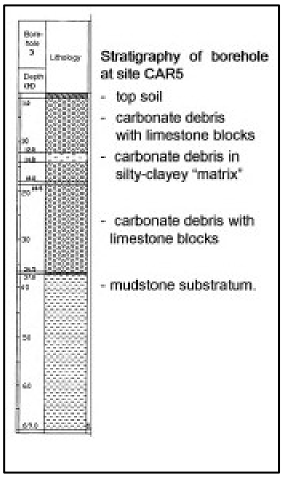

Fig. 4.14: Borehole stratigraphy available at station CAR5, used to constrain the thickness of the most superficial colluvium deposits (after Coccia et al., 2010).

Thanks to these constraints, it was possible to define the initial ranges of the parameters needed to perform the inversion. These ranges were adjusted in successive runs of the programs until to obtain a satisfactory minimization of the misfit. The results of the ellipticity curve inversion obtained at stations CAR1, CAR2 and CAR5, respectively, are shown graphically in Fig. 4.15 and summarized in Table 4.2.

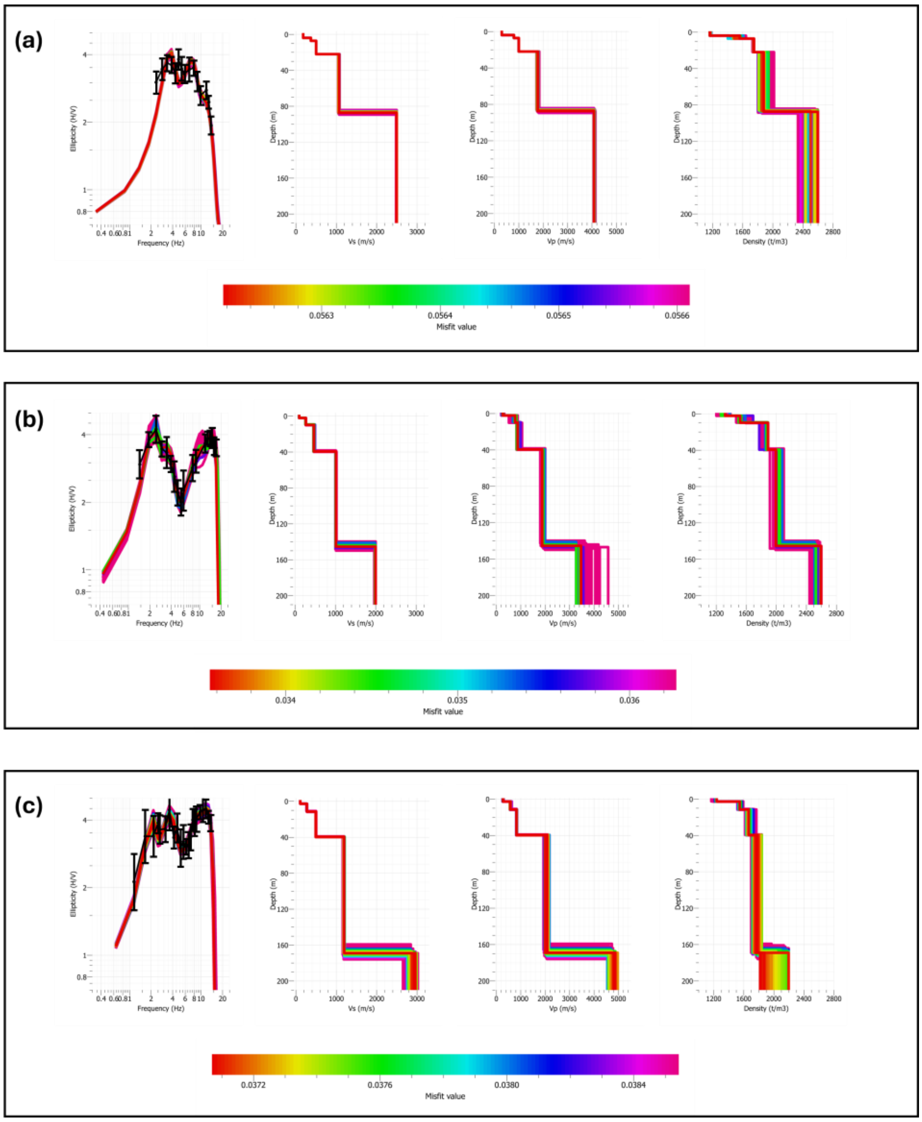

*Fig. 4.15: Results of the inversion of Rayleigh wave ellipticity curves, obtained from the HVIP analysis of ambient noise recordings, in terms of 1D S-wave velocity profile, as calculated by the DINVER software (Wathelet, 2005) for stations CAR1 (**a**), CAR2 (**b**) and CAR5 (**c**). On the left side of each panel the experimental ellipticity curve (in black) is shown with vertical bars representing the uncertainty interval within one standard deviation and is overlaid with theoretical curves (in colors) corresponding to the vertical V_P, V_S and density profile of the same color shown on the right side. The colors are assigned according to the underlying misfit color scale.*

Table 4.2: Vertical S-wave velocities profiles obtained by DINVER code (Wathelet, 2005) inversion and the corresponding V_{S30} value obtained for CAR1, CAR2 and CAR5, respectively (Fredella et al., 2025).

CAR1		**CAR2**		**CAR5**	
Thickness (m)	**Vs (m/s)**	**Thickness (m)**	**Vs (m/s)**	**Thickness (m)**	**Vs (m/s)**
4	180	2	105	3	108
3	370	8	269	9	272
15	502	30	470	28	497
-	1080	-	1015	-	1160
	V_{S30} (m/s)		V_{S30} (m/s)		V_{S30} (m/s)
	444		328		309

4.2.3 Estimation of Arias intensity amplification factor from 1D modeling of site response

After obtaining the velocity profile at the three stations, work focused on using the STRATA software to perform 1D modeling of the site response. Based on the results obtained from the inversion performed with DINVER software, the "SOIL TYPES" and "SOIL PROFILE" sections were compiled, defining both the unit weight and the thickness and V_S of the layers.

Furthermore, for each identified layer, the damping and shear modulus curves were defined, based on the indications of a previous study (Muscillo, 2014) and plotted in Fig. 4.16: for the Pliocene mudstone outcropping at CAR1, curves were obtained from laboratory tests on a sample from a nearby borehole; for colluvial material, the curves proposed by Vucetic and Dobry (1996) for plasticity index 0 were used. Generally, the site response prediction is sensitive to the uncertainties affecting nonlinear soil properties, but for the shaking intensity of the recorded events (with PGA at most of the order of 0.1g) this sensitivity can be considered very low (cf. Guzel et al., 2020).

The accelerometer recordings of the 18 events selected and recorded at the CAR4 reference station were entered in the "MOTION(S)" section as seismic inputs applied to the bedrock, deconvolved to represent the ground motion acting at depth ("Outcrop 2 A" option).

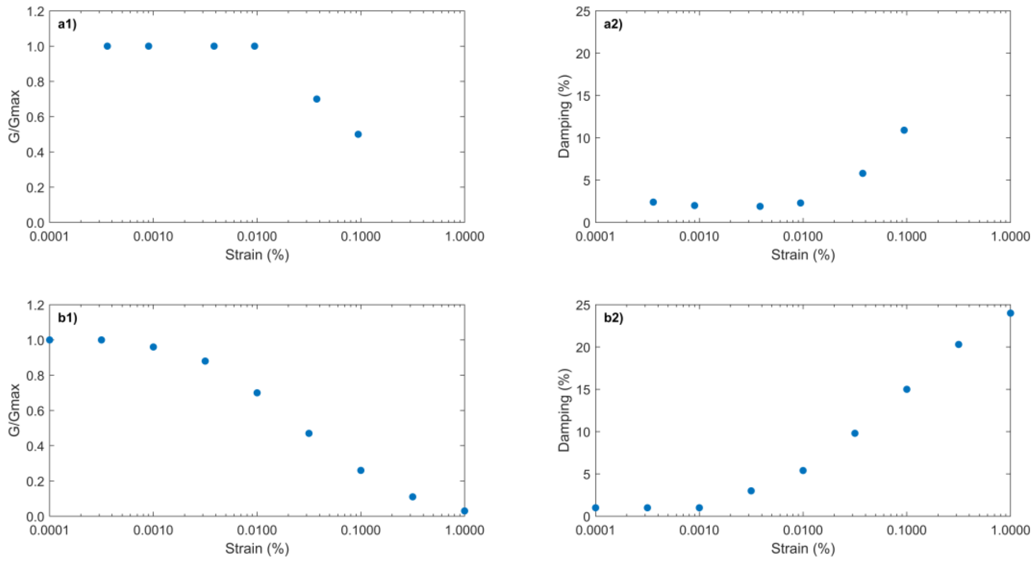

*Fig. 4.16: Shear modulus degradation and damping curves as a function of the strain used in the STRATA software for taking into account the nonlinear response of mudstone (**a1,a2** – from a laboratory test) and colluvial deposits (**b1,b2** – from Vucetic and Dobry, 1996) (Fredella et al., 2025).*

The "GENERAL SETTING" was configured as follows:

- equivalent linear (EQL) method was selected as analysis type, to consider the effects of soil strain response non-linearity, using the time series approach;
- calculation parameters were set to the default values, i.e.: error tolerance 2%, maximum number of iterations 10 and effective strain ratio 0.65;
- as parameters controlling layer discretization, maximum frequency was set to 20 Hz and wavelength fraction to 0.20.

For the effective strain ratio, the default value of 0.65 was preferred over the one provided by the magnitude dependent empirical relationship $R = (M - 1)/10$ (Idriss and Sun, 1992). Indeed, for the magnitude of the selected events (between 4.0 and 6.5), R would result to be between 0.3 and 0.55, which according to a study that compared the results obtained from equivalent linear and fully non-linear approaches (Aimar et al., 2024) could cause a strong underestimation of the effects of non-linearity and a strong overestimation of the amplification factor.

To verify the applicability of the equivalent linear approach, some preliminary tests were conducted showing that the selected seismic inputs can generate shear deformation values of up to 0.01%, i.e., within the range for which the equivalent linear model shows good predictive power (Kaklamanos et al., 2013).

The program last run provided, for each site and for each of the 18 accelerograms chosen as seismic inputs, the acceleration time series expected at the surface due to the propagation of seismic waves from the bedrock. Finally, the Arias intensity was calculated using formula [2.1] and estimates of the amplification factors AF_e were obtained for the three slope sites (CAR1, CAR2 and CAR5) by calculating the ratio [4.11].

4.2.4 Measurement of Arias intensity amplification factors from accelerometer recordings

The ratio of the Arias intensity calculated from the accelerograms recorded at stations CAR1, CAR2 and CAR5 to that at the reference station CAR4 provided a direct measurement of the Arias intensity amplification factor AF_m resulting for each event (Table 4.3).

Observing the scatter plot of AF_m values as a function of Arias intensity calculated at the CAR4 reference station (Fig. 4.17) shows that there is no correlation between AF_m and the intensity of the shaking energy. Indeed, the AF_m values scatter around an average value, which remains constant across three orders of magnitude of variation in I_A.

The results show that the average AF_m values at stations CAR2 and CAR5 are similar, while at station CAR1 they are lower: this can be related to the fact that the overburden lithologies and their V_S are comparable for CAR2 and CAR5 (where V_{S30} is equal to 309 and 328 m/s, respectively, as shown in Table 4.2), while CAR1 is characterized by a higher V_{S30} value (444 m/s), caused by the presence of a thin soil cover overlying the mudstone substratum.

Table 4.3: Amplification factors measured from the accelerogram recorded at stations CAR1, CAR2 and CAR5. The magnitude M of the events and the epicentral distances d (in km) from each station are reported (Fredella et al., 2025).

EVENTS	M	AF_m CAR1	d_{CAR1} (km)	AF_m CAR2	d_{CAR2} (km)	AF_m CAR5	d_{CAR5} (km)
1	4.0	0.49	38.8	0.44	38.7	2.06	38.8
2	6.3	7.66	58.6	21.21	59.3	10.40	59.3
3	4.6	8.21	59.5	19.56	60.1	17.80	60.2
4	4.8	8.82	62.1	25.29	62.8	18.26	62.9
5	4.7	10.03	54.8	29.23	55.5	27.31	55.5
6	5.3	4.26	46.4	12.01	47.0	11.03	47.1
7	4.2	10.13	57.4	20.42	58.1	17.07	58.2
8	5.1	10.56	65.6	19.84	66.3	16.67	66.4
9	4.2	3.37	50.9	6.46	51.6	8.96	51.7
10	4.0	11.09	57.9	19.16	58.6	17.95	58.7
11	4.9	11.45	65.8	17.40	66.5	13.66	66.6
12	4.9	8.80	65.5	15.29	66.2	14.81	66.3
13	4.0	8.67	44.0	21.73	44.6	17.36	44.7
14	4.5	11.94	62.4	16.19	63.1	17.00	63.2
15	4.1	3.82	44.7	3.98	44.9	4.93	44.9
16	5.4	9.30	108.1	20.37	108.9	21.18	108.9
17	5.9	7.68	110.4	17.19	111.2	15.95	111.2
18	6.5	7.50	105.2	19.04	105.9	10.24	106.0

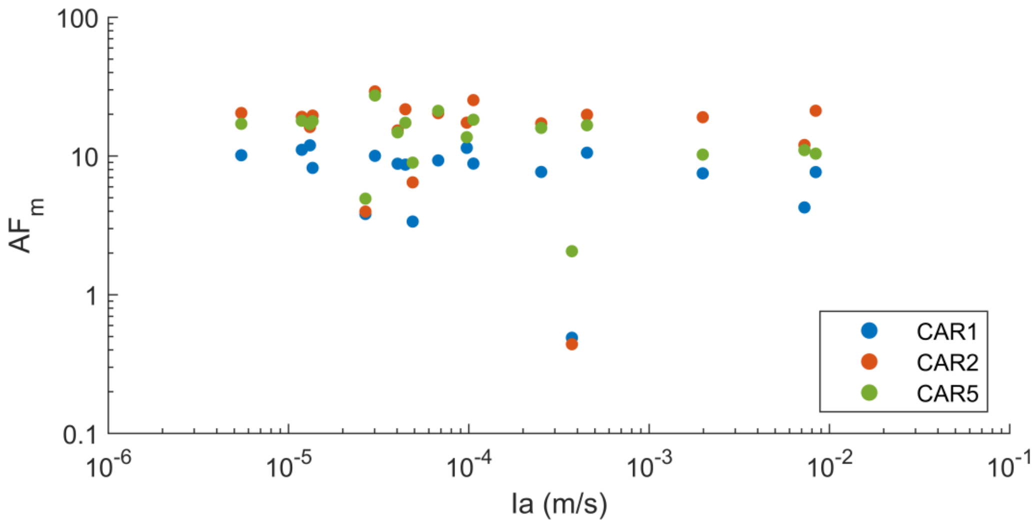

Fig. 4.17: Scatter plot of AF_m values relative to the Caramanico slope site stations (CAR1, CAR2 and CAR5) as a function of the I_A of the recordings at the CAR4 reference station (Fredella et al., 2025).

Table 4.3 shows that for events 1, 6, 9 and 15, the AF_m values are much smaller than that obtained for the other events. In particular:

- at CAR1 AF_m = 0.5-4.3 for these events, while AF_m = 7.5-11.9 for the others;
- at CAR2 AF_m = 0.4-6.5 for events 1, 9 and 15, while AF_m = 12.0-29.2 for the others;
- at CAR5 AF_m = 2.1-4.9 for events 1 and 9, while AF_m = 9.0-27.3 for the others.

Trying to explain this anomalous behavior, the characteristics of these events were considered in more detail. AF_m appears to be underestimated for low-magnitude events (4.0-4.2) and/or short epicentral distances (<50 km), although this does not occur systematically in all cases. Indeed, there are events that have an AF_m value comparable to that obtained for other events at the same station, even though the magnitude and distance are low: for example, event 13 is characterized by M=4.1 and d<50 km, but AF_m is equal to 8.7, 21.7 and 17.4 for CAR1, CAR2 and CAR5 respectively, while for the events 10 and 7, which have M=4.0-4.2 and d=50-60 km, AF_m is equal to 11.1-10.1, 19.1-20.4 and 18.0-17.1.

The spectra of the recordings obtained at the CAR4 reference station for these events were also analyzed (Fig. 4.18). For events 1, 6, 9 and 15, the spectrum shows the presence of high spectral amplitudes at frequencies greater than 10 Hz (Fig. 4.18a-b-c-d). Conversely, Fig. 4.18e-f shows that the spectral energy of the main shocks of the 2009 L'Aquila and 2016 Central Italy seismic sequences, are lower at these frequencies.

A high content of seismic energy at relatively high frequencies (10-20 Hz) can characterize the recordings of events with i) epicenters close to the recording stations, ii) small to moderate magnitudes and iii) high fault rupture velocities, whose waves are little attenuated over short distances. In such cases, the anomalous results obtained when measuring amplification factors can depend on an inadequacy of the station CAR4, located on rocky ground, to serve as a reference station for calculating the amplification factor in I_A, because rocks

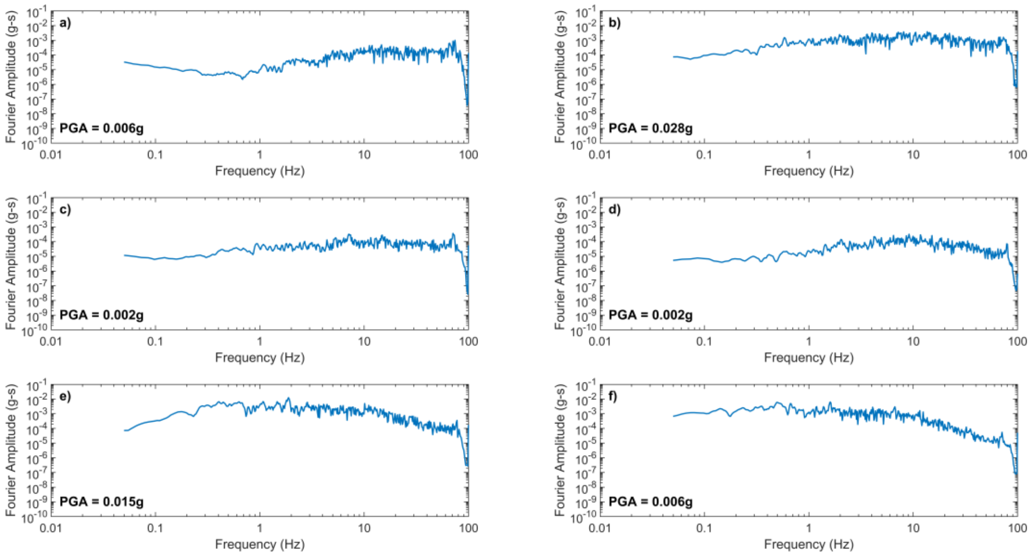

*Fig. 4.18: Fourier spectra of the EW component of the recordings obtained at the CAR4 reference station for events 1 (**a**), 6 (**b**), 9 (**c**), 15 (**d**), 2 (**e**) and 18 (**f**). Events 2 and 18 represent the main shocks of the 2009 L'Aquila earthquake and the 2016 Norcia earthquake, respectively. The PGA values (in g units) are reported for each event represented (Fredella et al., 2025).*

transmit high-frequency waves more effectively than soil. Indeed, the attenuation of this type of wave when crossing softer soils can be so strong that it considerably reduces the amplification related to the impedance contrast with the underlying bedrock. In extreme cases the shakings at the surface may even be weaker than at the reference site, as occurred for the event 1, where $AF_m < 1$ at stations CAR1 and CAR2.

As a general consideration, the concentration of spectral energy on a limited frequency band can result in highly variable responses depending on whether that band is closer to or further from the resonance frequencies of the site. Therefore, to obtain reliable estimates of the amplification factors, it is necessary to carefully choose the seismic inputs for site response modeling: the selected accelerograms should have, as far as possible, a homogeneous and balanced distribution of spectral energy across all frequencies relevant for landslide mobilization, excluding those for which there is a strong concentration of energy on specific frequency bands.

4.2.5 Comparison between estimated and measured amplification factors

To compare the amplification factor AF_e estimated by the procedure described in section 4.1 with the factor AF_m measured directly from the accelerometer recordings, the percentage error (E) was calculated by

$$E = \frac{AF_e - AF_m}{AF_e}\ x\ 100 \qquad [4.13].$$

The results obtained at stations CAR1 and CAR5 are shown in Table 4.4: it shows that the percentage error remains within 50% for all events except events 15, 16 and 17 for both stations, event 1 for CAR1 and event 5 for CAR5. High overestimates (E = 60-85%) are found for events 1 and 15 and could be due to the high frequency content of these events and the mentioned inadequacy of using CAR4 as a reference station under these conditions. Conversely, very high underestimations (E = between -115 and -138%) result for events 5, 16 and 17: events 16 and 17 are characterized by d >100 km and M equal to 5.4 and 5.9 respectively, while event 5 has d = 58 km and M = 4.7.

To better understand this behavior, Fig. 4.19 shows the spectra of the EW component (the largest one) of the accelerograms recorded at the CAR4 reference station and at CAR5, together with those obtained at CAR5 from STRATA modeling. For comparison, Fig. 4.19d shows also the spectrum of event 18 (the main shock of the 2016 Norcia earthquake), as this is the one for which the lowest error (E < -2%) is obtained in the estimation of the amplification factor at the CAR5 station.

The underestimation of AF_e seems to be more pronounced at frequencies between 0.5 and 3 Hz, where the spectra of accelerograms resulting from the 1D modeling of site response (blue curves in Fig. 4.19) are significantly below the recorded spectra (red curves). This also occurs to some extent for event 18 (characterized by greater intensity) without compromising the estimation of the amplification factor, although the maximum differences appear here centered on slightly lower frequencies (around 1 Hz).

Table 4.4: Comparison between the amplification factors estimated using the STRATA code (AF_e) and the amplification factors measured from accelerometer recordings (AF_m) for CAR1 and CAR5 stations. The error in percent and the events features (identification number ID, magnitude, epicentral distance and Arias intensity at the reference station) are shown. The results are reported in order of increasing absolute error (Fredella et al., 2025).

CAR 1	**ID**	**AF_e**	**AF_m**	**E (%)**	**M**	**d (km)**	**$I_A \cdot 10^4$ (m/s)**
	7	10.67	10.13	4.99	4.2	57.4	0.055
	4	9.48	8.82	7.01	4.8	62.1	1.059
	12	9.88	8.80	10.93	4.9	65.5	0.403
	8	9.37	10.57	-12.71	5.1	65.6	4.522
	10	9.59	11.09	-15.61	4.0	57.9	0.118
	13	10.45	8.67	17.04	4.0	44.0	0.445
	14	9.61	11.94	-24.32	4.5	62.4	0.131
	11	9.17	11.45	-24.87	4.9	65.8	0.974
	3	10.96	8.21	25.07	4.6	59.5	0.136
	5	7.96	10.03	-25.99	4.7	54.8	0.302
	2	5.95	7.66	-28.69	6.3	58.6	83.858
	9	4.73	3.37	28.87	4.2	50.9	0.488
	18	5.24	7.50	-43.15	6.5	105.2	19.827
	6	8.04	4.26	47.03	5.3	46.4	72.654
	15	9.60	3.82	60.24	4.1	44.7	0.267
	1	3.49	0.49	85.86	4.0	38.8	3.725
	17	3.22	7.68	-138.27	5.9	110.4	2.520
	16	3.82	9.30	-143.23	5.4	108.1	0.676
CAR5	**ID**	**AF_e**	**AF_m**	**E (%)**	**M**	**d (km)**	**$I_A \cdot 10^4$ (m/s)**
	18	10.07	10.24	-1.64	6.5	106.0	19.827
	8	17.19	16.67	3.06	5.1	66.4	4.522
	11	14.41	13.66	5.22	4.9	66.6	0.974
	3	16.09	17.80	-10.62	4.6	60.2	0.136
	12	13.31	14.81	-11.23	4.9	66.3	0.403
	13	15.59	17.36	-11.38	4.0	44.7	0.445
	7	19.94	17.07	14.4	4.2	58.2	0.055
	2	8.57	10.40	-21.38	6.3	59.3	83.858
	4	14.40	18.26	-26.79	4.8	62.9	1.059
	10	14.05	17.95	-27.82	4.0	58.7	0.118
	14	12.84	17.00	-32.44	4.5	63.2	0.131
	6	7.79	11.03	-41.55	5.3	47.1	72.654
	1	3.74	2.06	44.99	4.0	38.8	3.725
	9	5.99	8.96	-49.56	4.2	51.7	0.488
	15	12.59	4.94	60.80	4.1	44.9	0.267
	5	12.65	27.31	-115.85	4.7	55.5	0.302
	17	6.56	15.95	-143.19	5.9	111.2	2.520
	16	8.38	21.18	-152.87	5.4	108.9	0.676

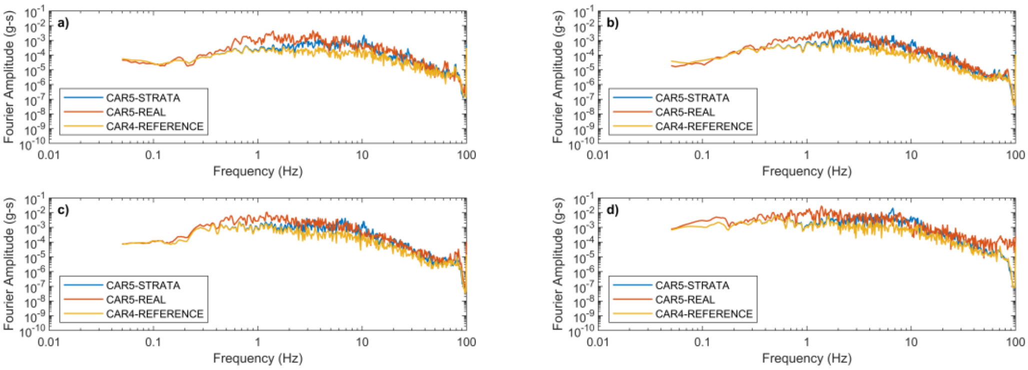

*Fig. 4.19: Accelerometer recordings spectra (EW component) for the events 5 (**a**), 16 (**b**), 17 (**c**) and 18 (**d**) acquired at CAR4 and CAR5 stations (yellow and red curves, respectively), compared with those obtained from STRATA site response modeling at CAR5 (blue curves) (Fredella et al., 2025).*

For the CAR5 site, a frequency around 2-3 Hz was identified as a main resonance frequency (Del Gaudio et al., 2008), related to the claystone-colluvium interface located at a depth of about 40 m. Thus, the underestimation of spectral amplitudes at these frequencies, especially for relatively distant events of magnitude less than 6, suggests that the damping curves and shear modulus may not accurately represent soil material behavior, at least at relatively low strain level.

Overall, however, estimates with errors < 50% have been obtained for events with higher magnitudes and shorter distances, which are typically representative of scenarios used for probabilistic seismic risk assessments and regional-scale slope resistance assessments.

The same kind of analysis, applied to the CAR2 station, gives rather different results, which are reported in Table 4.5. These results are characterized by errors in the estimation of the amplification factor that are much higher (in most cases E > 50%, up to about 300%) and more scattered than at the other stations (see also the boxplots in Fig. 4.20). The site conditions are more complex here because CAR2 is located at the head of a pre-existing deep-seated landslide, which reactivated in 1989 and moved westward (Wasowski, 1998).

Table 4.5: Comparison between the amplification factors estimated using the STRATA code (AF_e) and the amplification factors measured from accelerometer recordings (AF_m) for CAR2 station. The error in percent and the events features (ID, magnitude, epicentral distance and Arias intensity) are shown, together with the amplification factors for the EW and NS components and for their directional averages. The results are reported in order of increasing absolute error (Fredella et al., 2025).

ID	AF_e EW	AF_m EW	AF_e NS	AF_m NS	AF_e	AF_m	E (%)	M	d (km)	$I_A \cdot 10^4$(m/s)
6	8.76	17.50	10.78	6.26	9.75	12.01	-23.25	5.3	47.0	72.654
9	7.61	7.51	10.15	4.66	8.54	6.46	24.35	4.2	51.6	0.488
12	12.96	20.89	9.81	10.46	11.27	15.29	-35.64	4.9	66.2	0.403
10	14.89	25.67	13.05	12.72	13.96	19.16	-37.19	4.0	58.6	0.118
14	11.54	22.52	11.96	9.98	11.75	16.19	-37.77	4.5	63.1	0.131
32	11.68	22.48	12.36	11.92	12.01	17.40	-44.94	4.9	66.5	0.974
3	13.58	30.10	11.91	10.43	12.69	19.56	-54.18	4.6	60.1	0.136
7	13.53	29.41	11.52	12.85	12.44	20.42	-64.18	4.2	58.1	0.055
13	12.65	34.01	13.37	11.84	13.05	21.73	-66.54	4.0	44.6	0.445
15	10.56	5.50	13.64	2.58	12.16	3.98	67.30	4.1	44.9	0.267
8	10.74	22.58	11.01	16.80	10.87	19.84	-82.55	5.1	66.3	4.522
1	4.96	0.60	5.31	0.30	5.15	0.44	91.39	4.0	38.7	3.725
4	12.49	36.90	10.74	15.14	11.56	25.29	-118.86	4.8	62.8	1.059
18	7.654	29.64	5.87	11.10	6.63	19.04	-187.07	6.5	105.6	19.827
2	7.81	32.81	6.73	13.12	7.18	21.21	-195.61	6.3	59.3	83.858
5	8.95	40.90	9.53	17.53	9.24	29.23	-216.36	4.7	55.5	0.302
16	5.48	25.48	5.39	16.13	5.43	20.37	-275.22	5.4	108.9	0.676
17	4.95	22.19	3.65	13.80	4.17	17.19	-311.95	5.9	111.2	2.520

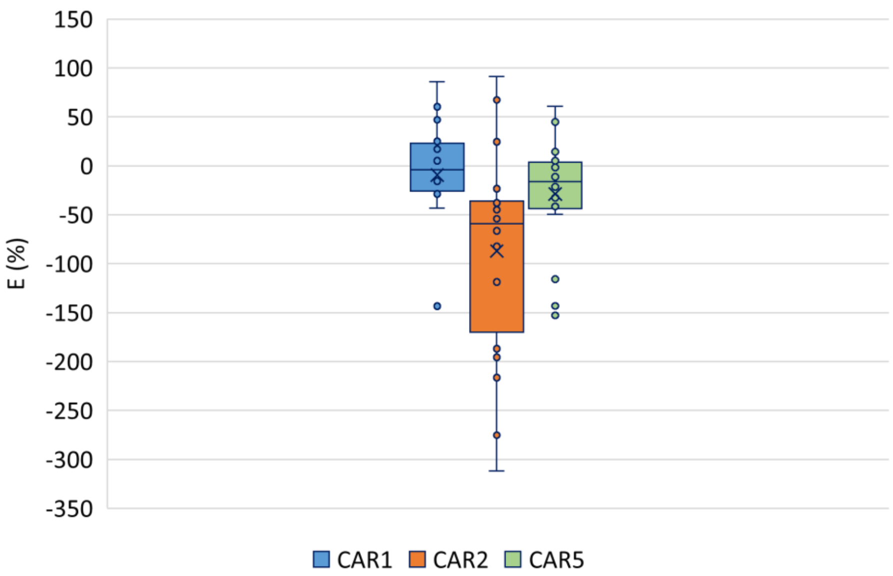

Fig. 4.20: Box plots of the percentage estimation errors of amplification factors AF_e at stations CAR1, CAR2 and CAR5.

To better analyze these results, Table 4.5 also shows the amplification factor values – measured and estimated – separately for the two horizontal components. What emerges is that larger differences between AF_m and AF_e affect especially the EW component, which approximately corresponds to the sliding direction. For this component the measured AF_m values are also systematically greater than the NS component, while the estimated values AF_e are similar for the two components. This confirms the strong anisotropy in the site response that was already noted in previous studies (Del Gaudio and Wasowski, 2007; 2011) and that was also recognized from directional analysis of ambient noise recordings (Del Gaudio et al., 2008; 2014). In these cases, the site response is not purely controlled by variations in velocity with depth but could be influenced by anisotropies in the soil's mechanical properties. For example, fissure systems affecting the 1989 landslide body can greatly weaken the constraints that limit the seismic ground motion transverse to the sliding direction (as fracture systems do in rock slopes according to Kleinbrod et al., 2019), thus increasing ground motion amplification in this direction.

Therefore, performing 1D modeling of the site response which only considers stratigraphic effects, would neglect these other effects and lead to underestimating the amplification factors. On the other hand, the occurrence of such situations can be revealed by a directional analysis of ambient noise recordings and suggests the need for additional investigations to obtain a more realistic estimate of the site amplification factor in the sliding direction.

Figure 4.21 shows the scatter plot of AF_e values as a function of Arias intensity calculated at CAR4 reference station. As for the analogous diagram relative to AF_e (Fig. 4.17), no particular trend is observed.

Interestingly, when data corresponding to anomalous measurement conditions (e.g., reference inadequacy or strong amplification directivity) or irrelevant conditions for hazard estimation (e.g., small magnitude or long epicentral distances) are removed, the estimated and measured values of the amplification factors yield consistent average results. At CAR1, the average and standard

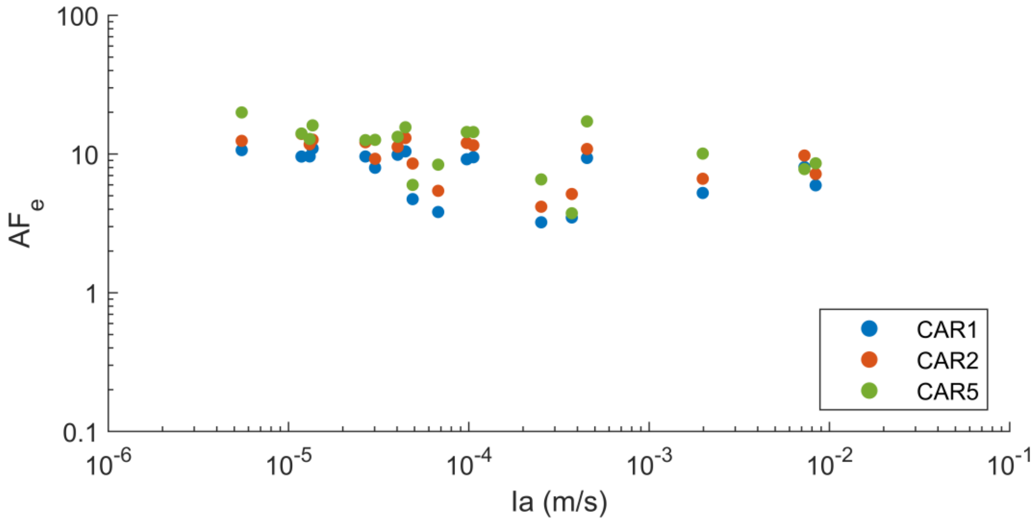

Fig. 4.21: Scatter plot of AF_e values represented as a function of the I_A of the accelerometric recordings obtained at the CAR4 reference station (Fredella et al., 2025).

deviation are 8.7 and 2.0, respectively, for AF_e, and 8.8 and 2.5 for AF_m. At CAR5, the average and standard deviation are 12.4 and 4.6 for AF_e, and 13.8 and 4.7 for AF_m. At CAR2, for the NS component solely, the average and standard deviation are 9.8 and 3.1 for AF_e, and 11.0 and 4.8 for AF_m. Therefore, excluding cases with a strong non-stratigraphic component of site response, the previously described procedure, when applied to a properly selected set of seismic inputs, appears capable of providing a reliable representation of the average amplification factor and its variability/uncertainty. Furthermore, the estimated uncertainty can be taken into account in probabilistic estimates of slope resistance demand following the procedure described in Section 4.1.4.

Given that i) frequencies of engineering interest usually stop at 20 Hz and ii) anomalous estimates of the amplification factor were found for cases with high spectral content at high frequencies (as for events 1, 6, 9 and 15), a test was performed to verify whether the estimation of amplification factors could be improved by a preventive filtering of accelerograms. Therefore, estimated and measured amplification factors were both recalculated using accelerograms filtered with a low-pass Butterworth filter set to a cut-off frequency of 20 Hz. The results are reported in Table 4.6 and show that:

Table 4.6: Estimated (AF_e) and measured (AF_m) amplification factors and errors in percent (E) obtained at stations CAR1, CAR2 and CAR5 after applying a low pass filtering with a cut-off frequency of 20 Hz to the accelerograms used both for calculating AF_m and AF_e (Fredella et al., 2025).

CAR1				CAR2				CAR5			
ID	**AF_e**	**AF_m**	**E (%)**	**ID**	**AF_e**	**AF_m**	**E (%)**	**ID**	**AF_e**	**AF_m**	**E (%)**
8	9.70	10.04	-3.51	9	20.70	18.23	11.93	11	16.30	15.16	7.01
7	11.00	10.60	3.62	6	13.90	9.11	34.46	3	16.60	17.94	-8.09
4	9.99	9.58	4.09	10	15.40	21.27	-38.09	12	14.30	15.81	-10.57
12	10.60	9.79	7.67	12	12.00	16.68	-39.03	13	18.30	20.82	-13.77
13	12.20	10.89	10.75	14	13.40	19.11	-42.61	18	10.30	8.62	16.36
2	7.14	6.05	15.32	11	13.30	20.04	-50.65	7	20.70	17.29	16.50
9	8.45	10.05	-18.91	13	15.40	23.63	-53.42	8	18.00	14.87	17.37
10	10.40	12.67	-21.78	3	13.00	20.13	-54.87	4	15.20	18.76	-23.41
3	11.40	8.66	24.04	8	11.30	18.06	-59.80	6	10.90	8.27	24.18
5	8.22	10.60	-28.98	2	8.16	13.23	-62.08	2	9.02	6.68	25.97
11	10.30	13.47	-30.79	7	12.90	21.07	-63.36	10	15.20	19.23	-26.49
18	5.32	7.11	-33.67	15	15.60	5.19	66.71	14	14.60	18.97	-29.96
14	10.90	14.59	-33.85	1	18.50	2.56	86.19	1	9.67	5.40	44.13
6	10.00	4.70	53.04	4	12.20	26.78	-119.50	15	15.20	5.78	61.96
15	11.80	5.32	54.89	18	6.77	15.74	-132.47	9	12.40	20.90	-68.53
1	8.51	3.16	62.85	5	9.71	30.40	-213.04	5	13.20	28.21	-113.70
17	3.23	7.73	-139.35	16	5.46	20.56	-276.54	17	6.57	16.02	-143.89
16	3.84	9.41	-144.95	17	4.18	17.29	-313.62	16	8.43	21.38	-153.57

1- no systematic improvement is obtained in the estimation of amplification factors;
2- there is an almost equal number of cases in which errors increase or decrease compared to the use of unfiltered accelerograms;
3- all events with $E > 50\%$ (i.e., events 1, 15, 16 and 17 for CAR1 and 5, 15, 16 and 17 for CAR5) continue to have such a high error even after filtering.

Therefore, applying a preventive filter to high frequencies does not seem to improve the estimation of the amplification factor, probably because high frequencies have little effect on the calculation of the Arias intensity.

The results of these estimations of site amplification factors in terms of Arias intensity were also compared with estimates of the site response contribution predicted by an empirical GMPE used to estimate the resistance demand of slopes on a regional scale, since previous studies have accounted for site response in this manner (e.g., Del Gaudio et al., 2003; Rajabi et al., 2013; Chousianitis et al., 2016).

For this comparison the equation [3.5] proposed by Sabetta et al. (2021) was used, where the site factor (*FS*) depends on the value of V_{S30} according to the expression [3.8]. Using the V_{S30} values obtained for CAR1, CAR2 and CAR5 (shown in Table 4.2), the site factor results equal to 1.83 for CAR1, 2.50 for CAR2 and 2.67 for CAR5, regardless of magnitude and distance values.

Compared with the AF_m values, the latter are up to 6.5, 10 and 6.8 times greater respectively at the three slope sites. These results show that evaluating the slope dynamic response in an approximate manner would lead to an underestimation of the amplification factor and, consequently, of the slope resistance demand. Indeed, using the relationship [3.4] proposed by Romeo (2000), considering values 6.5 to 10 times smaller would lead to an underestimation of the slope resistance demand $(A_c)_x$ by up to 4-5 times. For this reason, it would seem important to calculate the amplification factor more accurately in order not to significantly underestimate the susceptibility of slopes to seismic-induced failures.

4.3 Results of procedure implementation in Daunia municipalities

4.3.1 Data collection and calculation of amplification factors

The procedure for local incorporation of site response into slope resistance demand estimation, as described in Section 4.1, was applied to the study area of this thesis using data from the Seismic Microzonation (SM) studies currently underway in the Daunia Mountains. The procedure was tested on four municipalities namely Accadia, Bovino, Carlantino and Volturino. The data available for these municipalities are mainly those acquired during SM of Level 1 (SM1). In particular, these data derive from reports of the technicians in charge of the study, i.e. from ASSET-PUGLIA 2023a, 2023b and 2023c for Accadia, Carlantino and Volturino, respectively, and from Troncone et al. (2024) for Bovino.

SM1 is a preparatory level mainly relying on geological surveys and the collection of pre-existing data like the stratigraphies of boreholes drilled in the past and the results of previous geophysical surveys. These data are integrated by quick, low-cost investigations based on seismic ambient noise analyses aimed at identifying site resonance frequencies by the HVSR method (Nakamura, 1989).

SM1 is used for a preliminary, qualitative subdivision of the study area into "microzones" that differ in their expected response to seismic shaking. The site response is then characterized more quantitatively through further investigations carried out at subsequent levels. At Level 2 (SM2), simplified approaches based on schedules that provide amplification factors as a function of a few input parameters are used. At Level 3 (SM3), comprehensive, ad hoc numerical modeling is performed to calculate site amplification factors as a function of seismic ground motion frequency.

In the tests of the present study, data available from SM1 studies conducted in the aforementioned four municipalities were used to obtain 1D velocity modeling. First, noise recordings were reanalyzed with the HVIP technique (see Section 4.1.1). Then, the resulting Rayleigh wave ellipticity curves were inverted (see Section 4.1.2) with the support of constraints derived from the additional data (borehole stratigraphies, geophysical surveys) collected during the SM1 studies. For Bovino, the SM1 data were further integrated with additional on-field measurements consisting of supplementary noise recordings and electrical resistivity tomographies (ERT), which provided more constraints for the inversion of noise data.

With regard to the following stage of the 1D site response modeling with the STRATA code (see Section 4.1.3), the same general settings used for the test conducted at Caramanico Terme (see section 4.2.3) were adopted. At this stage geotechnical data on curves of shear modulus (*G*) and damping (*D*) as a function of strain are necessary, but at present they are still unavailable as they are commonly collected by investigations of SM3, which are behind schedule. Therefore, for these parameters, data drawn from literature were adopted, based on analogies of the lithological units with those forming the slopes where the site response was modelled in the study area. *G* and *D* curves were mostly selected following the choices made by Peruzzi and Albarello (2015) when preparing schedules for SM2 in Apulia. Table 4.7 shows the classification of the main lithological units identified by these authors in the Daunia Mountains area for simplified site response modeling, integrated with units identified on the basis of descriptions reported in SM1 studies. For each of these units, Table 4.8 reports the velocity range and density, as well as the reference to the *G* and *D* curves used for modeling.

Table 4.7: Main lithological units identified for simplified modeling of site response in the Daunia Mountains area.

	ACRONYM	MATERIAL
1	CL	Clays, marls and mainly clayey fill material
2	MLec	Low plasticity eluvial/colluvial sandy-clayey silts
3	DAC 1	Sandy-silty Unit with gravel lenses
4	LANDEB	Landslide debris
5	DetBl	Detrital blanket - Calcarenite pebbles in abundant sandy-clayey matrix
6	u.b.i.	Alternating layers of clay and sand
7	SUBMAF1	Brown Clay – Highly altered substratum from Faeto Flysch Unit
8	SUBMAF2	Grey Clay – Highly altered substratum from Faeto Flysch Unit
9	SUBMAF3	Highly altered substrate from Faeto Flysch Unit
10	u.b.i. (PI=30)	Claystones and marly clays, sandstones with a sandy-silty matrix, clays with intercalations of marls and alternating lithotypes typical of the Faeto Flysch
11	SUBF	Substrate - Flyschoid Units

Table 4.8: Properties assigned to the lithologic units of Table 4.7 for site response modeling: minimum and maximum V_s (m/s), unit weight (kN/m^3) and reference to the adopted G and D curve.

ID	ACRONYM	Min Vs (m/s)	Max Vs (m/s)	Density (kN/m^3)	Curves
1	CL	100	500	16	Idriss (1990), Clay
2	MLec	120	400	16	Silva et al., 1997
3	DAC 1	100	290	18	Vinale, 1988
4	LANDEB	300	700	20	Vucetic & Dobry (1991); Darendeli & Stokoe (2001)
5	DetBl	150	450	19.9	Puglia, 2005 – Detrital blanket
6	u.b.i.	180	490	18.5	Seed & Idriss
7	SUBMAF1	300	600	17.0	Puglia, 2005 – Brown clay
8	SUBMAF2	300	780	18.5	Puglia, 2005 – Grey clay
9	SUBMAF3	200	490	18.5	EPRI 93 (depth > 50 m)
10	u.b.i. (PI=30)	610	780	19.5	EPRI 93 (Plastic Index = 30)
11	SUBF	800	1570	22	Viscoelastic, 2% constant damping

For the selection of the test data, seismic noise recordings with the most evident peaks and which were closest to other types of surveys were identified in all four municipalities analyzed, using the "Investigation Map" produced in SM1 studies. In the following sections, more detailed information on these data and their processing is reported.

ACCADIA

In the area of the municipality of Accadia, recordings acquired at four sites (HV11, HV13, HV18 and HV21: Fig. 4.22) were selected as suitable for the application of the procedure. These recordings were first analyzed using the HVIP method, by averaging the results in case of double recording acquisition at the same site. The results of the inversion of the ellipticity curves performed with the DINVER software are shown graphically in Fig. 4.23 and numerically in Table 4.9. This Table also indicates the lithologic unit, as defined in Tables 4.7 and 4.8, to which each layer was assimilated, based on a comparison with the geological model provided by the SM1 studies and the V_S value obtained from DINVER inversion. The association of each layer to the lithological units summarized in Table 4.8 was also used to select the *G* and *D* curves for site response modeling with the STRATA code, which are shown in Fig. 4.24.

Fig. 4.22: Location of noise recording sites at Accadia (in yellow) near to boreholes (in blue) and geophysical survey profiles (red lines), whose data were used to support Rayleigh wave ellipticity curve inversion in terms of S-waves vertical velocity profile.

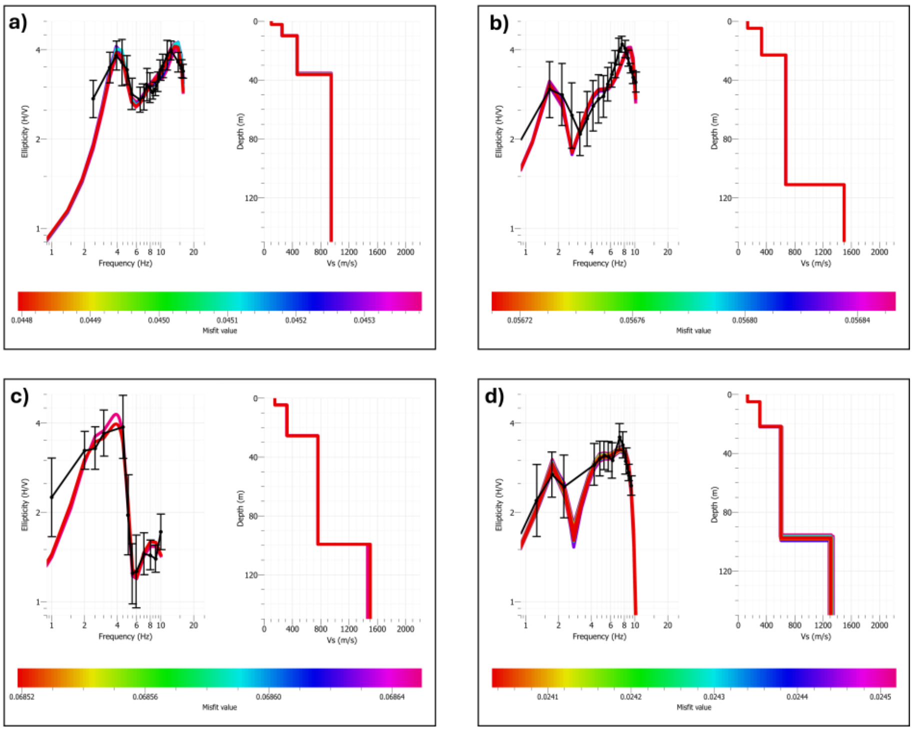

*Fig. 4.23: Results of the inversion of Rayleigh wave ellipticity curves, obtained from the HVIP analysis of ambient noise recordings acquired at Accadia in terms of 1D S-wave velocity profile: (**a**) HV11, (**b**) HV13, (**c**) HV18 and (**d**) HV21. Lines, symbols and colors as in Fig. 4.15.*

Table 4.9: S-wave vertical velocity profiles obtained from the inversion carried out for sites HV11, HV13, HV18 and HV21 of Accadia municipality. Thickness in meters (h) and velocity of S-waves in m/s (V_s) of each layer are reported for each site. For each layer, the numerical code next to the V_s value indicates the lithologic unit from Table 4.8 to which it was assimilated to select the G and D curves.

	LAYER 1		**LAYER 2**		**LAYER 3**		**LAYER 4**	
Site	h (m)	Vs (m/s)	h (m)	Vs (m/s)	h (m)	Vs (m/s)	h (m)	Vs (m/s)
HV11	2.5	100 (3)	7.5	250 (6)	26	460 (6)	Bedrock	950
HV13	5	135 (3)	19	335 (6)	86	670 (9)	Bedrock	1500
HV18	5	150 (3)	21	315 (6)	74	760 (9)	Bedrock	1500
HV21	5	135 (3)	18	336 (6)	77	593 (9)	Bedrock	1300

The seven accelerograms (4 real and 3 simulated) used as seismic input for STRATA were selected using the procedure proposed by Pierri et al. (2025) (described in section 3.2.1) specifically for the municipality of Accadia (Fig. 4.25). Their general characteristics are described in Table 4.10.

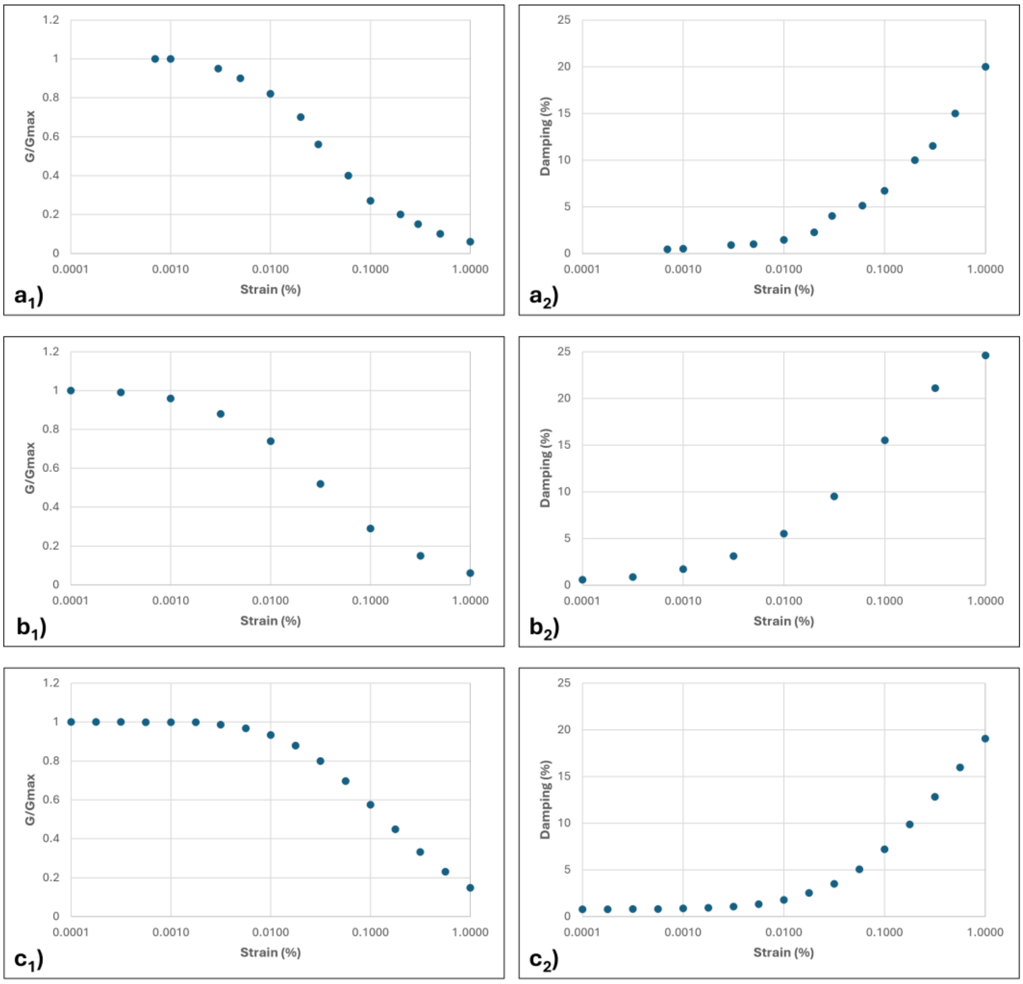

Fig. 4.24: Shear modulus degradation and damping curves as a function of the strain used in STRATA for taking into account the nonlinear response of layer material for Accadia municipality: ***a$_1$***, ***a$_2$*** *for DAC1 (Vinale, 1989);* ***b$_1$***, ***b$_2$*** *for u.b.i. (Seed & Idriss, 1970);* ***c$_1$***, ***c$_2$*** *for SUBMAF3 (EPRI,1993).*

Table 4.10: 7 accelerograms (4 real and 3 simulated) chosen as seismic input for the STRATA modeling carried out for the sites of Accadia municipality. Date, time, latitude, longitude, hypocentral depth (z), magnitude (M), epicentral distance (d), number of data and duration (T) of each accelerogram are reported.

Acc.	Date	Time	Lat	Lon	z (km)	M	d (km)	n data	T (s)
Real 1	15/09/1976	09:21:18	46.30	13.17	11.3	6.0	15.8	3375	16.875
Real 2	26/12/2018	02:19:17	37.64	15.11	-	4.9	5.3	11581	57.905
Real 3	30/10/2016	06:40:18	42.83	13.11	9.2	6.5	10.5	12384	61.920
Real 4	21/06/2000	00:51:47	63.91	-20.74	10	6.5	13.2	9600	48.000
Sim 1	-	-	-	-	-	6.5	0.0	4253	21.265
Sim 2	-	-	-	-	-	7.0	10.0	6295	31.475
Sim 3	-	-	-	-	-	7.0	20.0	7827	39.135

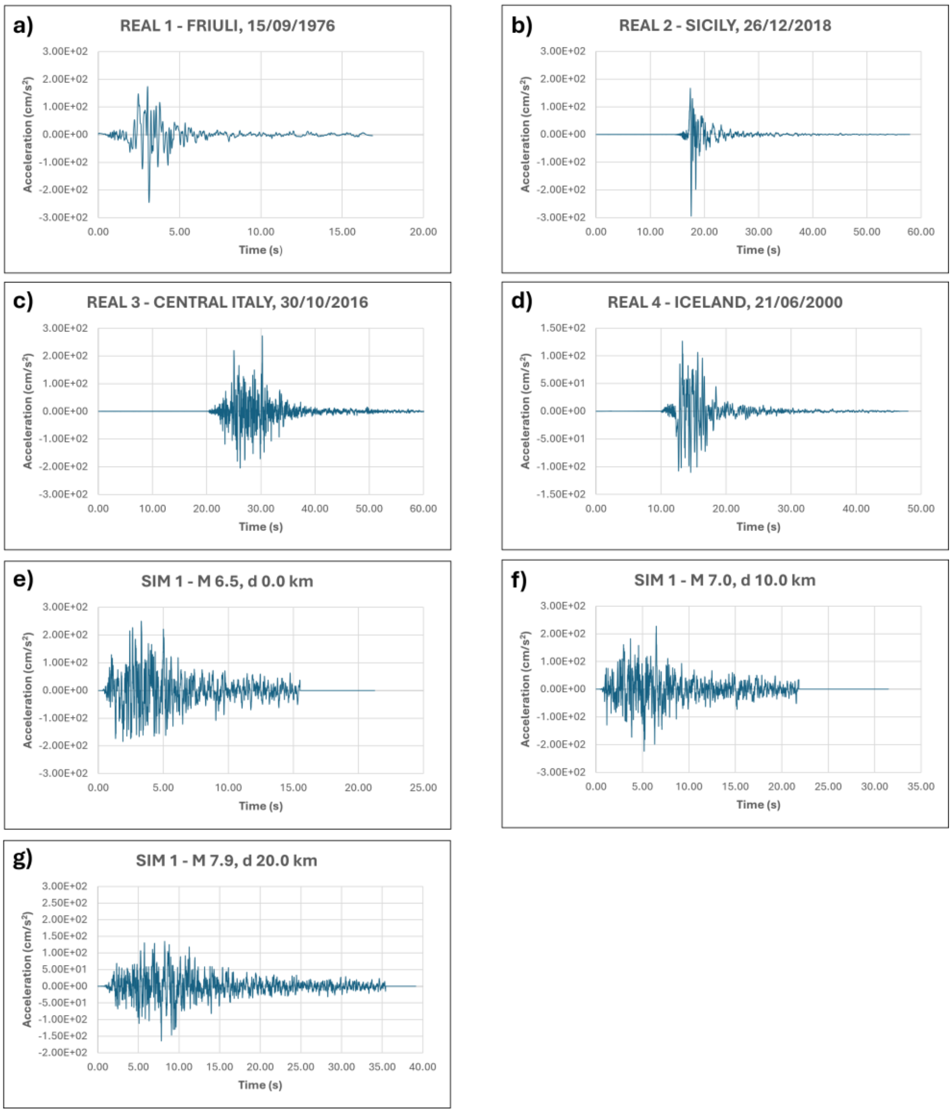

*Fig. 4.25: Accelerograms used as seismic input for Accadia sites: (**a**) REAL 1, (**b**) REAL 2, (**c**) REAL 3, (**d**) REAL 4, (**e**) SIM 1, (**f**) SIM 2 and (**g**) SIM 3 (see Table 4.10 for more details).*

BOVINO

Here, ambient noise recordings were purposely acquired in addition to those derived from the ongoing SM1 studies. Among these, those acquired at seven sites (HV7n, HV8n, HV13n, HV14n, HV15n, HV29n and HV32n: Fig. 4.26) were considered suitable for application of the procedure for site amplification calculation.

Fig. 4.26: Location at Bovino of noise recording sites (in yellow), boreholes (in blue and green, labelled with an identification code) and geophysical survey profiles (red straight lines), whose data were used to support Rayleigh wave ellipticity curve inversion in terms of S-waves vertical velocity. The boundary of the complex of the "Pianello landslide" is shown with curves of different color representing the different landslide bodies. The green straight lines represent the trace of the AB section of Fig. 4.27.

In the municipality of Bovino, there is a large complex landslide called "Pianello landslide", which affects the southwestern part of the town. It involves clay-rich lithologies that form a poorly drained slope. Although the slope is not very steep, the high degree of tectonization and plasticity, together with the heterogeneity of the present materials (generally flysch), makes the slope very prone to landslides, especially slow ones, which can undergo sudden accelerations before ending in a state of equilibrium (Cotecchia et al., 2015). This roto-translational landslide originated in medieval times and was reactivated by the Irpinia earthquake of November 23, 1980 (M_s=6.9) (Del Gaudio et al., 2003), undergoing further remobilizations in 1984, 1991 and in the period 2008-2014 (Cotecchia et al., 2016).

Fig. 4.27 shows section AB of the Pianello landslide (whose trace is marked in Fig. 4.26 with a green line). Depths values of the landslide bottom from 17 m to 50 m were derived from some boreholes of the studies by Refice et al. (2016) and Cotecchia et al. (2016), equipped with inclinometer sensors. Some of these (S_6, S_10 and S_12) are shown in Fig. 4.28.

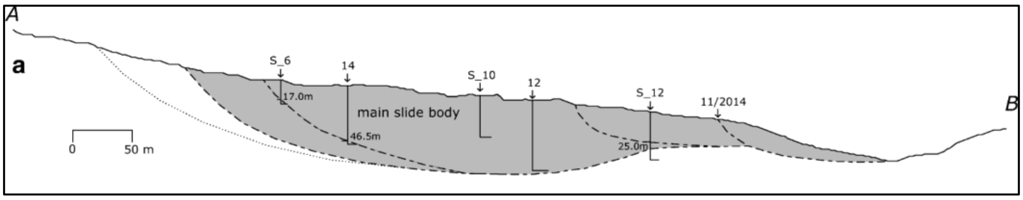

Fig. 4.27: Section AB of Fig. 4.26, in which the boreholes position and basal/internal cutting surfaces are shown (from Wasowski and Pisano, 2020).

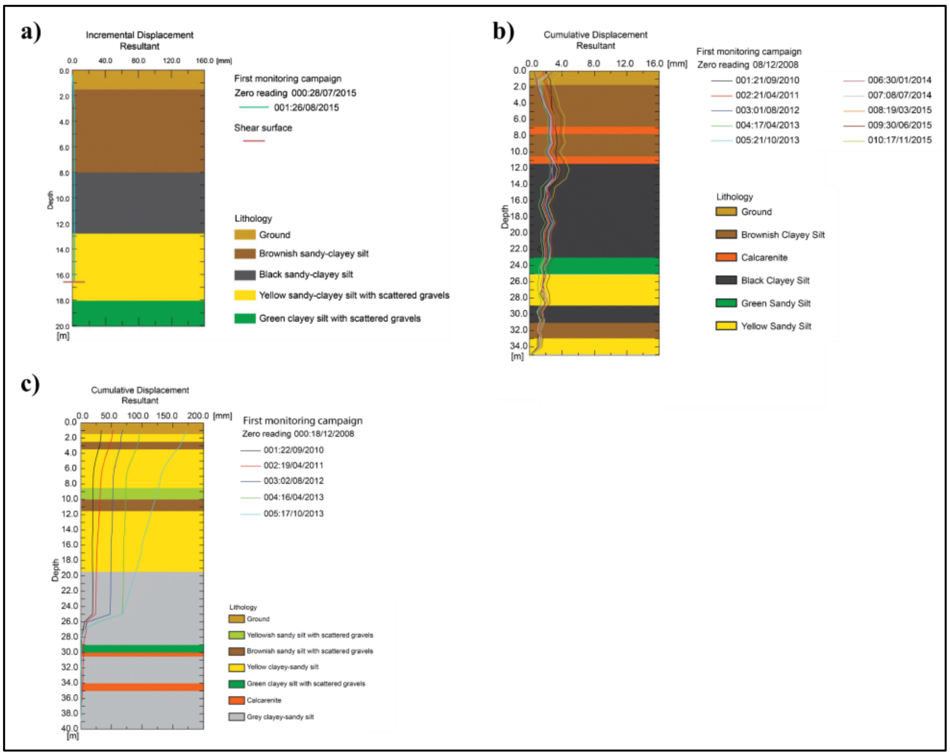

*Fig. 4.28: Borehole stratigraphies and inclinometer displacement results: (**a**) shows the incremental displacement recorded for S_6 between 28 July and 26 August 2015, (**b**) and (**c**) shows the resultant cumulative displacement for S_10 and S_12, respectively, between 2010 and 2013. The corresponding lithology is reported for each borehole (modified from Refice et al., 2018).*

The same procedure adopted for Accadia was followed for the sites chosen in Bovino. The results of the inversion of the Rayleigh wave ellipticity curves are shown graphically in Fig. 4.29 and numerically in Table 4.11.

Two accelerograms used as seismic inputs in the STRATA software for the municipality of Accadia (i.e., those referring to the 1976 Friuli and 2000 Iceland earthquakes) were also used for the municipality of Bovino, to which two real and three simulated ones were added (Fig. 4.30), whose characteristics are shown in Table 4.12. The choices for curves *G* and *D* are shown in Table 4.11 and Fig. 4.31. At all sites, a damping of 2% was set for the bedrock layer, as suggested by Peruzzi and Albarello (2015).

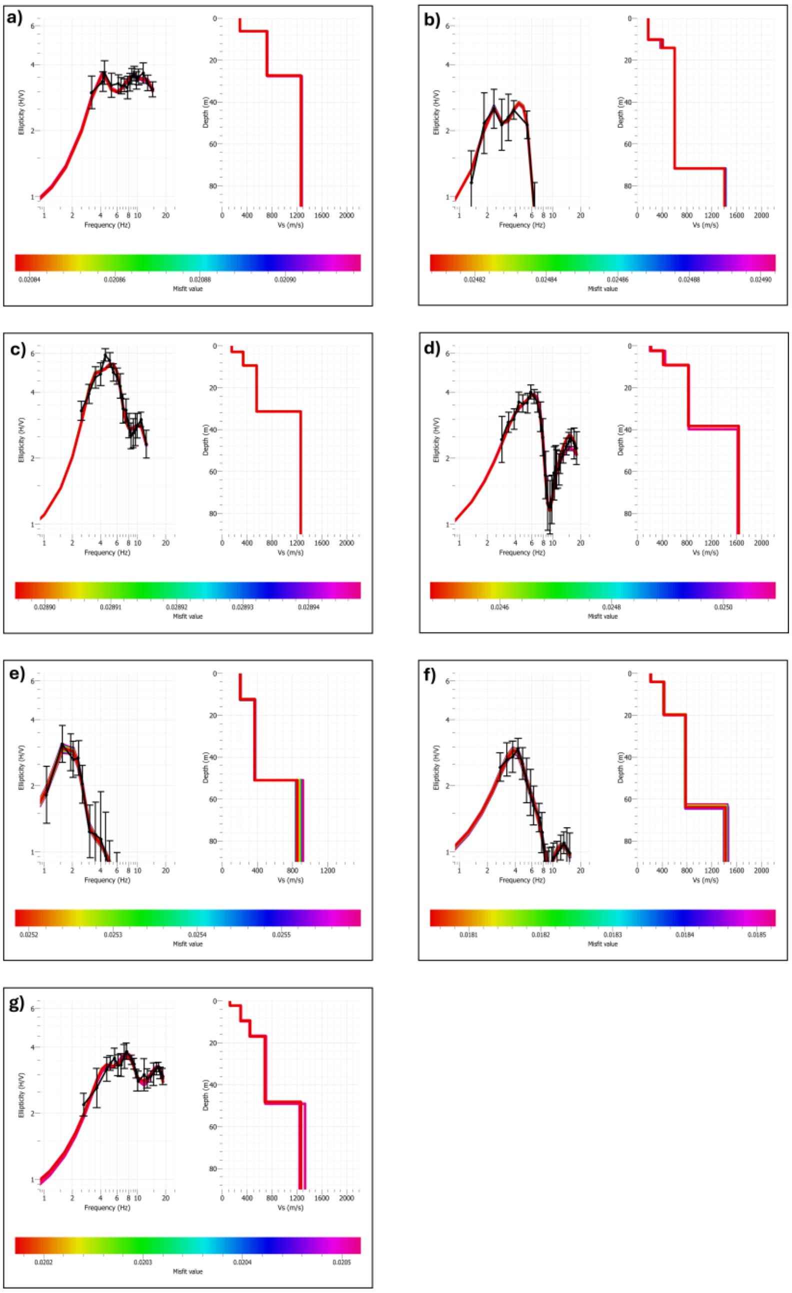

*Fig. 4.29: Results of the inversion of Rayleigh wave ellipticity curves, obtained from the HVIP analysis of ambient noise recordings acquired at Bovino, in terms of 1D S-wave velocity profile: (**a**) HV7n, (**b**) HV8n, (**c**) HV13n, (**d**) HV14n, (**e**) HV15n, (**f**) HV29n and (**g**) HV32n. Lines, symbols and colors as in Fig. 4.15.*

Table 4.11: S-wave vertical velocity profiles obtained from the inversion carried out with DINVER for sites HV7n, HV8n, HV13n, HV14n, HV15n, HV29n and HV32n of Bovino municipality. Thickness in meters (h) and velocity of S-waves in m/s (V_S) of each layer are reported for each site. For each layer, the numerical code next to the Vs value indicates the lithologic unit from Table 4.8 to which it was assimilated to derive the G and D curves.

	LAYER 1		LAYER 2		LAYER 3		LAYER 4		LAYER 5	
Site	**h**	**V_S**	**h**	**V_S**	**h**	**V_S**	**h**	**V_S**	**h**	**V_S**
HV7n	7	290 **(2)**	21	725 **(8)**	Bedrock	127				
HV8n	10	180 **(2)**	5	398 **(5)**	57	595 **(9)**	Bedrock	1400		
HV13n	3	150 **(2)**	7	300 **(8)**	22	550 **(8)**	Bedrock	1260		
HV14n	3	227 **(2)**	6	395 **(7)**	Bedrock	820				
HV15n	13	207 **(2)**	39	375 **(5)**	Bedrock	853				
HV29n	4.5	215 **(2)**	15.5	425 **(4)**	44	780 **(8)**	Bedrock	1420		
HV32n	2	120 **(2)**	7	295 **(2)**	8	450 **(8)**	32	700 **(8)**	Bedrock	1250

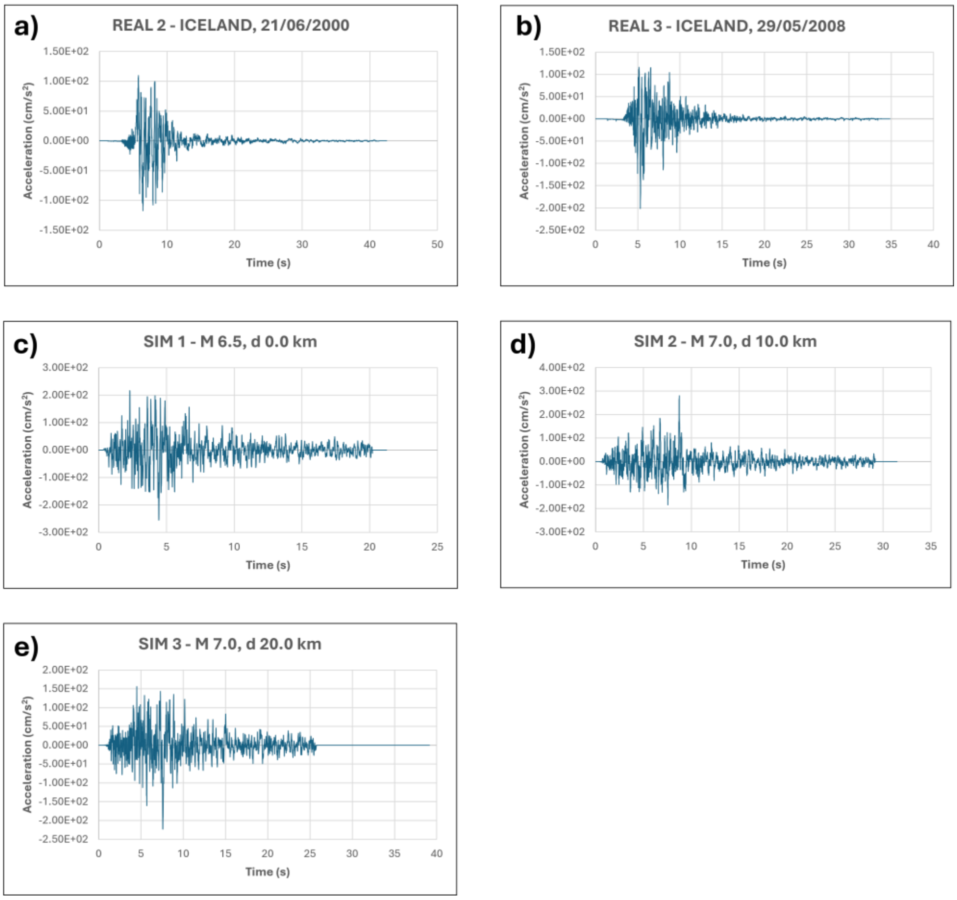

*Fig. 4.30: Accelerograms used as seismic input for Bovino: (**a**) REAL 2, (**b**) REAL 3, (**c**) SIM 1, (**d**) SIM 2 and (**e**) SIM 3 (details in Table 4.12).*

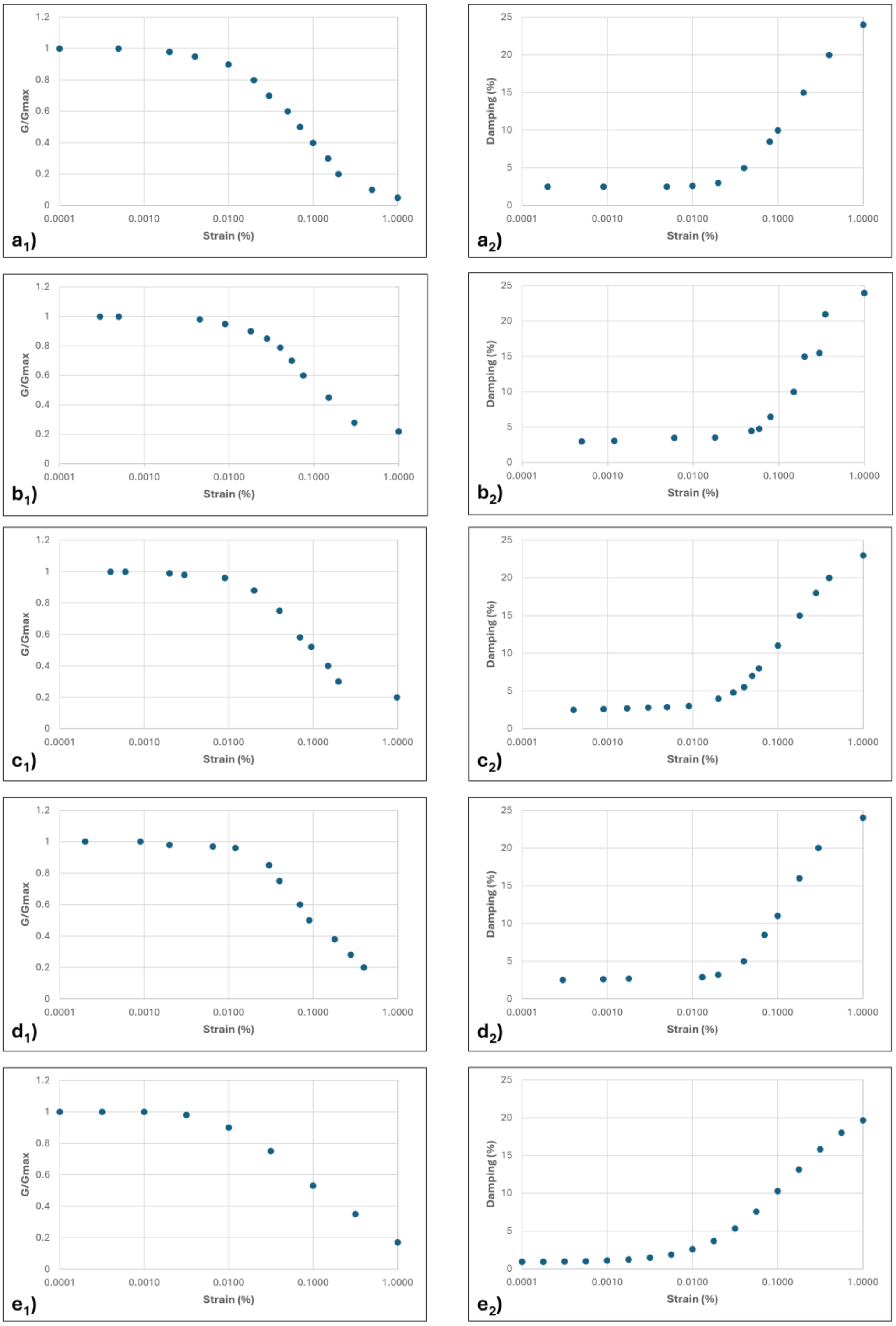

*Fig. 4.31: G and D curves as a function of the strain used for STRATA modeling at Bovino municipality for taking into account the nonlinear response of different layer materials assimilated at the lithological units of Table 4.8: **a**$_1$, **a**$_2$ for MLec (Silva et al., 1997); **b**$_1$, **b**$_2$ for DetBl at HV8n and HV15n (Puglia, 2005); **c**$_1$, **c**$_2$ for SUBMAF1 at HV14n (Puglia, 2005); **d**$_1$, **d**$_2$ for SUBMAF2 at HV7n, HV13n, HV29n and HV32n (Puglia, 2005); **e**$_1$ (Vucetic and Dobry, 1991) and **e**$_2$ (Darendeli and Stokoe, 2001) for LANDEB.*

Table 4.12: 7 accelerograms (4 real and 3 simulated) chosen as seismic input for the 1D STRATA modeling carried out for the sites of Bovino municipality. Date, time, latitude, longitude, hypocentral depth (z), magnitude (M), epicentral distance (d), number of data and duration (T) of each accelerogram are reported. Real 1 and Real 4 accelerograms are identical to those of Accadia.

Acc.	Date	Time	Lat	Lon	z (km)	M	d (km)	n data	T (s)
Real 1	15/09/1976	09:21:18	46.30	13.17	11.3	6.0	15.8	3375	16.875
Real 2	21/06/2000	00:51:47	63.91	-20.74	10.0	6.5	12.6	8498	42.490
Real 3	29/05/2008	15:46:00	63.96	-20.99	10.0	6.2	1.8	6970	34.850
Real 4	21/06/2000	00:51:47	63.91	-20.74	10	6.5	13.2	9600	48.000
Sim 1	-	-	-	-	-	6.5	0.0	4253	21.265
Sim 2	-	-	-	-	-	7.0	10.0	6295	31.475
Sim 3	-	-	-	-	-	7.0	20.0	7827	39.135

CARLANTINO

Noise recordings acquired at four sites (HV07, HV12, HV16 and HV18) were chosen for applying the procedure of site amplification calculation to the Carlantino municipality (Fig. 4.32). The results of Rayleigh waves ellipticity curves inversion are shown graphically in Fig. 4.33 and numerically in Table 4.13.

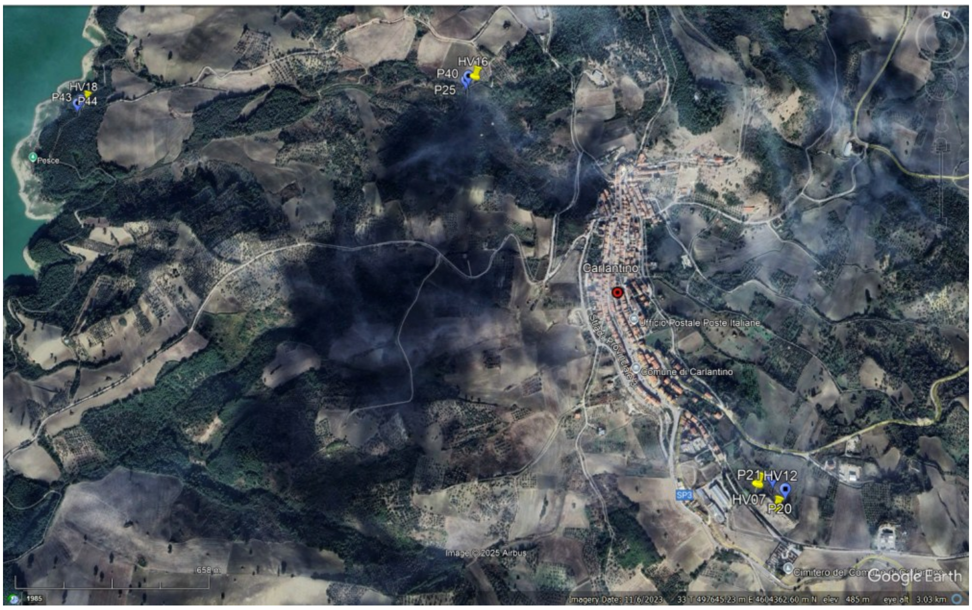

Fig. 4.32: Location of noise recording sites at Carlantino (in yellow) near to boreholes (in blue), whose data were used to support Rayleigh wave ellipticity curve inversion in terms of S-waves vertical velocity profile.

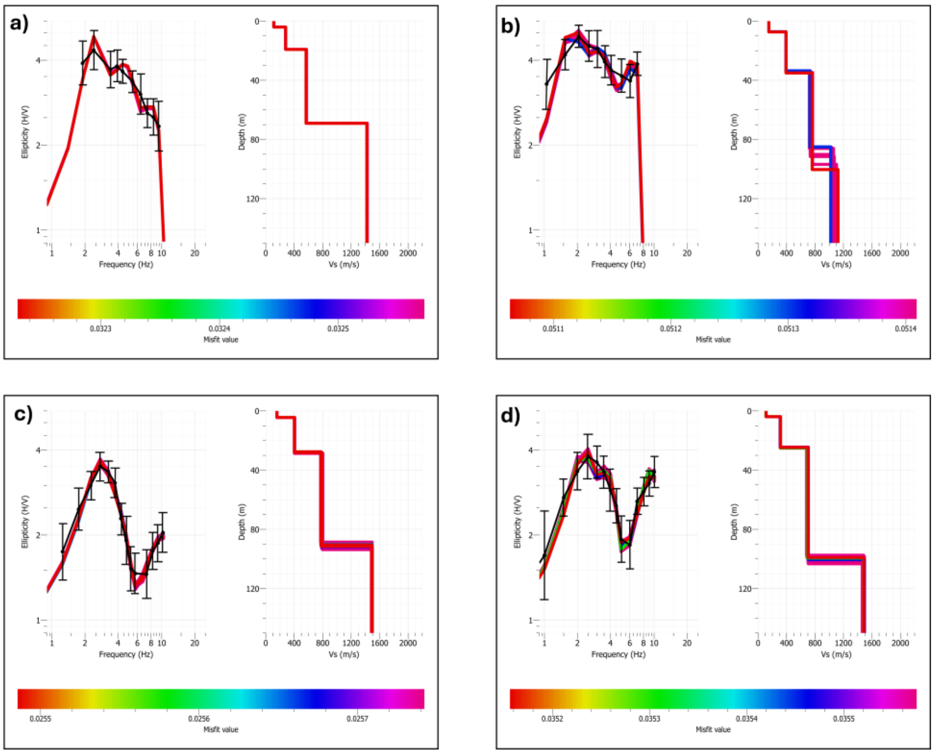

*Fig. 4.33: Results of the inversion of Rayleigh wave ellipticity curves, obtained from the HVIP analysis of ambient noise recordings acquired at Carlantino, in terms of 1D S-wave velocity profile: (**a**) HV7, (**b**) HV12, (**c**) HV16 and (**d**) HV18. Lines, symbols and colors as in Fig. 4.15.*

Table 4.13: S-wave vertical velocity profiles obtained from the inversion carried out with the DINVER code for sites HV07, HV12, HV16 and HV18 of the Carlantino municipality. Thickness in meters (h) and velocity of S-waves in m/s (V_s) of each layer are reported for each site. For each layer, the numerical code next to the Vs value indicates the lithologic unit from Table 4.8 to which it was assimilated to derive the G and D curves.

	LAYER 1		**LAYER 2**		**LAYER 3**		**LAYER 4**	
Site	h (m)	V_S (m/s)	h (m)	V_S (m/s)	h (m)	V_S (m/s)	h (m)	V_S (m/s)
HV07	4	115 $^{(1)}$	16	275 $^{(10)}$	48	575 $^{(10)}$	Bedrock	1415
HV12	8	160 $^{(1)}$	27	390 $^{(10)}$	65	760 $^{(10)}$	Bedrock	1125
HV16	5	160 $^{(1)}$	23	390 $^{(10)}$	62	770 $^{(10)}$	Bedrock	1480
HV18	4	120 $^{(1)}$	22	315 $^{(10)}$	72	690 $^{(10)}$	Bedrock	1480

The accelerograms used to perform the site response modeling with STRATA for Carlantino are shown in Fig. 4.34, while their characteristics are reported in Table 4.14. Real 2 is the same as that used for Accadia, while Real 3 is the same as that used for Bovino.

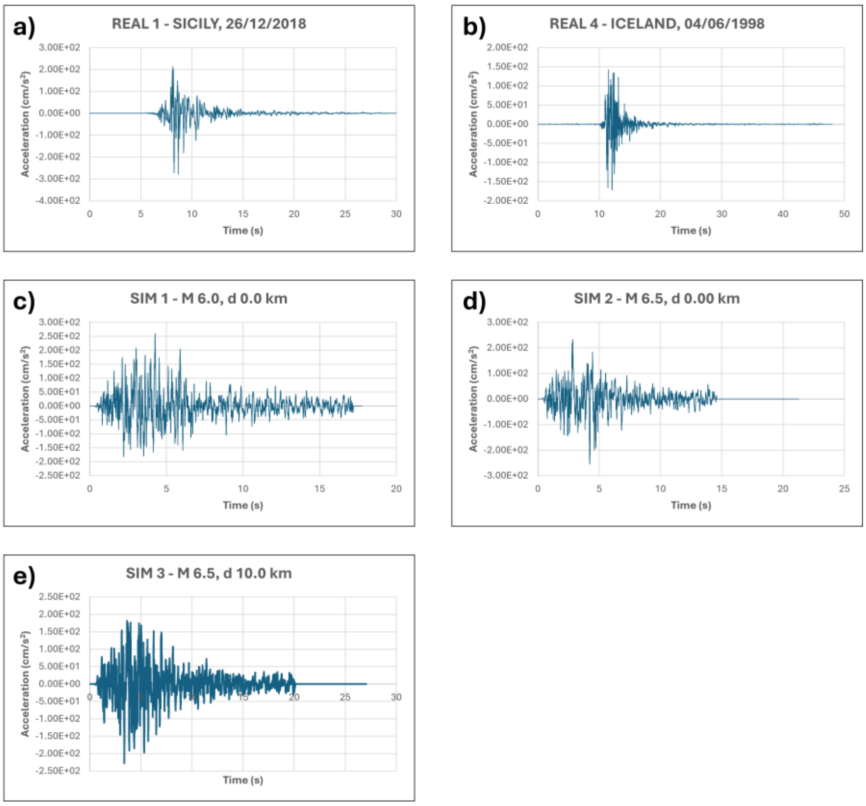

*Fig. 4.34: Accelerograms used as seismic input for Carlantino: (**a**) REAL 1, (**b**) REAL 4, (**c**) SIM 1, (**d**) SIM 2 and (**e**) SIM 3 (details in Table 4.14).*

Table 4.14: 7 accelerograms (4 real and 3 simulated) chosen as seismic input for the 1D STRATA modeling carried out for the sites of Carlantino municipality. Date, time, latitude, longitude, hypocentral depth (z), magnitude (M), epicentral distance (d), number of data and duration (T) of each accelerogram are reported. Real 2 and Real 3 accelerograms are identical to those of Accadia and Bovino, respectively.

Acc.	Date	Time	Lat	Lon	z (km)	M	d (km)	n data	T (s)
Real 1	26/12/2018	02:19:17	37.64	15.12	-	5.0	4.5	5996	29.980
Real 2	26/21/2018	02:19:17	37.64	15.12	-	4.9	5.3	11581	57.905
Real 3	29/05/2008	15:46:00	63.96	-20.99	10.0	6.2	1.8	6970	34.850
Real 4	04/06/1998	21:36:54	63.95	-21.28	10.0	5.4	7.2	8800	44.000
Sim 1	-	-	-	-	-	6.0	0.0	3553	17.765
Sim 2	-	-	-	-	-	6.5	0.0	4253	21.265
Sim 3	-	-	-	-	-	6.5	10.0	5411	27.055

The choices for curves *G* and *D* (Fig. 4.35) are shown in Table 4.13. A damping of 1%, corresponding to the STRATA default value, was set for the bedrock layer at all sites, once it was verified that using the value of 2% suggested by Peruzzi and Albarello (2015) did not modify the results.

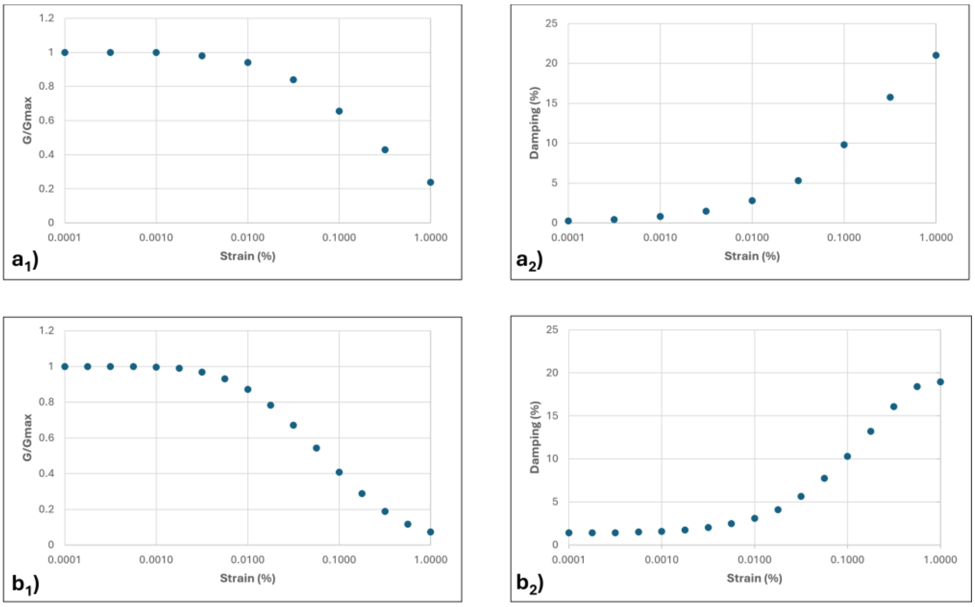

Fig. 4.35: G and D curves as a function of the strain used in the STRATA software for taking into account the nonlinear response of surficial deposits: ***a₁***, ***a₂*** *for CL (Idriss, 1990);* ***b₁***, ***b₂*** *for u.b.i. PI=30 (EPRI, 1993) used for Carlantino municipality.*

VOLTURINO

Noise recordings acquired at four sites (HV02, HV05, HV09 and HV15) suitable for application of the proposed procedure were also identified for the municipality of Volturino (Fig. 4.36). The results of Rayleigh waves ellipticity inversion are shown graphically in Fig. 4.37 and numerically in Table 4.15.

Table 4.15: S-wave vertical velocity profiles obtained from the inversion carried out with the DINVER code for sites HV02, HV05, HV09 and HV15 of Volturino municipality. Thickness in meters (h) and velocity of S-waves in m/s (V_S) of each layer are reported for each site. For each layer, the numerical code next to the V_S value indicates the lithologic unit from Table 4.8 to which it was assimilated to derive the G and D curves.

	LAYER 1		**LAYER 2**		**LAYER 3**		**LAYER 4**	
Site	h (m)	V_S (m/s)	h (m)	V_S (m/s)	h (m)	V_S (m/s)	h (m)	V_S (m/s)
HV02	4	125 **(1)**	18	315 **(10)**	60	640 **(10)**	Bedrock	1490
HV05	4	105 **(1)**	16	265 **(10)**	58	545 **(10)**	Bedrock	1400
HV09	4	105 **(1)**	13	265 **(10)**	45	490 **(10)**	Bedrock	1150
HV15	5	150 **(1)**	18	380 **(10)**	67	730 **(10)**	Bedrock	1495

Fig. 4.36: Location of noise recording sites at Volturino (in yellow) near to boreholes (in blue), whose data were used to support Rayleigh wave ellipticity curve inversion in terms of S-waves vertical velocity profile.

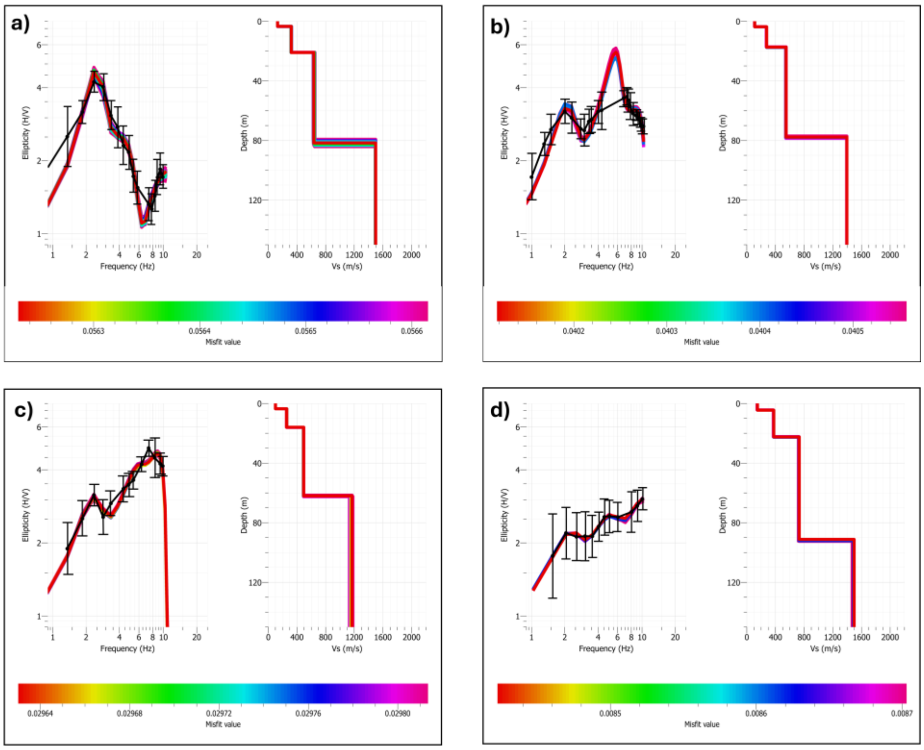

*Fig. 4.37: Results of the inversion of Rayleigh wave ellipticity curves, obtained from the HVIP analysis of ambient noise recordings acquired at Volturino, in terms of 1D S-wave velocity profile: (**a**) HV02, (**b**) HV05, (**c**) HV09 and (**d**) HV15. Lines, symbols and colors as in Fig. 4.15.*

The real accelerograms used as seismic inputs in the STRATA software are the same as those used for the previously described municipality, namely: real 1 and real 4 in Accadia, real 2 in Bovino and real 4 in Carlantino. The simulated accelerograms are shown in Fig. 4.38 and have the following characteristics:

- SIM 1: M = 6.5, epicentral distance = 20.0 km, number of data = 6927, duration = 34.635 s;
- SIM2: M = 7.0, epicentral distance = 20.0 km, number of data = 7828, duration = 39.135 s;
- SIM 3: M = 7.0, epicentral distance = 30.0 km, number of data = 9249, duration = 46.245 s.

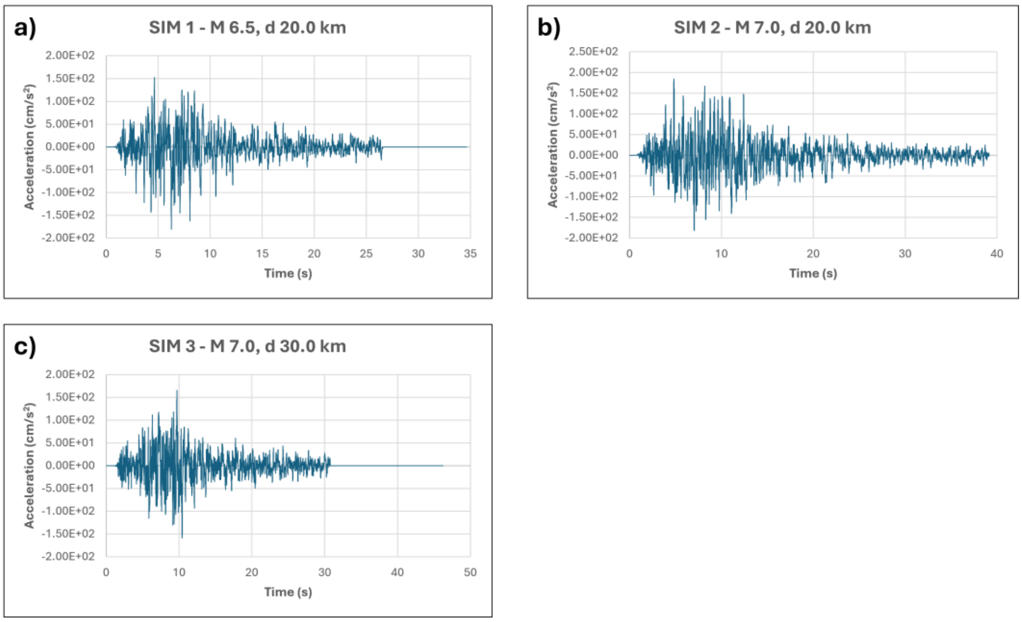

*Fig. 4.38: Simulated accelerograms used as seismic input for Volturino: (**a**) SIM 1, (**b**) SIM and (**c**) SIM 3.*

The damping and shear modulus curves used for Volturino are the same used for Carlantino (see Fig. 4.35). As for Carlantino, damping was set at the default value of 1% for the bedrock layer.

For each of the 19 sites analyzed, seven acceleration time series calculated at the surface were provided by STRATA as output from the seven accelerograms used as seismic inputs for the site response modeling. Then, Arias intensity was calculated both for the output and the input acceleration time series and their ratio provided 7 estimations of the amplification factor: by then taking the average, a single amplification factor and the associated standard deviation were obtained for each site, as shown in Table 4.16.

Table 4.16: Mean amplification factors (in term of I_A) and standard deviations, with the corresponding logarithmic values, obtained for the 19 sites analyzed with the proposed procedure.

	Site	AF	St. Dev.	Log AF	Log St. Dev
Accadia					
	Site	AF	St. Dev.	Log AF	Log St. Dev
	HV11	6.581	1.560	0.808	0.103
	HV13	7.696	2.415	0.867	0.143
	HV18	6.487	1.879	0.796	0.130
	HV21	6.598	2.059	0.800	0.142
Bovino					
	Site	AF	St. Dev.	Log AF	Log St. Dev
	HV7n	3.597	0.855	0.543	0.119
	HV8n	4.459	1.076	0.639	0.100
	HV13n	5.670	1.043	0.747	0.084
	HV14n	2.329	0.579	0.354	0.116
	HV15n	3.139	0.922	0.480	0.130
	HV29n	5.252	0.484	0.719	0.040
	HV32n	8.365	2.413	0.906	0.134
Carlantino					
	Site	AF	St. Dev.	Log AF	Log St. Dev
	HV07	5.653	1.219	0.745	0.083
	HV12	4.807	1.004	0.675	0.081
	HV16	5.677	0.928	0.749	0.067
	HV18	5.422	0.861	0.730	0.065
Volturino					
	Site	AF	St. Dev.	Log AF	Log St. Dev.
	HV02	6.228	0.609	0.793	0.042
	HV05	6.498	0.892	0.810	0.057
	HV09	6.150	0.554	0.787	0.039
	HV15	6.087	0.439	0.783	0.032

4.3.2 Update of the D_N prediction equation

Table 4.16 shows that implementing the procedure described in Section 4.1 for localized site-specific estimation of amplification factors in terms of Arias intensity I_A in the four test areas provided values between 2.3 to 8.4. For a preliminary evaluation of the effect on the slope resistance demand estimates, these values were inserted in equation [4.2] resulting in a median increase of $(A_c)_x$ by a factor ranging from 2.5 to 9.7. Considering that the $(A_c)_x$ values obtained in the study area for reference site conditions reach maxima of 0.04-0.07g, according whether 10% or 5% exceeding probabilities are adopted (see Fig. 3.36), it is apparent that the regression dataset used to calibrate the D_N prediction equation, which includes a_c values up to 0.08g, does not cover the possible range of $(A_c)_x$ variability for the case of site amplification conditions.

Therefore, it was deemed appropriate to extend the dataset used to calibrate the D_N-I_A-a_c relationship by adding 10 a_c values (0.10, 0.12, 0.14, 0.17, 0.20, 0.24, 0.29, 0.35, 0.42 and 0.50g), again equally spaced on a logarithmic scale.

The steps followed in section 3.2 were repeated, considering all 21 a_c values, using the same accelerograms for the regression and validation datasets. Considering the 65 accelerograms of the regression 1 dataset, 1365 D_N values were obtained. They were used to perform a D_N-I_A-a_c multivariate regression, whose results are summarized in Table 4.17.

Table 4.17: Coefficients and statistics for the regression performed with the extended dataset.

Regression Coefficients		
	Value	St. Err.
a_1	1.292	0.045
b_1	-1.775	0.030
c_1	-1.458	0.042
Regression Statistics		
R^2	0.762	
St. Err.	0.514	
Number of observations	1248	

The number of observations actually used for the regression is lower than the initial ones (1248 vs. 1365) as the data for which $D_N=0$ cm were removed. Applying the procedure for the removal of outliers, 168 more data were removed, thus obtaining the new calibrated relationship:

$$logD_N = 1.065logI_A - 1.268loga_c - 0.605 \qquad [4.14].$$

The regression statistics are reported in Table 4.18.

Table 4.18: Coefficients and statistics for the regression performed with the extended dataset, after removing the outliers.

Regression Coefficients		
	Value	St. Err.
a_1	1.065	0.022
b_1	-1.268	0.016
c_1	-0.605	0.023
Regression Statistics		
R^2	0.878	
St. Err.	0.229	
Data number	1080	

Having extended both the regression dataset and the two validation datasets (in which the accelerograms are still the same as those used originally), the estimation errors were analyzed again to verify the lognormal distribution. Fig. 4.39 shows the comparison between the exceedance probability curves of the three datasets and the curves expected for a normal distribution of the estimation errors, and Tables 4.19, 4.20, 4.21 and 4.22 report the results of the χ^2 test for the regression and validation datasets. These tests confirmed that only the regression dataset shows a good agreement with the hypothesis of a lognormal distribution of the estimation errors, while strong deviations are observed for the two validation datasets, related to an excess of large overestimations.

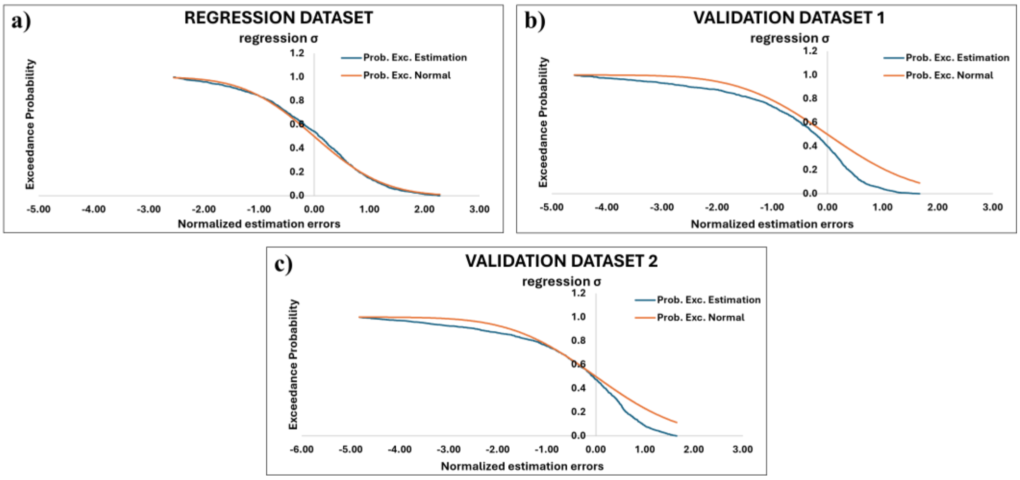

*Fig. 4.39: Comparison between the exceedance probabilities of the normalized estimation errors ε (blue curve) and those expected for a normal distribution (orange curve) for the extended regression dataset (**a**), validation datasets 1 (**b**) and 2 (**c**).*

Table 4.19: Chi-squared test results for the extended regression dataset. Columns report for each class: central values of normalized error classes, number of errors observed for each class, its percentage, the percentage expected for a lognormal distribution and the relative contribution to the chi-squared value. At the bottom of the last column, the total chi-squared value is reported.

REGRESSION DATASET				
Normalized Class	n. obs	freq. % obs	freq. % norm	χ2
< -2.75	0	0.00	0.06	0.058
-2.50	6	0.56	0.56	0.000
-2.00	37	3.43	1.65	1.898
-1.50	50	4.63	4.41	0.011
-1.00	80	7.41	9.18	0.344
-0.50	144	13.33	14.99	0.183
0.00	178	16.48	19.15	0.371
0.50	231	21.39	19.15	0.263
1.00	193	17.87	14.99	0.554
1.50	101	9.35	9.18	0.003
2.00	44	4.07	4.41	0.025
2.50	16	1.48	1.65	0.018
> 2.75	0	0.00	0.56	0.563
				Σ= 4.291

Table 4.20: Chi-squared test results for the extended validation dataset 1. Columns report for each class: central values of normalized error classes, number of errors observed for each class, its percentage, the percentage expected for a lognormal distribution and the relative contribution to the chi-squared value. At the bottom of the last column, the total chi-squared value is reported. Anomalously high discrepancies are highlighted in red.

VALIDATION DATASET 1				
Normalized Classes	n. obs	freq. % obs	freq. % norm	$\chi 2$
< -2.75	30	2.40	0.06	**95.080**
-2.50	42	3.36	0.56	**13.886**
-2.00	53	4.24	1.65	4.043
-1.50	47	3.76	4.41	0.095
-1.00	96	7.68	9.18	0.247
-0.50	173	13.84	14.99	0.088
0.00	307	24.56	19.15	1.531
0.50	373	29.84	19.15	5.973
1.00	111	8.88	14.99	2.489
1.50	18	1.44	9.18	6.531
2.00	0	0.00	4.41	4.406
2.50	0	0.00	1.65	1.654
> 2.75	0	0.00	0.56	0.563
				Σ=136.585

Table 4.21: Chi-squared test results for the extended validation dataset 2. Columns report for each class: central values of normalized error classes, number of errors observed for each class, its percentage, the percentage expected for a lognormal distribution and the relative contribution to the chi-squared value. At the bottom of the last column, the total chi-squared value is reported. Anomalously high discrepancies are highlighted in red.

VALIDATION DATASET 2				
Normalized Classes	n. obs	freq. % obs	freq. % norm	$\chi 2$
< -2.75	18	1.46	0.06	**34.072**
-2.50	48	3.89	0.56	**19.683**
-2.00	36	2.92	1.65	0.968
-1.50	54	4.38	4.41	0.000
-1.00	79	6.41	9.18	0.840
-0.50	147	11.92	14.99	0.627
0.00	265	21.49	19.15	0.287
0.50	362	29.36	19.15	5.448
1.00	186	15.09	14.99	0.001
1.50	38	3.08	9.18	4.055
2.00	0	0.00	4.41	4.406
2.50	0	0.00	1.65	1.654
> 2.75	0	0.00	0.56	0.563
				Σ=72.605

Table 4.22: Summary of the results of the chi-squared test. For each extended dataset the table reports the critical threshold for rejecting the null hypothesis with a significance level of 0.05 and the observed χ^2.

	Degree of freedom	Critical χ^2	Experimental χ^2
Regression dataset	10	18.307	4.291
Validation dataset 1	12	21.026	**136.585**
Validation dataset 2	12	21.026	**72.605**

The predictive capability of equation [4.14] on an extended range of a_c values was verified and compared with that of the other relationships tested in section 3.2 (i.e., [3.3], [3.4] and [3.17]). In addition, two other relationships adopting a more complex functional form were tested. One was calibrated by Hsieh and Lee (2011) on a global dataset, according to the following formulation:

$$logD_N = 0.847logI_A - 10.62a_c + 6.587a_c \cdot logI_A + 1.84 \pm 0.295 \quad [4.15].$$

It adopts a functional form in which the rate at which D_N increases with I_A is not constant for any a_c value, as is assumed by the functional form of [3.14]. Indeed, the results of calculating D_N for a large worldwide dataset suggested that such a rate significantly increases as a_c increases over a large range of a_c variations (see Fig. 4.40). Therefore, this trend can be better matched by a functional form like [4.15], which includes an additional term proportional to the product $a_c \cdot \log I_A$.

Another relationship with a similar functional form was proposed by Chousianitis et al. (2014) for Greece, an area with geological and tectonic characteristics more similar to southern Italy, although affected by relatively higher earthquake magnitudes. The equation obtained in this case was:

$$logD_N = 2.228logI_A - 2.498loga_c + 0.373loga_c \cdot logI_A - 5.495 \pm 0.231 \quad [4.16].$$

The functional form of this relationship differs from the previous one, in that it replaces a_c with its logarithm in each term; it was calibrated using a Greece dataset, rather than a global one, due to its seismotectonic regime and significant attenuation in certain parts of the territory.

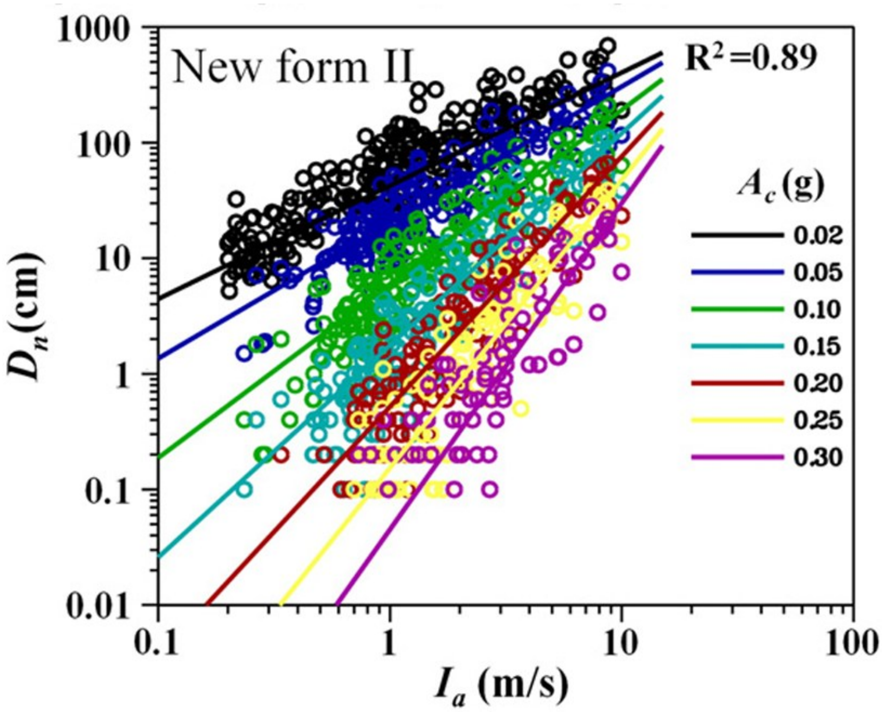

Fig. 4.40: Results of the application of the equation [4.15] on a worldwide dataset (from Hsieh and Lee, 2011).

Table 4.23 shows the results of the predictive capability test conducted on the extended dataset for different equations.

The use of extended datasets substantially confirmed the outcome of the tests conducted on smaller datasets (see Table 3.12 in Section 3.2): the region-specific relationship [4.14] performed much better than relations calibrated on data deriving from other regions, regardless of the functional form. It showed the lowest RMSE (0.186 for validation dataset 1 and 0.198 for validation dataset 2), and the mean logarithmic error closest to zero, which indicates a good balance between overestimates and underestimates.

Relationship [4.15], on the other hand, shows better predictive capability than relationships [3.3], [3.4], [3.17] and [4.16], returning estimates that deviate from actual values within a narrower range, with a mean logarithmic error closer to 0 and a lower RMSE.

Table 4.23: Results of predictive capability test performed on the two extended validation datasets using the new regional-specific relationship and other more general equations available in literature. For each relationship and for both validation datasets, minimum, maximum and average logarithmic errors are reported with the relative RMSE. The lowest RMSE values are highlighted in red.

		New empirical eq. [4.14]	**Jibson et al. eq. [3.3]**	**Romeo eq. [3.4]**	**Romeo eq. [3.17]**	**Hsieh and Lee eq. [4.15]**	**Chousianitis et al. eq. [4.16]**
	Log errors						
	MIN	-0.514	-1.082	-1.968	-0.922	-0.716	-1.256
Validation	MAX	0.389	0.565	0.603	0.210	0.403	0.414
Dataset 1	MEAN	-0.048	-0.184	-0.496	-0.358	-0.158	-0.369
	RMSE	**0.186**	0.391	0.732	0.419	0.269	0.488
	Log errors						
	MIN	-0.532	-1.028	-1.944	-0.967	-0.720	-1.141
Validation	MAX	0.378	0.585	0.623	0.298	0.475	0.512
Dataset 2	MEAN	-0.008	-0.143	-0.460	-0.287	-0.123	-0.326
	RMSE	**0.198**	0.367	0.704	0.373	0.266	0.449

To explore the possibility of improving predictive capability by calibrating more complex functional forms on region-specific data, regressions were carried out using the functional forms of equations [3.17] and [4.15] on the same dataset used for equation [4.14]. The results are as follows:

$$\log D_N = 0.699 \cdot \log I_A - 3.774 \cdot \frac{a_C}{PGA} + 0.406 \qquad [4.17]$$

$$\log D_N = 0.707 \cdot \log I_A - 11.040 \cdot a_c + 7.229 \cdot a_c \log I_A + 1.790 \qquad [4.18].$$

Table 4.24 reports the regression statistics and the results of tests on their predictive capabilities, compared with those of relationship [4.14].

Table 4.24: Regression statistics and predictive capability test results obtained using equations [4.14], [4.17] and [4.18].

	Regression Statistics		
	Regression (eq. [4.14])	Regression (eq. [4.17])	Regression (eq. [4.18])
R^2	0.878	0.945	0.935
St. Err.	0.229	0.219	0.218
Obs	1080	1197	1123
	Predictive Capability		
	RMSE	RMSE	RMSE
Val. Dataset 1	0.186	0.232	0.229
Val. Dataset 2	0.198	0.237	0.242

Both equation [4.17] and [4.18] show a slightly lower standard error compared to the simpler equation [4.14], but this could depend on the introduction of an additional parameter (such as PGA in [4.17]) or term (such as the one proportional to $a_c \cdot \log I_A$ in [4.18]), which allows a better fit with the regression dataset. However, when tested on independent datasets, their predictive capabilities, although improved compared to the original relationships (with a considerable reduction of RMSE) remain inferior to the simpler equation [4.14], which, once again, has a lower RMSE for both validation datasets.

4.3.3 Estimation of slope resistance demand accounting for site amplifications

Based on the results of the previous tests, the $(A_c)_{10}$ maps for a 10% and 5% probability of exceeding the critical threshold D_N=10cm in 50 years were recalculated for reference site conditions using the new relationship [4.14] (Fig. 4.41). Adopting a probability of 10% gives $(A_c)_{10}$ values ranging from a minimum of 0.009g to a maximum of 0.032g, while with a probability of 5%, the resistance demand values are in the range 0.014-0.051g. Passing from 10% to 5% exceedance probability, the $(A_c)_{10}$ increase is more pronounced in the northernmost and southernmost parts of the Daunia Mountains, where it reaches values of 0.02-0.03g and 0.04-0.05g, respectively, in the two maps. Notably, compared to the $(A_c)_{10}$ values obtained with the relationship [3.14] (up to 0.04 and 0.07g for 10% and 5% exceedance probability, respectively), recalibrating the equation on an extended dataset leads to a general decrease.

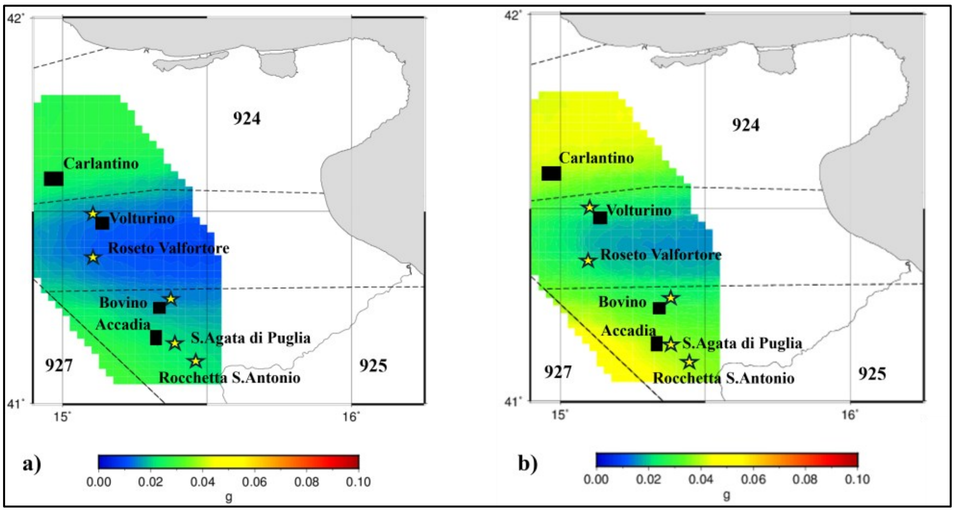

*Fig. 4.41: Maps of $(A_c)_{10}$ values calculated for a 10% (**a**) and a 5% (**b**) probability of D_N exceeding 10 cm in 50 years using the new empirical relationship [4.14] for reference site conditions. The seismogenic sources closest to the Daunia Mountains (924, 925 and 927 according to ZS9) are shown. The black quadrangles mark the areas of the four municipalities (Accadia, Bovino, Carlantino and Volturino) in which the amplification factors AF were estimated. The stars mark municipalities that have been affected by earthquake-induced landslides in the past (Bovino, Rocchetta Sant'Antonio, Roseto Valfortore, Sant'Agata di Puglia and Volturino).*

To highlight the changes that can occur using different relationships to calculate the resistance demand, Fig. 4.42 shows, for the 5% exceedance probability, the differences between the values of $(A_c)_{10}$ obtained using the new relationship [4.14] and those obtained using the relationships [3.3] by Jibson et al. (2000), [3.4] by Romeo (2000), [4.15] by Hsieh and Lee original (2011) and [4.18] derived by recalibrating the Hsieh and Lee's formulation on the regional dataset.

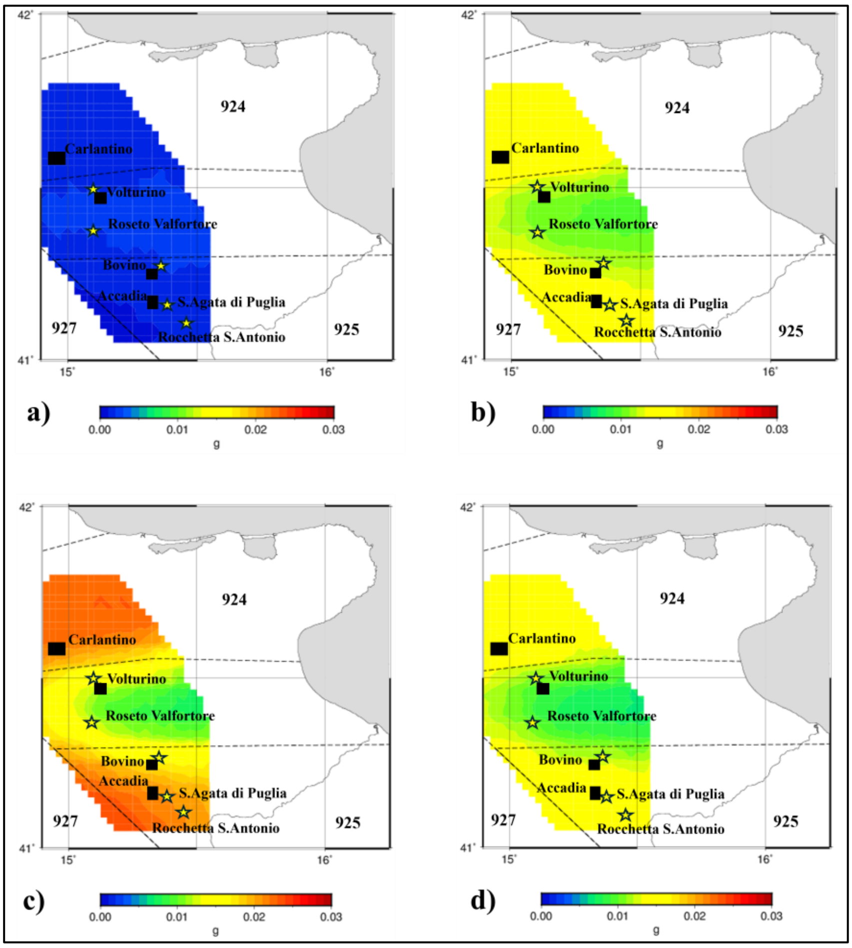

*Fig. 4.42: Maps of differences between the $(A_c)_{10}$ values calculated using the relationship [3.3] (**a**), [3.4] (**b**), [4.15] (**c**) and [4.18] (**d**) for a 5% exceedance probability and the values obtained using the new relationship [4.14]. The seismogenic zones closest to the Daunia Mountains (924, 925 and 927 according to ZS9) are shown. Black quadrangles and stars as in Fig. 4.41.*

The differences in the values of $(A_c)_{10}$ from the results obtained with equation [4.14] are always positive but are modest, reaching a maximum overestimation by 0.024g with equation [4.15] in the southwestern part of the study area.

At this point, the values of $(A_c)_{10}$ obtained for a 5% and 10% probability of D_N exceeding 10 cm in 50 years were recalculated incorporating the effect of site amplification in two alternative ways: i) at the stage of seismic hazard estimates performed by R-CRISIS (see Section 3.1.2) the site factor *FS* (equation [3.8]) was added in the calculation of the GMPM; ii) at the stage of slope resistance demand calculation, the probabilistic estimates of I_A provided by R-CRISIS for reference site conditions were locally modified by EXCRIT by the factor *AF* obtained using the procedure described in Section 4.1.4.

Preliminarily, a comparison was made between the amplification factor *AF* obtained using the procedure described in Section 4.1 for the 19 tested sites (as reported in Table 4.16) and the amplification estimated for the same sites using the empirical relationship based on V_{S30} (equal to 10^{FS}) (reported in Table 4.25). To calculate the site-specific *FS* factor, the V_{S30} values were derived from the V_S vertical profiles obtained by inverting the Rayleigh wave ellipticity curves with the DINVER software, as reported in Tables 4.9, 4.11, 4.13 and 4.15.

Table 4.25: Comparison between amplification factors estimated from empirical relationships based on V_{S30} (10^{FS}) and from 1D site-response modeling (AF mean, as in Table 4.16) for the 19 tested sites. The last column shows the differences between AF and 10^{FS}.

	SITE	LON	LAT	V_{S30} (m/s)	10^{FS}	AF Mean	Diff.
ACCADIA	HV11	15.329	41.155	305	2.704	6.581	3.877
	HV13	15.338	41.160	292	2.825	7.696	4.871
	HV18	15.338	41.161	285	2.897	6.487	3.590
	HV21	15.333	41.158	293	2.818	6.598	3.780
BOVINO	HV13n	15.339	41.248	376	2.178	5.670	3.492
	HV14n	15.341	41.248	555	1.455	2.329	0.874
	HV15n	15.340	41.246	277	2.979	3.139	0.160
	HV29n	15.343	41.246	427	1.910	5.252	3.342
	HV32n	15.338	41.246	391	2.094	8.365	6.271
	HV7n	15.337	41.249	549	1.476	3.597	2.121
	HV8n	15.342	41.250	321	2.559	4.459	1.900
CARLANTINO	HV07	14.982	41.589	272	3.041	5.653	2.612
	HV12	14.982	41.590	282	2.931	4.807	1.876
	HV16	14.969	41.599	323	2.547	5.677	3.130
	HV18	14.953	41.597	275	3.006	5.422	2.416
VOLTURINO	HV02	15.123	41.475	295	2.793	6.228	3.435
	HV05	15.123	41.478	257	3.228	6.498	3.270
	HV09	15.124	41.483	264	3.141	6.150	3.009
	HV15	15.127	41.480	332	2.472	6.087	3.615

The differences show that *AF* is always greater than 10^{FS}, by an amount ranging from a minimum of 0.2g to a maximum of 6.3g, found at Bovino stations HV15n and HV32n, respectively. In most sites, the *AF* value is more than double the value of 10^{FS}.

New maps of $(A_c)_{10}$ values that take into account the site amplification effect were then obtained by introducing the *FS* factor in the calculation of the expected I_A values. This factor was added in the calculation of the GMPM, reported in tabular form in the .ATM files used in R-CRISIS (see in Section 3.1 the part relative to the "ATTENUATION DATA"). Following a cautious approach, a unique value of *FS* was adopted by selecting the minimum V_{S30} value among those obtained from the velocity profiles of the 19 sites, i.e. 257 m/s. Fig. 4.43 shows the results obtained for a 10% and 5% probability of D_N exceeding 10 cm in 50 years.

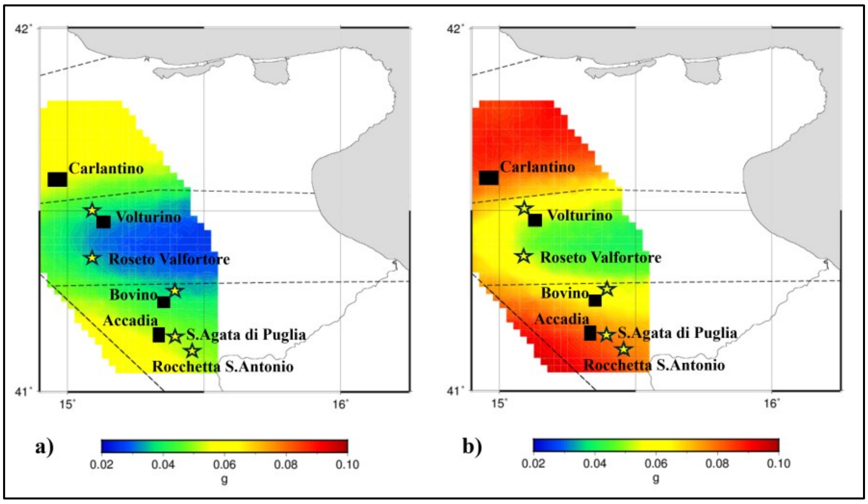

*Fig. 4.43: Maps of $(A_c)_{10}$ values for 10% (**a**) and 5% (**b**) probability of D_N exceeding 10 cm in 50 years, calculated introducing the site effect factor FS in the GMPM used by R-CRISIS to estimate the expected I_A values. The seismogenic zones closest to the Daunia Mountains (924, 925 and 927 according to ZS9) are shown. Black quadrangles and stars as in Fig. 4.41.*

Furthermore, compared to the maps obtained for reference site conditions (Fig. 4.41), the resistance demand values obtained by introducing the *FS* site factor are significantly increased, producing almost a doubling across the entire area.

Finally, the resistance demand calculation was also performed providing to EXCRIT the I_A values expected for reference site conditions and the *AF* values in logarithmic form, as reported in Table 4.16. To include these factors, the *aimax* parameter (See section 3.1) was set to a negative value (-5 m/s) and data of the .gra file generated by R-CRISIS were added with the following specifications (as described in Section 4.1.4):

- at sites where *AF* was not available, the variable *fa*, which is entered next to the coordinates, was set to 0;
- at the 19 sites for which *AF* had been calculated, the variables *fa* and *sdfa* were assigned the average of the logarithm of *AF* and the relative standard deviation, as reported in Table 4.16; *sdmax* was set to 2.5 and *nsd* to 5 (indicating that the calculation has to be divided into 5 intervals from -2.5σ to +2.5σ).

After introducing the amplification factor, the resistance demand value increased significantly, reaching a maximum of approximately 0.2g. Compared to the $(A_c)_{10}$ values calculated using the *FS* factor (Table 4.26) these values were found higher in all but one case (in which the ratio between the two values was 0.95), sometimes more than doubling the values obtained using the factor *FS*, with differences that reached a maximum of 0.13g.

Table 4.26: $(A_c)_{10}$ values obtained for a 5% probability of D_N exceeding 10 cm in 50 years under reference site condition and with site amplification expressed using the AF and FS factors, for the 19 tested sites. The difference and the ratio between the $(A_c)_{10}$ values obtained with AF and FS are reported in the last two columns.

LON	LAT	$(A_c)_{10}$ under reference conditions	$(A_c)_{10}$ with AF	$(A_c)_{10}$ with F_S	DIFF	RATIO
15.329	41.155	0.038	0.188	0.082	0.106	2.287
15.338	41.160	0.038	0.211	0.081	0.130	2.600
15.338	41.161	0.038	0.183	0.081	0.101	2.249
15.333	41.158	0.038	0.187	0.081	0.105	2.292
15.339	41.248	0.030	0.129	0.064	0.064	2.002
15.341	41.248	0.030	0.061	0.064	-0.003	0.948
15.340	41.246	0.030	0.079	0.064	0.014	1.224
15.343	41.246	0.030	0.121	0.064	0.057	1.883
15.338	41.246	0.030	0.180	0.064	0.116	2.804
15.337	41.249	0.030	0.088	0.064	0.023	1.366
15.342	41.250	0.030	0.104	0.064	0.040	1.627
14.982	41.589	0.040	0.171	0.084	0.087	2.035
14.982	41.590	0.040	0.149	0.084	0.065	1.781
14.969	41.599	0.041	0.176	0.087	0.089	2.020
14.953	41.597	0.041	0.171	0.087	0.084	1.967
15.123	41.475	0.019	0.089	0.050	0.039	1.775
15.123	41.478	0.019	0.094	0.051	0.043	1.849
15.124	41.483	0.020	0.092	0.052	0.040	1.765
15.127	41.480	0.020	0.089	0.051	0.038	1.747

Finally, the slope resistance demand estimations obtained in this study were compared with those obtained for other regions. Rajabi et al. (2013) and Chousianitis et al. (2016) reported $(A_c)_{10}$ values for Iran and Greece, respectively, for a 10% probability of exceeding D_N=10cm in 50 years, by incorporating a site factor dependent on soil type and classified based on V_{S30}. Locally, in those regions, maximum values were obtained of 0.11g and 0.17g for Iran (Fig. 4.44a) and Greece (Fig. 4.44b), respectively. Following the same approach and incorporating the FS from the GMPE by Sabetta et al. (2021), the $(A_c)_{10}$ values obtained for Daunia (Fig.4.43a) are lower, reaching a maximum of approximately 0.06g. This reflects the lower level of seismic activity affecting Daunia, compared to the most seismically active regions of Iran and Greece.

However, it is noteworthy that introducing the site-specific amplification factor *AF*, roughly doubles the $(A_c)_{10}$ values obtained for Daunia, reaching values of around 0.12g, which are comparable to those obtained with a V_{S30}-based estimation of site effect in areas with higher seismicity. It can therefore be deduced that applying the new approach to those regions would also lead to a considerable increase in slope resistance demand estimations.

These results demonstrate that the introduction of a simple site factor based on V_{S30} is not reliable to describe the site response and could lead to a significant underestimation of the resistance demand of slopes.

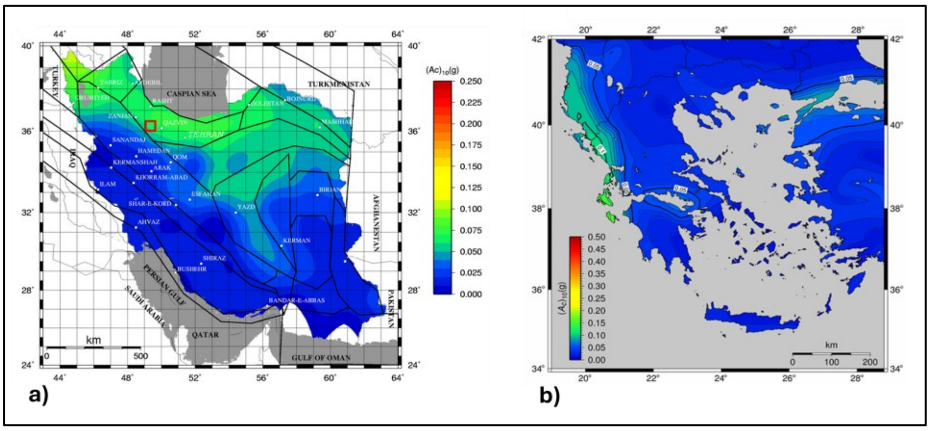

*Fig. 4.44: $(A_c)_{10}$ values obtained for a 10% probability of exceeding D_N=10 cm in 50 years for (**a**) Iran (Rajabi et al., 2013) and (**b**) Greece (Chousianitis et al., 2016), taking into account a site factor based on V_{S30}.*

5. MODELING TESTS FOR EVALUATING 2D EFFECTS INFLUENCE

The procedure described in the previous section for accounting for site response effect on the slope resistance demand adopted a simplified approach considering the influence of stratigraphic amplification alone, calculated using purely mono-dimensional modeling. For a first evaluation of the errors introduced by this simplification, which neglects 2D/3D effect on site response, the topographic effects on the amplification factor in terms of Arias intensity were estimated by exploiting the availability of ITASCA software for geomechanics problems, including a module for fully non-linear dynamic analysis. A 2D modeling of the site response was performed using the UDEC (**U**niversal **D**istinct **E**lement **C**ode) code (Itasca Consulting Group, Inc., 2014) made available by the Department of Geology at the University of Liège under the supervision of Prof. Hans-Balder Havenith.

For this test, sites in the municipality of Bovino were selected where 1D modeling of the site response had already been performed and for which more detailed information was available for reliable 2D modeling.

5.1 UDEC code overview

This software allows the response of discontinuous media to be simulated, and it is based on the distinct element method (DEM). Although this code is generally used for geomechanics problems related to discontinuous rock masses, the dynamic module for estimating the dynamic response of a site to seismic loading can be used more broadly. With appropriate arrangements, it can also model the behavior of a soil slope, like that affected by the Pianello landslide at Bovino.

A discontinuous medium is characterized by the existence of different contacts or interfaces between the different bodies that make up a geomechanical model; in this regard, the medium is divided into a set of discrete blocks, each of which must be assigned a constitutive law (linear or nonlinear, depending on the situation) and various parameters. The blocks can behave as either rigid or deformable material (by dividing them into a finite element mesh). The software can implement seven constitutive models for deformable blocks: these range from a null model, used for wells and/or excavations (where material is removed), to more commonly used models (such as the elastic model or the Mohr-Coulomb model). Once these models have been assigned, the software discretizes the blocks into constant-strain finite-difference triangular zones, making them deformable. Furthermore, the contacts between the different blocks must also be assigned properties in order to define their degree of deformability.

The analysis can be performed under both static and dynamic conditions. For dynamic analysis, it is necessary to specify velocity or stress waves as external boundary conditions or as internal excitation, as well as to define the boundary conditions and the free field condition. However, before performing dynamic analysis, it is essential to perform static analysis in order to achieve static equilibrium.

Basically, UDEC assumes a 2D plane-strain state and discontinuities are interpreted as planar features oriented normal to the analysis plane, provided that the normal stresses to the cross section can also be set to zero. The program is based on the Lagrangian calculation scheme and uses time-marching to solve the equations of motion.

The software uses the FISH language, through which commands can be written to define the modeling process. The software can be used in both command-driven mode (as done for this job) and graphic mode; indeed, everything that is done manually/graphically within the software is converted into a FISH command. It is also possible to create plots directly within the user interface at different stages of the modeling process in order to check the progress of the process, identify any problems, or verify that the model generated is working correctly.

The model was initially designed to perform high-speed modeling by using a small number of elements to reduce the computational time, since the computational speed is directly proportional to the number of blocks that make up the model.

5.1.1 Dynamic analysis

Using UDEC software, it is possible to perform two-dimensional dynamic analysis – to verify what happens to the surface as a result of seismic wave propagation starting from the bedrock – using the explicit finite difference scheme to solve the equation of motion.

To represent dynamic behavior, a time stepping algorithm is adopted to calculate contact forces and displacements at the interfaces of an assembly of blocks. Their movements are due to the propagation of disturbances caused by the resultant of the surface stress and body forces applied to these blocks. The choice of the time step is subject to limitation due to assuming constant velocities and accelerations during such a time interval, because it must be sufficiently small to prevent the propagation of disturbances between a discrete element and adjacent ones during a single step.

The timestep restriction applies to both contacts and blocks: for rigid blocks it is controlled by the mass of the block and the stiffness of the interface; for deformable blocks, the time step limitation depends on the block size, and the stiffness of the system depends on the modulus of the rock elements and the stiffness at the interfaces.

A distinct element modeling alternates the application of i) a force-displacement law and ii) Newton's second law to each block. This is because applying a force-displacement law allows the contact forces to be found from known displacements, while Newton's second law provides the motion of the blocks resulting from known forces acting on them. If the blocks are deformable, the movement is calculated at the points of the grid of triangular elements that discretize the blocks.

The motion of each block depends on the amplitude and direction of the resulting imbalance moment and on the forces acting on it.

According to Newton's second law:

$$\frac{d\dot{u}}{dt} = \frac{F}{m} \qquad [5.1]$$

where $\dot{u}$ is the velocity, *t* is the time and *m* is the mass.

Given the central difference scheme:

$$\frac{d\dot{u}}{dt} = \frac{\dot{u}^{(t+\frac{\Delta t}{2})} - \dot{u}^{(t-\frac{\Delta t}{2})}}{\Delta t} \qquad [5.2]$$

substituting [5.2] into [5.1] gives:

$$\dot{u}^{(t+\frac{\Delta t}{2})} = \dot{u}^{(t-\frac{\Delta t}{2})} + \frac{F^{(t)}}{m}\Delta t \qquad [5.3].$$

The displacement can therefore be expressed as:

$$u^{(t+\Delta t)} = u^{(t)} + \dot{u}^{(t+\frac{\Delta t}{2})}\Delta t \qquad [5.4].$$

The force/displacement calculation is performed in a single instant, since the force depends on the displacement.

In case of 2D blocks, the velocity equations become:

$$\dot{u}_i^{(t+\frac{\Delta t}{2})} = \dot{u}_i^{(t-\frac{\Delta t}{2})} + \left(\frac{\sum F_i^{(t)}}{m} + g_i\right)\Delta t \qquad [5.5]$$

$$\dot{\theta}^{(t+\frac{\Delta t}{2})} = \dot{\theta}^{(t-\frac{\Delta t}{2})} + \left(\frac{\sum M^{(t)}}{I}\right)\Delta t \qquad [5.6]$$

where $\dot{\theta}$ represents the angular velocity of the block about the centroid, *I* is the moment of inertia of the block, $\sum M$ is the total moment acting on the block, *i* is the index indicating the components in the Cartesian plane, $\dot{u}_i$ are the components of the velocity of the block centroid and g_i are the components of gravitational acceleration.

From the velocities thus obtained, the new position of the block can be derived, namely:

$$x_i^{(t+\Delta t)} = x_i^{(t)} + \dot{u}_i^{(t+\frac{\Delta t}{2})}\Delta t \quad [5.7]$$

$$\theta^{(t+\Delta t)} = \theta^{(t)} + \dot{\theta}^{(t+\frac{\Delta t}{2})}\Delta t \quad [5.8]$$

where θ is the rotation of the block about the centroid and x_i are the coordinates of the block centroid.

Each time interval produces new block positions that generate new contact forces which, together with the movements produced, are used to calculate the linear and angular accelerations of the blocks themselves. By integrating the increments over time, the velocity and displacement of the blocks can be obtained. The procedure is repeated until equilibrium is reached, so that mechanical damping can be used in the equations of motion [5.5] and [5.6] to provide solutions in both static and dynamic conditions.

In dynamic analysis, "real" masses are used in the centroids of rigid blocks or in the grid points of deformable blocks, and the time step must be reduced to ensure stability when using damping proportional to stiffness.

When performing a dynamic analysis, there are three fundamental elements to consider:

1- dynamic loading and boundary conditions;
2- wave transmission through the model;
3- mechanical damping.

DYNAMIC LOADING AND BOUNDARY CONDITIONS

To model a portion of material under dynamic loading conditions (both internal and external), it is necessary to define the dynamic input boundary conditions. To minimize waves reflection upon contact with the model boundaries, either quiet/viscous or free field boundary conditions must be defined.

To apply the seismic input, one of the following ways can be used:

- velocity histories;
- stress (or pressure) histories;
- force histories;
- pressure histories within joints.

The history function can be provided in four different forms: harmonic function (sine or cosine), table, history input and FISH function.

Dynamic input can be applied either in the x-direction or in the y-direction, for both static and dynamic models, using different commands. When dynamic input is applied in terms of velocity, it is not possible to apply a quiet/viscous boundary condition to the model boundaries to which velocity histories are applied. To overcome this problem, a velocity record can be transformed into a stress record and applied to a quiet boundary, using the following relationships, applicable to plane waves:

$$\sigma_n = 2(\rho C_P)v_n \qquad [5.9]$$

or

$$\sigma_s = 2(\rho C_S)v_s \qquad [5.10]$$

where:

- σ_n = applied normal stress;
- σ_s = applied shear stress;
- ρ = density;

- C_P = P-waves velocity;
- C_S = S-waves velocity;
- υ_n = input normal particle velocity;
- υ_s = input shear particle velocity.

In detail:

$$C_P = \sqrt{\frac{k+4G/3}{\rho}} \quad [5.11]$$

and

$$C_S = \sqrt{G/\rho} \quad [5.12]$$

where K and G are respectively the bulk and the shear modulus, which are linked to Young's modulus (E) and Poisson's ratio (υ) according to the following relations:

$$K = \frac{E}{3(1-2\upsilon)} \quad [5.13]$$

$$G = \frac{E}{2(1+\upsilon)} \quad [5.14].$$

The velocity history at the boundary may differ from the original one: if the quiet boundary works correctly, the velocity is doubled due to the effect of the free surface.

To avoid residual velocity and displacement after seismic ground motion finishes, preventive baseline correction should be applied to the velocity time history (Fig. 5.1). For this case study, however, this was unnecessary because the accelerograms provided by the SM studies had already undergone this correction.

When modeling a section of a slope, artificial boundaries must necessarily be defined, even if they do not exist. However, when performing dynamic analyses by applying seismic inputs, these boundaries can give rise to reflections of the waves that propagate outward. To remove this problem, a very large model can be used so that the damping of the material can absorb most of the reflected waves.

As an alternative to this, which would require a large computational cost, viscous

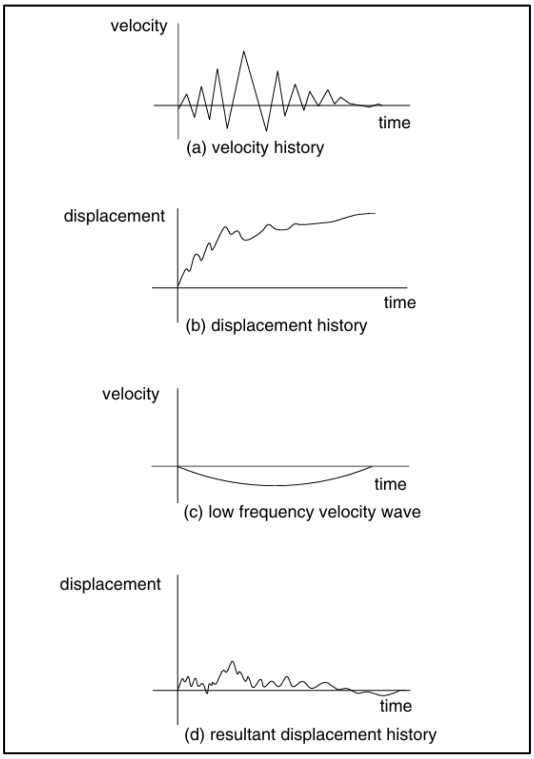

Fig. 5.1: Baseline correction process (UDEC manual, Version 6.0).

boundaries (Lysner and Kuhlemeyer, 1969) can be used which, by using independent dashpots in the normal and shear directions at the boundaries of the model, are able to effectively absorb volume waves that incise at an angle greater than 30° on the boundary. Waves with incident angle less than 30° are also absorbed, albeit less effectively.

The dashpots used in this method provide normal and shear stresses using the following formulas:

$$t_n = -\rho C_p v_n \qquad [5.15]$$

$$t_s = -\rho C_s \upsilon_s \quad [5.16]$$

where υ_n and υ_s are the normal and shear components of velocity at the boundary, ρ is the density, and C_P and C_S are the P-wave and S-wave velocities, respectively.

When there is no engineering structure at the surface of the section to be modeled, free field conditions must be taken into account. Sometimes, elementary side boundaries placed at a great distance would be sufficient to minimize reflections, while a shorter distance would suffice with material with high damping. However, if the distance is too great, the model may be impractical; in this case, free field condition can be imposed in the software in order to continue eliminating reflections at the boundaries. To do this, UDEC performs a 1D free field calculation in parallel with the main analysis of the system. By imposing this condition, the plane waves propagating from bottom to top are not distorted, as the free field simulates the conditions of an infinite model, avoiding these undesirable effects.

When seismic input is applied to the base, it must be appropriately manipulated to avoid errors during simulation. In general, the accelerometer recordings available come from acquisitions made at the surface, often on rocky outcrops that represent standard reference conditions; however, when seismic input is applied in modeling, it is applied to the base of the model. In this regard, therefore, it is necessary to “transfer” the seismic input to the depth of the base of the model by performing a deconvolution (Fig. 5.2) using codes for 1D modeling. In this work, the STRATA code – previously described for performing 1D modeling of site response – was used.

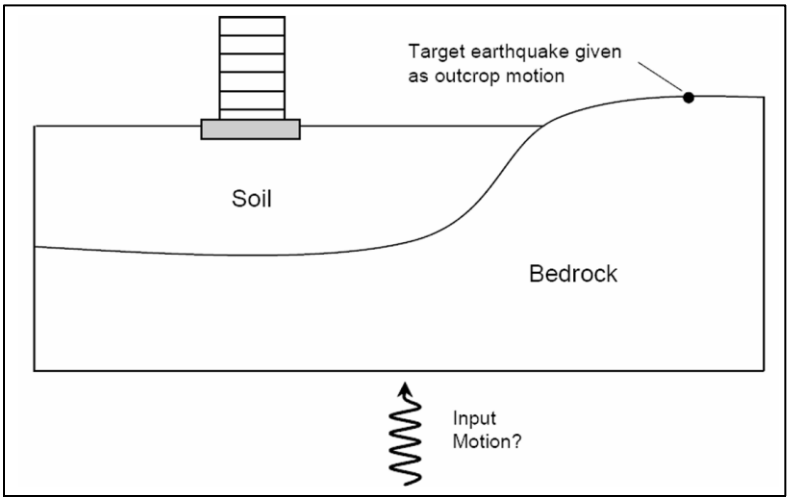

Fig. 5.2: Sketch showing the correct positioning of the seismic input in UDEC modeling making a deconvolution (UDEC manual, Version 6.0).

Furthermore, seismic input can be applied to two different types of bases:

- rigid base, where an acceleration-time history is specified at the base of the model;
- compliant base, where an absorbing boundary is used at the base of the model.

The rigid base is easier to use but completely blocks the movement at the model base; it is only suitable when there is a strong seismic impedance contrast, as it acts as a fixed displacement boundary. For general applications, therefore, it is preferable to use a compliant base, as the waves propagating downward are absorbed.

It is important to remember that the movement at a specific point on the base of the model depends by the overlapping of the effects of the waves propagating both upwards and downwards.

WAVE PROPAGATION

In order to accurately and realistically model the wave transmission through the medium, it is important to remember that the stiffness of the joints in a rock mass can influence seismic wave propagation (as they are responsible for high-frequency attenuation) and travel time.

The numerical accuracy of wave transmission depends on the frequency content of the input wave and the velocity of the medium; for optimal accuracy, the size of the spatial element must be less than approximately 1/10 of the wavelength associated with the highest frequency component of the input wave (Kuhlemeyer and Lysmer, 1973), so that:

$$\Delta l \leq \frac{\lambda}{10} \qquad [5.17]$$

where λ is the wavelength associated with the higher frequency that contains a significant energy.

Often, the normal and shear stiffness values of joints are unknown, but they can be calculated based on the elastic deformation properties of the intact material. In general, to prevent movement along a joint, the stiffness values must be high, but this will result in very slow convergence of the solution.

To calculate the stiffness values, the rule of thumb is used whereby the stiffness of the joints must be equal to the "equivalent stiffness" of the stiffest adjacent zone. The following relationship can be used to calculate the normal stiffness:

$$k_n = factor\ x \max\left[\frac{(K + 4/3G}{\Delta_{zmin}}\right] \qquad [5.18]$$

where *factor* represents a multiplicative factor, generally set to 10, *K* and *G* indicate the bulk and shear modulus, respectively, while Δ_{zmin} is the minimum width of the block zone adjacent to the joint interface in the normal direction (Fig. 5.3).

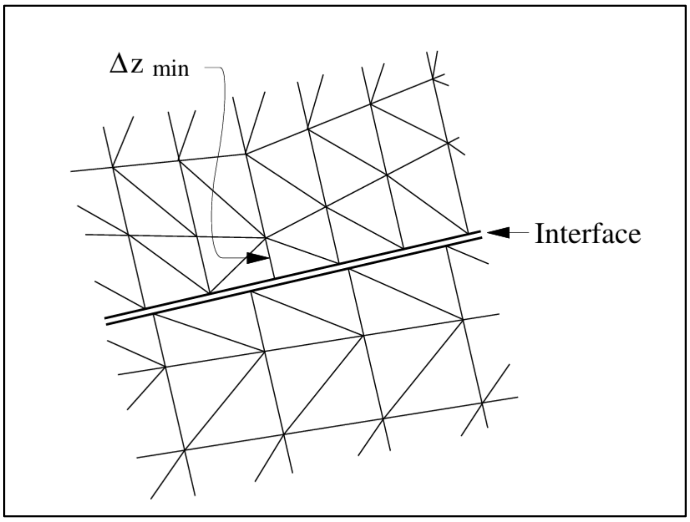

Fig. 5.3: Graphical representation of the minimum size Δ_{zmin} of the zone adjacent to the joint interface, used to calculate normal stiffness k_n (UDEC manual, Version 6.0).

Normal and shear stiffness are generally assumed to be equal for simplifying the problem.

MECHANICAL DAMPING

When the analysis is performed under a dynamic load, there is a damping of the vibration energy, which implies a loss of energy and prevents the system from oscillating indefinitely. This loss of energy depends on i) friction within the intact material and ii) slippage along the interfaces.

In modeling soil or rock behavior, damping is assumed to be hysteretic, i.e., dependent on the stress/strain time history, but does not depend on frequency (Gemant and Jackson, 1937; Wegel and Walther, 1935). Two main problems arise in damping numerical reproduction (Cundall, 1976):

1- many simple hysteretic functions do not dampen all components in the same way when different waveforms overlap;
2- the results are difficult to interpret because they depend on the path followed.

Two different models of damping can be used by UDEC to reproduce rock and soil behavior under a seismic loading:

- Rayleigh damping, which includes two viscous elements, where frequency-dependent effects cancel each other out at the frequencies of interest;
- local damping, generally used for static problem solution, which can also be used in dynamic analysis using damping coefficients appropriate for waves propagation.

However, when waveforms are complex the latter model fails to correctly represent energy loss, especially in the case of multiple frequency cycling loading.

RAYLEIGH DAMPING

Rayleigh damping is commonly used to model the damping of the natural oscillation modes of structures. It is assumed to be proportional to mass *M* and stiffness *K* of the system elements and is expressed in the form of a matrix, according to the equation:

$$C = \alpha M + \beta K \qquad [5.19]$$

where α and β are the damping constants proportional to mass and stiffness, respectively.

Both the *C* terms, when considered separately, depend on frequency, but by choosing the appropriate parameters, their combination can be made practically constant over the frequency range of interest for soil/rock behavior modeling.

The critical damping ratio ξ at an angular frequency ω can be obtained as (Bathe and Wilson, 1976):

$$\xi = \frac{1}{2}\left(\frac{\alpha}{\omega} + \beta\omega\right) \qquad [5.20].$$

From the variation of the normalized critical damping with angular frequency (Fig. 5.4), it can be seen that the mass-dependent damping dominates at low angular frequencies, while stiffness-dependent damping dominates at high angular frequencies.

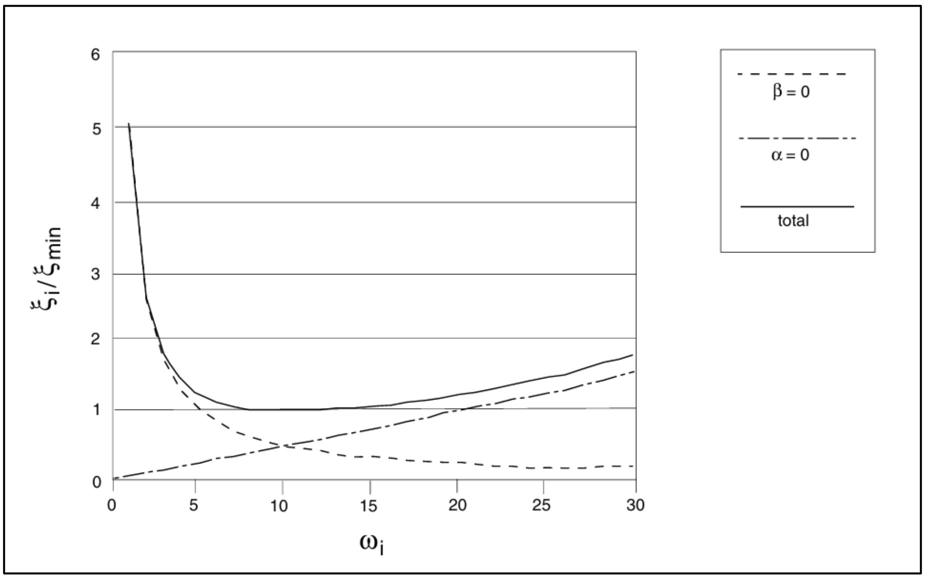

Fig. 5.4: Representation of the variation in normalized critical damping as a function of angular frequency (UDEC manual, Version 6.0).

The curve representing the sum of the two components reaches its minimum value:

$$\xi_{min} = (\alpha\beta)^{1/2} \quad [5.21]$$

at frequency:

$$\omega_{min} = (\alpha/\beta)^{1/2} \quad [5.22]$$

from which it follows that:

$$\alpha = \xi_{min}\omega_{min} \quad [5.23]$$

$$\beta = \xi_{min}/\omega_{min} \quad [5.24].$$

The frequency at which the minimum is obtained will therefore be:

$$f_{min} = \omega_{min}/2\pi \quad [5.25]$$

so that mass and stiffness damping each define half of the total damping.

Performing the dynamic analysis with UDEC, the automatic selection of the time step depends on damping proportional to stiffness, but if instability occurs (for example, in the case of very large deformations), it must be reduced manually. In general, to make damping independent of frequency, ω_{min} is chosen so that it is at the center of the frequency range of interest. To reproduce frequency-independent damping at a correct level for geological material, ξ must generally be between 2 and 5% (Biggs, 1964); if, on the other hand, large deformations are expected in the blocks and along the joints, then a minimum damping of, for example, 0.5% is sufficient.

Although Rayleigh damping is frequency-dependent, there is a flat zone in the frequency-dependent velocity spectrum for a frequency range of 3:1 (Fig. 5.5).

The f_{min} must therefore be chosen so that its 3:1 interval coincides with the interval of the frequencies relevant for the analysis, which are given by a combination of the input frequencies and the natural modes of the system. In this regard, the fundamental frequency associated with natural oscillation motion is expressed as:

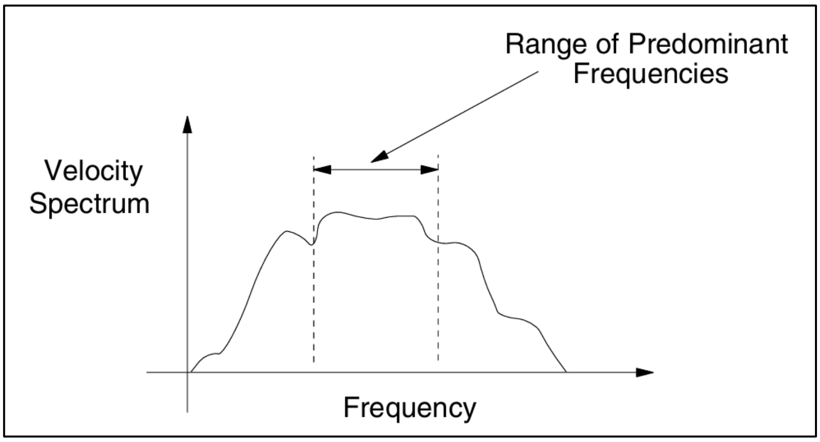

Fig. 5.5: Velocity spectrum as a function of frequency, where there is the flat region representing the 3:1 frequency interval that helps define the f_{min} of the damping.

$$f = \frac{C}{\lambda} \qquad [5.26]$$

where C and λ represent the wave propagation velocity and the major wavelength (which depends on the boundary conditions) associated with the oscillatory motion.

LOCAL DAMPING

Local damping is generally used to solve static equilibrium problems, but it could also be adapted to dynamic analysis.

This type of damping operates by adding or subtracting mass from a grid point at specific instants of the oscillation cycle, without however producing a net change in mass because the amount added is equal to that subtracted. The kinetic energy also remains constant, as mass is added when the velocity changes sign and subtracted at times when velocity reaches its maximum and minimum. According to Kolsky (1963), the local damping coefficient is equal to:

$$\alpha_L = \pi D \qquad [5.27]$$

where D indicates the critical damping fraction.

Applying either Rayleigh or local damping to the same problem yields almost identical results; although local damping is easier to use – since it does not depend on frequency – it must be used with caution because, for complex waveforms, it under-dampens high-frequency components, introducing noise. Therefore, it is not recommended for simulations using seismic time series.

5.1.2 UDEC commands for numerical simulations of site response

To create the geometry to be modeled within the UDEC software, it is necessary to write scripts containing a list of commands using the FISH language, which is useful both for generating models and for solving problems to be modeled.

To model portions of a slope, site-specific data on material properties is required, although the definition of many properties (especially those relating to deformability, strength, rock mass stresses and discontinuity) is affected by uncertainty. The more appropriate the input data, the more accurate and reliable the output results will be.

In order to simulate a dynamic analysis, it is necessary to define:

- the geometry of both the topography and the internal layers;
- the position of geological structures, such as faults and cracks;
- the behavior of the material;
- the initial conditions;
- the external load.

To create the geometry model, it is first necessary to define a general configuration that specifies two elements:

1- a constant distance for the rounding length of corners with the ***round*** command (set at 0.5 by default);
2- a minimum value for the length of the block edge with the ***edge*** command (by default, it is set to twice the value indicated by the *round* command, but it can be modified manually).

The command useful to define the topography of the section to be modeled is ***block***. This command must be followed by the *(x,y)* coordinates of each vertex in order to create a closed polygon.

Within the main block, discontinuities that constitute the separation interfaces between one layer and another can be defined, in order to accurately construct the geological model. The command used to create these interfaces is ***crack***, which is used to create fractures between two points with different coordinates (Fig. 5.6).

However, the *crack* command only creates a segment of the interface; to create a continuous interface, given by the union of all these small cracks, it is necessary to repeat the *crack* command several times, ensuring that the coordinates of the starting point of the next crack coincide with the coordinates of the end point of the previous crack. The *crack* command can also be used to create faults.

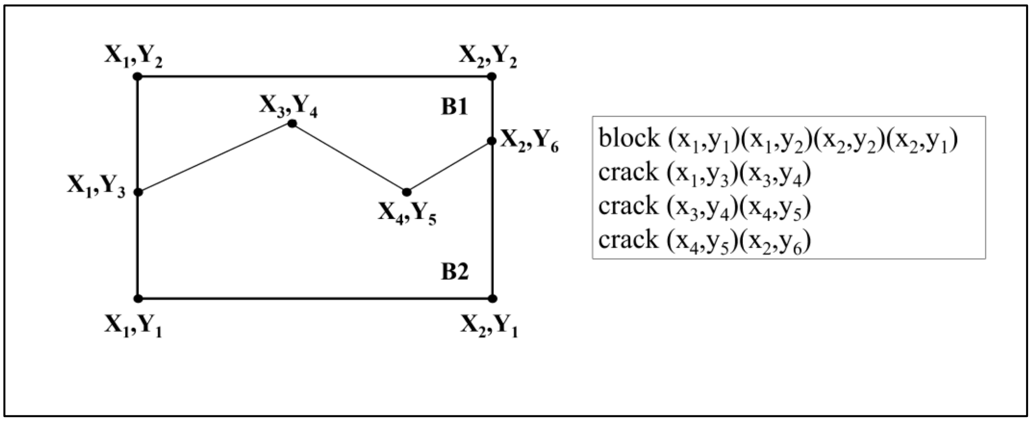

Fig. 5.6: Simplified sketch of a rectangular block containing an interface, generated by several cracks, which separates an upper block (B1) from a lower block (B2) and the correspondent FISH commands for implementing what is shown in figure.

Once all the interfaces have been identified to create the smaller blocks that divide the larger block and represent the layers of the model, these blocks must be made deformable. Making a block deformable means discretizing it into triangular zones, which can be done using the ***generate edge*** command followed by a number representing the size of the triangular zones; the thinner the layers to be discretized, the smaller the size of the triangular zones must be (Fig. 5.7). To make the software understand which block that command should be assigned to, ***range atblock (x,y)*** is entered after the command itself, where *(x,y)* represent the coordinates of a single point that falls within the block to which it refers, for example:

gen edge 3.5 range atblock (x1,y1)(x2,y2).

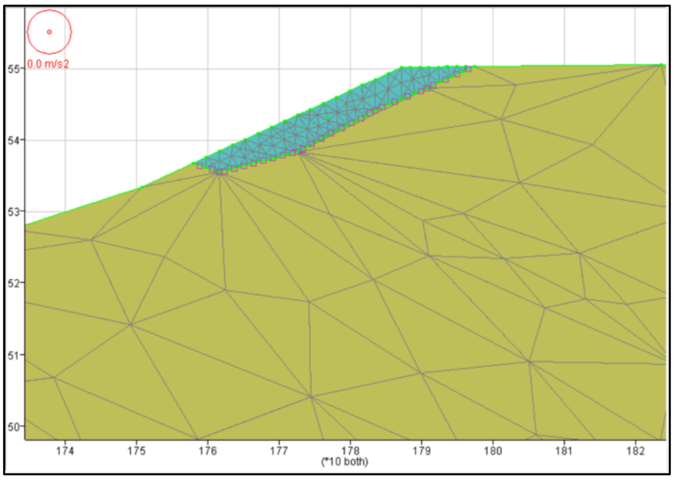

Fig. 5.7: Example of discretization into triangular finite-difference zones of two layers of different sizes. Note the different sizes of the triangular zones, as the upper layer (in light blue) is smaller than the lower one (in mustard yellow).

At this point, it is necessary to define the groups. Groups are sets of objects identified by a name. Each block can be "transformed" into a group so that it can be identified by a name. Groups cannot overlap each other, and an object belonging to one group cannot also belong to another.

To assign a name to all objects within a selected element, the ***group zone*** command is used as follows:

group zone 'group name' range atblock (x,y)

where the main command is followed by the name to be assigned to the group in quotation marks, followed by the command to identify the point that falls within that group.

This assignment must be repeated for all blocks, so that each smaller block within the main block has a name that identifies it: in this way, subsequent commands can refer to the group and no longer to the coordinates of one of its points.

After defining the groups, the properties of the materials that make up the different layers/blocks must be defined. In the case of the models created for estimating topographic amplification, an elastic constitutive model was assumed.

To associate a constitutive model already incorporated in the UDEC software, the ***zone model*** command must be used, which assigns local properties to each area of interest. With this command, the user can also assign models manually defined and that are not necessarily built in. The zone model command must be repeated for each group in this way:

zone model elastic density... bulk... shear... range group 'group name'

where the command must be followed by the name of the constitutive model (in this case ***elastic***), the properties and their values (for the elastic model, density, bulk modulus and Young's modulus must be specified), and the command *range group 'group name'* to specify which group those properties should be assigned to.

The properties of the joints must also be defined. To do this, the name *'layer contact'* is first assigned to the group of joints with the following command:

group joint 'layer contact'

so that all interfaces are called *'layer contact'*.

To add properties to these joints, the command used is:

joint model area jks...jkn...range group 'layer contact'

where jk_s and jk_n indicate the shear and normal stiffness of the discontinuities.

If new fractures are expected to be generated during the simulation, the properties of the new cracks must also be defined with the command:

set jconf joint model area jks...jkn…

After defining the geometric characteristics and materials present, the user has to move on to solving the static problem; indeed, before performing the dynamic analysis, it is necessary to achieve static equilibrium.

First, gravity must be applied using the command:

set grav 0 -10

which acts along the y-axis (therefore, it is set to 0 along the x-axis) and is negative as it acts downwards, while on UDEC – by convention – the positive sign is upwards.

Next, the velocity of the bottom (along the y-axis) and the sides (along the x-axis) is set to 0, so that there are no movements and/or unwanted collapses during the simulation. To do this, the following command is used:

boundary xvelocity 0 range…

boundary xvelocity 0 range…

boundary yvelocity 0 range…

where, after the range command, the coordinates that cover all the boundaries to be set must be entered. The command *boundary xvelocity* is repeated twice to fix both left and right sides of the model.

Next, damping must be set; in this case, automatic damping is used for the static analysis with the command:

damp auto.

Finally, the number of steps to be taken to reach static equilibrium must be set with the command ***solve ratio*** followed by the number indicating the equilibrium limit ratio: this ratio is automatically set to 10^{-5}, but it can be reduced to obtain greater precision.

An example of a script used to solve the static equilibrium problem is shown in Fig. 5.8.

```
;fix the bottom
set grav 0 -10
boundary xvelocity 0 range  -1 , 1   -1 , 396
boundary xvelocity 0 range  3646.293 , 3648.293   -1 , 602
boundary yvelocity 0 range  -1 , 3648.293   -1 , 1
damp auto
solve rat 1e-9
```

Fig. 5.8: Example of UDEC script showing all the commands used to achieve the limit equilibrium state.

After running this script, it is necessary to verify that static equilibrium has actually been achieved. To do this, a plot of the unbalanced force is created: if the curve (Fig. 5.9) tends towards zero, then this means that static equilibrium has been achieved.

Once static equilibrium has been achieved, the actual dynamic analysis can begin. First, the dynamic boundary conditions is applied by entering the ***boundary ffield*** command (free field option), and then – for both the x-axis and the y-axis – viscous boundaries are set with the ***boundary xvisc*** and ***boundary yvisc*** commands, followed by the elastic properties (bulk modulus, shear modulus and density) of the layer in contact with the bottom and its coordinates following the *range* command (Fig. 5.10).

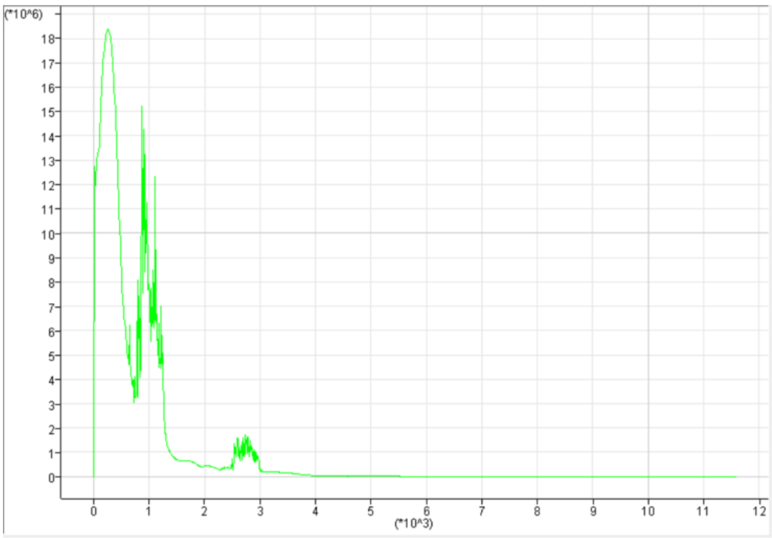

Fig. 5.9: Example of an unbalanced force plot useful for understanding whether static equilibrium has been achieved. The green curve tends towards zero, demonstrating that static equilibrium has been achieved.

```
;apply dynamic boundary condition
boundary ffield
boundary xvisc ff_bulk=6.77E9 ff_shear=2.2E9 ff_density=2.2E3 range -1 3648.293 -1 1
boundary yvisc ff_bulk=6.77E9 ff_shear=2.2E9 ff_density=2.2E3 range -1 3648.293 -1 1
```

Fig. 5.10: Example of script used for dynamic analysis in which free field conditions and viscous boundaries are set in both x and y directions.

At this point, it is necessary to apply the actual seismic input. First, with the ***reset time*** command, the user must specify that the application of the seismic waves is starting.

Before starting the dynamic analysis, the files containing the acceleration time series must be converted into velocity time history files. To do this, a specific utility, named "*Dynamic input wizard*" is available in the ITASCA software package. This tool allows to convert a specified file, indicating the format type (table, history, PEER), the type of ground motion (acceleration or velocity) and the input units (g, cm/s², gal, m/s² and ft/s²). By selecting the type of file to be produced (acceleration, velocity, displacement, amplitude and response spectrum, and Arias intensity), the name of the file to be produced, and the file format (table or history), it is possible to perform the desired conversion. In this case, by selecting as input a file containing the acceleration history in cm/s², a velocity history file in m/s was produced for each of the seven accelerograms chosen as seismic input.

The basic command used to tell the software where to read the seismic input is as follows:

bou hread 2 filenamevelocity.txt.

This command applies the contents of the *filenamevelocity.txt* as seismic input. The number that follows the *bou hread* command indicates a particular history number with which the file is associated.

An example of velocity file is shown in Fig. 5.11, whose structure is as follows:

- first line: begins with a semicolon to indicate that it is a comment used to identify the accelerogram origin;
- second line: specifies the number of data points contained in the file and the sampling interval;
- third line and onward: contain the actual velocity values.

```
1  ;Friuli 1976 - M = 6.0
2  3376, 0.005
3  0.0000000000e+00
4  3.0713074250e-05
5  1.2292792700e-04
6  2.4573416375e-04
7  3.6830690825e-04
8  4.9060567175e-04
9  6.1259089075e-04
10 7.3422398950e-04
11 8.5546735500e-04
12 9.7628433750e-04
13 1.0966392623e-03
14 1.2164974298e-03
15 1.3358251288e-03
16 1.4545895980e-03
17 1.5727590515e-03
18 1.6903026788e-03
19 1.8071905195e-03
20 1.9233933888e-03
21 2.0388830645e-03
22 2.1536325750e-03
23 2.2676162990e-03
24 2.3808097407e-03
25 2.4931894170e-03
26 2.6047330828e-03
27 2.7154196685e-03
```

Fig. 5.11: Example of a file containing velocity data, which must be applied as seismic input to the base of the model.

Next, the following command is specified:

bound stress 0 -σ_S 0 hist 2 range ....

where *hist 2* and *range* have the same meaning as in the previous commands. This command is used to apply the stress, expressed through the components σ_{xx}, σ_{xy} and σ_{yy}. To apply a seismic input, the shear stress σ_{xy} must be activated, which must be negative by convention.

Following the equation [5.10], the value σ_S of the shear stress can be obtained from:

$$\sigma_S = 2(\rho C_S) \qquad [5.28]$$

where ρ is the density and C_S the shear-wave velocity of the most rigid layer in contact with the bottom. This parameter represents a multiplier of the velocity history values in order to convert the velocity record into a stress record, thus allowing it to be applied to a quiet boundary.

At this point, Rayleigh damping must be applied using the command:

$$damp\ \xi\ f_{min}\ mass\ stiff$$

where both the damping ratio and the center frequency must be specified, as explained in Section 5.1.1.

Next, mass scaling, which sets the masses of zones and blocks, must be disabled with the command ***mscale off***.

Since the internal calculation of the time step is conditioned by damping proportional to stiffness, and since in the case of very strong block deformations instability situations could occur, the ***fraction*** command can be used to manually reduce the time step to prevent this from happening.

After setting everything up, it is necessary to specify what to obtain and where to obtain it. Specifically, for this study, the goal is to obtain the accelerogram at specific points on the surface of the model. To do this, the following commands are used:

hist xacc x,y

hist yacc x,y.

The software will then return both x and y components of the accelerogram at the points specified by the *x,y* coordinates. Obviously, this can be obtained for all the desired points, simply by repeating these commands for each pair of *x,y* coordinates.

After listing all the points at which to obtain the accelerogram (bearing in mind that it is also possible to obtain the velocity and the displacement), the time step for performing the dynamic analysis must be specified, which indicates the time required to absorb all the energy needed to reach equilibrium, using the command ***cycle time*** followed by the number of seconds chosen.

As a final command, the software needs the specification of the output file in which the output accelerogram is to be written. To do this, for each site indicated in the previous section, the user must use the command:

history write 1 1

history write 2 2

so that the file can be easily associated with the point on the surface. The first number in this command is a sequential number and represents the number of the file in which the output referred to the second number is saved. Two numbers are used for each point, the first referring to the x component and the second referring to the y component; for the purposes of this thesis, only the x component was used to calculate the Arias intensity.

5.2 Construction of the 2D section of the site model

For the creation of 2D models of the site response, a section from the municipality of Bovino was chosen, as this is one of the municipalities for which the greatest amount of data is available, due to the investigations conducted on the "Pianello landslide" (see Section 4.3.1).

A section that crosses this landslide (along the direction of maximum slope) and also reaches the other side of the hill, where the landslide is not present, was selected: in this way, it is possible to construct a topographic profile to evaluate the topographic effect on the amplification factor.

The trace of the section (in green) is shown in Fig. 5.12; along the trace of this section, the positions of the surveys (boreholes and ERT traces) conducted in the municipality of Bovino close to the selected section are shown. Data from these surveys can support the reconstruction of a geological model.

Green pointers indicate the intersection of the modeled section with landslide crown and toe.

Figure 5.13 shows a geological map of the Bovino area around the selected section obtained from MS1 studies (Troncone et al., 2024). The section crosses different materials:

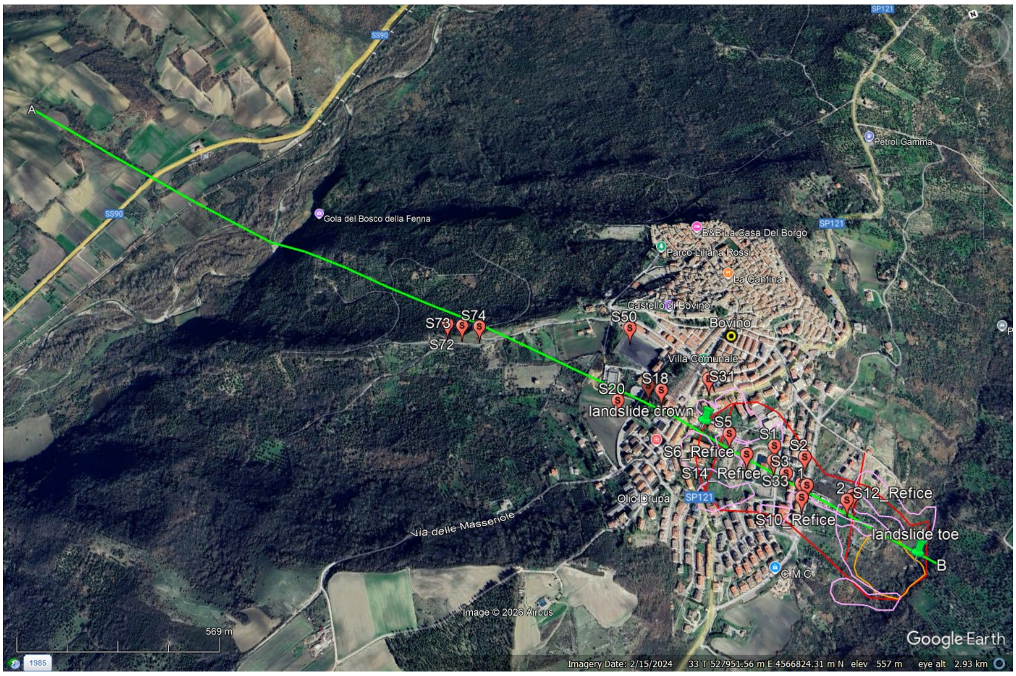

Fig. 5.12: Location of the Pianello landslide complex affecting the Bovino built-up area, with the trace (in green) of the section chosen for the 2D site response modeling. The green pointers mark the intersections with the crown and toe of the main landslide body, whose boundary is outlined in red. The red pointers indicate the position of the boreholes, while the ERT profiles are marked by red straight lines.

- **ANTHROPIC DEPOSITS** (Holocene): consisting of clasts of various sizes and types in a predominantly sandy and sandy-silty matrix, alternating with silty clay layers. The thickness can range from a minimum of 3 m to a maximum of 10 m;
- **LANDSLIDE DEBRIS** (Holocene): mostly clayey, which can reach a thickness of 50 m in some places;

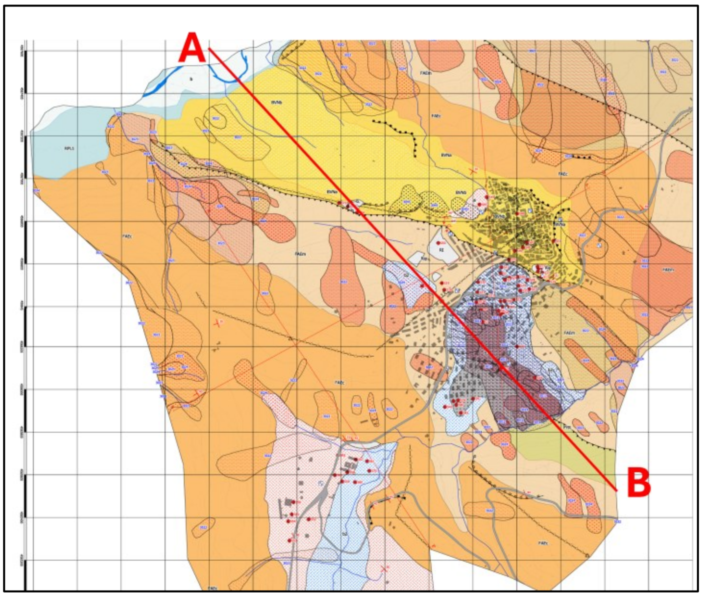

Fig. 5.13: Geological map of Bovino area around the trace of the section modeled using UDEC.

- **b-RECENT ALLUVIAL DEPOSITS** (Holocene): consisting of gravel and sand in evolution in riverbed, with a thickness varying from 3 m to 5 m;
- **b_2-COLLUVIAL ELUVIAL DEPOSITS** (Holocene): consisting of sandy-clayey silt with clasts generated by the alteration of the substrate. This is a mixture of silt, yellow-gray sand, carbonate pebbles and limestone fragments, with a thickness ranging from 2 to 8 m;
- **BVN_b-CLAY AND SAND FROM VALLONE MERIDIANO** (Piacenzian): these are layers and banks of silty clay alternating with weakly cemented grayish sandy layers, with a maximum thickness of about 80 m;
- **BVN_a-SANDSTONES AND CONGLOMERATES OF CASTELLO SCHIAVO** (Piacenzian): these are conglomerates alternating with medium-coarse sandstones. The texture ranges from grain- to matrix-supported where the matrix consists of calcareous sand. The maximum thickness reaches 120 m;

- **TPC-CLAYEY MARLS OF TOPPO CAPUANA** (Tortonian): silty clays alternating with gray marls, with a maximum thickness of 100 m;
- **FAE$_c$-CALCAREOUS MARLY MEMBER OF THE FAETO FLYSCH** (Upper Miocene): calcarenites alternating with calcilutite and gray-greenish marls. The layers are highly fractured, and the maximum thickness can be hundreds of meters;
- **FAE$_m$-MARLY MEMBER OF THE FAETO FLYSCH** (Lower Miocene): whitish marls alternating with greenish clays and layers of calcarenite. The thickness can be in the order of hundreds of meters;
- **FYR-RED FLYSCH** (Cretaceous-Aquitanian): gray, green and red claystones alternating with calcarenites and calcilutites, with a maximum thickness of 100 m.

Fig. 5.14 shows the topographic profile of the section, indicating the location of the various surveys used to reconstruct the geological model.

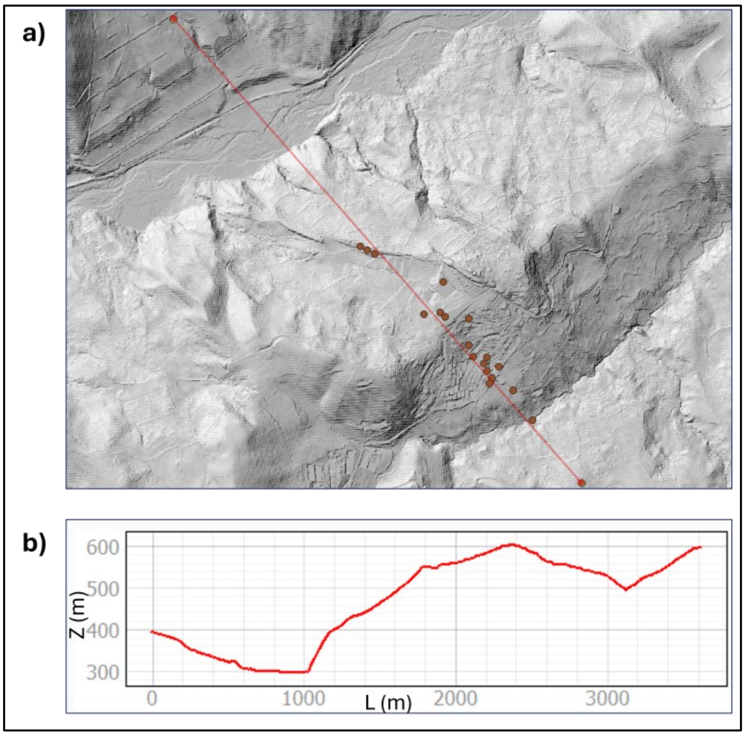

*Fig. 5.14: (**a**) Digital elevation model of the study area on which the trace of the section chosen for modeling and the location of nearby boreholes are reported; (**b**) topographic profile of the selected section.*

5.3 Topographic amplification factor computation with 2D modeling

The 2D modeling of the site response was performed to evaluate the purely topographic effect in the calculation of the amplification factor. In this regard, the section shown in Fig. 5.14 was filled with the most rigid material, namely FAE_c.

By constructing the block that simulates the topography, the model shown in Fig. 5.15 was obtained. The block obtained was divided into 24968 triangular meshes in order to make it deformable, and it was assigned the following characteristics: density = 2200 Kg/m^3, $K = 6.77 \cdot 10^9$ Pa, $G = 2.2 \cdot 10^9$ Pa.

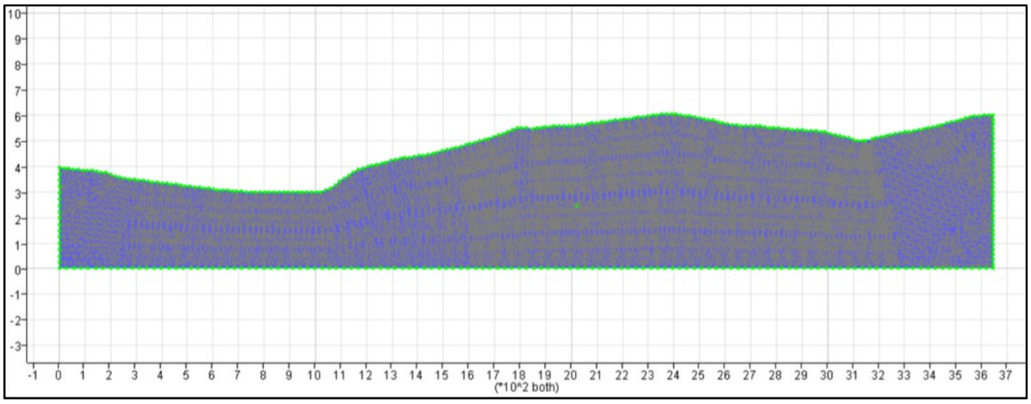

Fig. 5.15: Topographic model of the Bovino section showing the mesh of triangular cells into which the block is divided to make it deformable.

After reaching static equilibrium, the dynamic analysis was performed. First the free field condition and the viscous boundaries were applied. Then, the analysis was carried out by applying as seismic input – one at a time – the seven accelerograms used to calculate the amplification factors, converted in terms of velocity, using for the coefficient σ_s a value of $-4.4 \cdot 10^6$ Kg·m^{-2}·s^{-1} for FAE_c (obtained using eq. 5.28).

After setting a damping value (0.02 and 2.5 for damping ratio and central frequency, respectively) and specifying the points at which the output was to be obtained, as well as the number of seconds in the cycle (15 s), the run was performed, generating an output file for each point at which the result was to be obtained. In this specific case, the file containing the surface accelerometer series was produced at the location of sites HV7n, HV13n, HV14n, HV15n and HV29n (in the same points where the *AF* values were obtained for 1D modeling).

For each specified point, two files are produced, one containing the x component (files 1, 3, 5, 7 and 9) and the other containing the y component (files 2, 4, 6, 8 and 10) of the output acceleration. The points at which the calculation was performed are shown in Fig. 5.16.

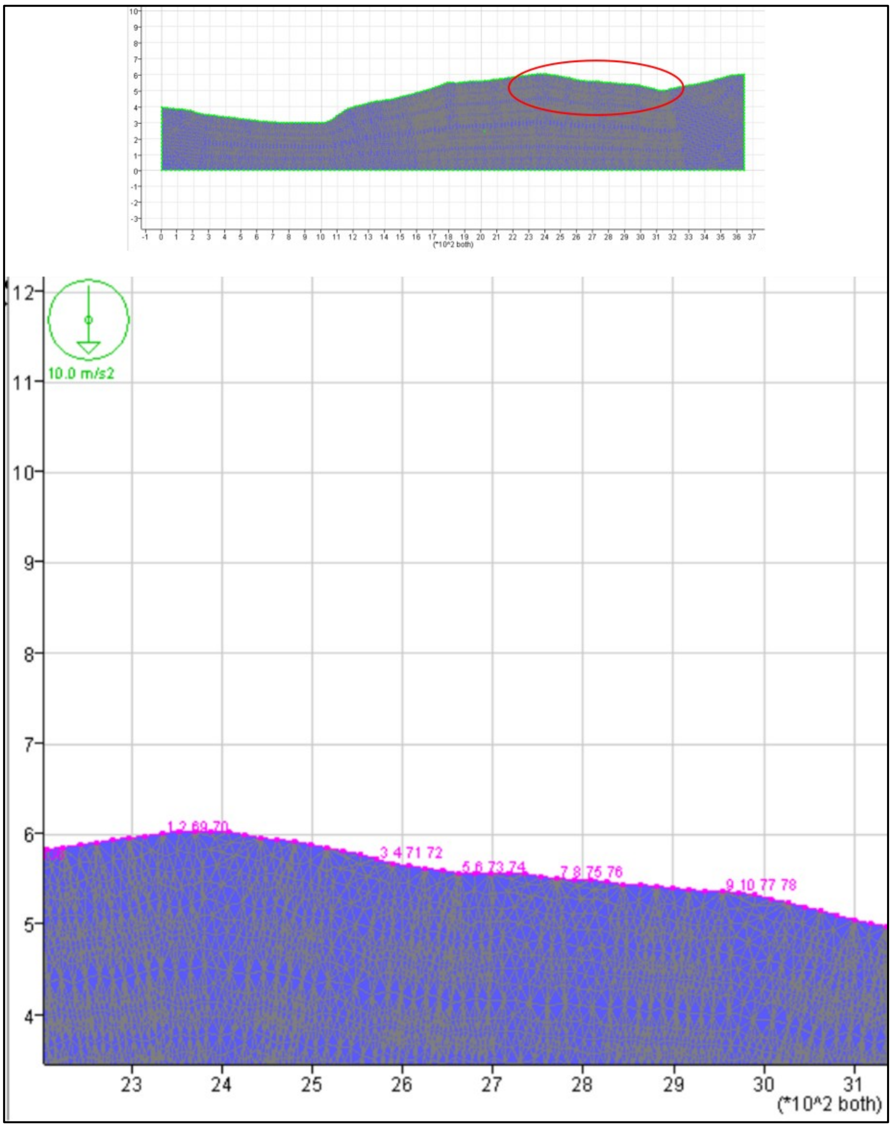

Fig. 5.16: Zoom in on the points where the acceleration time series calculation was performed on the surface, considering the topographic effect only. The points are 1-2 for HV7n, 3-4 for HV13n, 5-6 for HV14n, 7-8 for HV15n and 9-10 for HV29n. At the top left, there is a green indication of the gravity applied to the model to achieve static equilibrium and then perform the dynamic analysis.

To calculate the amplification factor in terms of Arias intensity, the x component of the accelerogram was used, as representative of the horizontal component of seismic ground motion. First, using formula [2.1], the Arias intensity value was calculated for each point of interest and for each of the seven accelerograms used as seismic input. Then, the amplification factor [4.11] was obtained for each accelerogram and, as in the one-dimensional case, for each point the average and standard deviation of the seven values obtained were calculated. Table 5.1 shows the results.

Table 5.1: Mean amplification factors in terms of Arias intensity and relative standard deviations obtained for the topographic effect alone by performing 2D modeling of the site response with UDEC.

Site	Mean AF	St. Dev.
HV7n	1.312	0.721
HV13n	0.908	0.491
HV14n	0.902	0.494
HV15n	1.598	0.956
HV29n	1.388	0.789

As can be seen from the results, the amplification factor values appear to be below 2 in all cases, reaching a maximum of 1.6 at site HV15n, showing that the topographical effect is very mild in the overall calculation of the amplification factor. Indeed, the topography relief is rather smooth, so it does not have a significant effect on the evaluation of the amplification factor. This confirms the initial hypothesis of giving greater importance to the stratigraphic effect.

6. DISCUSSION AND CONCLUSION

6.1 General results

The main objective of this thesis was to develop a simple and expeditious procedure for determining the susceptibility of slopes to earthquake-induced landslides at a regional scale, in order to highlight the most critical areas where further investigations may be necessary at a local scale.

With this objective, a probabilistic procedure for estimating slope resistance demand proposed by Del Gaudio et al. (2003) was revisited. Based on the Newmark (1965) model, this procedure aimed at determining the critical acceleration a_c that a slope should have to keep the probability that seismicity affecting a region causes the exceedance of a critical threshold of Newmark's displacement D_N within a prefixed level.

The main novelty introduced here in the new implementation of this procedure lies in the different way the site response is accounted for in the estimation of the resistance demand. Previously it had been introduced in a roughly approximated form using site factors included in ground motion prediction equations, which depend on either a qualitative classifications of soil type (e.g., stiff, shallow and deep soil), as in the equation proposed by Sabetta and Pugliese (1996) or, more recently, average S-wave velocity in the first 30 m of subsoil (V_{S30}), as in the equation proposed by Sabetta et al. (2021). In this new tested procedure, the site response is introduced by means of site-specific amplification factors expressed in terms of Arias intensity (I_A). These amplification factors are estimated using a procedure based on a site response modeling that considers only the lithostratigraphic effect, starting from the analysis of ambient noise recordings made available by seismic microzonation studies.

This procedure was first tested in the Caramanico Terme area (Abruzzo Region, Central Italy) taking advantage of the permanent accelerometer network installed there in 2002. This network made it possible to compare the amplification factor calculated using the tested procedure with that measured directly from accelerometer recordings acquired for the same events on both bedrock and landslide-prone slopes.

This test showed that:

- the procedure developed can provide estimates of the amplification factor with an acceptable approximation for a preliminary regional-scale assessment of the slope dynamic response, since errors remain mostly within 50%;
- the mean values and standard deviations of the amplification factors estimated using the tested procedure are generally in good agreement with those measured directly from the accelerometer recordings, thus these estimates can be used for probabilistic estimates of the site effect on the slope resistance demand;
- to obtain this agreement it is, however, necessary to accurately choose the accelerometer recordings used as seismic inputs for site response modeling; these recordings should have, as far as possible, a uniform and homogeneous average spectrum, in order to avoid anomalous results due to a higher concentration of energy on a limited frequency band;
- a contraindication arises where the site response is strongly influenced by anisotropy of the mechanical properties of the slope materials – for examples due to the intense fracture/fissure systems affecting the slope itself – causing strong directional variability of site response. If not taken into account, this phenomenon leads to an underestimation of the amplification factors. However, its occurrence can be recognized from the results of ambient noise analysis, which correspondingly show a strong directional variation of Rayleigh wave ellipticity (cf. Del Gaudio et al., 2019).

After verifying its validity, the procedure was applied to 19 sites of four municipalities in Daunia (Accadia, Bovino, Carlantino and Volturino), obtaining the average values and standard deviations of the amplification factors at each site. These site-specific factors were then incorporated into the calculation of slope resistance demand, resulting in a significant increase compared to that obtained by accounting for the site effect using V_{S30}-based empirical relationships.

As additional refinement of the procedure, in order to calculate the resistance demand of slopes on a specific area of Italy, a new empirical relationship predicting D_N as a function of I_A and a_c was calibrated specifically for the Daunia area, using a regression dataset consisting of the most representative accelerograms of the seismic hazard of Daunia itself, distributed uniformly over a wide range of Arias intensity values.

A validation test carried out on two datasets different from the regression one made it possible to compare the predictive capability of the new Daunia-specific equation with that of other equations calibrated for other regions with the same functional forms or with more complex ones including additional terms and/or factors. This test showed that the relationship calibrated specifically for Daunia region with the simplest functional form has a better predictive capability than all the other relationships tested. The use of equations with more complex functional forms, even recalibrated on the Daunia dataset, does not improve the predictive performances on the validation datasets. Despite a slightly lower standard error resulting from regression, probably due to the increase of the regression dataset fitting allowed by the presence of additional terms, the root mean square of the errors observed for estimations on other data was not lower than that of the new simplest relationship.

However, certain limitations have emerged regarding the effectiveness of simple D_N-I_A-a_c empirical relationships, in relation to the neglect of potentially relevant variables. Tests showed that significant prediction errors can result when the frequency content of an accelerogram differs significantly from that of the accelerogram dataset used to calibrate the relationships. Therefore, special attention should be paid to the selection of the most relevant seismic scenarios to be included in the regression dataset, since the frequency content of the selected recordings may depend on this choice.

The test carried out in this thesis used accelerograms selected as seismic inputs for site response modeling in seismic microzonation. These are suitable for studying the seismic response of ordinary engineering structures, which have resonance periods of 0.1-1 s, with greater weight assigned to the shorter periods. However, depending on the slope characteristics, the range of periods most affecting slope stability may not coincide entirely with this range. Therefore, additional tests should be carried out using different inputs, focused on different period ranges.

The use of different empirical relationships for estimating D_N does not appear to excessively affect the estimates of the resistance demand obtained. What does bring about significant changes, instead, is the introduction of a new way of representing the site effect. For a comparison, the resistance demand was recalculated alternatively in two ways:

- on the one hand, the site factor *FS* depending on V_{S30} (according to the relationship of Sabetta et al., 2021), was included into the ground motion prediction equation at the stage of calculating the probability of different possible values of Arias intensity expected at a site. This is then used as input of predictive equations to estimate at that site the probability of D_N exceeding critical thresholds. Such an approach allows the adoption of a single estimate of the site effect for the entire region analyzed (e.g., corresponding to the maximum expected effect following a precautionary approach), without differentiating among local conditions;
- on the other hand, site-specific amplification factors *AF*, expressed in terms of Arias intensity, are calculated using 1D modeling of the site response. These factors are used to modify the probability of I_A values expected for reference site conditions, also taking into account the uncertainty affecting the *AF* estimates, which is expressed through the combination of its mean value and standard deviation obtained for the specific site.

Compared to standard site conditions, the estimated resistance demand appears significantly higher with the introduction of these factors. Adopting the first of the two methods, the *FS* corresponding to the minimum V_{S30} measured in the study region (according to a precautionary approach) results in a generalized doubling of the slope resistance demand with respect to unamplified site conditions. Following the second method, the resulting amplification factors *AF* present a considerable variability of amplification values. In few cases amplification is similar to that obtained with the first method, but mostly is significantly larger, up to four times. This leads the estimated resistance demand value based on calculated site-specific *AF* values to be greater than that obtained with a V_{S30}-based approach almost across the entire study area by a factor of up to 2.8.

The result obtained highlights how the use of a site factor based roughly on a parameter such as the V_{S30} is not able to fully represent the site effect, and using only the latter could lead to a significant underestimation of the resistance demand values compared to those that would be obtained by incorporating a site-specific amplification factor appropriately estimated considering the lithostratigraphic amplification effects.

After exploring the influence of lithostratigraphic effects using 1D site response modeling, 2D modeling was performed to assess the entity of the error introduced by neglecting the effect of topographic amplification.

By performing a dynamic analysis of the slope response on a single section modeled to reflect the actual topography, a seismic input was applied at the base to obtain a surface accelerogram (like in 1D modeling). By calculating the amplification factor in terms of Arias intensity at some of the 19 sites mentioned above, it was found to be at most 1.60: this means that, at least at the analyzed site, the pure topographic effect is negligible, as it generates an increase in shaking energy of no more than 60%. This justified the choice of prioritizing 1D modeling of the site response – based only on the lithostratigraphic effect – in the procedure for calculating the amplification factor to be introduced in the estimation of the slope resistance demand for the present case study.

It should be noted that this can depend on the presence of a relatively not rugged morphology in the Daunia Mountains. However, conditions could occur that result in topographic effects with amplification factors higher than 2.

For instance, Garcia-Perez et al. (2021) evaluated the topographic effects in northern Chile in the 0.1-3.5 Hz frequency range, considering two shocks of M_W 4.5 and 5.4 in the sequence of the Iquique earthquake (M_W=8.1-April 1, 2014). The amplification factor was calculated by comparing the total energy obtained from the velocity seismograms for the model with topography and that obtained for the flat model. The highest value obtained was 2.2 (120% amplification), obtained near a 1 km high coastal cliff. However, amplification factors of up to 3.6 were observed in the 0.5-1 Hz frequency range in the presence of secondary waves caused by the irregularities in the topographic surface which, by prolonging the duration of the ground motion and increasing the amplitude of the incident waves, increase the total energy of the seismic waveforms.

Consequently, it would be useful to carry out further tests in different topographic conditions characterized by more pronounced ridges, to observe the influence of the topographic effect in such situations.

6.2 Future perspectives

In light of the results obtained in this study, some future developments could be envisaged.

1) First of all, this strategy could be applied not only to long-term probabilistic assessments (as done in this work, considering a 50-years interval), but to specific seismic scenarios.
   In the case of an event with a magnitude *M* occurring at a distance *R*, having a GIS-based map of slope critical accelerations, it would be

possible to quickly localize slope zones where that event is most likely to have triggered landslides: e.g., by calculating the critical acceleration for a slope to have a 50% probability of being subject to a Newmark's displacement exceeding a critical threshold and comparing it with the actual critical acceleration of the slopes, it would be possible to identify those with a higher probability of having failed as a result of the earthquake. Such a procedure could be applied in seismic emergency management or preventively, to improve preparedness for specific seismic scenarios.

2) Considering the possible influence of the frequency content of the seismic shaking on the predictive performance of the D_N-I_A-a_c empirical relationship, relationships that take into account the different frequency content by using an additional parameter (e.g., the seismogram central period, derived as a weighted average based on spectral power) could be tested. This entails additional difficulties for a probabilistic analysis, because it requires the definition of matrices of probabilities of co-occurrence of Arias intensity (I_A) and central wave period (T) values, for all the possible I_A-T combinations expected for each combination of magnitude and distance of events that can destabilize slopes.

   Creating such a matrix will require the collection of a large dataset of accelerograms; despite the degree of complexity required to do this, it might be useful to perform these additional tests because the frequency content could alter the predictive power of the relationship and thus modify the effectiveness of the relationship itself.

3) Additional tests of 2D/3D modeling of the site response could be performed to verify the relevance of the topographic amplification and to evaluate the combined effect of lithostratigraphic and topographic amplification. These tests could verify how the three-dimensionality and different orientation of the interfaces between the different layers could modify the amplification factor estimates, which in turn would modify the values of the slope resistance demand.

Modeling different morphological conditions would help us to understand if, and when, topography can produce significant amplification effects, which must necessarily be taken into account together with lithostratigraphic effects.
These tests could be carried out either on real sections or using virtual test beds, such as the RETURNLAND digital platform designed within the VS2 spoke of the PNRR-RETURN project, which funded the present PhD project. This platform is intended as an "imaginary" place where different morphological situations, which really exist, are combined like a mosaic to form a single large heterogeneous territory.

Depending on the results of these tests, in cases where topographic amplification should prove to be significant, empirical relationships that provide estimates of topographic amplification factors based on morphological parameters could be tested. Examples of such relationships are reported by several authors.

Some schedules were created to assess the topographic effect within the context of the guidelines provided for the Seismic Microzonation in Italy (SM Working Group, 2015). Using different combinations of geomorphological parameters (e.g., height and inclination of the rocky escarpment), these schedules provide amplification factor values in terms of acceleration response spectra (T=0.1-0.5s), with values ranging from 1.1 to 1.3.

Rai et al. (2016) proposed a topographic amplification correction factor to be incorporated into GMPEs to account for topographic effects on ground motion. To do this, they used small- and medium-magnitude earthquakes and extrapolated an empirical model with a multilinear functional form. This model was based on relative elevation, derived by taking the difference between the elevation at the center of each cell of a raster map and the average elevation over cells included within a specified neighborhood of that cell. This approach yielded amplification factors in terms of *PSA* (pseudo-spectral acceleration) of up to 1.2 for periods equal to 0.3 and 1s.

Molina et al. (2019) also developed an empirical model to assess the topographic effect, particularly for ridges and hills, that was period-dependent, yielding greater amplifications. First, a linear relationship based on *PGA* was established, and then five different classes of shape ratio (*H/L*) were considered. Considering a period range between 0.065 and 3.91s, the amplification factor values reached a maximum of 3.04, decreasing as the period increased, though with a large dispersion.

The application of approaches of these types to the calculation of the slope resistance demand according to the procedure outlined in this thesis would, however, require calibrating the empirical relationships in terms of Arias intensity and conducting further tests to verify their relevance for the assessment of slope susceptibility to seismic failures.

4) Using software capable of modeling both slope dynamic response to seismic shaking and the resulting evolution of slope failures could be useful for verifying or redefining Newmark's critical displacement thresholds for landslide seismic triggering reported in literature (as 2 cm for rock slopes and 10 cm for earth slopes, as proposed by Wilson and Keefer, 1985).

   Applying seismic inputs consisting of different accelerograms at the base of slope models having known critical accelerations and calculating both the Newmark's displacement from the resulting accelerograms and the effect of seismic shaking on slope destabilization, would allow to verify the D_N values corresponding to high probability of landslide triggering.

   The ITASCA software could be used for this purpose by implementing this kind of modeling on the virtual test bed of the RETURNLAND digital platform mentioned above; this digital platform offers the possibility of performing tests aimed at reaching more general conclusions, compared to modeling based on a single real region.

ACKNOWLEDGMENTS

I gratefully acknowledge the Civil Protection Department of the Apulia Region for providing access to the results of investigations conducted within the seismic microzonation studies, as well as Dr. Vincenzo Troncone and the ASSET group for their contribution to data availability.

I extend my sincere gratitude to Prof. Hans-Balder Havenith and Dr. Valmy Dorival for their guidance and support in 2D numerical modeling during my research stay at the University of Liège, Belgium.

I also thank Dr. Brunella Giacoia for her valuable assistance in the management and interpretation of seismic microzonation data during the initial phase of this work.

I further acknowledge Professors Salvatore Martino, Francesca Bozzano, Domenico Calcaterra and Diego Di Martire, coordinators of Spoke VS2 within the RETURN–PNRR project, for sharing the project results, and Dr. Rosa Colacicco for her support in illustrating the RETURNLAND digital platform.

REFERENCES

Aimar M., Ciancimino A., Foti S. (2024). Influence of the effective strain ratio on equivalent linear ground response simulations. 8th International Conference on Earthquake Geotechnical Engineering, Japanese Geotechnical Society Special Publication, 10 (28): 1047–1052. https://doi.org/10.3208/jgssp.v10.OS-17-04

Ashford S.A., Sitar N., Lysmer J., Deng N. (1997). Topographic effects on the seismic response of steep slopes. Bull Seism Soc Am, 7(3): 701–709. https://doi.org/10.1785/BSSA0870030701

Ardizzone F., Bucci F., Cardinali M., Fiorucci F., Pisano L., Santangelo M., Zumpano V. (2023). Geomorphological landslide inventory map of the Daunia Apennines, sourhern Italy. Earth Syst., Sci. Data, 15: 753–767. https://doi.org/10.5194/essd-15-753-2023

Arias A. (1970). A measure of earthquake intensity, in Seismic Design for Nuclear Power Plants, R. J. Hansen (ed), MIT Press, Cambridge, Massachusetts, pp 438–483.

ASSET-Puglia (Agenzia regionale Strategica per lo Sviluppo Ecosostenibile del Territorio) (2023a). Relazione Illustrativa della Microzonazione Sismica di primo livello nel comune di Accadia (Regione Puglia).

ASSET-Puglia (Agenzia regionale Strategica per lo Sviluppo Ecosostenibile del Territorio) (2023b). Relazione Illustrativa della Microzonazione Sismica di primo livello nel comune di Carlantino (Regione Puglia). https://protezionecivile.regione.puglia.it/documents/3171874/3287060/Carlantino.zip

ASSET-Puglia (Agenzia regionale Strategica per lo Sviluppo Ecosostenibile del Territorio) (2023c). Relazione Illustrativa della Microzonazione Sismica di primo livello nel comune di Volturino (Regione Puglia).

https://www.regione.puglia.it/documents/3171874/3287060/Volturino.zip/af350f47-e166-3360-bdb5-64e1963bee4c?t=1689866468713

Baise L.G., Kaklamanos J., Berry B.M., Thompson E.M. (2016). Soil amplification with a strong impedance contrast: Boston, Massachusetts. Engineering Geology, 202: 1–13. https://doi.org/10.1016/j.enggeo.2015.12.016

Baratta M. (1901), I terremoti d'Italia. Torino 1901, 950 pp.

Bates D., Mächler M., Bolker B., Walker S. (2015). Fitting linear mixed-effects models using lme4. J Stat Softw, 67(1): 1–48.

Bathe K.J., Wilson E.L. (1976). Numerical Methods in Finite Element Analysis. Englewood Cliffs, New Jersey: Prentice-Hall Inc.

Bender B., Perkins D.M. (1987). SEISRISK III: a computer program for seismic hazard estimation, U.S. Geol. Surv. Bull., 1772, 48.

Biggs J.M (1974). Introduction to Structural Dynamics. New York: McGraw-Hill.

Bonnefoy-Claudet S., Cotton F., Bard, P.Y. (2006). The nature of seismic noise wavefield and its implications for site effects studies – a literature review. Earth-Sci. Rev., 79: 205–227.

Boschi E., Guidoboni E., Ferrari G., Valensise G., Gasperini P. (1997). Catalogo dei forti terremoti in Italia dal 461 a.C. al 1990. ING-SGA, Bologna.

Boschi E., Guidoboni E., Ferrari G., Mariotti D., Valensise G., Gasperini P. (2000). Catalogue of strong Italian earthquakes from 461 B.C. to 1997. Introductory texts and CD-ROM, Version 3 of the Catalogo dei forti terremoti in Italia. Annali di Geofisica, 43(4): 609–868.

Bozzano F., Lenti L., Martino S., Paciello A., Scarascia Mugnozza G. (2008). Self-excitation process due to local seismic amplification responsible for the reactivation of the Salcito landslide (Italy) on 31 October 2002. Journal of Geophysical Research, vol 113.

Bouckovalas G.D., Papadimitriou A.G. (2005). Numerical evaluation of slope topography effects on seismic ground motion. Soil Dyn Earthq Eng, 25(7): 547–558.
https://doi.org/10.1016/j.soildyn.2004.11.008

Bourdeau C., Havenith H.B. (2008). Site effects modelling applied to the slope affected by the Suusamyr earthquake (Kyrgyzstan, 1992). Eng Geol, 97: 126–145.

Brozzetti, F., Boncio, P., Lavecchia, G., and Pace, B. (2009). Present activity and seismogenic potential of a low-angle normal fault system (Città di Castello, Italy): Constraints from surface geology, seismic reflection data and seismicity. Tectonophysics, 463: 31–46. https://doi.org/10.1016/j.tecto.2008.09.023

Brunetti M., Buffoni L., Mangianti F., Maugeri M., Nanni T. (2004). Temperature, precipitation and extreme events during the last century in Italy. Global and Plan etary Change, 40: 141–149.

Camassi R., Stucchi M. (1997). A parametric catalogue of damaging earthquakes in the Italian area, http://emidius.mi.ingv.it/NT/ home.html, GNDT (technical report), Version NT4.1.1.

Casero R., Roure F., Endignoux L., Moretti I., Muller C., Sage L., Vially R. (1988). Neogene geodinamic evolution of the southern Apennines. Mem Soc Geol It, 41: 109–120.

Chousianitis, K., V. Del Gaudio, I. Kalogeras, and A. Ganas (2014). Predictive model of Arias intensity and Newmark displacement for regional scale evaluation of earthquake-induced landslide hazard in Greece. Soil Dyn. Earthq. Eng., 65: 11–29.

Chousianitis K., Del Gaudio V., Sabatakakis N., Kavoura K., Drakatos G., Bathrellos G. D., Skilodimou H. D. (2016). Assessment of Earthquake- Induced Landslide Hazard in Greece: From Arias Intensity to Spatial Distribution of

Slope Resistance Demand. Bulletin of the Seismological Society of America, Vol. 106, No. 1, pp. 174–188.

Ciaranfi N., Gallicchio S., Loiacono F. (2011). Note illustrative della CARTA GEOLOGICA D'ITALIA alla scala 1:50.000, foglio 421, ASCOLI SATRIANO. ISPRA, Servizio Geologico D'Italia.

Ciarcia S., Di Nocera S., Matano F., Torre M. (2003). Evoluzione tettono-sedimentaria e paleogeografica dei depocentri 'wedge-top' nell'ambito del 'foreland basin system' pliocenico dell'Appennino meridionale (settore Irpino–Dauno). Bollettino della Società Geologica Italiana, 122: 117–137.

Coccia S., Del Gaudio V., Venisti N., Wasowski J. (2010). Application of Refraction Microtremor (ReMi) technique for determination of 1-D shear wave velocity in a landslide area. J Appl Geophys, 71: 71–89. https://doi.org/10.1016/j.jappgeo.2010.05.001

Cotecchia F., Vitone C., Santaloia F., Pedone G., Bottiglieri O. (2015). Slope instability processes in intensely fissured clays: case histories in the southern Apennines. Landslides 12: 877–893. https://doi.org/10.1007/s10346-014-0516-7

Cotecchia F., Vitone C., Petti R., Soriano I., Santaloia F., Lollino P. (2016). Slow landslides in urbanised clayey slopes: An emblematic case from south of Italy. Landslides and Engineered Slopes. Experience, Theory and Practice – Aversa et al (Eds.). Associazione Geotecnica Italiana, Rome, Italy, ISBN 978-1-138-02988-0.

Cotecchia F., Santaloia F., Tagarelli V. (2020). Towards A Geo-Hydro-Mechanical Characterization of Land slide Classes: Preliminary Results. Appl. Sci., 10, 7960. https://doi.org/10.3390/app10227960

Crostella, A., L. Vezzani (1964). La geologia dell'Appennino Foggiano, Bollettino della Società Geologica Italiana, 83: 121–141.

Cundall P.A. (1976). Explicit Finite Difference Methods in Geomechanics. Numerical Methods in Engineering (Proceedings of the EF Conference on Numerical Methods in Geomechanics, Blacksburg, Virginia, 1: 132–150.

Crozier M.J. 1986. Landslides: Causes, Consequences, and Environment. Croom Helm, London.

Darendeli M.B., Stokoe II K.H. (2001). Development of a new family of normalized modulus reduction and material damping curves. University of Texas, Geotechnical Engineering Report GD01-1.

Dazzaro L., Di Nocera S., Pescatore T., Rapisardi L., Romeo M., Russo B., Senatore M. R., Torre M. (1988). Geologia del margine della Catena Appenninica tra il F. Fortore ed il T. Calaggio (Monti della Daunia-Appennino Meridionale), Mem. Soc. Geol. Italiana, 41: 411–422.

Del Gaudio V., Pierri P., Wasowski J. (2003). An Approach to Time Probabilistic Evaluation of Seismically Induced Landslide Hazard. Bull Seismol Soc Am 93(2): 557–569. https://doi.org/10.1785/0120020016

Del Gaudio V., Wasowski J. (2004). Time probabilistic evaluation of seismically induced landslide hazard in Irpinia (Southern Italy). Soil Dyn Earthq Eng, 24(12): 915–928. doi:10.1016/j.soildyn.2004.06.019

Del Gaudio V., Wasowski J. (2007). Directivity of slope dynamic response to seismic shaking. Geophys Res Lett 34: L12301. https://doi.org/10.1029/2007GL029842

Del Gaudio V., Wasowski J (2011). Advances and problems in understanding the seismic response of potentially unstable slopes. Eng Geol, 122: 73–83.

Del Gaudio V., Pierri P., Frepoli A., Calcagnile G., Venisti N., Cimini G.B. (2007). A critical revision of the seismicity of Northern Apulia (Adriatic microplate — Southern Italy) and implications for the identification of seismogenic structures. Tectonophysics, 436: 9–35.

Del Gaudio V., Coccia S., Wasowski J., Gallipoli M.R., Mucciarelli M. (2008). Detection of directivity in seismic site response from microtremor spectral analysis. Nat Hazards Earth Syst Sci, 8: 751–762.

Del Gaudio V., Zhao B., Luo Y., Wang Y. & Wasowski J. (2019). Seismic response of steep slopes inferred from ambient noise and accelerometer recordings: the case of Dadu River valley, China. Engineering Geology. doi:10.1016/j.enggeo.2019.105197

Del Gaudio V., Wasowski J., Pierri P., Moretti A., Ferrini G. (2021). Multi-temporal analysis of ambient noise polarization to characterize site response in the town of Amatrice, shattered by the 2016 central Italy earthquake. Geophys. J. Int., 224: 739–759. doi:10.1093/gji/ggaa335

Di Lernia A., Cotecchia F., Elia G., Tagarelli V., Santaloia F., Palladino G. (2022). Assessing the influence of the hydraulic boundary conditions on clay slope stability: The Fontana Monte case study, Eng. Geol., 297, 106509. https://doi.org/10.1016/j.enggeo.2021.106509

DISS Working Group (2025). Database of Individual Seismogenic Sources (DISS), Version 3.3.1: A compilation of potential sources for earthquakes larger than M 5.5 in Italy and surrounding areas. Istituto Nazionale di Geofisica e Vulcanologia (INGV). https://doi.org/10.13127/diss3.3.1

EPRI (1993). Guidelines for Determining Design Ground Motions. EPRI TR-102293.

Falcone G., Elia G., Di Lernia A. (2023). Investigating the Influence of a Pre-Existing Shear Band on the Seismic Response of Ideal Step-like Slopes Subjected to Weak Motions: Preliminary Results. Geosciences, 13(5): 148. https://doi.org/10.3390/geosciences13050148

Fan X., Juang C.H., Wasowski J., Huang R., Xu Q., Scaringi G., vanWesten C.J., Havenith H.B. (2018). What we have learned from the 2008 Wenchuan

Earthquake and its aftermath: a decade of research and challenges. Eng Geol, 241: 25–32. https://doi.org/10.1016/j.enggeo.2018.05.004

Fracassi U., Valensise G. (2007). Unveiling the sources of the catastrophic 1456 multiple earthquake: Hints to an unexplored tectonic mechanism in southern Italy. Bulletin of the Seismological Society of America, 97(3): 725–748.

García-Pérez T., Ferreira A.M.G., Yáñez G., Iturrieta P., Cembrano J. (2021). Effects of topography and basins on seismic wave amplification: the Northern Chile coastal cliff and intramountainous basins. Geophysical Journal International, 227 (2): 1143–1167. https://doi.org/10.1093/gji/ggab259

Gizzi F.T. (2010). Il terremoto del 23 luglio 1930: nuovi dati macrosismici a scala regionale. In: Gizzi F.T. & Masini N. (a cura di), Dalle Fonti all'Evento. Percorsi strumenti e metodi per l'analisi del terremoto del 23 luglio 1930 nell'area del Vulture, 117–127. Napoli, Edizioni Scientifiche Italiane. ISBN 978-88-495-2050-7.

Geli L., Bard P.Y., Jullien B. (1988). The effect of topography on earthquake ground motion: A review and new results. Bull Seismol Soc Am, 78(1): 42–63. https://doi.org/10.1785/BSSA0780010042

Gemant A., Jackson W (1937). The Measurement of Internal Friction in Some Solid Dielectric Materials. The London, Edinburgh, and Dublin Philosophical Magazine & Journal of Science, XXII: 960–983.

Glinsky N., Bertrand E., Régnier J. (2019). Numerical simulation of topo graphical and geological site effects. Applications to canonical topographies and Rognes hill, South East France. Soil Dyn Earthq Eng, 116: 620–636. https://doi.org/10.1016/j.soildyn.2018.10.020

Gutenberg B., Richter C.F. (1944). Frequency of earthquakes in California. Bulletin of the Seismological Society of America, 34: 185–188.

Guzel Y., Rouainia M., Elia G. (2020). Effect of soil variability on nonlinear site response predictions: Application to the Lotung site. Comput Geotech, 121: 103444. https://doi.org/10.1016/j.compgeo.2020.103444

Harp E.L., Wilson R.C., Wieczorek G.F. (1981). Landslides from the February 4, 1976, Guatemala earthquake. USGS Professional Paper 1204-A: 40.

Harp E. L., R. C. Wilson (1995). Shaking intensity thresholds for rock falls and slides: evidence from 1987 Whittier Narrows and Supersti tion Hills earthquake strong-motion records, Bull. Seism. Soc. Am., 85: 1739–1757.

Harp E.L. and Jibson R.W. (2002). Anomalous concentrations of seismically triggered rock falls in Paicoma Canyon: are they caused by highly susceptible slopes or local amplification of seismic shaking? Bull Seismol Soc Am, 92: 3180–3189.

Hsieh S.Y., Lee C.T. (2011). Empirical estimation of the Newmark displacement from the Arias intensity and critical acceleration. Engineering Geology, 122: 34–42. https://doi.org/10.1016/j.enggeo.2010.12.006

Idriss I.M. (1990). Response of soft soil sites during earthquakes, in Proc. of the H. Bolton Seed Memorial Symposium, J. M. Duncan (Editor), Vol. 2, University of California, Berkeley: 273–289.

Idriss I.M., Sun J. (1992). User's manual for SHAKE91: a computer program for conducting equivalent linear seismic response analyses of horizontally layered soil deposits. In. Davis, California: Center for Geotechnical Modeling, Department of Civil Engineering, University of California.

ISPRA, Progetto CARG – Cartografia Geologica e Geotematica.

ISPRA (2022). IFFI – Inventario dei fenomeni franosi in Italia.

Jibson, R.W., 1993. Predicting earthquake-induced landslide displacement using Newmark's sliding block analysis. Transportation Research Board, National Research Council, Washington D.C., TR record 1411: 9–17.

Jibson R.W., Harp E.L., Michael J.A. (2000). A method for producing digital probabilistic seismic landslide hazard maps. Eng Geol, 58: 271 289. https://doi.org/10.1016/S0013-7952(00)00039-9

Jibson R.W., Rathje E.M., Jibson M.W., Lee Y.W. (2013). *SLAMMER-Seismic Landslide Movement Modeled using Earthquake Records*. U.S. Geological Survey Techniques and Methods.

Joyner W. B., Boore D.M. (1981). Peak horizontal acceleration and velocity from strong-motion records including records from the 1979 Imperial Valley, California, earthquake. Bulletin of the Seismological Society of America, 71(6): 2011–2038. https://doi.org/10.1785/BSSA0710062011

Kaklamanos J., Bradley B.A., Thompson E.M., Baise L.G. (2013). Critical Parameters Affecting Bias and Variability in Site-Response Analyses Using KiK-net Downhole Array Data. Bull Seismol Soc Am, 103(3): 1733–1749. https://doi.org/10.1785/0120120166

Keefer, D. K. (1984), Landslides caused by earthquakes, Geol. Soc. Am. Bull., 95: 406–421.

Keefer D.K., Wilson R.C. (1989). Predicting earthquake-induced landslides, with emphasis on arid and semi-arid environments, in Landslides in a Semi-Arid Environment, Inland Geological Society, P. M. Sadler and D. M. Morton (Editors), Vol. 2: 118–149.

Khan S., van der Meijde M., van der Werff H., Shafique M. (2020). Nat. Hazards Earth Syst. Sci., 20: 399–411. https://doi.org/10.5194/nhess-20-399-2020

Kleinbrod U., Burjánek J., Fäh D. (2019). Ambient vibration classification of unstable rock slopes: A systematic approach. Eng Geol, 249: 198–217.

Kolsky H (1963). Stress Waves in Solids. New York: Dover Publications.

Konno K., Ohmachi T. (1998). Ground motion characteristics estimated from spectral ratio between horizontal and vertical components of microtremor. Bull. Seism. Soc. Am. 88(1): 228–241.

Kuhlemeyer R.L., Lysmer J (1973). Finite Element Method Accuracy for Wave Propagation Prob lems. J. Soil Mech. & Foundations Div., ASCE, 99(SM5): 421–427.

Lanzano G., Luzi L., Pacor F., Felicetta C., Puglia R., Sgobba S., D'Amico M. (2019). A revised ground motion prediction model for shallow crustal Earthquakes in Italy. Bull Seism Soc Am, 109(2): 525–540.

Lee S.J., Chan Y.C., Komatisch D., Huang B.S., Tromp J. (2009). Effects of Realistic Surface Topography on Seismic Ground Motion in the Yangminshan Region of Taiwan Based Upon the Spectral-Element Method and LiDAR DTM. Bull Seism Soc Am 99(2A): 681–693. https://doi.org/10.1785/0120080264

Legesse A., Mammo T. (2024). Topographic amplification of seismic ground motion at the broad rift zone of SW Ethiopia. All Earth, 36(1): 1–9. https://doi.org/10.1080/27669645.2023.2293282

Limongelli L., Uricchio V., Zurlino G. (eds) (2006). La valutazione ambientale strategica per lo sviluppo sostenibile della puglia: un primo contributo conoscitivo e metodo logico. FESR Regione Puglia Assessorato Ecologia, Bari.

Locati M., Camassi R., Rovida A., Ercolani E., Bernardini F., Castelli V., Caracciolo C.H., Tertulliani A., Rossi A., Azzaro R., D'Amico S., Antonucci A. (2022). Database Macrosismico Italiano (DBMI15), versione 4.0 [Data set]. Istituto Nazionale di Geofisica e Vulcanologia (INGV). https://doi.org/10.13127/dbmi/dbmi15.4

Losacco N., Bottiglieri O., Santaloia F., Vitone C., Cotecchia F. (2021). The Geo-Hydro-Mechanical Properties of a Turbiditic Formation as Internal Factors of Slope Failure Processes. Geosciences, 11, 429. https://doi.org/10.3390/geosciences11100429

Louie J.N. (2001). Faster, Better: Shear-Wave Velocity to 100 Meters Depth from Refraction Microtremor Arrays. Bull Seism Soc Am 91(2): 347–364. https://doi.org/10.1785/0120000098

Luo Y., Fan X., Huang R., Wang Y., Yunus A.P., Havenith H.B. (2020). Topographic and near-surface stratigraphic amplification of the seismic response of a mountain slope revealed by field monitoring and numerical simulations. Eng Geol 271: 105607. https://doi.org/10.1016/j.enggeo.2020.105607

Lysmer J., Kuhlemeyer R. (1969). Finite Dynamic Model for Infinite Media. J. Eng. Mech., Div. ASCE, 95:EM4: 859–877.

Mayoral J.M., Asimaki D., Tepalcapa S., Wood C., Roman-de la Sancha A., Hutchinson T., Franke K., Montalva G. (2019). Site effects in Mexico City basin: Past and present. Soil Dyn Earthq Eng, 121: 369–382. https://doi.org/10.1016/j.soildyn.2019.02.028

Meletti C., Patacca E., Scandone P., Figliuolo B. (1988). Il terremoto del 1456 e la sua interpretazione nel quadro sismotettonico dell'Appennino Meridionale. Estratto da: B. Figliuolo: Il terremoto del 1456. Osseratorio Vesuviano Istituto Italiano di Studi Filosofici—Storia e Scienza della Terra Vol. I: 71–108; Vol. II: 35–163.

Meletti C., Galadini F., Valensise G., Stucchi M., Basili R., Barba S., Vannucci G., Boschi E. (2004). Zonazione sismogenetica ZS9 [Data set]. Istituto Nazionale di Geofisica e Vulcanologia (INGV). https://doi.org/10.13127/sh/zs9

Ministero delle Infrastrutture e dei Trasporti (2018) - Aggiornamento delle "Norme tecniche per le costruzioni. "Supplemento Ordinario n.8 alla Gazzetta Ufficiale n.42 del 20 febbraio 2018.

Molina S., Lang D.H., Singh Y., Meslem A. (2019). A period-dependent topographic amplification model for earthquake loss estimation. Bulletin of

Earthquake Engineering, 17: 3709–3725. https://doi.org/10.1007/s10518-019-00608-1

Morozov I.B., Smithson S.B. (1996). Instantaneous polarization attributes and directional filtering. Geophysics 61: 872–881.

Mostardini F., Merlini S. (1986). Appennino centro-meridionale. Sezioni geologiche e proposta di modello strutturale. Mem Soc Geol It, 35: 177–202.

Muscillo S. (2014). The contribution of ambient noise analysis to characterize the seismic response of marginally stable slopes. PHD Thesis, University of Bari “Aldo Moro”, 232 pages.

Nakamura Y. (1989). A method for dynamic characteristics estimation of subsurface using microtremor on the ground surface. Q Report Railway Tech Res Inst 30: 25–33.

Newmark N.M. (1965). Effects of earthquakes on dams and embankments. Geotechnique, 15: 139–160.

Ojomo O., Rathje E.M., Wang P., Lavrendiatis G., Zimmaro P., Asimaki D., Stewart J.P. (2024). Regional earthquake-induced landslide assessments for use in seismic risk analyses of distributed gas infrastructure systems. Eng Geol 340: 107664. https://doi.org/10.1016/j.enggeo.2024.107664

Ordaz M., Martinelli F., Aguilar A., Arboleda J., Meletti C. and D’Amico V. (2017). R-CRISIS. Program and platform for computing seismic hazard.

Parise M., Wasowski J. (2000). Fenomeni di dissesto nell’Appennino Dauno, ed implicazioni per il patrimonio archeologico e storico culturale, in Atti del Convegno “Condizionamenti geologici e geotecnici nella conservazione del patrimonio storico culturale”, Torino, Italy, 7–9 June 2000, 749–756.

Parise M., Federico A., Palladino G. (2012). Historical evolution of multi-source mudslides. Landslides and engineered slopes. In: Eberhardt E, Froese C, Turner

AK, Leroueil S (eds) Landslides and engineered slopes: protecting society through improved understanding. Balkema, Rotterdam, pp 401–407.

Parise M., Fiorillo F., Pagnozzi M., Addesso R., Cafaro S., D'Angeli I.M., Esposito L., Leone G., Liso I.S. (2021). Uncertainties in understanding groundwater flow and spring functioning in karst. ESS Open Archive. October 22.

Patacca E., Sartori R., Scandone P. (1990). Tyrrhenian basin and apenninic arcs: kinematic relations since late Tortonian times. Mem Soc Geol It, 45: 425–451.

Patacca E., Scandone P. (2007). Geology of the Southern Apennines. Boll Soc Geol It, Spec Issue, 7: 75–119.

Pellicani R., Frattini P., Spilotro G. (2014). Landslide susceptibility assessment in Apulian Southern Apennine: heuristic vs. statistical methods. Environ. Earth Sci., 72: 1097–1108. https://doi.org/10.1007/s12665-013-3026-3

Peruzzi G., Albarello D. (2015). Realizzazione di abachi regionali per amplificazioni litostratigrafiche finalizzati alla redazione di cartografie di microzonazione sismica di livello II relative alla Puglia Centrale e Settentrionale. Relazione Finale relativa alle attività svolte nell'ambito della Convenzione fra la L'Autorità di Bacino della Regione Puglia e il Dipartimento di Scienze Fisiche, della Terra e dell'Ambiente dell'Università degli Studi di Siena.

Pescatore T., Renda P., Schiattarella M., Tramutoli M. (1999). Stratigraphic and structural relationship between Meso-Cenozoic Lagonegro basin and coeval carbonate platforms in southern Apennines, Italy. Tectonophysics, 315: 269–286.

Piccardi L. (1998) - Cinematica attuale, comportamento sismico e sismologia storica della faglia attiva di Monte Sant'Angelo (Gargano): la possibile rottura superficiale del 'leggendario' terremoto del 493 d.C. Geografia Fisica e Dinamica Quaternaria, 21: 155–166.

Piccarreta M., Capolongo D., Boenzi F. (2004). Trend analysis of precipitation and drought in Basilicata from 1923 to 2000 within a southern Italy context. International Journal of Climatology, 24: 907–922.

Pieri P., Gallicchio S., Moretti M. (2011). Note Illustrative della Carta Geologica d'Italia alla scala 1: 50.000. F° 407 "San Bartolomeo in Galdo". ISPRA, Servizio Geologico d'Italia.

Pierri P., Romeo A., Casarano D., Capone P., Del Gaudio V. (2025). Combined Selection of Real and Simulated Accelerograms as Input for Seismic Site Response Modelling in Seismic Microzonation. Journal of Earthquake Engineering, 29(10):2067–2098.
https://doi.org/10.1080/13632469.2025.2486420

Polemio M., Casarano D. (2004). Rainfall and drought in southern Italy (1821–2001). In: Rodds J.C. & Ubertini L. (eds) Proceedings of UNESCO–IAHS–IWHA Sympo sium 'Water Science? A Basis for Civilization', Rome, December 2003. IAHS Publications, 286: 217–227.

Puglia R. (2005). Analisi della risposta sismica locale di San Giuliano di Puglia. PhD thesis, 231 pages.

Rai M., Rodriguez-Marek A., Yong A. (2016). Earthquake Spectra, 32(2): 1033–1054. https://doi.org/10.1193/113014eqs202m

Rajabi A.M., Khamehchiyan M., Mahdavifar M.R., Del Gaudio V., Capolongo D. (2013). A time probabilistic approach to seismic landslide hazard estimates in Iran. Soil Dynamics and Earthquake Engineering, 48: 25–34.

Rathje E.M., Saygili G. (2008). Probabilistic seismic hazard analysis for the sliding displacement of slopes - Scalar and vector approaches. J Geotech Geoenvironm Eng, 134: 804–814.

Refice A., Spalluto L., Bovenga F., Fiore A., Miccoli M.N., Muzzicato P., Nitti D.O., Nutricato R., Pasquariello G. (2019). Integration of persistent scatterer interferometry and ground data for landslide moni toring: the Pianello landslide (Bovino, Southern Italy). Landslides, 16: 447–468.

Rizzitano S., Cascone E., Biondi G. (2014). Coupling of topographic and stratigraphic effects on seismic response of slopes through 2D linear and equivalent linear analyses. Soil Dyn Earthq Eng, 67: 66–84. https://doi.org/10.1016/j.soildyn.2014.09.003

Romeo R., Delfino L. (1997). Catalogo nazionale degli effetti deformativi del suolo indotti da forti terremoti, Rapporto Tecnico SSN/ RT/97/04, Roma, Maggio 1997. www.serviziosismico.it/RT/rt9704/ frameset.html

Romeo R. (2000). Seismically induced landslide displacements: a predictive model. Eng Geol, 58(3–4): 337–351. https://doi.org/10.1016/S0013-7952(00)00042-9

Rovida A., Locati M., Camassi R., Lolli B., Gasperini P., Antonucci A. (2022). Catalogo Parametrico *dei Terremoti Italiani (CPTI15), versione 4.0 [Data set]. Istituto Nazionale di Geofisica e Vulcanologia (INGV). https://doi.org/10.13127/cpti/cpti15.4*

Sabetta F., A. Pugliese (1996). Estimation of response spectra and simulation of nonstationary earthquake ground motions, Bull. Seism. Soc. Am. 86(2): 337–352.

Sabetta F., Pugliese A., Fiorentino G., Lanzano G., Luzi L. (2021). Simulation of non-stationary stochastic ground motions based on recent Italian earthquakes. Bulletin of Earthquake Engineering, 19: 3287–3315. https://doi.org/10.1007/s10518-021-01077-1

Saygili G. and Rathje E.M. (2009). Probabilistically based seismic landslide hazard maps: An application in Southern California. Eng Geol, 109(3–4): 183–194. https://doi.org/10.1016/j.enggeo.2009.08.004

Sambridge M. (1999). Geophysical inversion with a neighbourhood algorithm: I. Searching a parameter space. Geophys. J. Int., 138: 479–494.

Scandone P. (1997). Linea di ricerca 2 “Sismotettonica,” in L’attivita` del GNDT nel triennio 1993–1995, A. Corsanego, E. Faccioli, C. Gavar ini, P. Scandone, D. Slejko and M. Stucchi (Editors), CNR-GNDT, Rome, 67–96. Scandone P, Mazzotti A, Fradelizio GL, Patacca E, Stucchi E, Tozzi M, Zanzi I (2003). Line Crop 04: southern Apennines. Mem Descr Carta Geol d’It, 62: 155–166.

Schiattarella M., Di Leo P., Beneduce P., Ivo Giano S. (2003). Quaternary uplift vs tectonic loading: a case study from the Lucanian Apennine, southern Italy. Quatern. Int., 101–102: 239–251. https://doi.org/10.1016/S1040-6182(02)00126-X

Schimmel M., Gallart J. (2003). The use of instantaneous polarization attributes for seismic signal detection and image enhancement, Geophys. J. Int., 155: 653–668.

Schimmel M., Gallart J. (2004). Degree of polarization filter for frequency dependent signal enhancement through noise suppression, Bull. seism. Soc. Am., 94: 1016–1035.

Seed H.B., Idriss I.M. (1970). Moduli and Dynamic Factors for Dynamic Response Analyses. University of California, Berkeley: Earthquake Engineering Research Center.

Sepúlveda S.A., Murphy W., Jibson R.W., Petley D.N. (2005). Seismically induced rock slope failures resulting from topographic amplification of strong ground motions: the case of Pacoima Canyon California. Eng Geol, 80: 336–348.

Silva W.J., Abrahamson N., Toro G., Costantino C. (1997). Description and validation of the stochastic ground motion model. Upton, New York: Brookhaven National Laboratory.

SM Working Group (2015) Guidelines for Seismic Microzonation. Conference of Regions and Autonomous Provinces of Italy – Civil Protection Department, Rome, 2015.

Spalluto L., Fiore A., Miccoli M.N., Parise M. (2021). Activity maps of multi-source mudslides from the Daunia Apennines (Apulia, southern Italy). Natural Hazards, 106: 277–301. https://doi.org/10.1007/s11069-020-04461-3

Sun P., Huang D. (2023). Regional-scale assessment of earthquake induced slope displacement considering uncertainties in subsurface soils and hydrogeological condition. Soil Dyn Earthq Eng, 164:107593. https://doi.org/10.1016/j.soildyn.2022.107593

Teramo A., Stillitani E., Bottari A., Termini D. (1999). The December 5th, 1456 Central Italy Earthquake: A Discussion of a Possible Reshaping of Intensity Distribution by Vectorial Modelling. Pure appl., geophys. 155: 131–148.

Troncone L., Troncone C., Castigliego A. (2024). Bozza della Relazione Illustrativa della Microzonazione Sismica di primo livello nel comune di Bovino (Regione Puglia).

Valensise, G., Pantosti D. (eds.) (2001). Database of Potential Sources for Earthquakes Larger than M 5.5 in Italy, Ann. Geophys. 44, Suppl. 1, with CD-Rom.

Valensise G., Pantosti D., Basili R. (2004). Seismology and Tectonic Setting of the Molise Earthquake Sequence of October 31-November 1, 2002, Earthq. Spectra, 20: S23–S37.

Vezzani L., Festa A., Ghisetti F.C. (2010). Geology and Tectonic Evolution of the Central-Southern Apennines, Italy. The Geological Society of America, Special Paper 469.

Vinale F. (1988). Caratterizzazione del sottosuolo di un'area campione di Napoli ai fini d'una microzonazione sìsmìca. Rivista Italiana di Geotecnica, 2: 77–100.

Visini F., Meletti C., Rovida A., D'Amico V., Pace B., Pondrelli S. (2022). An updated area-source seismogenic model (MA4) for seismic hazard of Italy, Nat. Hazards Earth Syst. Sci., 22: 2807–2827. https://doi.org/10.5194/nhess-22-2807-2022

Vucetic M., Dobry R. (1991). Effect of soil plasticity on cyclic response. J Geotech Eng, 117: 89–107.

Wasowski J. (1998). Understanding rainfall-landslide relationships in man-modified environment: a case history from Caramanico Terme (Italy). Env Geol, 35: 197–209.

Wasowski J., Del Gaudio V. (2000). Evaluating seismically induced mass movement hazard in Caramanico Terme (Italy). Eng Geol, 58(3–4): 291–311.

Wasowski J., Lamanna C., Casarano D. (2010). Influence of land-use change and precipitation patterns on landslide activity in the Daunia Apennines, Italy. Quarterly Journal of Engineering Geology and Hydrogeology, 43, 387–401. DOI 10.1144/1470-9236/08-101

Wasowski J., Lamanna C., Gigante G., Casarano D (2012). High resolution satellite imagery analysis for in ferring surface–subsurface water relationships in unstable slopes. Remote Sens. Environ., 124: 135–148. https://doi.org/10.1016/j.rse.2012.05.007

Wathelet M., Jongmans D., Ohrnberger M. (2005). Direct inversion of Spatial Auto Correlation Curves with the Neighborhood Algorithm. Bull. Seism. Soc. Am., 95: 1787–1800.

Wegel R.L., Walther H. (1935). Internal Dissipation in Solids for Small Cyclic Strains. Physics, 6: 141–157.

Wessel P., Luis J.F., Uieda L., Scharoo R., Wobbe F., Smith W.H.F., Tian D. (2019). The Generic Mapping Tools – GMT – Version 6.

Wieczorek, G.F. (1996). Landslide triggering mechanisms. In: Turner, A.K. & Schuster, R.L. (eds) Landslides, Inves tigations and Mitigation. National Research Council, Transportation Research Board Special Report, 247: 76–90.

Wilson R.C., Keefer D.K. (1985). Predicting the aerial limits of earthquake-induced landsliding. In: Ziony J.I. (ed) Evaluating earthquake hazards in the Los

Angeles region - an earth science perspective. US Geol Surv Profess Pap, 1360: 316–345.

Zezza F., Merenda L., Bruno G., Crescenzi E. and Iovine G. (1994). Condizioni di instabilità e rischio da frana nei comuni dell'Appennino Dauno Pugliese. Geologia Applicata e Idrogeologia, 29: 77–141.

Zumpano V., Ardizzone F., Bucci F., Cardinali M., Fiorucci F., Parise M., Pisano L., Reichenbach P., Santaloia F., Santangelo M., Wasowski J., Lollino P. (2020). The relation of spatio-temporal distribution of landslides to urban development (a case study from the Apulia region, Southern Italy). J Maps. https://doi.org/10.1080/17445647.2020.1746417